University of Southampton

Faculty of Engineering and the Environment

Computational Analysis of the Flow Field and Noise Radiation of a Generic Main Landing Gear Configuration

by

Koenraad Johannes van Mierlo

Thesis for the degree of Doctor of Philosophy

February 2014

UNIVERSITY OF SOUTHAMPTON

ABSTRACT

Faculty of Engineering and the Environment

Doctor of Philosophy

Computational Analysis of the Flow Field and Noise Radiation of a Generic Main Landing Gear Configuration

by Koenraad Johannes van Mierlo

This study investigates the flow field and acoustics of a generic four wheel main landing gear. The landing gear is an important airframe noise source during the approach phase. The characteristics of the flow field around the bogie area of the main landing gear are largely unknown. CFD simulations using the DES turbulence model have been used to calculate the unsteady flow field around a generic landing gear model. The surface pressure data has been sampled and used in a FW-H solver to determine far field noise levels. Two different landing gear models have been used, a simplified geometry and a more realistic complex geometry. Three different bogie angles have been simulated: horizontal bogie aligned with the flow, 10° toe up and 10° toe down.

Strong streamwise vortices are generated at the front wheels of the landing gear. The trajectory of these vortices determines where the turbulent flow interacts with the downstream components. This interaction leads to surface pressure fluctuations which are a major noise source. The flow field of the simplified configurations shows a consistent trend of the trajectory of the streamwise vortices with respect to changes in bogie angle. The far field noise levels generated by the different components of the simplified configurations are related to the distance at which the streamwise vortices pass.

The additional components of the complex landing gear geometry change the characteristics of the flow field. The strong streamwise vortices persist but they do not show the same trend as for the simplified configurations. The wake of the articulation link generates a turbulent inflow for the other components. The different characteristics of the flow field of the complex configurations lead to significant changes in the far field noise levels of the components compared to the simplified configurations.

Contents

List of Figures

List of Tables

Declaration of Authorship

I, Koenraad Johannes van Mierlo

declare that the thesis entitled

Computational Analysis of the Flow Field and Noise Radiation of a Generic Main Landing Gear Configuration

and the work presented in the thesis are both my own, and have been generated by me as the result of my own original research. I confirm that:

- this work was done wholly or mainly while in candidature for a research degree at this University;
- where any part of this thesis has previously been submitted for a degree or any other qualification at this University or any other institution, this has been clearly stated;
- where I have consulted the published work of others, this is always clearly attributed;
- where I have quoted from the work of others, the source is always given. With the exception of such quotations, this thesis is entirely my own work;
- I have acknowledged all main sources of help;
- where the thesis is based on work done by myself jointly with others, I have made clear exactly what was done by others and what I have contributed myself;
- parts of this work have been published as: a conference paper [1]. A second conference paper has been submitted [2]. A journal paper is currently under preparation.

Signed:

Date:

Acknowledgements

I would like to thank the following people for their support and encouragement during my study for a PhD. Professor Xin Zhang, my supervisor, for the opportunity to do a PhD in Southampton. Airbus and EPSRC for the funding of the project. My colleagues and friends at the university for the great times both at and away from the university. The AFM 5-a-side football team for the weekly sessions which are a perfect way to let off some steam. The J-Dream sailing team for all the great races and events we have participated in. Finally a special thanks to my parents and family who have continued to believe in me.

Abbreviations

AIAA	the American Institute of Aeronautics and Astronautics
ANDANTE	Aircraft Noise Disturbance Alleviation by Novel Technology
BANC	Benchmark problems for Airframe Noise Computations
CAA	Computational Aero Acoustics
CFD	Computational Fluid Dynamics
CFL	Courant Friedrichs Lewy
DES	Detached Eddy Simulation
DGPS	Differential Global Positioning System
fas	front axles
FFT	Fast Fourier Transform
FW-H	Ffowcs Williams - Hawkings
fwbs	front wheels and brakes
fws	front wheels
GCI	Grid Convergence Index
GPS	Global Positioning System
LES	Large Eddy Simulation
LHS	Left Hand Side
LIC	Line Integral Convolution
MLG	Main Landing Gear
MPI	Message Passing Interface

NAL	National Aerospace Laboratories
NASA	National Aeronautics and Space Administration
NTS	New Technologies and Services
OASPL	Overall Sound Pressure Level
PIV	Particle Image Velocimetry
QTD	Quiet Technology Demonstrator
RAIN	Reduction of Airframe and Installation Noise
RANS	Reynolds Averaged Navier Stokes
ras	rear axles
RHS	Right Hand Side
RMS	Root Mean Square
rwbs	rear wheels and brakes
rws	rear wheels
SA	Spalart Allmaras
SILENCER	Significant Lower Community Exposure to Aircraft Noise
SIMPLE	Semi-Implicit Method for Pressure-Linked Equations
SPL	Sound Pressure Level
std	standard deviation
URANS	Unsteady Reynolds Averaged Navier Stokes

Symbols

symbol	unit	description
α	$^\circ$	inclination angle
δ_{ij}	$-$	Dirac delta function
η	$-$	efficiency
$\boldsymbol{\eta}$	$[m]$	Lagrangian coordinate
ρ	$\left[\frac{kg}{m^3}\right]$	density
τ	$[s]$	retarded time
A	$-$	surface expansion factor
a	$\left[\frac{m}{s}\right]$	speed of sound
C_d	$-$	drag coefficient
C_l	$-$	lift coefficient
C_p	$-$	pressure coefficient
C_s	$-$	side force coefficient
D	$[m]$	wheel diameter
F	$[N]$	force
f	$\left[\frac{1}{s}\right]$	frequency
f	$-$	generalized function
I	$\left[\frac{W}{m^2}\right]$	sound intensity
J	$-$	Jacobian
L	$[m]$	length of the main strut
l	$[m]$	length

M	$-$	Mach number
P_{ij}	$\left[\frac{kg}{ms^2}\right]$	stress tensor
r	$[m]$	radiation distance
Re	$-$	Reynolds number
S	$\left[m^2\right]$	surface area
St	$-$	Strouhal number
T_{ij}	$\left[\frac{kg}{ms^2}\right]$	Lighthill stress tensor
t	$[s]$	time
U	$\left[\frac{m}{s}\right]$	free stream velocity
u_i	$\left[\frac{m}{s}\right]$	velocity
v_i	$\left[\frac{m}{s}\right]$	velocity
v_n	$\left[\frac{m}{s}\right]$	velocity of the surface
W	$[W]$	sound power
x_i	$[m]$	Cartesian coordinate

Chapter 1

Introduction

The growth in air transportation each year has led to pressure from the community living near airports to reduce the noise generated by the aircraft. Engine noise has reduced significantly during the past decades due to the introduction of the high-bypass ratio turbo fan. With the increase in the size of aircraft, airframe noise has become just as important as engine noise during the approach phase [3].

Airframe noise can be split into noise generated by the high lift devices and landing gear noise. Flight tests have shown that for large wide body aircraft landing gear noise is dominant over the noise of the high lift devices [3]. A lot of experimental research has been done to determine the major noise sources on the landing gear. Noise reduction treatments such as fairings [4] can be used to change the flow around the landing gear and reduce the level of the noise sources. The application of a bogie fairing has shown to reduce the high frequency noise but does not change the low frequency noise levels (<2 kHz) [5]. Phased array measurements used during fly over and wind tunnel tests have difficulties to pinpoint the low frequency noise sources which makes the reduction of low frequency noise extra complicated.

A different approach to the study of landing gear noise is the use of Computational Fluid Dynamics (CFD) which can be used to get a better insight in the unsteady flow field around a landing gear [6]. Relatively recently turbulence models have been developed which provide accurate CFD results and can be solved using modern computing facilities [7]. CFD has been applied to the flow around landing gear but there is room for improvement. During this project CFD will be used to calculate the flow field around two different landing gear models at multiple bogie inclination angles. The results of the CFD will be used to investigate the flow phenomena around the landing gear and determine their effect on the noise generation.

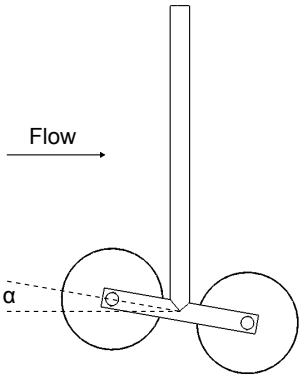

FIGURE 1.1: Definition of the bogie inclination angle α, the angle between the free stream velocity and the bogie centre line.

1.1 Aims and objectives

The aim of this research are two folds; the first aim is to obtain a better understanding of the flow field around the bogie area and the noise generated by the flow field; the second aim is to investigate the influence of the bogie inclination angle (see Figure 1.1) on the flow field and the noise generation. The aims are summarised as follows:

- to get a better understanding of the flow field around the bogie area of a main landing gear and to locate the major noise sources.
- to investigate the effect of the bogie inclination angle on the flow features and the aeroacoustic noise.

An incremental approach is used to get a better understanding of the noise contribution from different components and flow phenomena. To achieve these aims CFD simulations will be done and the results will be used to calculate the far field noise generated by the landing gear. Different inclination angles of the bogie will be simulated to investigate the influence of the bogie inclination angle on the flow features and far field noise levels.

1.2 Outline of the thesis

The structure of the thesis is as follows: the next chapter gives an overview of aeroacoustic theory and summarises previous aeroacoustic research (both experimental and numerical) applied to the landing gear noise problem. The different methods used during the study are described in chapter three. This includes a description of the landing gear

geometries, the setup of the CFD and FW-H solvers and the post processing routines. The aerodynamic results of the CFD simulations of the simple landing gear geometry are described in the fourth chapter followed by the acoustic results in the fifth chapter. This is followed by a chapter comparing OpenFOAM and Fluent and a chapter discussing the error and uncertainty. The next two chapters describe the aerodynamic and acoustic results of the complex landing gear geometry followed by last chapter with conclusions and recommendations.

Chapter 2

Literature Review

This chapter will give an overview of the development in aeroacoustic research in relation to main landing gear noise. The first section describes the aeroacoustic theory. The second section gives an overview of commonly used research methods in aircraft aeroacoustics: experimental, empirical and computational research. The chapter ends with a summary of the state of the current research.

2.1 Aeroacoustic theory

Aeroacoustic theory describes the generation and propagation of sound in an unsteady flow. Derivation of the aeroacoustic theory follows a similar approach as the derivation of the acoustic (wave) equations which describe the propagation of sound in a medium at rest. The next section therefore describes the derivation of the acoustic equations in a medium at rest before the derivation of the aeroacoustic equations is described.

2.1.1 Acoustic equations

The basic equations in acoustics, which follow from the conservation of mass and conservation of momentum principle, are the continuity equation (2.1) and the linearised momentum equation (2.2).

$$\frac{\partial \rho}{\partial t} + \frac{\partial}{\partial x_i}\left(\rho u_i\right) = 0, \tag{2.1}$$

$$\frac{\partial}{\partial t}\left(\rho u_i\right) + a^2 \frac{\partial \rho}{\partial x_i} = 0, \tag{2.2}$$

where ρ is the density, t is the time, x_i is the Cartesian coordinate, u_i is the flow velocity and a the speed of sound.

By taking the derivative of the continuity equation (2.1) with respect to t and the derivative of the approximate momentum equation (2.2) with respect to x_i and subtracting these, the ρu_i term cancels out. The result is the homogeneous wave equation (2.3) which describes the propagation of sound in an uniform medium at rest.

$$\frac{\partial^2 \rho}{\partial t^2} - a^2 \nabla^2 \rho = 0, \tag{2.3}$$

where ∇ is the gradient operator $\frac{\partial}{\partial x_i}$.

2.1.2 Aeroacoustic equations

The basis of the aeroacoustic theory has been developed by Lighthill [8] by using the continuity and the exact momentum equations to derive a wave equation with source terms. The theory explains the generation of sound by fluctuations in a medium at rest in an infinite domain. Instead of using the linearised momentum equation (2.2) the exact momentum equation (2.4) is used.

$$\frac{\partial}{\partial t}\left(\rho u_i\right) + \frac{\partial}{\partial x_j}\left(\rho u_i u_j + P_{ij}\right) = 0, \tag{2.4}$$

where $\rho u_i u_j$ are the Reynolds stresses and P_{ij} is the compressive stress tensor.

The exact momentum equation (2.4) is rewritten in a form similar to the approximate momentum equation (2.2).

$$\frac{\partial}{\partial t}\left(\rho u_i\right) + a^2 \frac{\partial \rho}{\partial x_i} = -\frac{\partial T_{ij}}{\partial x_j}, \tag{2.5}$$

where T_{ij} is Lighthill's stress tensor which represents the fluctuating stresses in the flow.

$$T_{ij} = \rho u_i u_j + P_{ij} - a^2 \rho \delta_{ij}, \tag{2.6}$$

where $\delta_{ij} = 1$ for $i = j$ and 0 otherwise.

By taking the derivative of the continuity equation (2.1) with respect to t and the derivative of the momentum equation (2.5) with respect to x_i and subtracting these,

the ρu_i term cancels out. The result is an inhomogeneous wave equation (2.7) which describes the propagation of sound caused by turbulent fluctuations in a medium at rest.

$$\frac{\partial^2 \rho}{\partial t^2} - a^2 \nabla^2 \rho = \frac{\partial^2 T_{ij}}{\partial x_i \partial x_j}, \tag{2.7}$$

is exact since no approximations have been made. For low Mach number (M) flows the pressure and density fluctuations will be small and the equation (2.6) for the applied stresses can be simplified.

$$T_{ij} \approx \rho u_i u_j. \tag{2.8}$$

Sound generated by the fluctuating stresses is comparable to that of a quadrupole and thus T_{ij} is referred to as a quadrupole term. Lighthill has used dimensional analysis to show that the acoustic intensity of the quadrupole term (I_Q) can be approximated by:

$$I_Q(r) \approx \rho_0 U^8 a_0^{-5} \left(\frac{l}{r}\right)^2, \tag{2.9}$$

where r the distance from the source and l the characteristic length of the object in the flow is. The sound power (W_Q) of a quadrupole source is calculated by multiplying the intensity with the surface area of a sphere (proportional to r^2) surrounding the source.

$$W_Q \approx \rho_0 U^8 a_0^{-5} l^2. \tag{2.10}$$

The energy supplied by the flow is proportional to $\rho_0 U^3 l^2$ which means that the efficiency of the sound production of a quadrupole (η_Q) can be calculated by dividing the sound power (2.10) with the supplied energy ($\rho_0 U^3 l^2$).

$$\eta_Q \propto M^5. \tag{2.11}$$

Curle [9] extended Lighthill's work to include the effect of solid boundaries in the flow. This led to the following equation.

$$\frac{\partial^2 \rho}{\partial t^2} - a^2 \nabla^2 \rho = \frac{\partial^2 T_{ij}}{\partial x_i \partial x_j} - \frac{\partial}{\partial x_i} P_{ij}, \tag{2.12}$$

the extra term $\left(\frac{\partial}{\partial x_i}P_{ij}\right)$ in this inhomogeneous wave equation (2.12) is the effect of fluctuating pressures on the surface of a solid object. The sound generated by the fluctuating pressures corresponds to the sound generated by a dipole. A dimensional analysis of the dipole term gives the following approximation for the acoustic intensity I_D.

$$I_D(r) \approx \rho_0 U^6 a_0^{-3} \left(\frac{l}{r}\right)^2, \tag{2.13}$$

where r the distance from the source is. Multiplying the intensity with the area of a sphere around the source gives the sound power of the dipole (W_D).

$$W_D \approx \rho_0 U^6 a_0^{-3} l^2. \tag{2.14}$$

Dividing the sound power with the energy supplied by the flow gives the efficiency of the dipole source (η_D).

$$\eta_D \propto M^3. \tag{2.15}$$

When the sound radiating efficiency of the dipole (2.15) and quadrupole term (2.11) at low Mach number flow are compared it becomes clear that the dipole is a much more efficient sound radiator.

The above theory describes the sound generated by turbulence and pressure fluctuations on the surface of an object in an unbounded medium at rest. Ffowcs Williams and Hawkings [10] developed the theory further to include the effect of moving surfaces in arbitrary motion. The derivation follows the same process as done by Lighthill but uses generalised function theory. Generalised functions are a mathematical concept generalising the classical concept of a function. Dirac [11] was the first to use generalised functions with the δ-function and its derivatives. Generalised functions are used to make non continuous distribution behave like a classical function and are therefore very useful in physics and engineering. More information on the subject of generalised functions can be found in work done by Vladimirov [12].

$$\left(\frac{\partial^2}{\partial t^2} - a^2\frac{\partial^2}{\partial x_i^2}\right)(\overline{\rho - \rho_0}) = \frac{\partial}{\partial t}\left(\rho_0 v_i \delta(f)\frac{\partial f}{\partial x_i}\right) - \frac{\partial}{\partial x_i}\left(p_{ij}\delta(f)\frac{\partial f}{\partial x_j}\right) + \frac{\partial^2 \overline{T_{ij}}}{\partial x_i x_j}, \tag{2.16}$$

where $\overline{\rho - \rho_0}$ the generalised density perturbation is, v_i is the velocity of the surface, $\delta(f)$ is the Dirac delta function and $\overline{T_{ij}}$ is the generalised form of Lighthill's stress tensor.

The three terms on the right hand side of the equation are often called the thickness (monopole), loading (dipole) and quadrupole source terms. The thickness source term models the sound generated by the displacement of fluid by the movement of the object. The loading term models the sound generated by the unsteady forces (pressure fluctuations) on the surface of the object and the quadrupole term models the sound generated by the turbulent stresses in the flow surrounding the object. The solution of equation (2.16) in integral form given by Ffowcs Williams and Hawkings [10] is listed below in equation (2.17).

$$\begin{aligned} 4\pi a^2(\rho(\mathbf{x},t)-\rho_0) &= \frac{\partial^2}{\partial x_i \partial x_j}\int\left[\frac{T_{ij}J}{r\,|1-M_r|}\right]d\boldsymbol{\eta} - \frac{\partial}{\partial x_i}\int\left[\frac{p_{ij}n_jA}{r\,|1-M_r|}\right]dS(\boldsymbol{\eta}) \\ &\quad + \frac{\partial}{\partial t}\int\left[\frac{\rho_0 v_n}{r\,|1-M_r|}\right]dS(\boldsymbol{\eta}), \end{aligned} \tag{2.17}$$

where J is the Jacobian accounting for any divergence of the source, r is the radiation distance, M_r is the component of M in the direction of r, $\boldsymbol{\eta}$ is a Lagrangian coordinate, A is a factor accounting for any expansion of the surface, S is the surface area of the object and v_n is the velocity of the surface. In this expression the terms in square brackets need to be evaluated at retarded time $\tau = t - r/a$.

Equation 2.17 can be used to calculate far field noise based on the sources in the near field region. In the near field region the flow is unsteady and there is interaction between the fluid dynamics and acoustics. In the far field region the flow is steady and the acoustic waves propagate through the fluid without interaction. To calculate the far field noise it is thus necessary to determine the sources in the near field first. The near field noise sources, the right hand side terms of equation 2.17, are in general determined using Computational Aeroacoustics (CAA) / Computational Fluid Dynamics (CFD) simulations.

The use of the term Computational Aeroacoustics (CAA) has become widespread recently and it is not always clear what the difference is between CAA and CFD. Traditionally the term CFD has been used for numerical simulations of the Navier Stokes equations with the main focus on resolving the flow field. Acoustic waves in a fluid are governed by the Navier Stokes equations which means that CAA is a subset of CFD. The main focus of CAA is not just the flow field but incorporates both the flow field and the acoustic field. However hybrid methods, which combine CFD with a separate numerical solver of the acoustic propagation to the far field, are also being described using the

term CAA. A hybrid method is used in this study which means it only complies with the latter description of CAA.

2.2 Landing gear noise

Landing gear noise is a major contribution to the overall airframe noise during the approach phase. The noise generation by a landing gear has initially been studied using experimental methods but the increase in computer power has led to an increase of the computational research. This section will give an overview of the current state of both experimental and computational landing gear noise research.

2.2.1 Experimental research

Fly-over measurements

Different fly-over measurements using microphone arrays are described in the literature [13–16]. The noise measurements are done with microphone arrays which differ in size from a 12m diameter circle to an approximate 90m square while the number of microphones varies from 161 to 614. The typical frequency range of the array measurements is from 250 Hz to 8 kHz. The flight height during the different studies varies from 43m to approximately 200m and the flight paths are registered either by using a Differential Global Positioning System (DGPS) or by laser tracking.

A GPS receiver uses the signal of different satellites to determine its location. The accuracy of the GPS system is not sufficient but can be improved. At certain fixed locations on earth the GPS position is compared to the real position. This difference is then broadcast such that the DGPS receivers can use this information to improve the accuracy of the system. Laser tracking uses multiple laser distance meters. When an object comes within range of a laser distance meter it will register the distance to the object. By using multiple laser distance meters spread some distance apart the results can be combined to determine the location of the aircraft.

The different results show that the engines, high lift devices and landing gear are the main noise sources but the resolution is not good enough to give more specific results. Piet et al. [17] have done fly-over measurements to test a low noise configuration and a clear noise reduction compared to the baseline configuration is measured. This shows that fly-over noise measurements are a useful tool to asses the noise production of different aircraft configurations.

Wind tunnel measurements

Wind tunnel tests have been used for a long time to investigate aircraft performance including noise production. One of the first papers about wind tunnel testing to determine landing gear noise is written in 1977 by Heller and Dobrzynski [18]. In this research a small scale landing gear model is tested in an open jet wind tunnel and also tested while it was attached to a glider to determine the aerodynamic noise. Since then the noise measurement and flow visualisation techniques have improved a lot. Noise measurements of small scale full aircraft models have been done and the results show that high lift devices and landing gear are the main noise sources [19–22]. Stoker et al. [23] have done aeroacoustic experiments in a pressurised wind tunnel to investigate the effect of Reynolds number on noise production. Although it is shown that Reynolds number has an effect on the noise the study also shows that many practical problems are encountered during the pressurised testing. These full aircraft model tests do not provide enough detailed information about noise generation because the scale of the models is too small and a lot of the important details of the landing gear have been removed. The small details of the landing gear are the main sources of high frequency noise and thus a large scale model is needed to get reliable results.

Nowadays only the landing gear is often wind tunnel tested and the scale factors are in the range of 25% to full scale. This reduces a lot of the scaling problems and more details (see figure 2.1) can be included into the model. Since the landing gear is only used during a short period of the flight it is designed to be functional and not aerodynamic which leads to a lot of turbulence around the landing gear. Wind tunnel experiments have been done to get a better understanding of the flow field around the landing gear. Flow visualisation techniques, particle image velocimetry and tufts, are used to show the different flow features around the landing gear.

Lazos [24] has done windtunnel test of a simple four wheel landing gear configuration with the bogie aligned with the flow. The research focuses on the interaction of the flow between the front and rear wheels. The flow is attached at the front part of the first wheel but separates when it reaches the back of the wheel. The separation leads to vortex shedding and the turbulent flow impinges on the second wheel. This vortex shedding and impingement of turbulent flow on a solid object are expected to be a significant noise source. The flow at the front of the second wheel is separated due to the turbulent wake of the first wheel. Outside the wake area the flow is attached until it reaches the back of the second wheel where it separates just like on the first wheel. The Particle Image Velocimetry (PIV) images show the presence of a vortex in the gap between the first and second wheel. This midwheel vortex is not in a stable location but

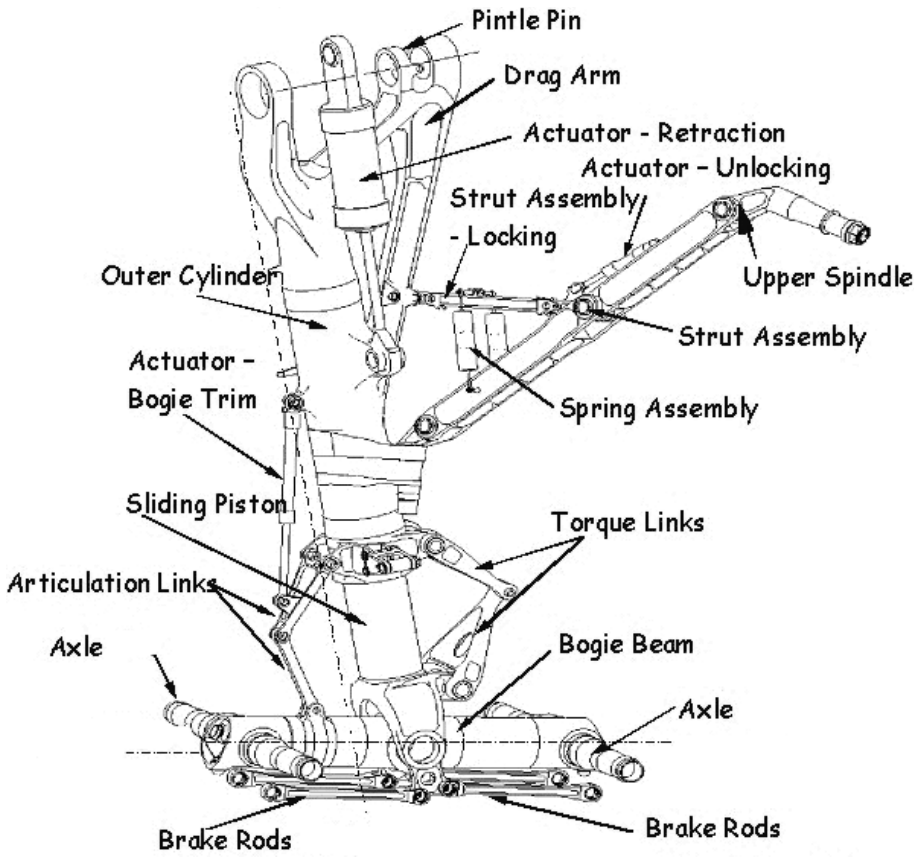

FIGURE 2.1: A schematic of main landing gear components, wheels and brakes have been removed for clarity (picture supplied by Airbus).

moves around. The asymmetric flow conditions and the resulting midwheel vortex are attributed to the asymmetric geometry created by the support strut.

The same landing gear geometry is again used by Lazos [25] to study the flow features around the wheels in more detail. Oilflow visualisation and pressure transducers are used to map the topology of the flow on the fore and aft wheel surface. Oilflow patterns are analysed to show the location of attachment and separation lines. The results show that analysing the surface flow topology is a powerful method to gain more insight in the flow features around the landing gear. The results show good agreement with the flow measurements of the previous study.

Full scale measurements of 2 and 4 wheel A320 landing gears in an open jet wind tunnel in an anechoic chamber [26] show that the landing gear generates a broadband noise of almost constant level. The noise is omnidirectional but shows a small increase in forward and aft directions. The results of tests at different flow velocities approximately collapse onto each other when compared using the Strouhal number $St = \frac{f \cdot L}{U}$ and the U^6 scale. The predicted noise level on the ground however will scale with U^7 due to the convective amplification. Convective amplification is the difference in sound pressure

between a stationary source and one in motion. The sound waves emitted by a moving source are compressed when the source is moving towards the observer and expand when the source moves away from the observer resulting in the well known Doppler shift in the frequency. The sound pressure is also influenced by the motion of the source and this effect is called convective amplification. Depending on the source type (monopole, dipole or quadrupole), the sound pressure can be corrected for convective amplification using formula described by Ruijgrok [27]. The opposite is needed when wind tunnel measurements are converted to fly over noise levels: the effect of convective amplification needs to be added to the measurements.

The RAIN research project (Reduction of Airframe and Installation Noise $1998 - 2001$) funded by the European Commission consisted of a cooperation between Airbus and different European research facilities and universities. Its goal was to gain knowledge of the noise and flow characteristics and then use this knowledge to reduce the airframe noise. Full scale nose and main $A340$ landing gears have been tested in an anechoic open jet wind tunnel [28, 29]. Different fairings were tested such as: bogie beam under tray, brake fairings, leg-door filler, torque link cover and wheel caps. A low noise configuration test was done using all fairings and a baseline test was done without any fairings. Further tests using different combinations of the fairings were done to investigate their effectiveness. The low noise configuration reduced broadband noise between 1 and 5 dB compared to the baseline configuration. The most efficient noise reducing fairing of this test is the bogie beam under tray. Another effective way to reduce noise which was found during this project is to align the bogie with the flow direction. Aligning the bogie with the flow shields the downstream components from the high speed flow which reduces the noise generation. The results from the measurement with a microphone array confirm this by showing that the source strength in the downstream part of the landing gear has been reduced.

Closed wind tunnel testing of a high fidelity 26% scale 6 wheel 777 main landing gear was done in the NASA Ames Research Center [30] to investigate the location of the main noise sources. Microphone array measurement revealed that the torque link, bogie, axles and brakes are the main noise sources on the landing gear. Integration of the noise source map is done to get the sound pressure level values. Tests of a fully faired simplified landing gear model with the bogie aligned with the flow show that a maximum noise reduction of 15 dB can be reached. The used configuration is unrealistic and so the future noise reduction potential is estimated at 6 to 8 dB.

The same high fidelity 26% scale 6 wheel 777 main landing gear has also been tested in the Virginia Tech wind tunnel [31]. A phased array consisting of 32 microphones was used to determine the location of the noise sources. After testing the complete landing

gear different components such as side stays were removed to investigate their influence on the noise production. It was found that the wake generated by the front side stay has a large influence on the noise generated by the rear side stay. The test results show that the main contributors to low frequency noise are the rear side stay, rear part of the bogie, the torque link and the wheel caps. The mid frequency noise is mainly generated by the brakes, axles and a hydraulic cylinder attached to the main strut. The most important high frequency noise sources are the brakes, axles and the rear lock link.

After the European Commission funded RAIN project a new research project was started in Europe by Airbus and partners called SILENCER (Significant Lower Community Exposure to Aircraft Noise) [4]. The approach to landing gear noise taken in the SILENCER project is different from all the other ones because it started with a clean sheet of paper. The goal of the project was to design a new functional low noise landing gear configuration based on the dimensions of an $A340$ landing gear. Using the experience from the RAIN project and CFD to evaluate different designs, led to an Advanced Low Noise landing gear. The main features of this design are that all the small parts have been relocated such that they are shielded from the high speed flow and aerodynamic fairings have been added to the large components. The Advanced Low Noise landing gear has been tested at full scale in an anechoic open jet wind tunnel to determine the noise characteristics. The results show that the Advanced Low Noise landing gear reduces the noise level by 5dB compared to the basic $A340$ landing gear. Unfortunately the noise reduction in the overhead position is only 3.7dB. The noise source distributions maps from the phased array microphone measurements show that the bogie area is the main low frequency noise source. Further reduction of landing gear noise is possible but to achieve a significant reduction a different airframe structure is needed.

As a part of the QTD II (Quiet Technology Demonstrator) program a number of different fairings for the Boeing 777 main landing gear have been designed and tested at Virginia Tech wind tunnel [32]. The fairings target the major noise sources found during earlier wind tunnel tests [30, 31]. The fairings are designed such that they do not interfere with normal aircraft operation. Four different fairings have been tested: cable harness fairing, main strut fairing, break cylinder fairing and a bogie beam (toboggan) fairing. The cable harness fairing has not shown a reduction in the measured noise. The main strut fairing closes the gap between the main strut and the side door thereby reducing the strut noise. The brake cylinder fairings reduce the noise sources at the brakes but become redundant when a wide bogie beam fairing is applied. Aligning the bogie with the flow gives an extra noise reduction. The fairings have also been tested during fly over sound measurements but a noise reduction could not be determined due to the presence of other strong noise sources [15].

A different type of fairing has been designed and tested by Ravetta et. al. [32, 33]. These fairing consist of elastic membrane (cloth) and cover the parts of the 777 landing gear where the major noise sources are located such as strut, braces and bogie. The strut fairing covers a large part of the strut and most of the landing gear door such that it shields the small components from the flow and closes the gap between the door and the strut. The braces fairing is wrapped around the front and rear brace which should eliminate the noise generated by the impingement of the wake from the front brace on the rear brace. The bogie beam fairing is wrapped around the bogie, brake rods and axles. Phased array measurements show a clear reduction in the source strength when the elastic fairings are applied. The integrated spectra show a noise reduction of 2 to 5 dB in the overhead direction compared to the baseline landing gear. Different fairing materials have been tested for the braces fairing and the bogie fairing but the results are inconclusive. The solid fairing around the braces performs better than the elastic one while the result for the bogie show that the elastic fairing better performs than the solid fairing. Although these fairings have shown promising results there are still questions about their interference with normal the landing gear operation.

Recently the Virginia Tech wind tunnel has been converted to a semi anechoic facility [34] and since then the 26% scale Boeing 777 landing gear tested previously by NASA [30] and Virginia Tech [31] has been retested [35]. Phased array measurements from three different locations were done and compared with results from previous tests in the hard walled tunnel. Comparison of the old data with the new measurements shows cleaner beam forming plots due to the reduced background and reflected noise. The integrated sound pressure levels in the semi anechoic tunnel are lower than in the hard walled tunnel due to the same reasons. Comparison of near field and far field measurements shows that the far field measurements contain more detailed information of the noise sources. The explanation for this effect is that when the array is located in the near field the landing gear model blocks part of the noise. Another measurement from the far field, using a different angle, shows even more details about the noise sources. This illustrates that measurements from directly below the landing gear are not the most appropriate when determining noise sources.

Humphreys et. al. [36] have done a noise directivity study in an anechoic wind tunnel with a 6.3% scale 777 main landing gear. Four different configurations of a baseline gear with side door and bogie fairing have been tested at four different Mach numbers between 0.11 and 0.17. A phased array has been placed at different locations around the model to measure noise from different directions. Post processing of the results show that the acoustic intensity scales with the sixth power of flow velocity as expected. The bogie fairing reduces the high frequency noise but leads to a small increase in low frequency noise compared to the baseline model. These measurements provide noise

directivity plots which are used by Burley et. al. to test NASA's empirical landing gear noise models [37]. Reynolds number effects are not mentioned in this study but will certainly have some influence on the results when testing such a small model.

Bogie noise research

After the SILENCER project a further experimental investigation of the noise from the bogie area was done in which the Advanced Low Noise landing gear at 25% model scale was wind tunnel tested [38]. The main parameters which were varied during these tests are: bogie inclination angle, bogie beam length and lateral wheel spacing. Different porous fairings have also been tested. Noise source locations are determined using a microphone array and sound pressure levels are calculated by integration of the main noise source areas on noise maps. The idea behind the porous fairing is that it deflects the main part of the flow and slows down the part of the flow that goes through it. This slow flow leads to an increase in the pressure behind the fairing such that the wake is not sucked back in. Noise levels are not significantly reduced by changing the bogie beam length and wheel spacing but the use of porous fairings is promising. The configuration producing the lowest sound pressure levels has an enlarged wheel spacing between the front wheels, an enlarged porous bogie fairing and a 10° toe down inclination of the bogie.

Flight tests with the fairings designed during the SILENCER project have shown that the fairings are efficient at the mid and high frequencies but lead to an increase in low frequency noise and also introduce a new tonal noise source. Li et al. [5] have done wind tunnel tests to determine the location of this tonal noise source. Different under tray fairings are also tested to try to reduce the mid and low frequency noise. The tonal noise is caused by a combination of aeroacoustic feedback mechanism and resonance between the leg door and the hinge door. Five different treatments to remove the tonal noise are tested of which three are successful: adding a serrated edge spoiler, rotation of the hinge door and removal of the hinge door. The placement of vortex generators on the leg door and covering the edge of the hinge door with soft material reduce the tone but do not remove it. The different under tray fairings that are tested are: a solid fairing, a porous fairing with brushes covering the brakes, a slotted fairing and a slotted fairing covered with cloth. All the new fairings show an improvement in the mid frequency range compared to the solid fairing. Application of the perforated fairing with brushes shows a reduction in the high frequency noise compared to the application of the slotted fairing which leads to an increase of the high frequency noise. Covering the slotted fairing with a cloth reduces the high frequency noise to the same level as the solid fairing. Although the fairings reduce the mid frequency noise they do not change

the low frequency noise. The low frequency noise is most likely caused by the large scale vortex shedding around the model which will be difficult to reduce.

Quayle et al. from Cambridge University [39] have done wind tunnel tests to investigate the influence of some basic parameters on landing gear noise. The parameters of a simplified landing gear model that are varied are bogie length, axle length and wheel edge radius. The longitudinal and transverse spacing of the basic wheels only has a small influence on the generated noise but does become important when more rounded wheels are used. The rounded wheels generate more noise especially when they are used in combination with the long bogie beam. The explanation for this effect is that more high speed flow is entrained by the wake from the front wheels. A combination of wheels with a large edge radius and wheels with a smaller edge radius has a remarkable effect: the noise increases when the rounded wheels are in front of the blunt wheels and decreases when the rounded wheels are behind the blunt wheels. A more streamlined landing gear is tested which has tracks instead of wheels. This streamlined model leads to a significant noise reduction compared to the baseline geometry. Addition of a fairing between the two axles reduces the noise even further especially at the lower frequencies. This shows that the flow around the axles and the junction between bogie and strut is responsible for a large part of the low frequency noise.

Remillieux et al. [40] have compared 2 different bogie fairings at the Virginia Tech semi anechoic wind tunnel: the NASA toboggan fairing and a flexible cloth fairing developed at Virginia Tech. The comparison shows that the flexible fairing reduces the noise levels but it is not as effective as the solid toboggan fairing. Both fairings block the noise from the strut and door directly below the landing gear. A measurement from a more downstream angle shows that the noise sources at the door and strut are dominant once a bogie fairing has been applied. It is suggested that the largest reduction could be achieved by applying the NASA toboggan fairing in combination with flexible cloth fairings around the door, strut and side stays.

Boorsma et al. [41] have investigated the use of perforated fairings to reduce landing gear noise. The application of solid fairings reduces the mid and high frequency noise but leads to an increase in low frequency noise. When perforated fairings are used a part of the flow goes through the perforations which breaks up the large structures in the flow and thereby reduces the low frequency noise. The perforations are most efficient when applied near the stagnation area, if applied at other locations the self noise of the perforations cancels the noise reduction.

2.2.2 Empirical aeroacoustics

Empirical models have been developed to predict the noise generation of airframe components such as landing gears. The models are derived from aeroacoustic theory combined with CFD and wind tunnel test results. Smith et al. [42] have developed a landing gear noise prediction method. This methods assumes the noise sources are compact and the intensity of the source follows the relation derived by Curle (2.13). The landing gear noise is split in different components such as directivity, fairings, struts, wheels, and dressings. Smith and Chow derive empirical formulas for the noise generated by each component based on results from anechoic wind tunnel measurements. Comparison of predictions using the empirical model with flyover measurements show good agreement but an over prediction in forward direction and under prediction in the rear direction.

Smith et al. [43] used their empirical model to predict the noise of the landing gear with different fairings. The predictions were compared with wind tunnel noise measurements and the correlation between them is reasonable. This makes the empirical model an useful method to investigate landing gear noise reduction. An effect of fairings that became clear during the measurements is that they may increase local flow velocity which will lead to an increase in sound level. The same empirical model was also used by Molin et al. [44] in the prediction and testing of low noise landing gear and good agreement between the empirical model and both fly-over tests and wind tunnel results is shown (see figure 2.2).

Guo et al. [45] split the landing gear noise based on frequency into a low, mid and high frequency part. The wheels are responsible for the low frequency noise while the struts are the main source of mid frequency noise. The wavelength of the low and mid frequency noise is long compared to the dimensions of the landing gear and thus are these sources compact. Sound pressure level of compact noise sources scales according to U^6. The small parts of the landing gear are responsible for the high frequency noise. The size of the small parts is comparable or larger than the wavelength of the high frequency noise such that these sources are not compact. To account for this effect Guo et al. scale the sound pressure level of these sources according to U^7. Other effects included in the empirical model are: distance to the observer, size of the components, number of components, directivity, Mach number, complexity factor and frequency (using a function based on the Strouhal number). The coefficients in the empirical model are determined by linear regression from anechoic wind tunnel data.

In [46] Guo uses statistical properties of the flow and aeroacoustic theory to derive asymptotic analytical solutions of the far field noise for the different frequency domains. These results are then used to construct an improved empirical model [47–49]. This

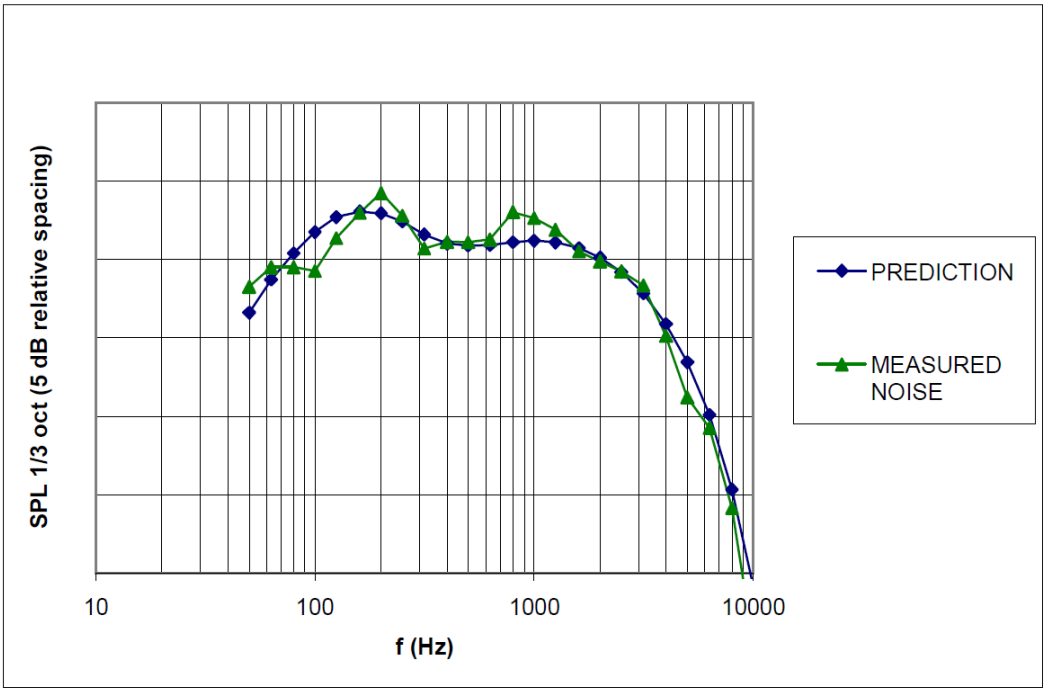

FIGURE 2.2: Comparison of A340 main landing gear measured and predicted noise spectra (Source: [44]).

prediction model is validated by comparing it with 737 wind tunnel results and 777 fly over measurements. Good agreement both in trends as in sound level is achieved.

Lopes et al. [50] have developed a tool kit to predict landing gear noise. The landing gear is split up in different objects. Besides the geometric parameters each object also has an upstream and downstream local environment. The local environment contains information on the flow velocity, turbulence intensity and acoustic field. Empirical formulas describe the noise generated by an object based on the geometric parameters and the local environment. Combining the noise generated by the different objects will give the total landing gear noise. The published results of this model only contain a cylinder element and a wheel object. The local environment assumed for each object is the free stream velocity. The sound level predicted by the model is not accurate yet but the whole tool kit is still under development. The results of this method are assumed to improve when more objects are added and when the local environments are better defined.

Smith et al. [51] have improved their previous model [43] by including installation effects. The effect of reduced flow velocity under the wing and the effect of the wake of other landing gear have been added to the model. Until now the model was able to predict landing gear noise from wind tunnel tests with a reasonable accuracy and these changes should improve the noise prediction of landing gear in real flight. The predictions of the model are compared to wind tunnel test data and fly over test data. It is found that

the model predicts a larger noise reduction in real flight than measured during fly over tests. There are two possible reasons given for this discrepancy: the flow in real flight is different from the flow in the wind tunnel and there may be secondary unidentified noise sources.

The local flow velocity has a strong effect on the amount of noise radiated by the landing gear. Guo [52] has used CFD to investigate the influence of the angle of attack on the local flow velocity at the location of the both the nose and main landing gear. The flow velocity at the nose landing gear is higher than free stream while the flow velocity at the main landing gear lower than free stream is. The flow velocity at the both the main and nose landing gear reduces with increasing angle of attack. The increase in lift reduces the flow velocity at the main landing gear while the movement of the stagnation point causes the reduced flow speed at the nose landing gear. The dependency of the local flow velocity on angle of attack is well behaved such that it can be modelled by a set of simple equations. These equations can be included in empirical models to improve the accuracy of the far field noise prediction.

2.2.3 Computational research

Computational aeroacoustics require large computer resources which only recently have become available. For this reason there are not many papers discussing computational aeroacoustics of main landing gear. Most of the published papers describe simulations using a simplified approximate model of a Boeing 757 main landing gear as the geometry. Different approaches are used to calculate the flow around this geometry. An overview of the different landing gear CFD simulations is given in table 2.1.

Souliez et al. [53] published one of the first computational landing gear results. In this study the Navier-Stokes equations are solved on an unstructured grid. The artificial dissipation of the integration scheme acts as a sub-grid turbulence model. The flow around two configurations is calculated: a basic configuration and a configuration without side strut. The near field noise is computed using three different methods: a direct calculation from the CFD results, a FW-H calculation using the sources on the landing gear surface and a FW-H calculation using the sources on a permeable surface around the landing gear. The result of the direct noise calculation of the CFD simulation is compared with the results of the two FW-H calculations. The direct noise level calculation in the near field compares very well with the porous FW-H prediction while the solid FW-H calculation misses some of the pressure fluctuations by more than 50 $/percent$. According to this paper the volume sources can therefore not be neglected for the calculation of near field noise levels even at low Mach number. The results of the solid and

authors	LG model	method	Re	grid type	grid cells	FW-H	ref.
Souliez et al.	757 MLG	LES	1.25×10^6	unstructured	1.2×10^6	yes	[53]
Hedges et al.	757 MLG	URANS, DES	6×10^5	structured overlapped	2.5×10^6	no	[6]
Li et al.	757 MLG	URANS	1.23×10^6	structured patched	13.3×10^6	no	[54]
Lockhard et al.	757 MLG	URANS	1.23×10^6	structured patched	1.8×10^6	yes	[55]
Lockhard et al.	757 MLG	URANS, DES	1.23×10^6	structured patched	13×10^6	yes	[56]
Khorrami and Lockard	757 MLG	URANS	1.23×10^6	structured patched	2.5×10^6	yes	[57]
Seror et al.	Messier Dowty NLG	lattice Boltzmann	1.046×10^7	Cartesian patched	88×10^6	no	[58]
Li et al.	Messier Dowty NLG	lattice Boltzmann	1×10^7	Cartesian patched	85×10^6	no	[59]

TABLE 2.1: Overview of different landing gear CFD studies.
[Overview of different landing gear CFD studies.]

porous FW-H calculations are also compared for far field noise level predictions. There is only a small difference in the predicted far field noise level of the two FH-W methods which shows that volume sources do not contribute much to the far field noise.

In [6] Hedges et al. describe the results of an Unsteady Reynolds Averaged Navier Stokes (URANS) and a Detached Eddy Simulation (DES) using a multi block structured grid of 2.5×10^6 points around an approximate 757 main landing gear. This research was done to investigate the difference between URANS and DES for separated high Reynolds number flow. The results are compared with each other and with experimental results from a wind tunnel test done by Lazos [24]. The pressure measured on different locations on the wheels are well predicted by both URANS and DES. The time averaged results of URANS and DES are similar but the instantaneous plots of the DES results show a wider range of length scales. Many flow features were only captured by the DES simulation.

Another URANS computation using the same geometry is described by Li et al. [54]. A more refined grid of 13.3×10^6 points has been used to get a high resolution result. The result is used to determine the important unsteady flow features which will have an influence on the noise production. Vortex shedding from the rear wheel, strut and side door edges is shown. The noise sources are not computed because of the large amount of data storage needed.

Lockhard et al. [55] did an URANS simulation of the same landing gear geometry on a structured multi block grid of 1.8×10^6 points. The far field noise was computed using a FW-H model. A flat plate was attached to the landing gear to model the underside of the wing. The noise generated by the interference of the wakes from the struts with this flat plate dominated the landing gear noise. It was shown that the difference in cell size on the block interfaces was responsible for these pressure fluctuations. The contribution to the far field noise of the different components was calculated. Because of the grid resolution the calculated maximum frequency of the landing gear noise was around 6 kHz model scale which would correspond to 600 Hz full scale.

Lockhard et al. [56] also did a high resolution URANS and DES simulation of this geometry using a multi block structured grid of 13×10^6 points. A FW-H solver is used to calculate the far field noise at a distance of 100 wheel diameters. The same problem with the patched block faces is encountered which causes the flat plate noise to dominate the landing gear noise. The results without the flat plate are used to analyse the landing gear noise. The maximum frequency in the URANS solution is around 8 kHz while the DES solution gives frequencies up to 20 kHz which shows that the DES model is capable of capturing a wider range of scales compared to the URANS simulation. The far field noise generated by the different parts of the landing gear is calculated using a FW-H

solver. This result shows that the wheels and the gearboxes on the bogie are the main contributors to the noise. A permeable surface around the landing gear has also been used to calculate the far field noise but this is not successful. The strong wake crossing the porous surface leads to large errors in the noise calculation.

An URANS simulation of the same landing gear with fairings was done by Khorrami and Lockard [57] to investigate the noise reduction capabilities of fairings. The fairings consisted of streamlined shapes added to the front and back of the bogie and of a shape designed to fill the gap between the front and rear wheels. The fairings should streamline the landing gear such that flow separation and impingement of turbulent flow on the rear wheels are reduced. A FW-H solver is used to calculate the far field noise at a distance of 100 wheel diameters. The ceiling above the landing gear is the dominant far field noise source of the landing gear. The difference in cell size on the block interfaces on the ceiling result in discontinuities in the pressure which generate artificial noise. The contribution of the ceiling has therefore been excluded from the rest of the results. The far field noise results of the simulation with the fairings show a decrease in broadband noise but a strong increase in one of the tones compared to the baseline. It is assumed that the fairings lead to an acceleration of the flow and that this enhances the noise level of the tone. The maximum frequency of the far field noise is around 6 kHz due to a combination of grid resolution and the URANS turbulence model.

Seror et al. [58] use the lattice Boltzmann method to calculate the flow field around a detailed nose landing gear. The lattice Boltzmann method uses relations between particle density distributions at the nodes to calculate the flow field. It has been shown that with a suitable choice of lattice and conditions this approach approximates the N-S equations. The result of the simulation is a high resolution flow solution which shows that the lattice Boltzmann method is able to capture high frequency pressure fluctuations.

Li et al. [59] have extended the work of Seror et al. [58] but use a different lattice model. The domain around the full scale geometry is divided into 11 regions with different resolution. The cartesian mesh consists of 85 million cubic cells. The simulation shows that small parts of the landing gear cause large pressure fluctuations in both the low and high frequencies. No FW-H solver has been used to determine far field noise levels but this is planned for the a later stage.

2.2.4 Benchmark problems for Airframe Noise Computations

The increase in computational resources has made Computation Aero Acoustics (CAA) a popular research topic which results in numerous publications by different research

groups. A wide variety of computer codes and methods are being used but there often is no clear proof of the accuracy and quality of the results. This led to the creation of the Benchmark problems for Airframe Noise Computations (BANC) workshops sponsored by the Aeroacoustics and Fluid Dynamics Technical Committees of the AIAA (the American Institute of Aeronautics and Astronautics). A set of CAA benchmark cases has been defined such that different research groups can use these to compare or validate the quality of their methods / codes. The benchmark cases are based on geometries for which experimental data is available such that the results of the simulations can be compared with measurements. The four benchmark cases of the first workshop are: airfoil trailing edge noise, tandem cylinder noise, four wheel rudimentary main landing gear and a partially dressed two wheel nose landing gear.

The four wheel rudimentary landing gear benchmark problem (sponsored by Boeing) is defined by Spalart [60] and especially designed to challenge unsteady CFD methods for airframe noise prediction. The geometry consists of a square strut, rectangular bogie and axles and simple wheels. The objective during the design of the landing gear was to create a geometry which is well suited for CFD simulations. The sharp corners of the axles, bogie and strut should generate well defined locations of flow separation such that during CFD the boundary layer can be treated as fully turbulent avoiding the need to model transition. The axles have a larger than normal cross section which is done to increase the blockage in the centre of the landing gear to compensate for the removal of the brakes and other parts.

Wind tunnel testing of the rudimentary landing gear geometry has been done at the National Aerospace Laboratories (NAL) in Bangalore, India [61]. The open circuit low speed wind tunnel was run at 40 m/s resulting in a Reynolds number of 1×10^6 based on the wheel diameter. The tests have been carried out with a zero degree bogie inclination angle but further tests with different bogie inclination angles are planned for the future. The loads on the complete landing gear have been measured with a balance while the geometry was instrumented with a large number of static and unsteady pressure transducers. One of the wheels contained a motor such that it could be rotated in 2° increments resulting in a complete pressure map of the wheel surface. A pressure map of the rear wheel has been created by rotating the total landing gear model 180° and repeating the same procedure. These pressure maps have been integrated to approximate the aerodynamic forces on the wheels.

Oil flow visualisation has been applied to show the surface flow features. The photographs have been used to reconstruct a virtual three dimensional model which is useful for pinpointing the exact location of the flow features. The wing and ground side

pressure measurements show an asymmetry due to the presence of the strut. The asymmetry is larger than during the test done by Lazos [25] which is attributed to the larger blockage of the square vertical strut. The flow features on the outside of the wheels show similarities to the results from Lazos but the small separation zone near the wheel shoulder is not present since the flow has been tripped. The flow on the inside of the wheels differs from Lazos results due to the larger frontal area and the sharp edges of the truck and axles. The steady and unsteady pressure measurements combined with the surface flow features and force measurements form a dataset which is a good starting point for the validation of numerical codes.

The first published numerical result of the rudimentary landing gear benchmark are by Spalart et al. [62]. The simulations are run with the high order NTS (New Technologies and Services) code using a fully structured grid with overset blocks (Chimera grid) of 18 million cells. The flow is assumed to be fully turbulent and the DES turbulence model is used during the simulations. Two different simulations are run: one using the incompressible flow assumption which includes the wind tunnel walls and the second which uses compressible flow with a large domain with buffer zones. Flow data is sampled at solid surface and at a permeable surface surrounding the landing gear to be used in FW-H solver. The wall pressure level is slightly higher for the incompressible simulation but the shape of the spectra is similar. The increased wall pressure level is attributed to the smaller domain resulting in a higher blockage ratio of the incompressible simulation. Four different FW-H source surfaces have been used to determine far field noise levels: solid wall of the geometry, closed permeable surface, open permeable surface and closed averaged permeable. The different permeable treatments agree well with each other and result in far field noise levels within 1 dB except for the open permeable integration surface. The open permeable surface leads to a nonphysical high far field noise levels at low frequencies and a large over prediction of the high frequencies in the direction of the open surface. Comparison of the solid and permeable surface integration approaches results in a difference in the far field noise levels between 4 and 10 dB which raises the question if is is justified to ignore the contribution of quadrupole sources for low Mach number flows.

A second paper by Spalart et al [63] contains the numerical results of six different research teams each using their preferred solver and turbulence model to calculate the flow field around the rudimentary landing gear. The focus is on aerodynamics which are compared with the wind tunnel measurements. The results are only summarised and more detailed individual papers by the different groups are expected in the near future. The mean pressure distribution on the wheels is well predicted but there are differences between measurements and simulations on the bogie and axles. The unsteady surface pressure distribution shows good qualitative agreement but the level at the low and

high end of the spectrum do differ which is assumed to be caused by the short sampling time of some of the simulations. Fair comparison of local quantities is difficult since a small displacement of a flow feature can lead to large differences in local quantities. It is not clear how much effect the differences in unsteady surface pressures have on far field noise levels since the interaction of pressure signals with different phase angles and retarded times is too complex to predict. The mean lift and drag coefficients of the complete landing gear show a spread of 15 % and 55 % respectively while the unsteady forces have a spread of more than 2 between the different CFD simulations which is disappointing since these unsteady forces are a first indicator of the amount of noise radiation.

2.3 Summary

The experimental research show complex turbulent flow fields around the landing gear. Measurements of the flow field around a landing gear model can be difficult due to restricted optical access. The flow field around the main landing gear is therefore not well understood. Phased array measurements are a powerful technique to pinpoint noise sources on the landing gear during windtunnel measurements. Phased array measurements are often not able to accurately locate low frequency noise sources due to limited size of the array and the short distance between the array and the landing gear model. The phased array measurements make it possible to apply noise reduction treatments to the sources on the landing gear model. The exact flow features which generate the noise sources are often unknown and noise treatments are often based on trial and error.

The current state of aeroacoustic calculations shows that the separated flows around a complex geometry such as the landing gear prove to be a challenge. An accurate unsteady near field flow solution is needed to get reliable far field noise levels. The URANS turbulence model does not capture a wide enough range of scales of the turbulence but DES might be able to deliver the required accuracy within reasonable costs. A lot of attention is needed in the construction of the grid since discontinuities in the grid have an adverse effect on the accuracy of the flow solution which can result in a polluted far field noise signal.

The FW-H noise calculation using only the solid surface (dipole) sources shows good results but ignores the noise contribution of the quadrupoles. The FW-H far field noise computation using the porous surface approach does include the contribution of the near field inside the permeable integration surface but there is no general agreement about the proper way to treat the interaction of a strong wake with the downstream integration surface. This makes the porous surface integration technique less suitable

for the separated flow around a landing gear. The results of the BANC rudimentary landing gear problem show the difficulties of applying CFD to a complex geometry to accurately calculate flow features and noise sources.

Chapter 3

Research methodology

This chapter gives a description of the research methodology that has been used during this study. It starts with an outline of the general approach and the restrictions and assumptions made. This is followed by a detailed description of the two geometries of the main landing gear models, the setup of the CFD simulations, the setup of the FW-H solver and the post processing that has been done. The aerodynamic and acoustic results of the simulations will be described in the following chapters.

3.1 General approach

The research goal of this study is to investigate the influence of main landing gear bogie inclination angle on the flow field and far field noise levels. To achieve this goal an incremental or two step approach is followed which starts with a simplified main landing gear geometry and then repeats the process with a more complex main landing gear configuration. By using two different geometries the number of bogie inclination angles has been restricted to three to keep the total number of simulations reasonable. The first bogie inclination angle which has been investigated is the bogie aligned with the freestream flow direction (horizontal). Although this is not the main landing gear attitude during the approach phase, it is the same configuration as used in most of the other computational main landing gear noise research [63]. The bogie inclination angle has been varied with + and - 10° around horizontal since these angles showed the most promising acoustic results during wind tunnel tests [38].

The general process followed for these six different cases is as follows: a grid is created and a steady CFD simulation is run to verify the quality of the grid. The steady solution is then used as a starting point for the unsteady CFD simulation. After the unsteady

simulation has run long enough to get rid of the transients the data sampling is started. Once enough aerodynamic data has been generated it is used as input for a FW-H solver to calculate far field acoustic pressure signals. The acoustic signals are post processed to determine far field noise spectra and sound pressure levels. The following sections will give a more detailed description of the steps in this general approach.

3.2 Assumptions

Research is limited by the available resources which results in the need to make assumptions and simplifications to model a problem. Another reason for these assumptions and simplifications is to avoid the research becoming too specific such that the results can be applied to similar problems. The different assumptions and simplifications which have been made during this study will be described in this section.

- The landing gear model is placed in a domain shaped like a wind tunnel and not under the wing of an aircraft. The flow field around a wing is strongly dependent on the weight and size of the aircraft and will have an influence on the noise generated by the different components. However to keep this research general applicable the main landing gear has been placed in a wind tunnel with uniform inflow.
- The main strut of the landing gear is placed perpendicular to the wind tunnel wall. This is not the case for a landing gear under a wing but this keeps the geometry symmetric which is an important benefit in the grid generation process.
- The scale of the geometry used during the study is 25 % of full scale. This is the same scale as most of the wind tunnel tests [38] and other computational research [63].
- The free stream velocity is 40 m/s (M = 0.12) which is approximately half the approach velocity of a modern large passenger aircraft. This velocity is the same as the wind tunnel tests [38] and together with the quarter scale geometry leads to a Reynolds number of 1 million based on the wheel diameter which is similar to that of the benchmark case [63].
- Detached Eddy Simulation (DES) has been used as the turbulence model for the CFD simulations. DES is a hybrid turbulence model which uses both RANS and LES (Large Eddy Simulation) and has been shown to give good agreement for separated flows around bluff bodies such as the landing gear.
- The FW-H integration surfaces have been placed on the solid surfaces of the landing gear geometry which means that only the dipole sources are included and the

contribution of the volume sources has been ignored. The aeroacoustic theory section (2.1) of the previous chapter has shown that for low Mach number flows the dipole type surface sources are more efficient noise radiators than the quadrupole volume sources. A permeable surface around the region of unsteady flow close to the landing gear is needed to include the contribution of the volume sources in the near field and this approach does not allow one to determine the far field noise contribution of the individual landing gear components within the volume. Placing the integration surface on the geometry avoids the issue of the wake passing through the permeable surface as highlighted in the previous chapter and makes it possible to determine the contribution of the different landing gear components to the far field noise level.

- The flow in the CFD simulations is treated as incompressible since the Mach number of the flow is low enough that compressibility effects can be ignored. The relatively complex geometry of the landing gear leads to the use of a second order accurate CFD solver and hybrid grid strategy which would need a lot of grid points to accurately calculate acoustic wave propagation. The computational resources are limited so it has been decided to use the incompressible flow assumption which means that compressible phenomena such as acoustic feedback, scattering and refraction have been ignored.

- The effect of convective amplification on the far field sound pressure has not been taken into account. The landing gear noise sources are stationary with respect to the observer similar as noise measurements during a windtunnel test.

3.3 Governing equations

The equations solved are the incompressible adiabatic Navier Stokes equations which describe the conservation of mass and momentum in the flow:

$$\frac{\partial u_i}{\partial x_i} = 0, \tag{3.1}$$

and

$$\rho\left(\frac{\partial u_i}{\partial t} + u_j\frac{\partial u_i}{\partial x_j}\right) = -\frac{\partial p}{\partial x_i} + \mu\frac{\partial^2 u_i}{\partial x_j \partial x_j}. \tag{3.2}$$

In the equations above u_i is the velocity, ρ is the density, t is time, p is the static pressure and μ is the molecular viscosity. Since the flow is assumed to be incompressible and

adiabatic the density ρ is constant which means that equation 3.2 can be re-written as follows:

$$\frac{\partial u_i}{\partial t} + u_j \frac{\partial u_i}{\partial x_j} = -\frac{1}{\rho}\frac{\partial p}{\partial x_i} + \nu \frac{\partial^2 u_i}{\partial x_j \partial x_j}, \tag{3.3}$$

where $\nu = \frac{\mu}{\rho}$ is the kinematic viscosity.

The Navier Stokes equations can be solved numerically using a Direct Numerical Simulation (DNS) but the large computational costs make this currently impossible for high Reynolds number flow. Instead the instantaneous velocity u_i is decomposed in an average $\bar{u_i}$ and fluctuating $u_i{}'$ velocity component:

$$u_i = \bar{u_i} + u_i{}'. \tag{3.4}$$

The decomposed velocity of equation 3.4 is then substituted in the Navier Stokes equations (3.1 and 3.3) and averaged which results in the Reynolds Averaged Navier Stokes equations:

$$\frac{\partial \bar{u_i}}{\partial x_i} = 0 \tag{3.5}$$

and

$$\frac{\partial \bar{u_i}}{\partial t} + \bar{u_j}\frac{\partial \bar{u_i}}{\partial x_j} + \overline{u_j'\frac{\partial u_i'}{\partial x_j}} = -\frac{1}{\rho}\frac{\partial \bar{p}}{\partial x_i} + \nu \frac{\partial^2 \bar{u_i}}{\partial x_j \partial x_j}. \tag{3.6}$$

Equation 3.6 can also be written as follows by using the product rule and the continuity equation:

$$\frac{\partial \bar{u_i}}{\partial t} + \bar{u_j}\frac{\partial \bar{u_i}}{\partial x_j} = -\frac{1}{\rho}\frac{\partial \bar{p}}{\partial x_i} + \nu \frac{\partial^2 \bar{u_i}}{\partial x_j \partial x_j} - \frac{\partial \overline{u_i' u_j'}}{\partial x_j}, \tag{3.7}$$

which can be re-written in the following form:

$$\rho\frac{\partial \bar{u_i}}{\partial t} + \rho\bar{u_j}\frac{\partial \bar{u_i}}{\partial x_j} = \frac{\partial}{\partial x_j}\left[-\bar{p}\delta_{ij} + \mu\left(\frac{\partial \bar{u_i}}{\partial x_j} + \frac{\partial \bar{u_j}}{\partial x_i}\right) - \rho\overline{u_i' u_j'}\right]. \tag{3.8}$$

The decomposition and averaging of the velocity results in a new term in the momentum equation, the so called Reynolds stress term:

$$- \rho\overline{u_i' u_j'}. \tag{3.9}$$

This additional Reynolds stress term means that there are now more unknowns than equations: a closure problem. A turbulence model is used to model the Reynolds stress term and close the equations.

3.4 Turbulence modelling

The turbulence model used is the Spalart Allmaras model which is based on the Boussinesq hypothesis to relate the Reynolds stress to the mean flow using the eddy viscosity ν_t:

$$- \rho\overline{u_i' u_j'} = \rho\nu_t \left(\frac{\partial \bar{u}_i}{\partial x_j} + \frac{\partial \bar{u}_j}{\partial x_i} \right) - \frac{2}{3} \left(\rho k + \rho\nu_t \frac{\partial \bar{u}_k}{\partial x_k} \right) \delta_{ij} \tag{3.10}$$

where k the turbulent kinetic energy is. The last term on the right hand side is equal to zero due to the continuity equation (3.5) and the contribution of the kinetic energy k is ignored in the Spalart-Allmaras turbulence model. The Spalart-Allmaras model solves a transport equation (3.11) for a viscosity-like variable $\tilde{\nu}$ which may be referred to as the Spalart-Allmaras variable:

$$\frac{\partial \tilde{\nu}}{\partial t} + u_i \frac{\partial \tilde{\nu}}{\partial x_i} = G_\nu + \frac{1}{\sigma_{\tilde{\nu}}} \left[\frac{\partial}{\partial x_j} \left\{ (\nu + \tilde{\nu}) \frac{\partial \tilde{\nu}}{\partial x_j} \right\} + C_{b2} \left(\frac{\partial \tilde{\nu}}{\partial x_j} \right)^2 \right] - Y_\nu \tag{3.11}$$

where G_ν the production of turbulent viscosity and Y_ν the destruction of turbulent viscosity is while $\sigma_{\tilde{\nu}}$ and C_{b2} are constants.

The turbulent viscosity is calculated according to the following equation, where f_{v1} the viscous damping function is:

$$\nu_t = \tilde{\nu} f_{v1}, \quad f_{v1} = \frac{\chi^3}{\chi^3 + C_{v1}^3}, \quad \chi \equiv \frac{\tilde{\nu}}{\nu} \tag{3.12}$$

The turbulent production G_ν is modelled as follows:

$$G_\nu = C_{b1} \tilde{S} \tilde{\nu} \tag{3.13}$$

and

$$\tilde{S} \equiv S + \frac{\tilde{\nu}}{\kappa^2 d^2} f_{v2}, \quad f_{v2} = 1 - \frac{\chi}{1 + \chi f_{v1}}. \tag{3.14}$$

C_{b1} and κ are constants, d is the distance to the nearest wall and $\tilde{S}$ is a measure of the deformation tensor. In the original Spalart Allmaras model S is based on the magnitude of the vorticity Ω_{ij}:

$$S \equiv \sqrt{2\Omega_{ij}\Omega_{ij}} \tag{3.15}$$

and

$$\Omega_{ij} = \frac{1}{2}\left(\frac{\partial \bar{u}_i}{\partial x_j} - \frac{\partial \bar{u}_j}{\partial x_i}\right). \tag{3.16}$$

Later it was acknowledged that S should also take into account the effect of the mean strain on the turbulence production which results in the following modifications:

$$S \equiv |\Omega_{ij}| + C_{\text{prod}} \ \min\left(0, |S_{ij}| - |\Omega_{ij}|\right) \tag{3.17}$$

where

$$C_{\text{prod}} = 2.0, \quad |S_{ij}| \equiv \sqrt{2S_{ij}S_{ij}}, \quad |\Omega_{ij}| \equiv \sqrt{2\Omega_{ij}\Omega_{ij}} \tag{3.18}$$

and S_{ij} is the mean strain tensor:

$$S_{ij} = \frac{1}{2}\left(\frac{\partial \bar{u}_j}{\partial x_i} + \frac{\partial \bar{u}_i}{\partial x_j}\right). \tag{3.19}$$

The turbulent destruction term Y_ν is modelled as follows:

$$Y_\nu = C_{w1} f_w \left(\frac{\tilde{\nu}}{d}\right)^2, \tag{3.20}$$

where

$$f_w = g\left[\frac{1 + C_{w3}^6}{g^6 + C_{w3}^6}\right]^{1/6}, \quad g = r + C_{w2}(r^6 - r), \quad r \equiv \frac{\tilde{\nu}}{\tilde{S}\kappa^2 d^2}, \tag{3.21}$$

and C_{w1}, C_{w2} and C_{w2} are constants.

The following list contains the default constants used in the Spalart Allmaras model:

$$\sigma_{\tilde{\nu}} = \frac{2}{3}$$
$$C_{b1} = 0.1355$$
$$C_{b2} = 0.622$$
$$\kappa = 0.4187$$
$$C_{w1} = \frac{C_{b1}}{\kappa^2} + \frac{(1+C_{b2})}{\sigma_{\tilde{\nu}}}$$
$$C_{w2} = 0.3$$
$$C_{w3} = 2.0$$
$$C_{v1} = 7.1$$

RANS simulations model the complete Reynolds stresses but if the grid is fine enough the large turbulent scales can be resolved and only the smaller subgrid scales need to be modelled which results in a Large Eddy Simulation (LES). This means that a smaller part of the turbulent spectrum is modelled which improves the accuracy. However the turbulent scales in the boundary layer of a high Reynolds number flow such as a landing gear become very small which makes LES computationally too expensive. Detached Eddy Simulation (DES) is a hybrid turbulence model which combines the RANS and LES models. The DES model treats the near wall region as a RANS model and the rest of the flow field as a LES model. This is achieved by replacing the nearest wall distance d with a modified distance function $\tilde{d}$ in the Spalart Allmaras model:

$$\tilde{d} = \min[d, C_{DES}\Delta], \tag{3.22}$$

where C_{DES} is a constant and Δ is the largest dimension of the grid cell. This modification causes the DES model to behave as a RANS model in regions close to walls and in a Smagorinsky-like subgrid scale model away from the walls.

3.5 Geometry

The main landing gear geometry for this study is based on the model used by Li et al. [5] for the Aircraft Noise Disturbance Alleviation by Novel Technology (ANDANTE) project. The geometry used in the ANDANTE project is a 1/4 scale look-a-like main A340 landing gear. The ANDANTE geometry as shown in Figure 3.1 is due to the level of detail too complex to use in the current study so two main landing gear configurations with different levels of complexity have been derived from the ANDANTE geometry and these will be described in the following two sub sections.

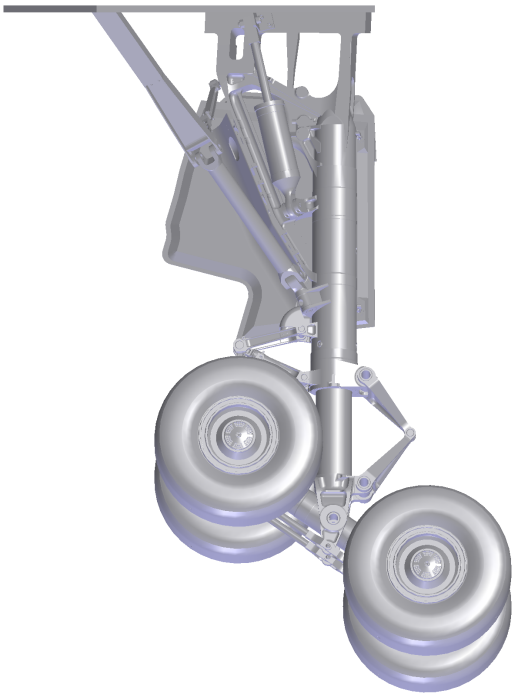

FIGURE 3.1: Side view of the ANDANTE geometry (flow direction from left to right).

3.5.1 Simplified Geometry

The simplified main landing gear geometry resembles the geometry tested by Lazos [24] and also the BANC benchmark case [63] and consists of only the major landing gear components: wheels, axles, bogie and strut as shown in Figure 3.2. The focus of this research is the flow and noise from the bogie area so the landing gear door as shown in the ANDANTE geometry has not been included and the upper part of the main landing gear is modelled by just the main strut. The lower part of the landing gear has been simplified by removing all small and medium sized parts and filling up the cavities. The bogie consists of a horizontal cylinder with flat front and rear surface. The diameter of the main strut has been reduced to the same diameter as the bogie which allows for a straight forward connection of the two parts since the yoke and swivel have been removed.

The wheels have been simplified by removing the brakes from the inside and filling the hub cavity on the outside such that both surfaces are flat. The axles which connect the wheels to the bogie are modelled by cylinders. Although some parts have been removed or altered the wheel diameter and the longitudinal and lateral wheel spacings have been

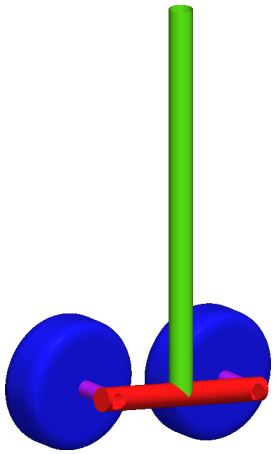

FIGURE 3.2: Simplified main landing gear geometry with two wheels removed to get a better view of the bogie area.

kept the same as the ANDANTE model since these are considered to be characteristic dimensions of the main landing gear. Although this geometry is simplified it should still give a good insight into the major flow features around a main landing gear. The 10° toe up and toe down configurations have been constructed by keeping the main strut in place and rotating the bogie, axles and wheels.

3.5.2 Complex Geometry

The complex main landing gear geometry is based on the simplified geometry but also includes the following medium sized parts: brake units, articulation link, torque link, yoke and swivel as shown in Figure 3.3. This creates a more realistic main landing gear geometry but does not include the small scale details to keep the computational costs of the simulations reasonable. The main strut of the complex geometry consists of two cylinders with different diameters to better resemble the shock absorber of the ANDANTE model. The fork shaped yoke has been added to the end of the strut and this component connects the strut to the bogie using a swivel (axle) which allows the bogie to rotate. The bogie and the axles are the same as for the simplified case only the axles are shorter due to the presence of the brake units on the inside of the wheels. The brake unit on the ANDANTE model consists of 14 hydraulic actuators but this number has been reduced to 12 to keep the shape of the brake units of the complex geometry symmetric. The hub cavity on the outside of the wheel is filled in just as for the simple geometry resulting in a flat outer wheel surface. The torque link has the standard double triangle shape but the holes and cavities have been filled to create a simpler more solid version. The articulation link also has been simplified by replacing the I beam shaped sections with square solid sections.

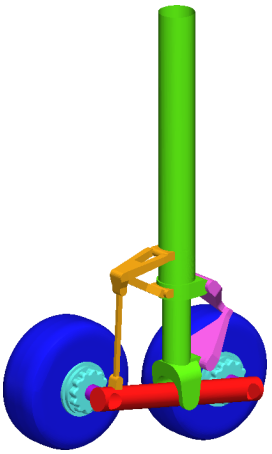

FIGURE 3.3: Complex main landing gear geometry with two wheels removed to get a better view of the bogie area.

The rotation of the bogie of a real world landing gear geometry leads to the compression or expansion of the shock absorber since the bogie is connected to the main strut via the articulation link. This effect is undesirable during this study since it leads to significant changes in the geometry of the landing gear which make it impossible to determine the influence of bogie inclination angle on the flow features. It has therefore been decided to keep the changes to the complex geometry to a minimum by using three different articulation links. The geometry of the main strut with shock absorber and torque link has been fixed and the length of the articulation link has been varied to achieve the three different bogie inclination angles. This is the same approach as used during wind tunnel tests.

3.6 Computational domain

The origin of the coordinate system is located at centre of the junction between the main strut and the bogie which coincides with the middle of the swivel for the complex geometry. The positive x-direction is in the flow direction (downstream) and the positive z-direction is up in the direction of the strut. This results in a positive y-direction to the left when looking downstream as can be seen in figures 3.4a and 3.4b.

The size of the computational domain needs to be big enough to avoid blockage effects but a disadvantage of a large domain is that it requires more cells and thus more computational power. For the current simulation the length of the main strut (1.1 m) has been used as a reference length (L). The length of the domain for the simplified geometry is 5 L, 1.5 L ahead of the centre of the landing gear and 3.5 L behind (see Figure 3.4b). The width and height of the domain are 2 L (see Figure 3.4a) which results in a maximum blockage ratio of 3.8% for the simplified geometry which is lower than during wind

tunnel tests such that the influence of the wall on the flow field around the geometry is avoided. For the complex geometry the same cross section is used but the length of the domain has been increased to 8 L, 3 L in the upstream direction and 5 L in the downstream direction as can be seen in Figure 3.5.

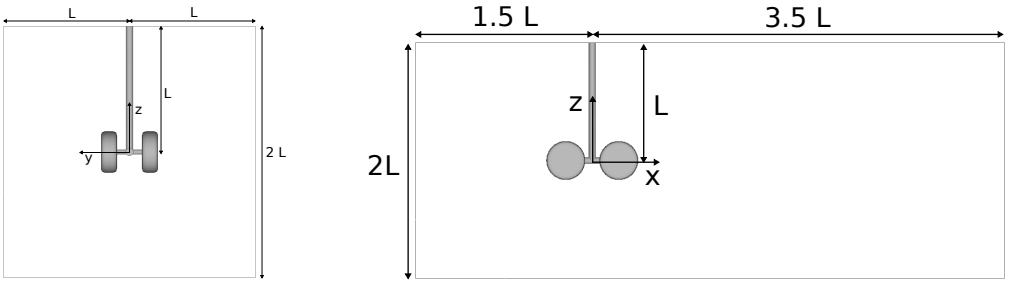

(A) front (B) side

FIGURE 3.4: Front and side view of the computational domain and coordinate system of the simplified landing gear simulations.

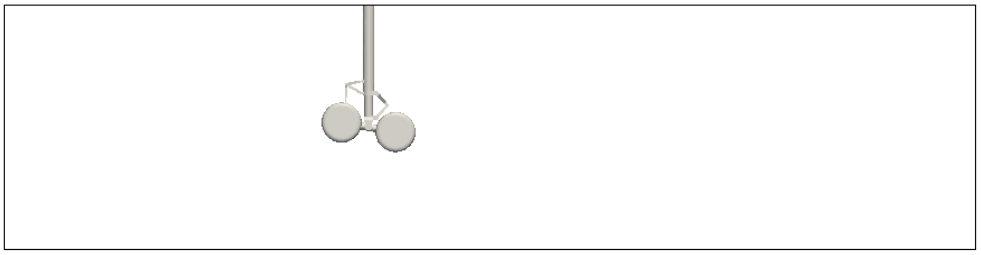

FIGURE 3.5: Side view of the computational domain of the complex landing gear simulations.

3.7 Grid generation

Grid generation is an important part of the CFD process since the quality of the grid has a direct influence on the quality of the results of the simulation. Grid generation is a compromise between accuracy and computational costs: a fine grid will result in an accurate flow solution but will also lead to high computational cost of the simulation and vice verse. The CFD solvers used in this study are based on the finite volume method which accepts different cell shapes and gives a number of options for the grid generation process:

- Grid type: a structured grid consisting of hexahedral cells, an unstructured grid of tetrahedral / polyhedral cells or a hybrid grid which combines the previous two types.
- Block topology (mainly important for structured grids): the way the different grid blocks are connected and placed around the geometry. Three examples for a simple two dimensional grid are the O, C and H grid topologies.
- Block interfaces: one to one cell connections at block interfaces or non conformal interfaces where the cells at different sides of the block interface do not match.
- Number of cells and their distribution along grid lines.

The ideal grid is capable of accurately resolving gradients of flow quantities which are present in flow features such as boundary layers, shear layers and vortices. A structured grid is preferred since it in general requires less cells compared to unstructured grids to achieve the same level of accuracy. The block interfaces would be one to one since the solution at non conformal interfaces require interpolation which leads to smoothing of the gradients. Cells with little skewness and aspect ratios close to unity result in small changes in cell volume leading to accurate results. It may be possible to satisfy all these requirements but for complex three dimensional geometries this would lead to a large number of cells and the simulation would require a lot of computational resources. The main challenge in grid generation is to reach a compromise and create a grid with a modest number of cells without sacrificing the accuracy of the results.

Spalart [64] has written a guideline for successful grid generation for DES which has been followed in this study. The following grid choices have been made for both the simplified and complex landing gear cases. A hybrid grid is used such that the advantages of structured and unstructured grids can be combined. A structured grid is used in close proximity to the geometry and the wake where strong gradients in the flow are expected while the unstructured grid is used further away from the body and in areas where different structured block topologies need to be joined together. The application of these unstructured blocks means that non conformal block interfaces are avoided and only one to one block interfaces are used. The unstructured cells in these joining blocks are quite fine to make sure the gradients in flow variables are captured while the unstructured blocks away from the geometry can be more coarse since the flow field in those areas is relatively smooth. The structured grid in the boundary layer and close proximity to the geometry uses the three dimensional version of the O block topology which is constructed by extruding / growing a structured surface mesh normal to the wall resulting in a fully structured body fitted grid. The advantage of this type of body fitted grid is that the boundary layer cells are not projected into the outer domain such that a spurious number

of cells and large cell volume jumps are avoided, the disadvantage is that this method introduces skewness near sharp corners of the geometry.

The previously described grid strategy is not a single step but part of a longer iterative process in which a grid is created and a steady RANS simulation run. The y^+ distribution at the wall and contours of pressure and vorticity are then used to inspect the grid quality and highlight areas which need improving. The block topology and cell distribution of the grid in these regions are adjusted / changed and the process is repeated.

The resulting grid for the simple main landing gear geometry has a completely structured surface mesh as can be seen in figure 3.6. This fully structured surface mesh is extruded perpendicular to the wall with a first cell thickness of 0.05 mm and the growth rate of the extrusion of 1.1 resulting in a $y^+ \leq 1$. This body fitted grid layer is 25 cells thick after which the extrusion rate is adjusted to create cells with an aspect ratio close to 1 as can be seen in figure 3.7. The clean geometry of the simple main landing gear makes it possible to use a fully structured block topology with an average cell edge length of approximately 5 mm or 1/72 D near the geometry. It would be possible to expand this structured blocks through the rest of the domain once the landing gear and the expected wake region have been meshed but this would lead to an excessive number of cells. So instead the outer domain has been filled by unstructured cells (tetrahedra) which grow in size the further they are away from the geometry as can be seen in figure 3.8. The transition from structured to unstructured cells has been made by inserting a layer of pyramid shaped cells thereby avoiding any non conformal block boundaries. The grids of the three simple landing gear configurations each consist of approximately 8 million cells, 5.5 million structured cells close to the geometry and 2.5 million unstructured cells in the outer domain.

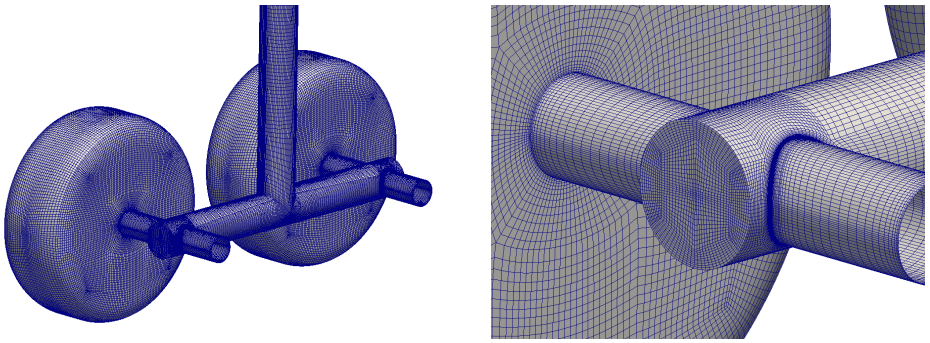

(A) Surface mesh.

(B) Mesh detail near the front axle.

FIGURE 3.6: Surface mesh of the horizontal simplified landing gear configuration.

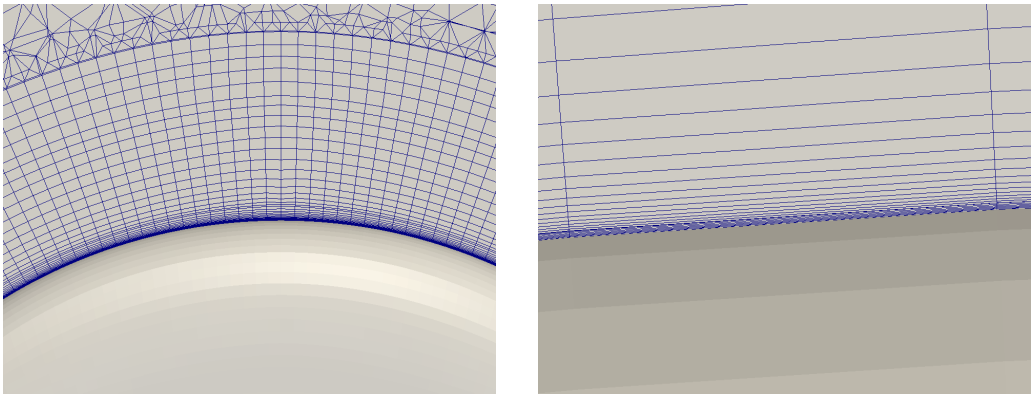

(A) Structured grid layer.

(B) Detail of the extruded grid layer near the wall.

FIGURE 3.7: Structured grid layer around the wheel of the simplified landing gear.

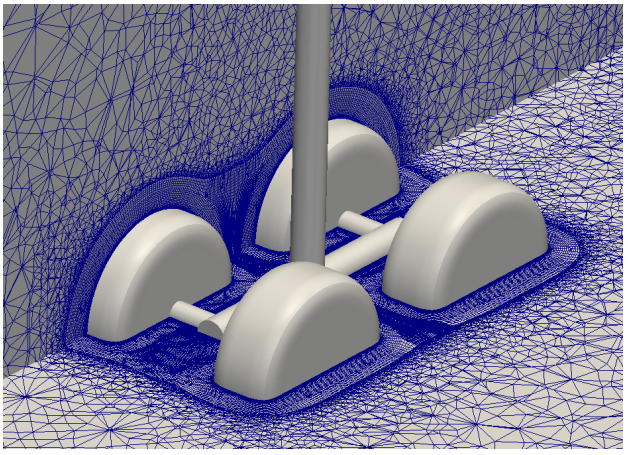

FIGURE 3.8: Volume mesh detail of the horizontal simplified landing gear configuration.

The same process has also been used for the complex main landing gear configurations but a fully structured block topology is impossible for this more complicated geometry. A fully structured surface mesh (figure 3.9) has been extruded to form a 25 cell thick body fitted grid layer with a first cell thickness of 0.01 mm and a growth ratio of 1.2. This layer has been expanded with more structured blocks until most of the space around the geometry has been filled. Unstructured blocks are used to fill the gaps in between the structured blocks (figure 3.10) and the transition from structured to unstructured has again been made by inserting a layer of pyramid cells. During the iterative grid generation process it was noticed that the quality of some of these pyramid cells is not acceptable. The gaps between the structured blocks are relatively small which results in some pyramid cells with a low aspect ratio (≤ 0.1). These low aspect ratio pyramid cells have a small cell volume compared to the surrounding cells and the surface normal vectors all point in approximately the same direction which causes numerical instabilities during the CFD simulation. This grid problem has been solved by merging the low aspect ratio pyramid cells with the underlying hexahedra cells to

form a polyhedra cell layer. The polyhedra cells have a slightly larger volume than the surrounding hexahedra cells but the cell surface normal vectors are not aligned any more such that numerical instabilities are avoided. The pyramid cells in the grid of the simple landing gear configuration did not have this problem since they all point towards the outside of the domain such that their height is not restricted. The outer domain of the complex geometry is again filled with unstructured cells which increase in volume with increasing distance from the geometry as can be seen in figure 3.11. The grids of the three complex configurations each consist of approximately 24 million cells, 8 million structured cells close to the geometry and 16 million unstructured cells in the rest of the domain.

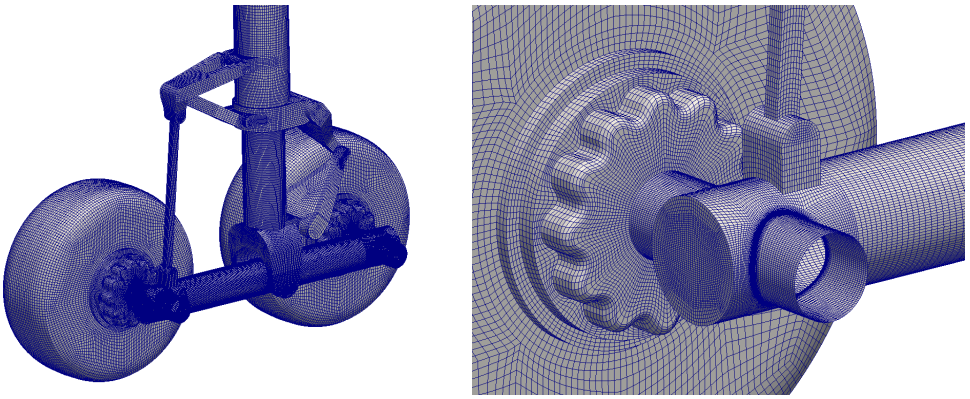

(A) surface (B) detail

FIGURE 3.9: Surface mesh of the horizontal complex landing gear configuration.

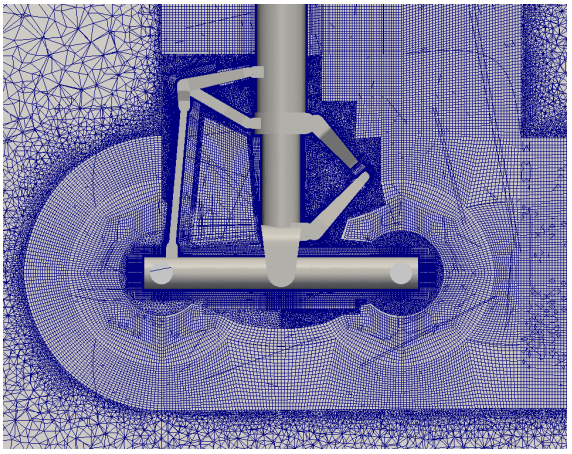

FIGURE 3.10: Centreline mesh slice showing the structured and unstructured block layout near of the horizontal complex landing gear configuration.

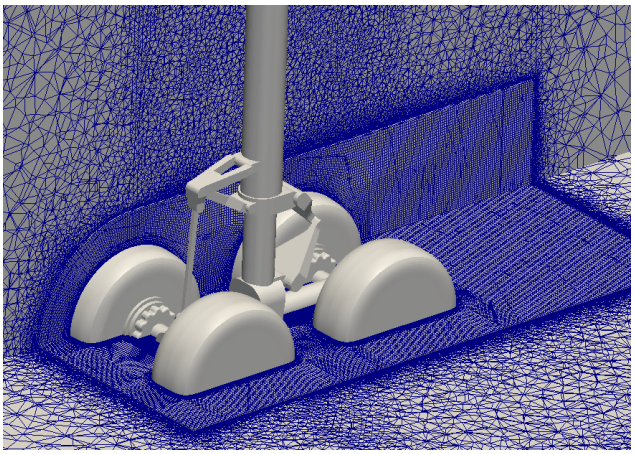

FIGURE 3.11: Volume mesh detail of the horizontal complex landing gear configuration.

3.8 Numerical method

Two different software packages have been used during this study: Ansys Fluent (version 12.0) and OpenFOAM (version 1.7.1) which are both based on the finite volume method using arbitrary shaped cells. More details of the two solvers are described in the following sections.

3.8.1 Fluent

Fluent is a commercial simulation software package that contains a broad range of physical modelling capabilities such as flow, turbulence, heat transfer and chemical reactions. Here the incompressible transient turbulent CFD solver has been used to model the flow around the landing gear. The governing equations have been solved using a pressure based cell centered solver. The SIMPLE (Semi-Implicit Method for Pressure Linked Equations) algorithm has been used for the pressure-velocity correction to obtain the pressure field. The discretisation scheme for pressure is second order and a bounded central differencing scheme is used for the momentum and turbulent viscosity equations. The bounded scheme is a based on combination of the second order central differencing scheme and an upwind scheme to avoid nonphysical oscillations in the solution. The time stepping is done using an implicit second-order time scheme which decouples the time step from the cell size allowing for larger time step than an explicit method. The equations are solved in segregated form using Algebraic Multi Grid method to speed up convergence. The grid has been partitioned automatically into similar sized subdomains that are solved in parallel using multiple nodes of the University's Linux computer cluster.

3.8.2 OpenFOAM

The development of OpenFOAM (Open source Field Operation And Manipulation) started at Imperial College London but has since moved to a commercial company while the copyright of the source code has been transferred to a not for profit organisation. OpenFOAM is a C++ toolbox for the development of customised numerical solvers for the solution of continuum mechanics problems [65]. The toolbox provides a large set of libraries which can be combined / used to create applications. The application which has been used here is pimpleFOAM, a large time step transient incompressible turbulent flow solver. PimpleFOAM, a cell centered pressure based solver, uses the merged PISO (Pressure Implicit with Splitting of Operator) and SIMPLE algorithm for the pressure-velocity coupling. The modular design of OpenFOAM means that there are a lot of different numerical schemes available to discretise the individual terms of the governing equations with. Second order discretisation is preferred for accuracy but this may create problems with unboundedness of the solution [66]. The discretisation schemes that have been used here are a mix of second order and limited schemes to ensure both good accuracy and to avoid nonphysical oscillations and can be found in Appendix A. The time stepping is done using the implicit, second order accurate 'backward' scheme. The governing equations are solved in segregated form using a Generalised Geometric Algebraic Multi Grid method to improve convergence. An incomplete Cholesky smoother is used for the pressure equation while a diagonal incomplete LU smoother is used for the velocity and viscosity equations. The grid has been partitioned using METIS [67] into similar sized subdomains that are solved in parallel using multiple nodes of the University's Linux computer cluster.

3.9 CFD setup

Although two different software packages have been used the process of setting up a simulation is similar. Each package requires the flow conditions, boundary conditions and time step to be specified. The flow velocity of the simulations in this study is the same as used during the wind tunnel measurements by Li et al. [5]: 40 m/s which is approximately half the flight speed during the final approach phase. This flow speed corresponds to a Mach number of 0.12 such that the incompressible flow assumption can be used. The combination of the quarter scale model and reduced flow velocity leads to a Reynolds number of 9.9×10^5, based on the wheel diameter.

A velocity inlet boundary condition has been used at the upstream boundary with the velocity set to the freestream value of 40 m/s. The boundary condition for the pressure is

zero gradient at the upstream boundary. A pressure outlet boundary condition has been used for the downstream boundary with the outlet pressure set to the reference pressure. The boundary condition for the velocity has been set to zero gradient at the downstream boundary. The no slip boundary condition is used on the surface of the landing gear geometry but not on the remaining four outer surfaces of the domain. The symmetry boundary condition is used on these four outer surfaces (wind tunnel walls) which avoids the need to resolve the boundary layer and therefore reduces the computational costs of the simulations. During experiments there will be a boundary layer present on the walls of the wind tunnel but the influence of this boundary layer on the flow features around the landing gear are assumed to be small such that it can be neglected in the simulations.

The CFD simulations are started by running a steady RANS simulation first to verify the quality of the grid. The Spalart Allmaras (SA) one equation turbulence model as described by Shur et al. [68] is used for the RANS simulation. The RANS solution provides a starting flow field for the DES. This approach avoids large changes during the initial phase of the DES which helps to speed up the simulation and reduces the risk of the simulations diverging.

The physical time step of the DES of the simple geometry is $2.5 \times 10^{-5} s$ which corresponds to a non dimensional time step of 2.76×10^{-3} based on the wheel diameter and freestream velocity. This means that 362 time steps are needed for the freestream flow to pass a single wheel diameter. The physical time step of the DES of the complex geometry is $1.0 \times 10^{-5} s$ which results in a non dimensional time step of 1.10×10^{-3} and it thus takes 905 time steps for the flow to move one wheel diameter. These time steps are chosen such that the maximum CFL number in the simulations stays below 10 while the average CFL number of the whole domain stays well below 0.1.

The DES has been run for a non-dimensional time of approximately 70 to completely wash the initial flow field out of the downstream boundary of the domain. During this initial part of the simulation global values like lift and drag have been monitored to make sure the transient effects have disappeared. After this initial stage the FW-H data collection and the time averaging of the flow variables is started and the DES is continued to run for a non-dimensional time of 50. The CFD simulation generates instantaneous flow variables at each cell but it is impossible to save all this information at each time step due to data storage restrictions. Instead the instantaneous results are used to calculate time average and root mean square (rms) values of the flow variables which are stored at the end of the simulation. Flow information that is exported at each time step are the aerodynamic force coefficients of the different landing gear components and the surface pressure data which is needed for the FW-H solver.

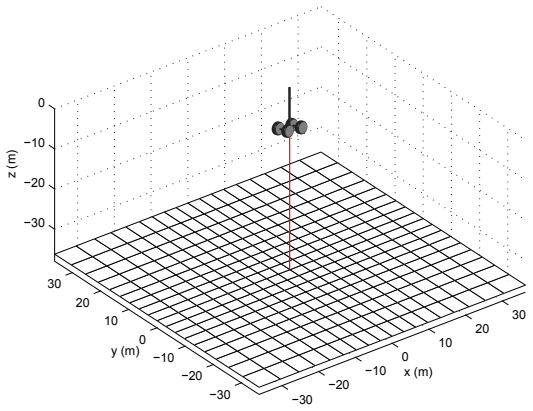

FIGURE 3.12: Receiver locations in the far field used to determine noise directivity (landing gear is not to scale).

3.10 FW-H setup

The software package Fluent includes a FW-H solver (based on [10]) which is used to calculate the far field acoustic signals. The solution of the FW-H equation is obtained using the free space Green's function. The FW-H solver in Fluent ignores the contribution of the volume integrals and only evaluates contribution of the surface integrals using the retarded time approach. OpenFOAM does not include a FW-H solver so the sampled surface pressure data has been converted into Fluents Acoustic Source Data (.asd) file format. The main part of this conversion consists of a function which sorts and re-orders the saved pressure data because OpenFOAM and Fluent save the grid-points in a different order. This conversion makes it possible to use Fluents FW-H solver with OpenFOAM pressure data. The FW-H integration surface has been placed on the landing gear wall and is split in zones such that the far field noise contribution of the different components of the landing gear can be determined.

The FW-H solver is used to calculate the far field noise signal at a distance of 100 wheel diameters below the centre of the landing gear. The far field noise signal is calculated not just in a single point but in 361 receiver locations on an observer plane to determine the directivity pattern of the noise. The receiver locations are spaced 5° apart spanning a range from $-45°$ to 45° in both longitudinal and transverse directions as can be seen in Figure 3.12. The method does not include the effect of convective amplification as described in the assumptions of section 3.2. The resulting far field noise levels are therefore not the same as fly over measurements but more similar to wind tunnel measurements. A correction is applied to the calculated sound pressure levels to compensate for the different distances between source and receiver which will be described in the following section.

3.11 Post processing

During the simulation the aerodynamic forces acting on the different components are monitored. The values have been made dimensionless using the following equation.

$$C_i = \frac{F_i}{1/2\rho U_\infty^2 S}, \tag{3.23}$$

in which C_i the non dimensional force coefficient, F_i the aerodynamic force, $1/2\rho U_\infty^2$ the dynamic pressure and S the surface area is. Each component has a different surface area so the area of a circle with the same diameter as the wheel ($S = 1/4\pi \times D^2$) has been used to make the comparison consistent.

The static pressures have been converted to non dimensional pressure coefficient (C_p) using the following equation:

$$C_p = \frac{p - p_\infty}{1/2\rho U_\infty^2}, \tag{3.24}$$

in which p_∞ the static pressure in the undisturbed flow, ρ the density and U_∞ the free stream flow velocity is.

The mean and root mean square (RMS) values of the different coefficients have been determined using equations 3.25 and 3.26 where n the number of data points is and x needs to be replaced with the coefficient of interest.

$$\bar{x} = \frac{1}{n}\sum_{i=1}^{n} x_i. \tag{3.25}$$

$$x_{RMS} = \sqrt{\frac{1}{n}\sum_{i=1}^{n}(x_i - \bar{x})^2}. \tag{3.26}$$

Time dependent data such as aerodynamic forces and acoustic pressure signals can be difficult to analyse unless they are converted to the frequency domain. The conversion from the time domain to the frequency domain is done using a Fourier Transform (FT).

$$x(f) = FT(x(t)) = \int_0^T x(t)e^{-i2\pi ft}dt, \tag{3.27}$$

in which $x(f)$ the signal in the frequency domain, $x(t)$ the signal in the time domain and T the total sample time is. Matlabs fast Fourier transform (FFT) algorithm has been

used to calculate the Fourier transform of the signals. This results in a discrete function of n frequencies with a resolution of $\Delta f = 1/T$. The function is symmetric around the centre (Nyquist) frequency which makes the second half of the spectrum redundant.

For the acoustic pressure $p'(t)$ the Sound Pressure Level (SPL) is the common way to show the spectral contents of the signal.

$$SPL(f) = 20log\frac{|FFT(p'(t)|}{n \cdot p_{ref}}, \tag{3.28}$$

where p_{ref}, the reference pressure, is 2.0×10^{-5} Pa. This results in a narrowband spectrum showing the pressure per frequency band. The complete far field noise signal has been split in overlapping blocks before it has been processed which reduces the frequency resolution of the spectrum but increases the reliability. The block size of the acoustic signal of the simple configuration is 4096 and it is 10240 for the complex configuration resulting in the same frequency resolution of 9.76 Hz. A Hanning window has been applied to each block before it is processed and the amplitude of the spectrum has been corrected for this. The SPL levels of the individual blocks have been averaged to calculate the narrowband spectrum. The third octave band spectrum has been calculated by summing the narrowband spectrum contribution over each passband.

The far field noise directivity contours of the landing gear have been determined based on the total amount of far field noise which is calculated using the Overall Sound Pressure Level (OASPL).

$$OASPL = 20log\frac{p'_{RMS}}{p_{ref}}, \tag{3.29}$$

where p'_{RMS} the root mean square of the acoustic pressure signal and p_{ref}, the reference pressure, is 2.0×10^{-5} Pa.

The distance from the centre of the landing gear to the locations of the different observers in the far field is not constant which leads to a reduction of the OASPL with increasing distance. This effect changes the shape of the noise directivity contours on the observer plane. The OASPL values on the observer plane have therefore been normalised according to the standard practice of industrial partner Airbus. The vertical (shortest) distance from the landing gear to the observer plane is 100 wheel diameters which has been used as the reference length. The sound pressure decreases with the square of the distance such that the following equation can be used to normalise the OASPL levels on the observer plane:

$$OASPL(100D) = OASPL(r) + 20log\frac{r}{100D}, \tag{3.30}$$

where $100D$ is the reference length and r is the distance between the centre of the landing gear and the observer.

Chapter 4

Aerodynamics of the simplified main landing gear

This chapter describes the aerodynamic results of the simplified main landing gear simulations which have been obtained using Fluent. One of the main advantages of CFD over experiments is that it gives a full description of the resolved flow field at each time step. This makes it possible to see what happens with the instantaneous structures (figure 4.1) in the flow but the large amount of data can be difficult to analyse. The instantaneous flow field (figure 4.2a) changes constantly and it is therefore not possible to pick a snapshot representative for the whole time series. This is not only the case for the flow field but also for the surface flow features (figure 4.3a). Although the shear stress at the wall is within the RANS region of the solution it is driven by the resolved flow structures in the LES region and thus changes constantly as well.

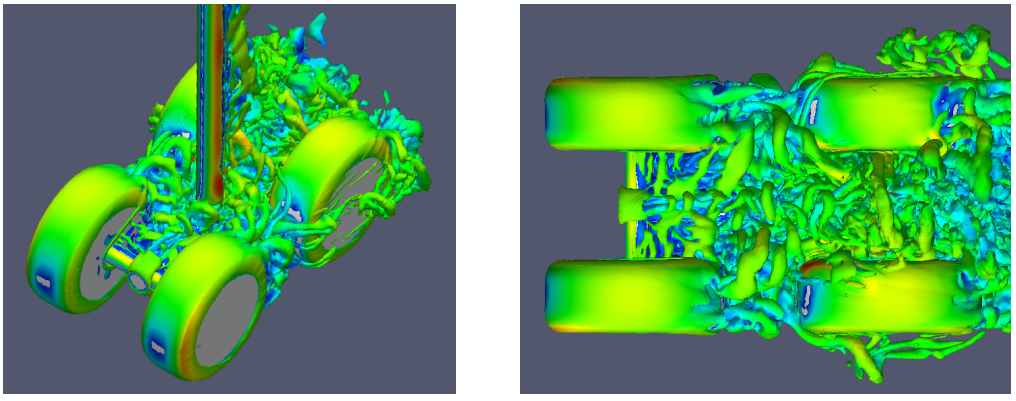

(A) isometric view (B) bottom view

FIGURE 4.1: Isosurface of Q-criterion coloured by velocity magnitude highlighting the instantaneous vortical flow structures around the simplified horizontal MLG.

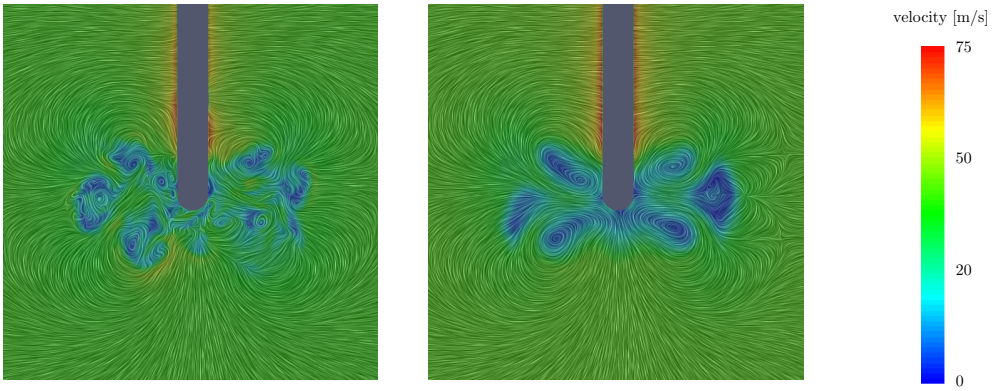

(A) instantaneous (B) time averaged

FIGURE 4.2: Instantaneous and time averaged velocity on a streamwise slice through the centre of the simplified horizontal MLG.

The focus of this study is therefore on the time averaged (figures 4.2b and 4.3b) and root mean square (rms) values of the flow field rather then the instantaneous values (figures 4.2a and 4.3a). This operation results in a large data reduction and makes it possible to focus on the analysis of the major flow features. The time averaging of the flow variables has been done during the same amount of time as the sampling of the surface pressure data for the FW-H solver as described in section 3.9 of the previous chapter.

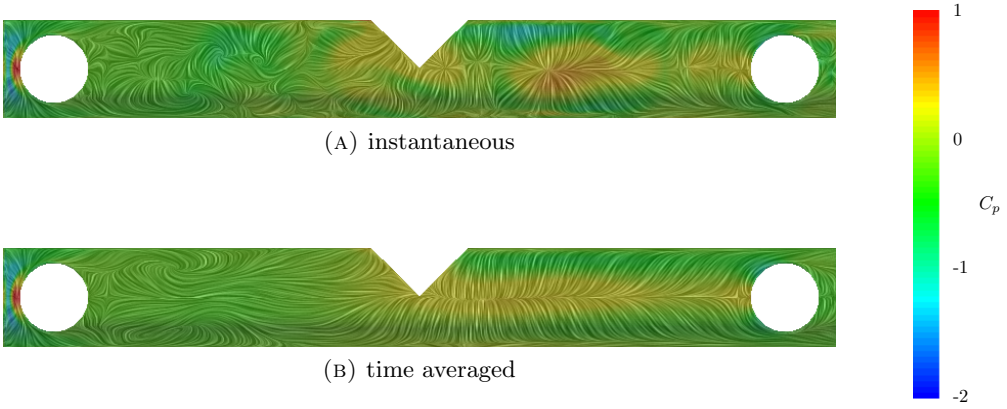

(A) instantaneous

(B) time averaged

FIGURE 4.3: Instantaneous and time averaged flow features on side of the bogie of the simplified horizontal configuration.

4.1 Horizontal configuration

The horizontal simplified landing gear configuration shows similarities to the four wheel main landing gear tested by Lazos [25]. Lazos used oil flow and pressure transducers to map the important surface topology on the fore and aft wheel of the landing gear. The results generated by the CFD simulations have been post processed such that they resemble the same format used by Lazos which allows a comparison between the two

studies. The components of the landing gear have been coloured according to the pressure coefficient while the oil flow patterns have been mimicked by visualising the wall shear stress vector field using the surface Line Integral Convolution (LIC) method [69]. Fluent [70] calculates the wall shear stress from the laminar stress-strain relationship (4.1) since the grid spacing at the wall is fine enough to resolve the laminar sublayer ($y^+ \leq 1$).

$$\frac{u}{u_\tau} = \frac{\rho u_\tau y}{\mu}, \tag{4.1}$$

with $u_\tau = \sqrt{\frac{\tau_w}{\rho}}$, where τ_w is the wall shear stress, u is the velocity, y is the normal distance to the wall and ρ is the density. Equation 4.1 can be re-written to:

$$\tau_w = \mu \frac{u}{y}, \tag{4.2}$$

where μ is the dynamic viscosity. The surface LIC visualisation technique puts a large number of randomly distributed dots on the surface and then calculates how these dots would move according to the local shear stress vector field. The integrated trajectory of these dots form lines which results in a surface texture similar to the patterns obtained experimentally with the oil flow visualisation technique. The surface LIC pattern does not show the direction of the shear stress so arrows have been added for clarity. The resulting surface pattern can be analysed in a similar manner to the oil flow patterns to show where important flow features, such as separation and attachment, take place.

4.1.1 Flow features

The first landing gear component that is encountered by the flow is the front wheel, which results in a large area of near stagnation pressure due to the relatively flat tread of the wheel (as can be seen in figure 4.4c). The surface LIC pattern shows that the stagnation point is at the middle of the wheel but slightly towards the centre of the landing gear and most of the flow moves to the flat inside and outside of the wheel. The area of low pressure on the outside edge of the wheel indicates a high local flow velocity which is not present on the inside edge of the wheel. This is due to the blockage created by the bogie, axles and strut in the centre of the landing gear.

The increase in pressure towards the front of the axle causes the flow on the inside surface of the front wheel to bend away from the axle. The surface LIC pattern in figure 4.4a shows a small area in front of the axle with reversed flow resulting in a saddle of separation which is similar to the pattern found by Lazos [25] and indicates the presence

of a horseshoe vortex. The wake downstream of the axle can be clearly identified by the disturbed surface LIC pattern. The pattern on the outside surface of the front wheel is smooth (see figure 4.4b) indicating that the flow follows the surface of the wheel until it reaches the downstream edge.

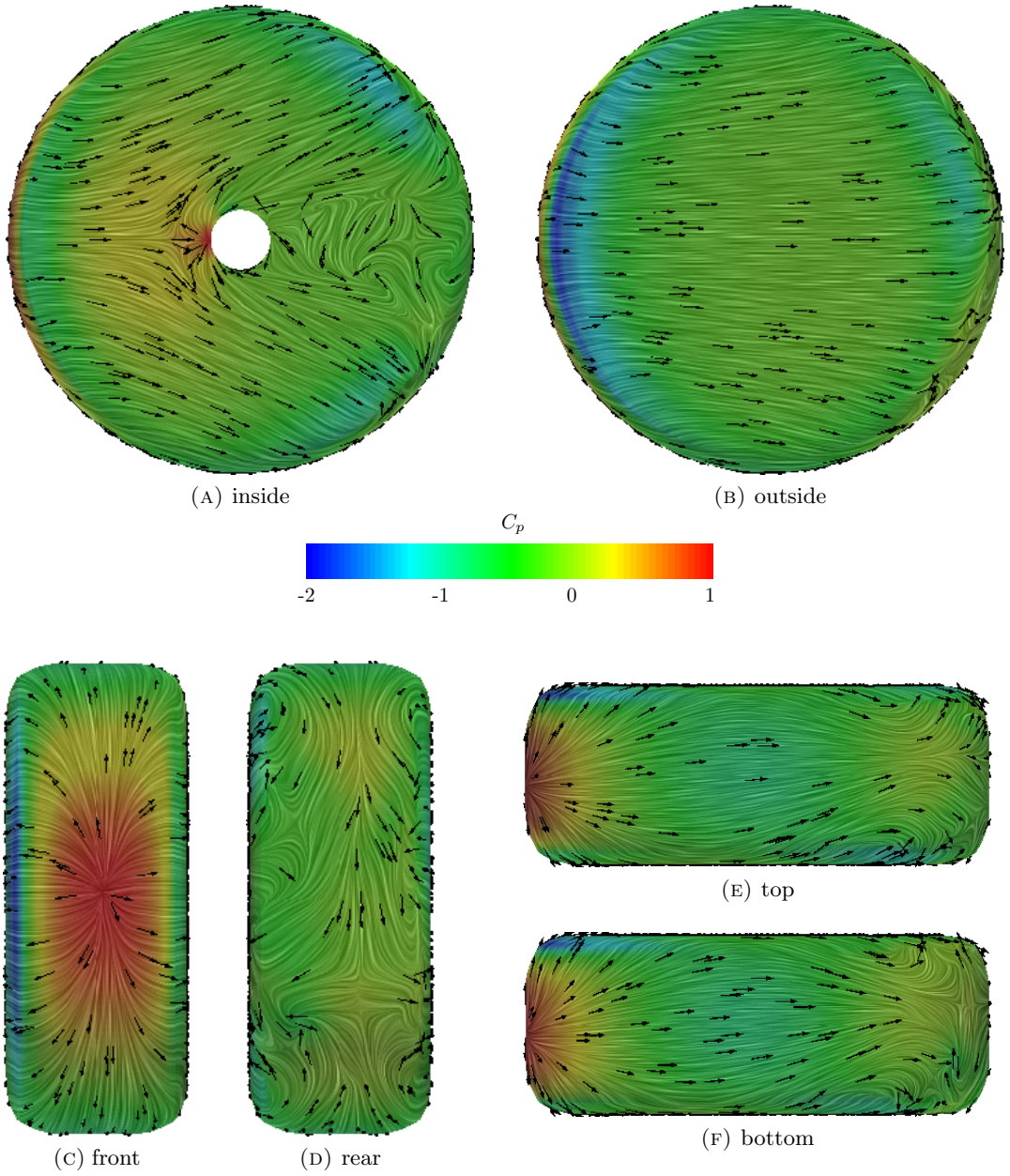

(A) inside (B) outside

(C) front (D) rear (E) top (F) bottom

FIGURE 4.4: Surface flow features of the time averaged flow field on the forward wheel of the simplified horizontal configuration.

The flow features on the top (figure 4.4e) and bottom (figure 4.4f) of the front wheel are similar and show that the flow accelerates from the stagnation point toward the top and bottom of the wheel. Once past the mid point of the wheel the flow slows down because it is subject to an adverse pressure gradient. This causes the flow to change direction towards the sides where it collides with the flow over the flat sides of the wheel

resulting in flow separation. The rear view of the wheel in figure 4.4d clearly shows the high curvature of the surface LIC pattern near these separation points, which indicates that a vortex is formed at each of the four shoulders of the front wheel. The two curved patterns on the inside of the wheel are more pronounced than those on the outside due to the presence of the axle at the inside of the wheel. The axle creates a diverging flow which increases the rotation of the flow when it reaches the edge of the wheel. The induced velocity generated by these four vortices helps the flow along the centreline to follow the curved tread of the wheel. The flow finally separates below the middle of the rear face of the front wheel. The flow velocity at the top of the front wheel is a bit higher than at the bottom of the wheel due to the blockage created by the presence of the strut. This higher flow velocity at the top of the wheel pushes the flow separation point to the lower half of the front wheel.

The front face of the rear wheel (in Figure 4.5c) shows a large area of high pressure with two attachment points connected by an attachment line. This attachment line lies close to the outside edge of the front face indicating that most of the flow that reaches the rear wheel moves toward the centre of the landing gear. The saddle point separating the two attachment points is below the middle of the front face of the rear wheel at a similar height as the flow separation on the aft face of the front wheel. The flow accelerates around the inside forward edge of the rear wheel resulting in an area of low pressure. The surface LIC pattern on the inside surface of the rear wheel (Figure 4.5a) shows that the direction of the flow accelerating around the forward edge is not parallel to the freestream direction. The flow is directed at the rear axle which is caused by the induced velocity of the strong vortices separating from the front wheel. The pressure increases towards the rear axle but not as pronounced as for the front axle due to the reduced flow velocity in the wake. The presence of the rear axle changes the flow direction to a more horizontal trajectory on the aft half of the rear wheel. The surface LIC pattern in front of the axle indicates the presence of a horse shoe vortex similar as the flow pattern around the front axle. The time averaged flow on the outside surface of the rear wheel follows the freestream direction and the surface LIC pattern in Figure 4.5b does not show any clear features.

The surface LIC pattern on the top and bottom of the rear wheel (Figures 4.5e and 4.5f) are similar to the pattern on the top and bottom of the front wheel (Figure 4.4). The flow moves along the tread of the wheel until it reaches the adverse pressure gradient. The flow changes direction towards the sides of the wheel which leads to another set of four vortices. The strength of these vortices however is less due to the reduced flow velocity and increased level of unsteadiness at the rear wheel. The surface LIC patterns on the surface of the rear wheel are smooth since the time averaged wall shear stress

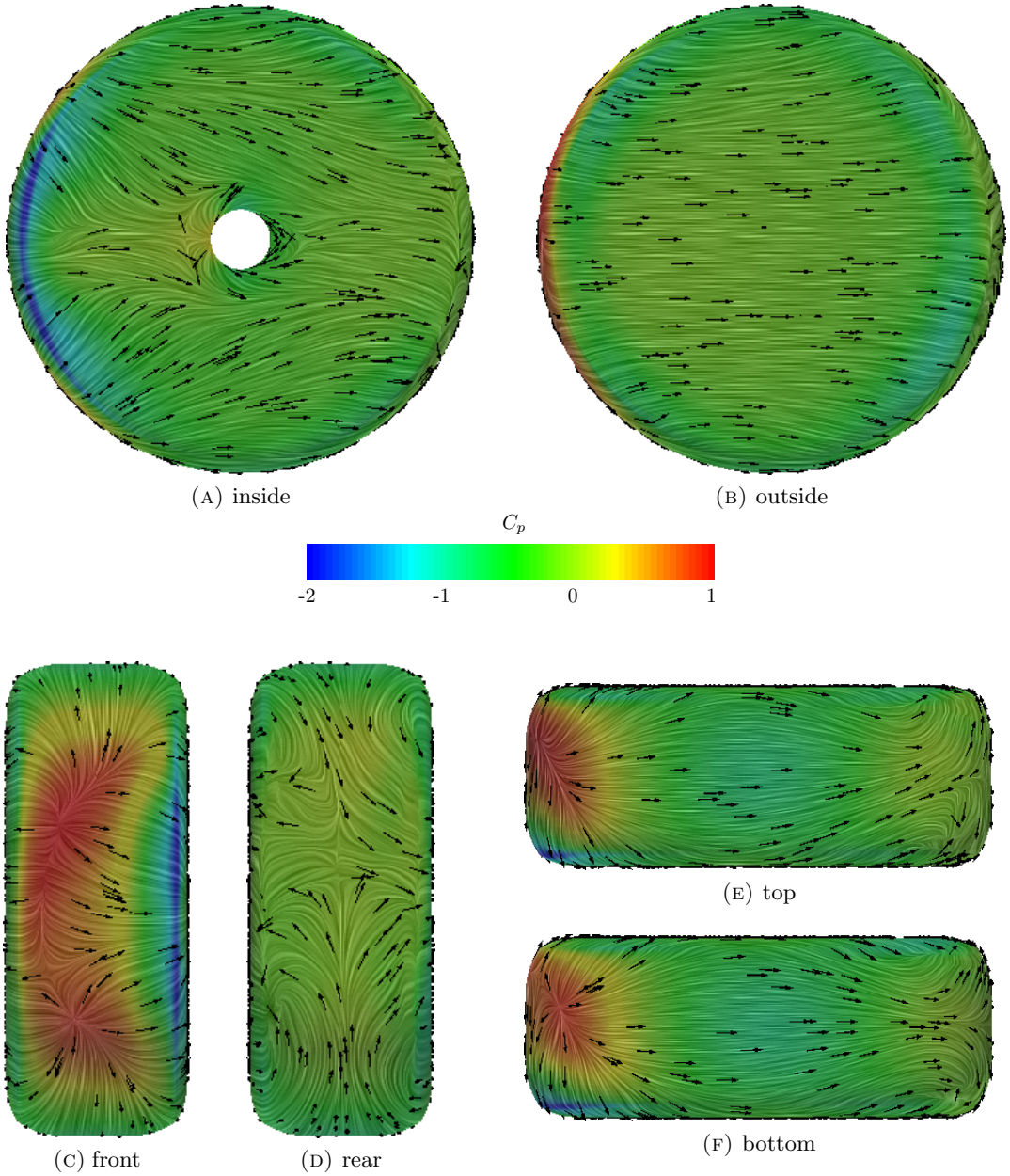

(A) inside (B) outside

(C) front (D) rear (E) top (F) bottom

FIGURE 4.5: Surface flow features of the time averaged flow field on the rear wheel of the simplified horizontal configuration.

field has been used to generate the figures. The instantaneous flow field around the rear wheel is far from smooth due to the turbulent wake of the forward components.

The small circular front face of the bogie is perpendicular to the freestream flow direction which results in a stagnation point and flow separation at the sharp forward edge of the bogie. The separated flow interacts with the wake of the front axles resulting in a complex surface LIC pattern on the forward half of the bogie (see Figure 4.6). The flow over the top of the bogie runs into the increasing pressure towards the junction with the main strut. This deflects the flow to the sides of the bogie where it merges with the

recirculation zone behind the front axles. There is no strut at the bottom of the bogie but the pressure does increase towards the middle of the lower bogie. This results in a similar surface LIC pattern on the forward part of the bottom face of the bogie (Figure 4.6c) as seen on the top of the bogie.

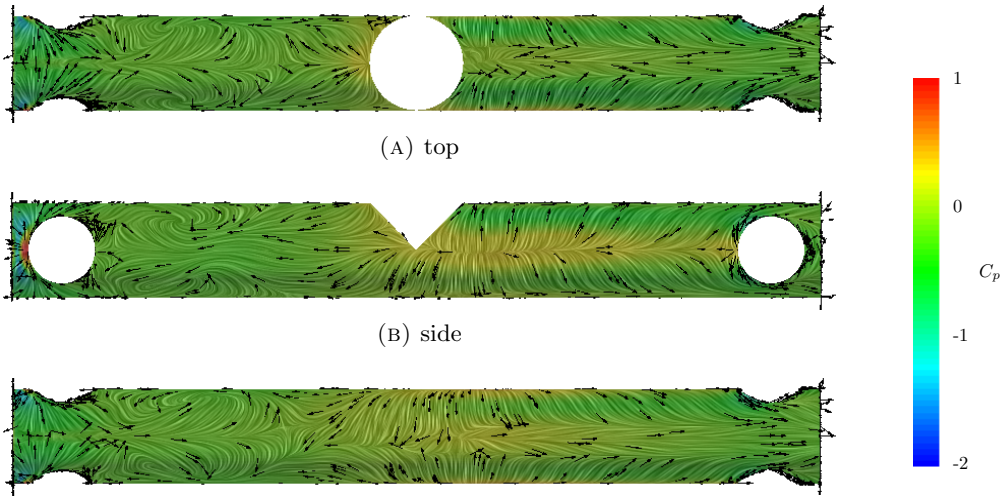

(A) top

(B) side

(C) bottom

FIGURE 4.6: Surface flow features of the time averaged flow field on the bogie of the simplified horizontal configuration.

The surface LIC pattern on the downstream half of the bogie is a lot less complex compared to the forward half. The pattern is dominated by the induced flow generated by the two strong streamwise vortices coming of the inside edge of the front wheel that move downstream along the length of the bogie. The vortices generate an induced flow field which is perpendicular to the side of the bogie and this creates an attachment line starting from the bogie to strut junction and ending at the front of the rear axle. The surface LIC patterns on the top and bottom surface (Figures 4.6a and 4.6c) of the bogie are almost identical and show that the induced flow separates from the surface before it reaches the symmetry plane of the bogie. This results in a narrow band of separated flow along the centreline of the top and bottom surface of the bogie.

The time averaged pressure and shear stress pattern on the strut (Figure 4.7) shows a stagnation line on the front of the cylinder and an area of low pressure on the sides where the flow accelerates around it. The surface LIC pattern (Figure 4.7b) shows a separation line just aft of the widest point of the strut. The rear face of the strut in Figure 4.7c shows a recirculation zone with the wall shear vectors at the lower part of the strut pointing upwards. This is due to the local velocity generated by the strong streamwise vortices coming of the top of the front wheels.

The surface flow features on the front wheel show that the flow separation results in the formation of streamwise vortices which are important since their interaction with

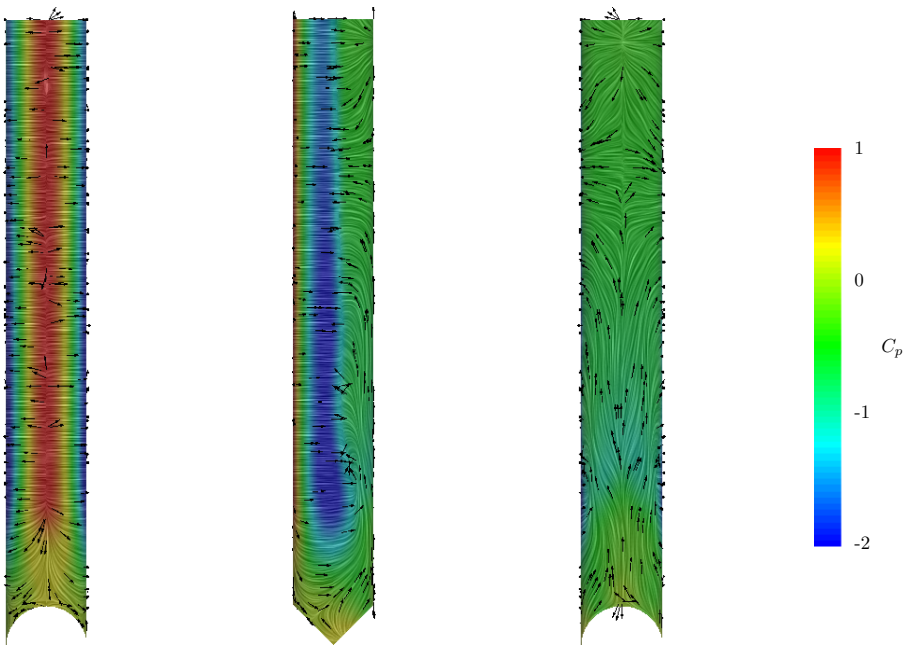

(A) front (B) side (C) rear

FIGURE 4.7: Surface flow features of the time averaged flow field on the lower half of the strut of the simplified horizontal configuration.

solid bodies leads to the generation of noise. Figure 4.8 shows the streamwise vorticity of the time averaged flow field at three different locations. The first figure (4.8a) shows the streamwise vorticity of the time averaged flow field at a plane through the aft part of the front wheels. The flow separation generates a total of eight vortices, two vortex pairs at each front wheel. The streamwise vortices on the inside of the front wheel are a bit bigger than the ones on the outside of the front wheel which shows the difference in vortex strength due to the presence of the front axles.

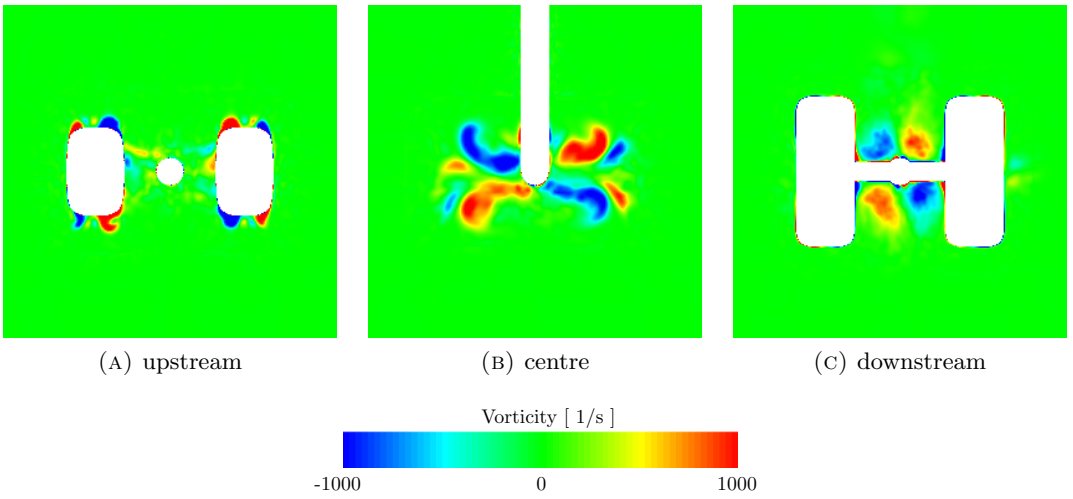

(A) upstream (B) centre (C) downstream

FIGURE 4.8: Streamwise vorticity of the time averaged flow field around the simplified horizontal configuration, upstream = aft part of the front wheels, centre = centre of the MLG, downstream = centre of the rear wheels.

Figure 4.8b shows the streamwise vorticity at a plane through the middle of the landing gear. The four strong vortices coming from the inside of the front wheels have moved toward the centre of the landing gear following the local flow direction. The area of the vortices in the figure has increased because the vortex core follows the time averaged flow direction and is not perpendicular to the plane of the figure. The vortices coming of the outside of the front wheels have moved together in the vertical direction.

The last figure (4.8c) shows the streamwise vorticity of the time averaged flowfield at a plane through the middle of the rear axles and wheels. The four strong vortices coming from the inside surface of the front wheels are trapped in between the rear wheels and surround the bogie while the four smaller vortices have moved to the outside of the rear wheels. The smaller vortices on the outside of the rear wheel are not trapped by the landing gear which allows them to move around more and they are therefore less visible in the time averaged flow field.

4.1.2 Unsteady surface pressure distribution

The root mean square (rms) of the pressure is used to show the strength of the pressure fluctuations at the surface of the landing gear. The root mean square pressure has been converted into decibel and plotted in 3 dB bands to clearly show the areas of the strongest pressure fluctuations. The strength of the dipole source term of the FW-H equation (2.17) has also been calculated but is presented and discussed in the next chapter which describes the acoustic results.

The flow that reaches the landing gear contains only a small amount of turbulence and this results in a low unsteady pressure level on the forward half of the front wheel and axle as can be seen in Figure 4.9. The inside surface of the front wheel (Figure 4.9a) shows two peaks in the unsteady pressure level where the turbulent wake generated by the front axle reaches the edge of the wheel. The outside surface of the front wheel (Figure 4.9b) also shows an increased unsteady pressure level at the downstream edge where the flow separates from the wheel but the area is relatively small compared to the area of the peaks on the inside of the wheel.

The aft face of the front wheel (Figure 4.9d) shows a large area of high unsteady pressure at the middle of the wheel towards the inside edge. The surface flow features in the previous section (Figure 4.4) show that the induced flow field of the strong vortices pushes the turbulent flow to the middle of the wheel. This turbulent flow interacts with the turbulent wake behind the front axles resulting in an area of high pressure fluctuations.

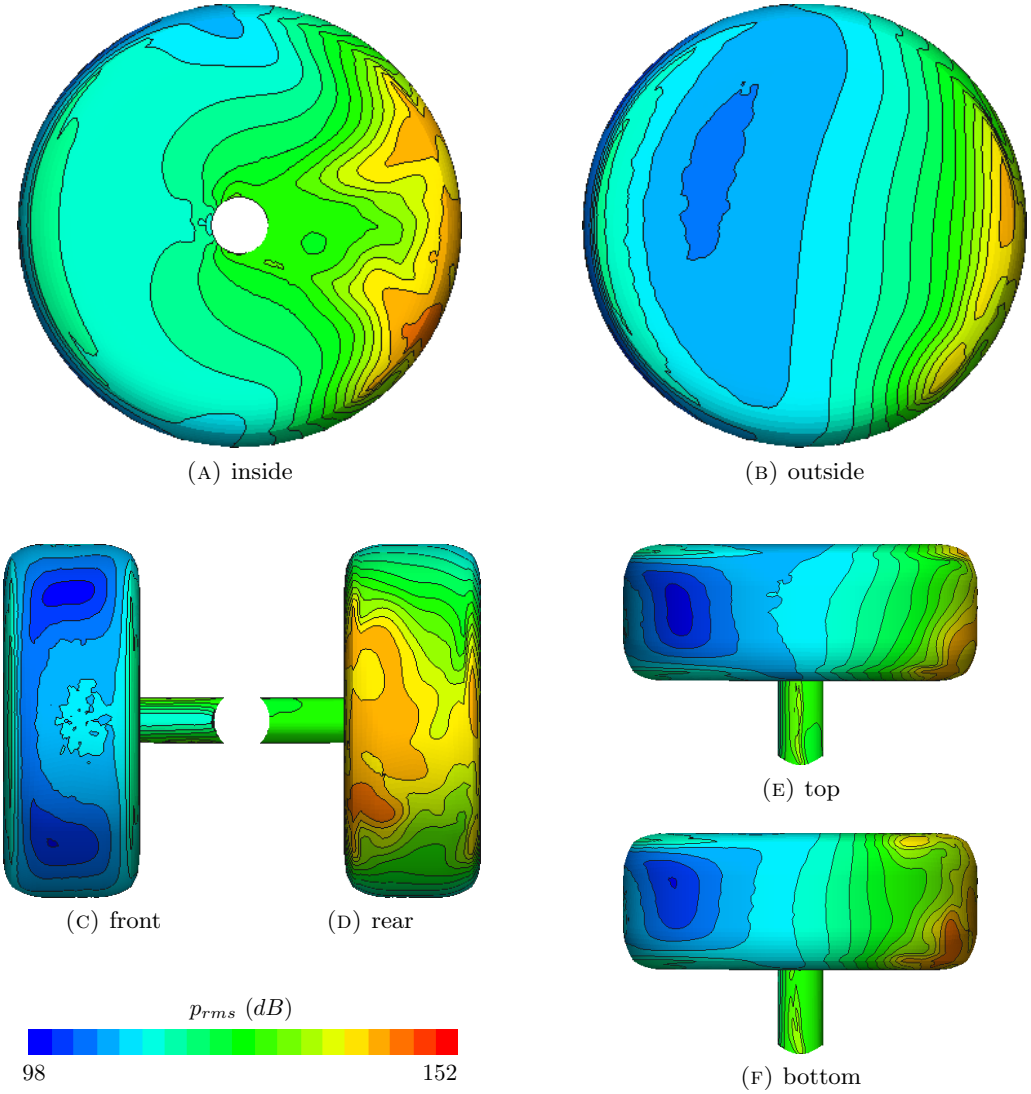

FIGURE 4.9: Unsteady surface pressure level on the forward wheel and axle of the simplified horizontal configuration.

The rear wheel is situated in the turbulent wake of the front wheel and this leads to large pressure fluctuations on the surface of the rear wheel as can be seen in Figure 4.9. The peak in the unsteady pressure level is not located near the stagnation area but at the inside edge of the rear wheel (see Figure 4.9a) where the flow has a higher velocity. The top half of the inside surface of the rear wheel (Figure 4.9a) shows a higher unsteady pressure level than the lower half due to the increased local flow velocity generated by the blockage of the strut. The lower half of the outside surface of the rear wheel (Figure 4.9b) shows an increase in the surface pressure fluctuations just below the centreline of the wheel at the location of the streamwise vortices.

The rear axle is completely immersed in turbulent flow which results in a high level of unsteady surface pressure on the front face. The levels are even higher on the top and

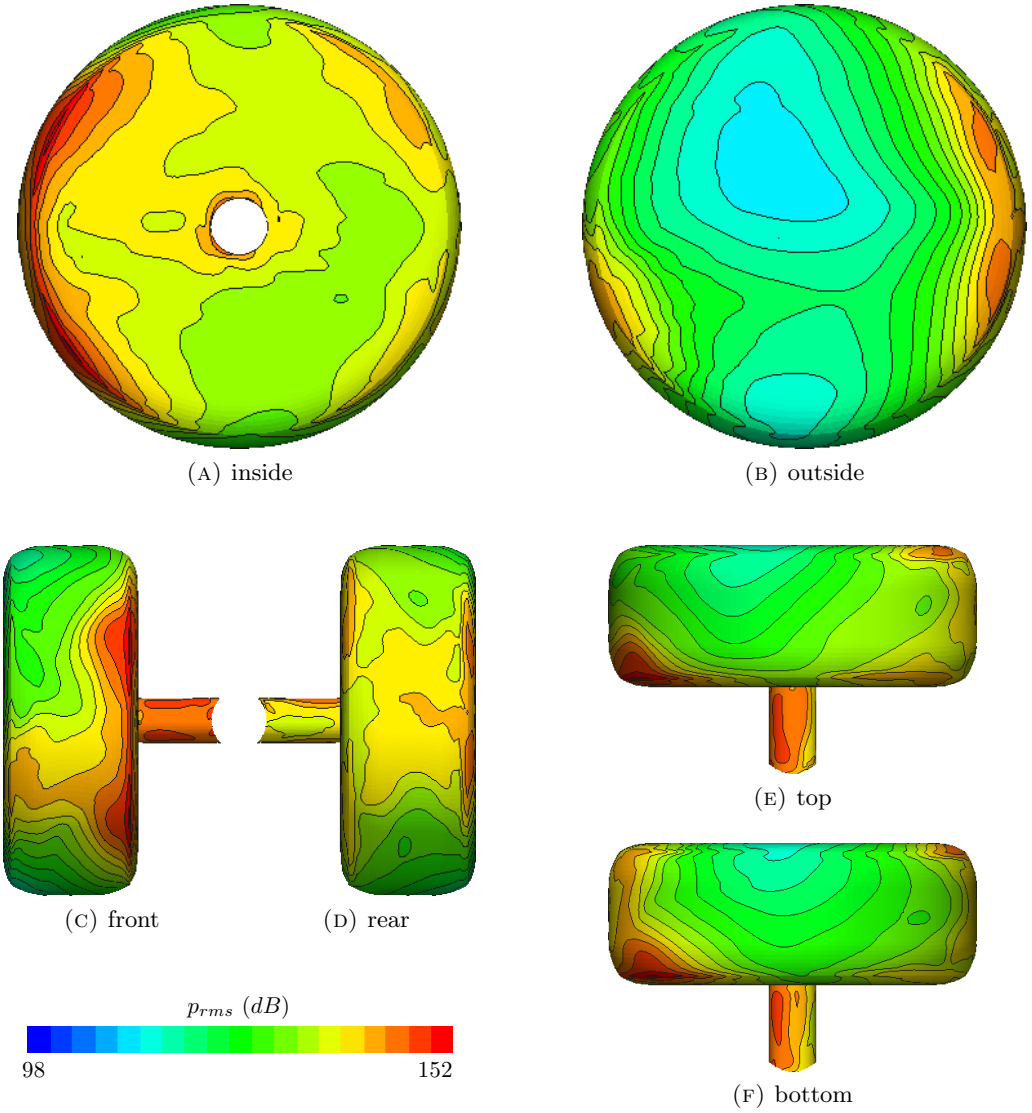

FIGURE 4.10: Unsteady surface pressure level on the rear wheel and axle of the simplified horizontal configuration.

the bottom of the rear axle due to the increase in the local flow velocity. Both the inside and outside surface of the rear wheel show peaks in the unsteady pressure level close to the downstream edge where the turbulent flow leaves the surface of the wheel.

Figure 4.11 shows a relatively low unsteady pressure level at the front of the bogie but the level increases towards the junction with the strut. The flow separates from the sharp forward bogie edge and this creates a recirculation zone with low local flow velocity. Further downstream the unsteady pressure level increases due to the wake generated by the front axles. The highest unsteady pressure level is reached on the downstream half of the bogie where the four strong streamwise vortices push the turbulent flow into the side of the bogie as shown by the attachment line in the time averaged surface flow

features in Figure 4.6b. This form of turbulent flow impingement leads to high unsteady pressure levels since the local flow velocity is much higher than near a stagnation point.

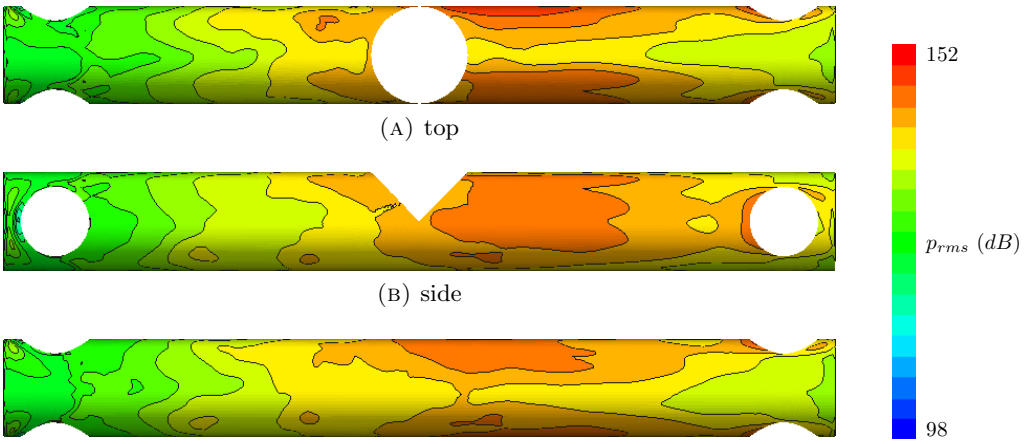

(A) top

(B) side

(C) bottom

FIGURE 4.11: Unsteady surface pressure level on the bogie of the simplified horizontal configuration.

The unsteady pressure distribution on the surface of the bogie is not completely symmetric as can be seen by the top and bottom view of the bogie in Figures 4.11a and 4.11c. The geometry, flow conditions and grid are all symmetric so this should in theory lead to a symmetric time averaged flow field. The current sampling time of 50 convective time units based on the wheel diameter is not enough to reach a perfectly symmetric time averaged flow field. Increasing the sampling time should improve this however this is not possible with the resources available for this study.

The flow that reaches the upper part of the strut is undisturbed while the lower part of the strut is immersed in the turbulent flow generated by the front axles and wheels. The wake of the front axles results in an increased level of the unsteady pressure on the front face of the strut close to the junction with the bogie as can be seen in Figure 4.12a. The peak in the unsteady pressure level is clearly visible on the side of the strut in Figure 4.12b where the turbulent flow moves past the surface at high velocity. The part of the strut above the wake of the front wheels shows an increase in the unsteady pressure level at the location where the flow reaches its highest velocity just before it separates from the surface.

4.1.3 Aerodynamic forces

The aerodynamic forces have been sampled during 50 convective lengths of the simulation and table 4.1 gives the mean and standard deviation of the force coefficients of the simplified horizontal main landing gear configuration. These coefficients have been calculated according to the procedure described in section 3.11. The standard deviation

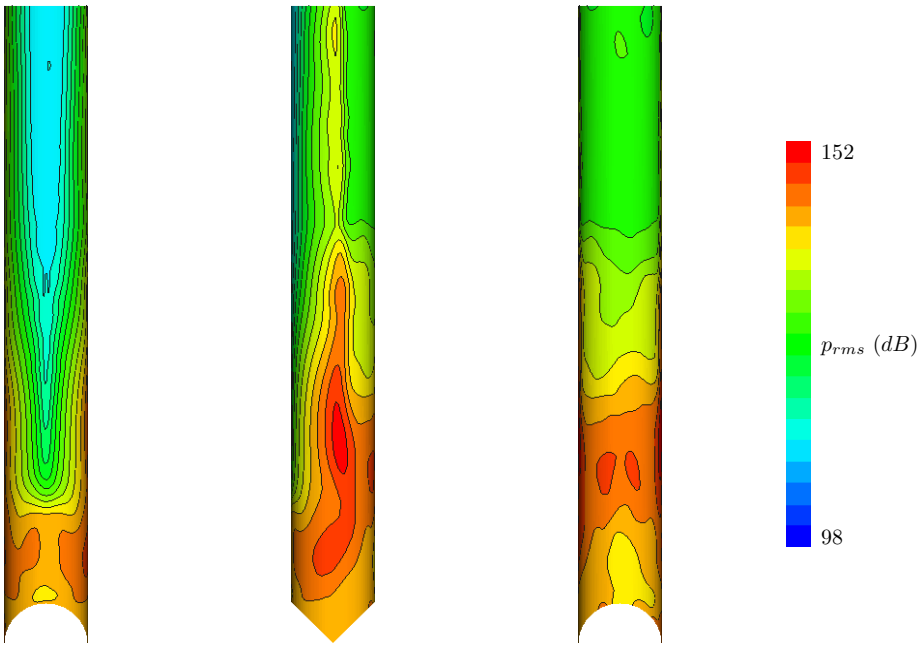

(A) front (B) side (C) rear

FIGURE 4.12: Unsteady surface pressure level on the lower half of the strut of the simplified horizontal configuration.

shows the force fluctuations around the mean value which can be used as an indication of the amount of far field noise a component generates. The simplified main landing gear consists of a combination of bluff bodies which each generate a significant amount of drag. The strut and wheels generate most of the drag because they have the largest frontal area. The drag of the rear wheels is higher than that of the front wheels due to the large area of high pressure on the front of the rear wheel as shown in Figure 4.5. The axles show the opposite trend with a lower drag coefficient for the rear axles compared to the front axles due to the lower mean flow velocity in the wake. The standard deviation of the drag of the front axles is relatively low due to the undisturbed inflow conditions while the rear axles experience larger fluctuations in the drag due to the turbulent inflow conditions generated by the wake of the forward components. The standard deviation of the drag coefficient of the front and rear wheels is similar which shows that the flow conditions do not make a difference for these bluff bodies which generate a relatively large wake containing strong vortices.

The symmetry of some of the components, such as the bogie, strut and complete main landing gear, should result in a mean side force coefficient of zero but table 4.1 shows that this is not the case. It is expected that a longer sampling time would improve this just as the asymmetry in the unsteady pressure distribution. The front wheels experience a large outward force due to the area of low pressure at the outside edge of the wheel as shown in Figure 4.4b. The much smaller side force on the rear wheels points to the centre of the landing gear. This is due to the low pressure area on the inside edge of the

horizontal	Cd ($\times 10^{-2}$)		Cs ($\times 10^{-2}$)		Cl ($\times 10^{-2}$)	
component	mean	std	mean	std	mean	std
bogie	3.90	0.18	-0.14	1.44	1.10	2.90
front axle rhs	1.38	0.07	0.00	0.00	0.29	0.18
front axle lhs	1.41	0.09	0.00	0.00	0.36	0.14
front wheel rhs	16.73	1.69	12.21	2.34	0.09	1.16
front wheel lhs	16.54	1.46	-12.94	2.70	-0.27	1.12
rear axle rhs	1.05	0.41	-0.01	0.01	0.38	0.96
rear axle lhs	1.09	0.46	0.01	0.01	0.36	1.06
rear wheel rhs	19.98	1.76	-3.76	3.29	-0.17	2.20
rear wheel lhs	20.02	1.56	3.22	3.94	2.43	2.50
strut	38.95	1.68	-0.01	12.53	0.09	0.02
MLG	121.05	3.71	-1.42	14.21	4.67	4.89

TABLE 4.1: Mean and std of the aerodynamic force coefficients of the simplified horizontal configuration.

rear wheel where the flow accelerates between the wheel and the strut. The side force on both the front and rear axles is negligible since it consists purely of viscous stresses which in general are a lot smaller than the forces generated by pressure differences.

The flow separation on the upper half of the strut leads to intermittent vortex shedding which combined with the turbulent flow over the lower half of the strut results in large fluctuations in the side force. The standard deviation of the side force on the wheels and bogie are a lot lower than that of the strut but still significant when compared to the standard deviation of the drag force. The aft half of the bogie is surrounded by turbulent wake of the forward components which leads to large changes in the side force. The standard deviation of the side force of the rear wheels is higher than that of the front wheels so the turbulent inflow does make a difference here. Clearly the side force coefficient of the wheel is more sensitive to the level of turbulent fluctuations in the inflow than the drag coefficient.

The mean lift coefficient of all components is small except for the rear wheel on the left hand side. The lift coefficient of the two rear wheels differ considerably which is another indication that the mean flow field is not completely symmetric. The bogie is aligned with the freestream flow direction but still experiences a small positive lift force. The variation in lift coefficient is largest for the bogie and rear wheels since they are exposed to turbulent wake of the forward components. The rear axles experience large fluctuations in lift considering their small surface area compared to that of the bogie or rear wheels.

4.2 Toe up configuration

This section describes the aerodynamic results of the simulation of the simplified main landing gear in the 10° toe up configuration. Toe up configuration means that the front wheels have moved up compared to the previous horizontal configuration. This section has the same structure as the previous section starting with the flow features followed by the unsteady pressure distribution and the aerodynamic forces.

4.2.1 Flow features

The surface flow features on the front wheel of the toe up configuration (Figure 4.13) show similarities with the horizontal case (Figure 4.4) and the main differences are visible on the aft part of the front wheel. The wake generated by the front axle is narrower than for the horizontal configuration resulting in a less diverging flow over the inside surface of the wheel (Figure 4.13a). The surface LIC pattern in the wake downstream of the axle is less confused and shows two areas of recirculating flow with upstream pointing shear stress vectors.

The surface LIC pattern shown in the top and rear view (Figure 4.13e and 4.13d) of the front wheel indicates that the flow separates across the whole width of the wheel tread at approximately three quarters of the wheel diameter downstream of the front face. The inside and outside view of the wheel (Figure 4.13a and 4.13b) confirms that the flow separates from the top of the front wheel before it reaches the downstream wheel edge as can be seen by the sudden change in direction of the shear stress vectors. The rear view of the front wheel (Figure 4.13d) shows a flow attachment point in the separated flow region at the top of the wheel. This means that the flow separation results in an area of recirculating flow. The bottom view of the front wheel (Figure 4.13f) shows the same features as found on the front wheel of the horizontal configuration: strong curvature in the surface LIC pattern which indicates the formation of a vortex pair. The induced velocity generated by the strong vortex pair at the bottom of the wheel helps the flow to stay attached to the surface of the front wheel until it encounters the area of separated flow at the top of the wheel as can be seen in Figure 4.13d.

The flow features around the rear wheel (Figure 4.14) are asymmetric with clear differences between the upper and lower half of the wheel. The toe up configuration moves the lower half of the rear wheel away from the wake of the forward components and into a relatively clean flow. This results in a surface LIC pattern on the lower half of the rear wheel which is similar to the surface LIC pattern on the lower half of the front wheel.

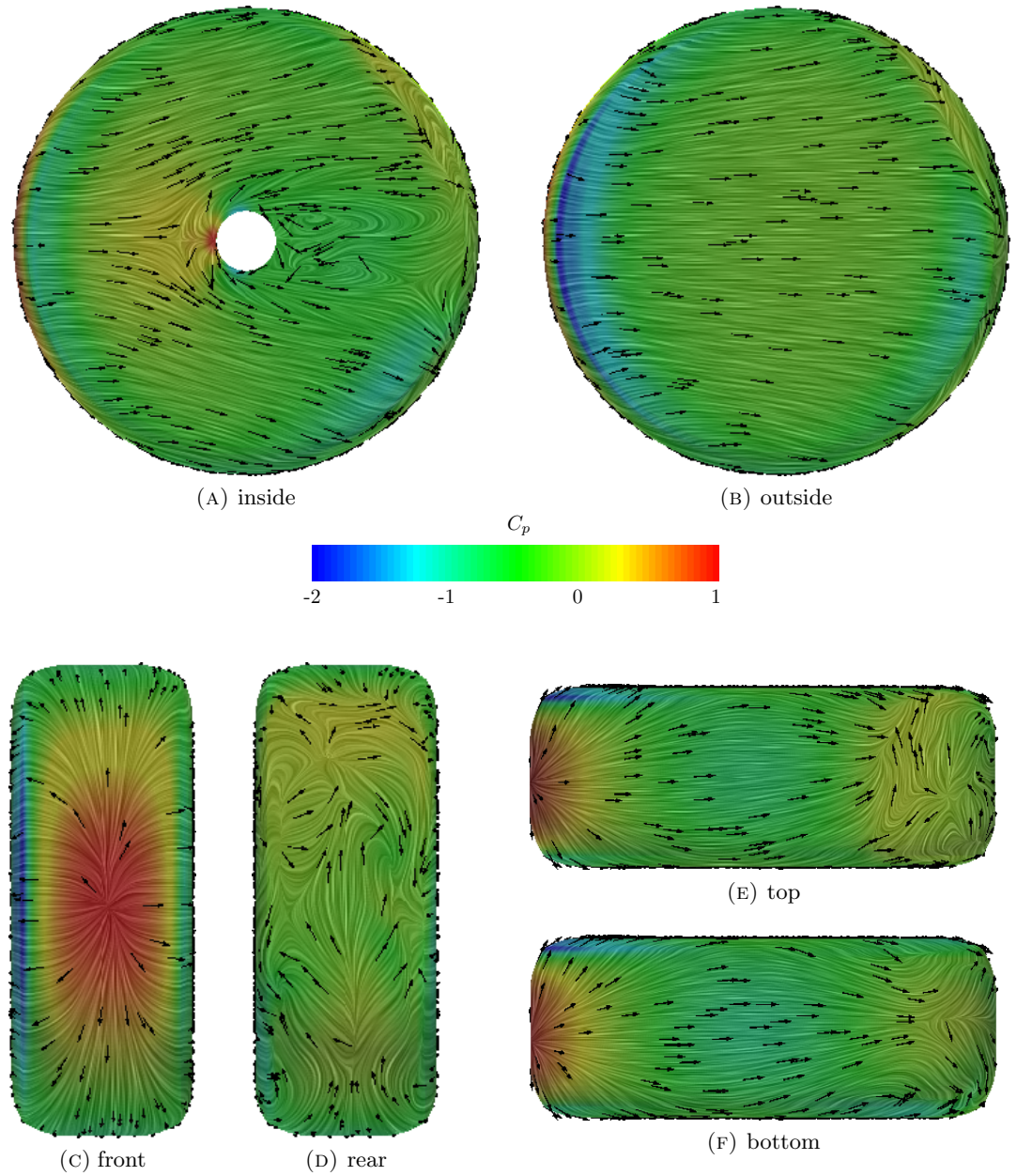

(A) inside (B) outside

(C) front (D) rear (E) top (F) bottom

FIGURE 4.13: Surface flow features of the time averaged flow field on the forward wheel of the simplified toe up configuration.

The flow follows the sides of the rear wheel until it reaches the downstream edge where it separates resulting in the formation of a vortex pair.

The flow features on the upper half of the rear wheel are under the influence of the wake and vortices coming of the upstream components. The attachment line on the front face of the rear wheel (Figure 4.14c) goes from the middle of the tread up towards the outside edge of the wheel. This means that a large part of the flow over the upper half of the rear wheel moves toward the centre of the landing gear. The surface LIC pattern on the top of the wheel (Figure 4.14e) shows the curved pattern indicating the formation of a

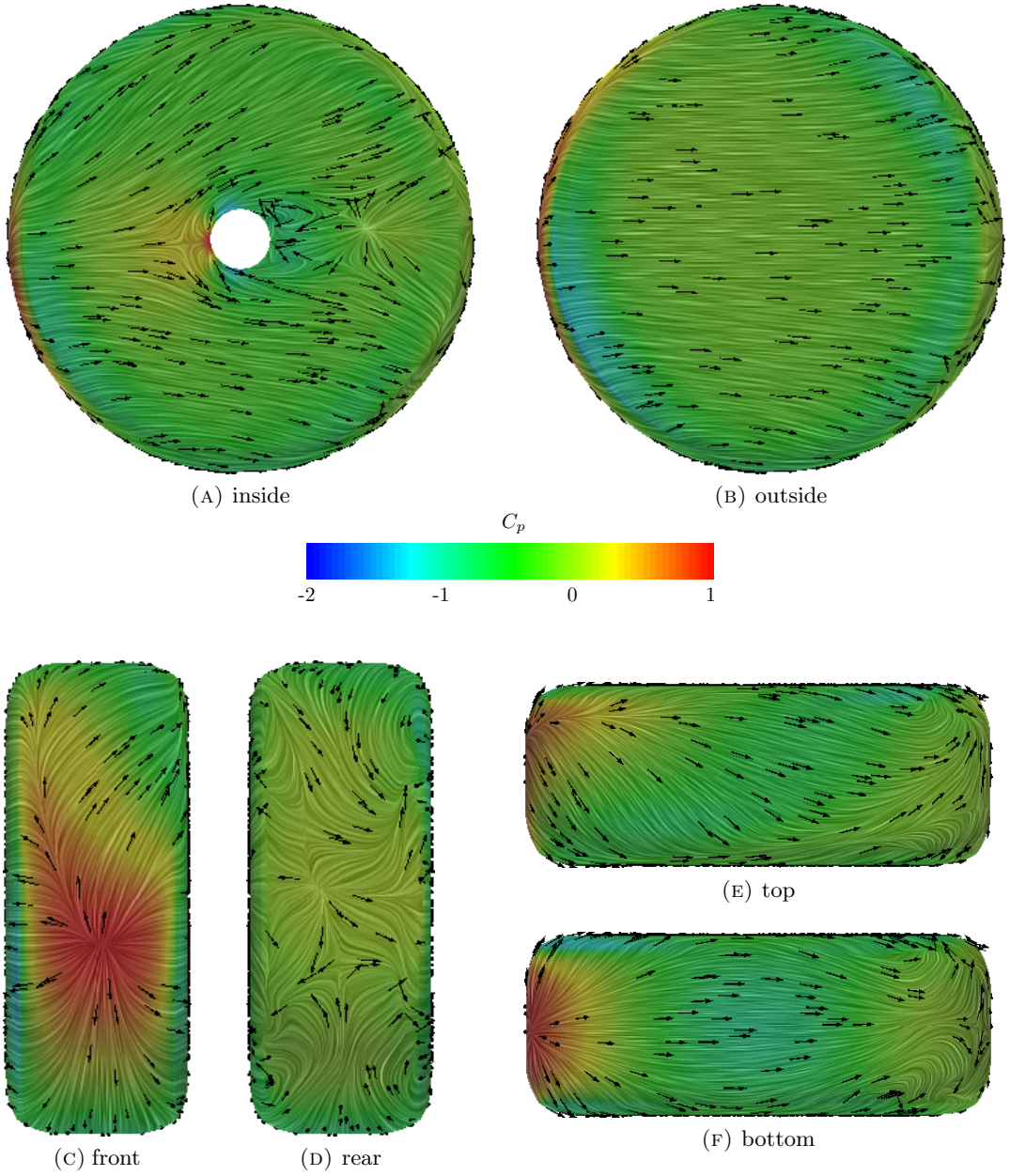

(A) inside (B) outside

(C) front (D) rear

(E) top

(F) bottom

FIGURE 4.14: Surface flow features of the time averaged flow field on the rear wheel of the simplified toe up configuration.

large vortex at the outside wheel edge. The aft face of the rear wheel (Figure 4.14d) shows a complex surface LIC pattern with an attachment point and shear stress vectors pointing in different directions which is characteristic for the separated recirculating flow region in the wake.

The toe up configuration means that the bottom of the bogie is facing the incoming flow. This leads to attached flow along the whole bottom surface as can be seen by the smooth surface LIC pattern in Figure 4.15c. The top and side view (Figures 4.15a and 4.15b) of the bogie show complex surface LIC patterns on the front half of the bogie. The shear

stress vectors on the top of the bogie point upstream indicating a recirculation zone generated by the flow separating of the sharp bogie edge. The side view of the bogie shows that the wake from the front axle moves up and joins the recirculation zone on the top of the bogie.

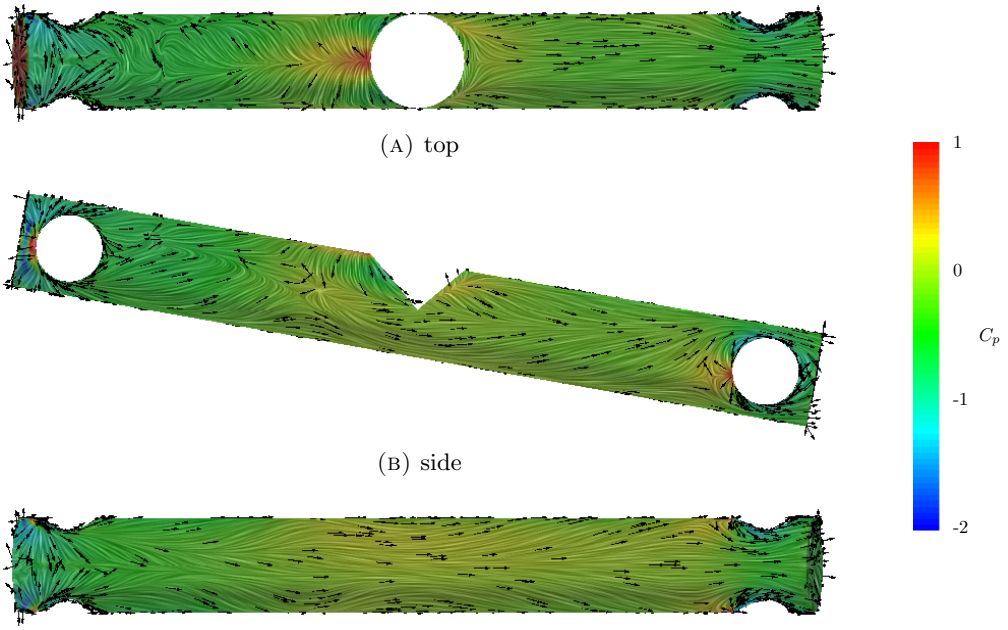

(A) top

(B) side

(C) bottom

FIGURE 4.15: Surface flow features of the time averaged flow field on the bogie of the simplified toe up configuration.

An increase in the pressure on the aft bottom half of the bogie surface causes the flow to change direction upwards. The shear stress vectors show that a significant amount of the flow moves over the top of the rear axle. The surface LIC pattern on the aft half of the bogie is smooth and without distinct features indicating that the flow follows the surface all the way to the end of the bogie.

The surface flow features on the strut of the toe up configuration (Figure 4.16) look similar to those of the horizontal configuration in the previous section (Figure 4.7). There is a stagnation line on the front face of the strut followed by the flow accelerating over the side which then separates just aft of the widest point of the strut. This results in a flow recirculation zone at the rear face of the strut. The direction of the time averaged flow in the wake behind the lower part of the strut is again upwards as indicated by the shear stress vectors.

The flow separation pattern on the front wheels of the toe up configuration is different compared to that of the horizontal configuration in the previous section. This is confirmed by Figure 4.17 showing the streamwise vorticity of the time averaged flow field. The streamwise vorticity plot at the aft end of the front wheels of the toe up configuration (Figure 4.17a) shows a pair of strong vortices at the bottom of each wheel

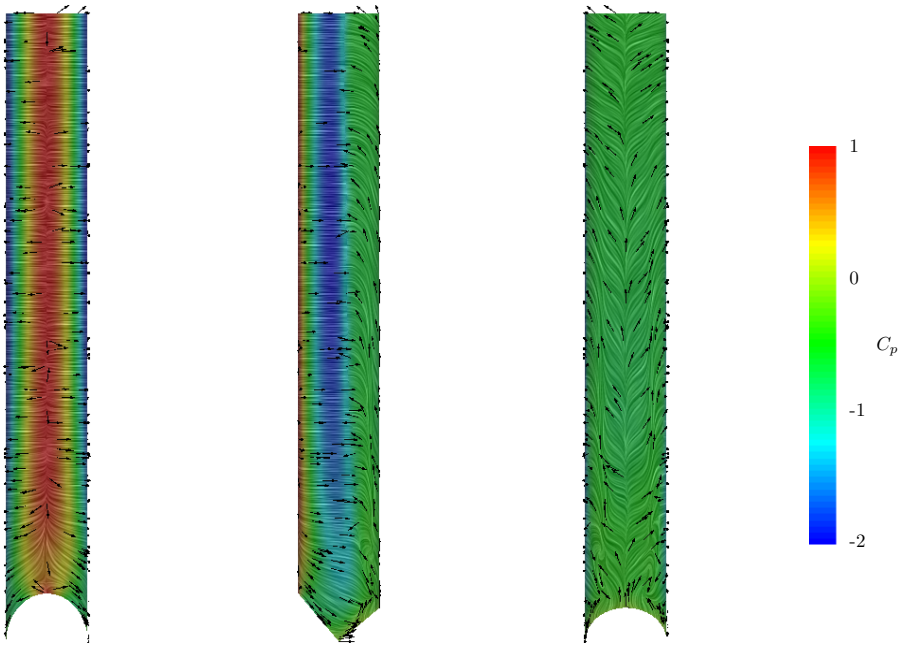

(A) front (B) side (C) rear

FIGURE 4.16: Surface flow features of the time averaged flow field on the lower half of the strut of the simplified toe up configuration.

and a weaker pair of vortices at the top of the wheels which have already separated from the wheel surface. There also is an area of opposite streamwise vorticity on top of the forward half of the bogie which is generated by the sideways movement of the recirculating flow due to the blockage of the strut.

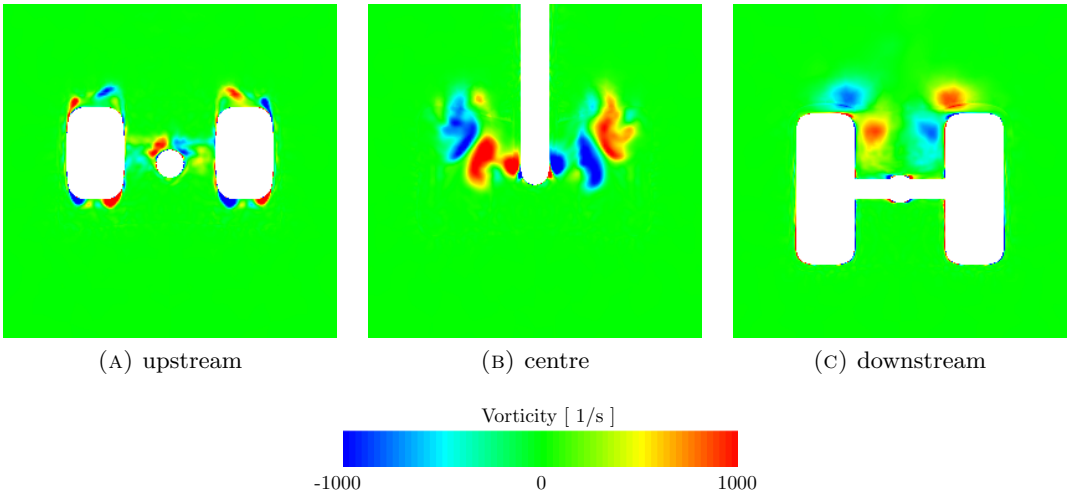

(A) upstream (B) centre (C) downstream

FIGURE 4.17: Streamwise vorticity of the time averaged flow field around the simplified toe up configuration, upstream = aft part of the front wheels, centre = centre of the MLG, downstream = centre of the rear wheels.

The plane at the centre of the landing gear (Figure 4.17b) shows how the strong vortex pairs from the bottom of the front wheels have moved upwards and inwards following the local flow direction. The area of vorticity in the figure has increased which is caused

by fact that the plane cuts through the vortex at an angle. The flow separation at the top of the front wheel generates a turbulent wake containing a lot of vorticity but this moves around and can no longer be distinguished in the time averaged flow field.

The last Figure 4.17c shows the streamwise vorticity of the time averaged flow field at a cut plane through the centre of the rear axles and wheels. The vortices have moved up and away from the bogie and towards the top of the rear wheels following the local flow direction. The area of vorticity has reduced compared to the second Figure 4.17b since the vortex core is more aligned with the freestream direction and therefore nearly perpendicular to the cut plane.

4.2.2 Unsteady surface pressure distribution

The flow features around the front wheel of the toe up configuration show a lot of similarities with the flow features around the front wheel of the horizontal configuration. The same is true for the unsteady pressure distribution as can be seen in Figure 4.18. The high unsteady pressure level generated by the wake of the front axle is clearly visible on the inside surface of the wheel (Figure 4.18a). The peaks are closer together and have moved upstream towards the front axle which coincides with the position of the flow recirculation region as shown by the surface flow features in Figure 4.13a.

The flow separation at the top of the front wheel differs compared to the horizontal configuration and this leads to a difference in the unsteady pressure distribution. The absence of the strong streamwise vortex pair results in an earlier flow separation and this leads to a slight increase in the unsteady pressure levels at the top of the wheel (Figure 4.18e). The rear face of the front wheel (Figure 4.18d) shows an increase in the unsteady pressure levels where the wake of the front axle interacts with the induced flow field generated by the strong vortex at the inside edge of the front wheel. An even stronger peak is visible at the top of the rear view of the front wheel where the induced flow generated by the strong vortex pair at the bottom of the wheel encounters the separated recirculating flow at the top of the wheel.

The lower half of the rear wheel and axle of the toe up configuration (Figure 4.19f) is situated in a relatively clean flow which leads to a lower unsteady pressure levels compared to the rear wheel and axle of the horizontal configuration. Increased unsteady pressure levels are visible on the top of the rear wheel (Figure 4.19e) where the strong streamwise vortices pass along the wheel surface. The inside surface of the rear wheel (Figure 4.19a) shows two peaks in the unsteady pressure level just downstream of the rear axle at the location of the flow recirculation zones.

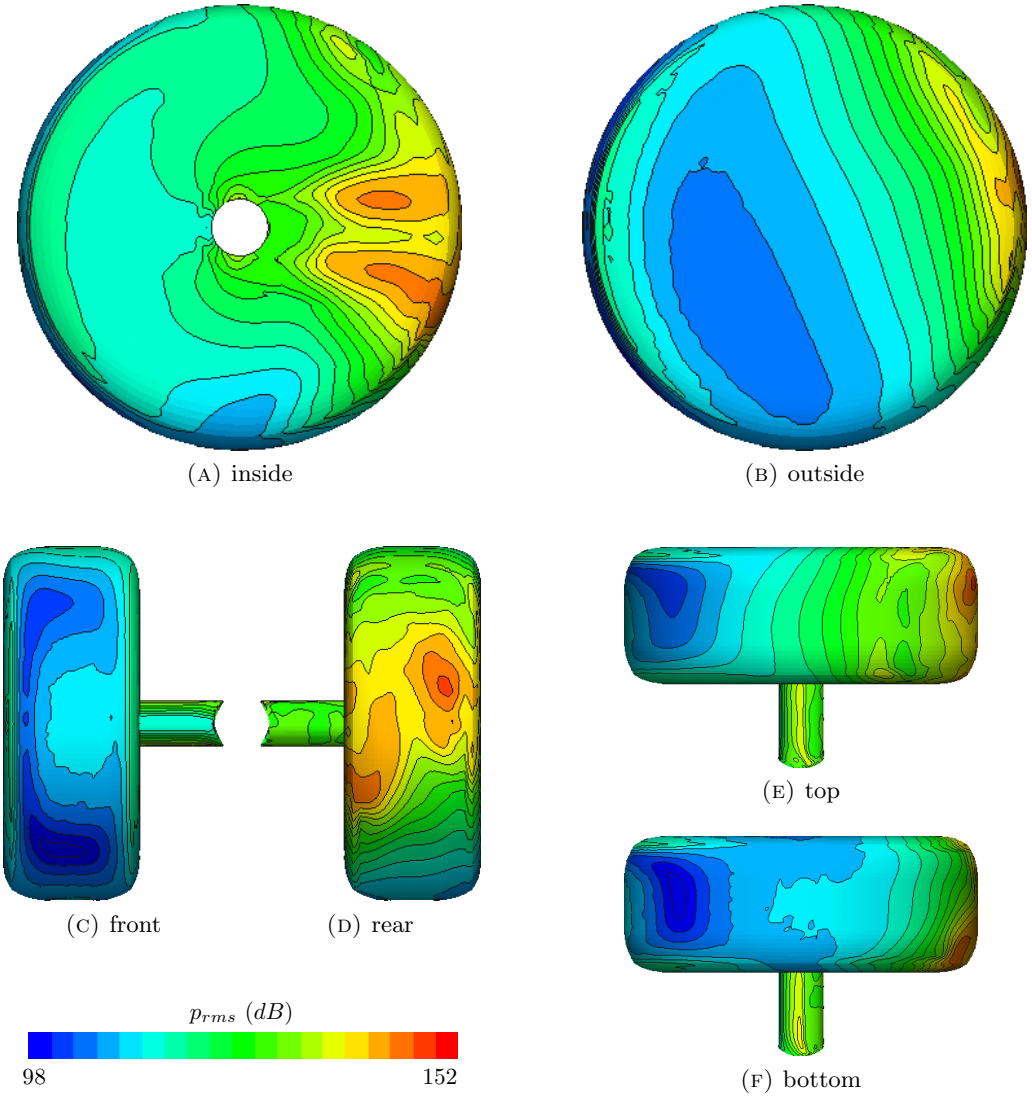

FIGURE 4.18: Unsteady surface pressure level on the forward wheel and axle of the simplified toe up configuration.

The unsteady pressure level on the outside surface of the rear wheel (Figure 4.19b) increases at the downstream edge where the flow separates from the surface similar to what happens on outside surface of the rear wheel in the horizontal configuration. The strong streamwise vortices move over the top of the rear axles resulting in a peak in the unsteady pressure on the top surface of the axle (Figure 4.19e). The peak in the unsteady pressure level on the bottom surface of the rear axle (4.19f) coincides with the location of the highest local flow velocity.

The surface flow features section has shown that there is attached flow over the bottom surface of the bogie and this results in a low unsteady pressure level (Figure 4.20c). The unsteady pressure level at the top of the bogie (Figure 4.20a) increases towards the bogie to strut junction due to the turbulent flow coming of the sharp bogie edge and front

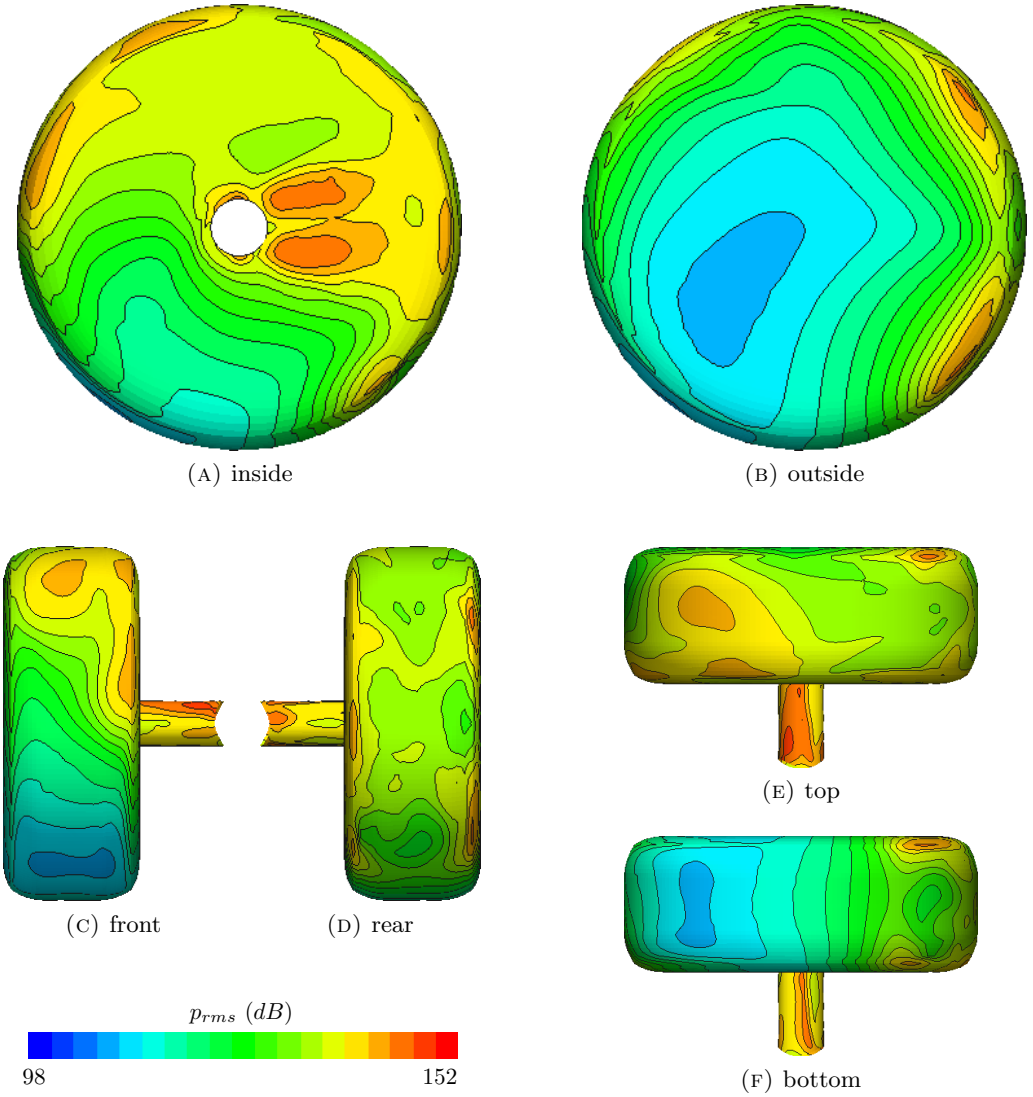

FIGURE 4.19: Unsteady surface pressure level on the rear wheel and axle of the simplified toe up configuration.

axles. The peak in the unsteady pressure level is not at the stagnation point in front of the strut but towards the sides of the bogie where the local flow velocity is higher.

A second peak in the unsteady pressure is visible on the side of the bogie (Figure 4.20b) which is located at the edge of the recirculation zone downstream of the front axle. The aft half of the bogie shows the highest unsteady pressure level just downstream of the bogie to strut junction. The turbulent flow at this location gets pushed to the surface under the influence of the strong streamwise vortices. The junction of the bogie with the rear axle also generates a peak in the unsteady pressure level due to the increase in the local flow velocity.

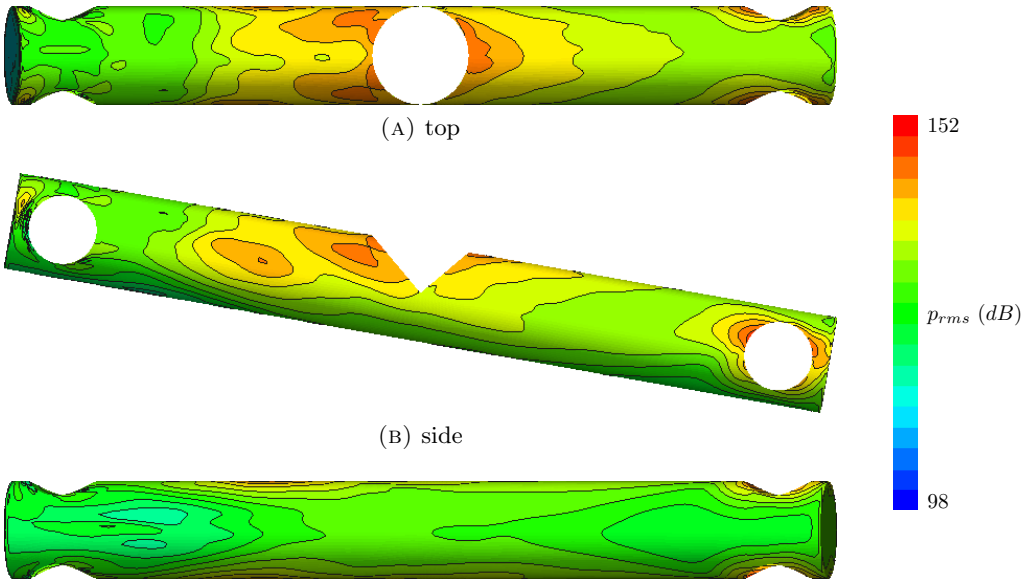

(A) top

(B) side

(C) bottom

FIGURE 4.20: Unsteady surface pressure level on the bogie of the simplified toe up configuration.

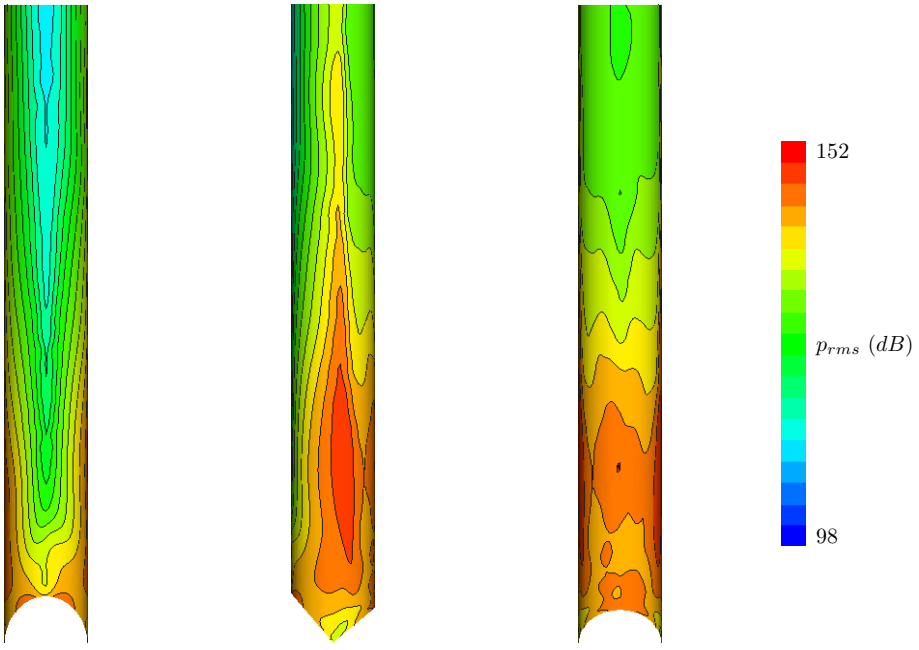

(A) front (B) side (C) rear

FIGURE 4.21: Unsteady surface pressure level on the lower half of the strut of the simplified toe up configuration.

The front view of the strut of the toe up configuration (Figure 4.21a) shows a lower unsteady pressure level than the strut of the horizontal configuration in the previous section. This is due to the flow recirculation zone with a relatively low flow velocity on the top of the bogie in front of the strut. The low local flow velocity results in a lower level of the unsteady pressure. The side and rear view of the strut in Figures 4.21b and 4.21c look similar to the strut of the horizontal configuration. The flow accelerates past the side of the strut resulting in a peak in the unsteady pressure level. The unsteady pressure level on the surface of the strut quickly reduces above the wake of the front wheels due to the relatively undisturbed inflow.

4.2.3 Aerodynamic forces

Table 4.2 lists the mean and standard deviation of the aerodynamic force coefficients of the components of the simplified landing gear in toe up configuration. The wheels and strut generate the largest contribution to the total drag just as for the horizontal configuration. The drag coefficient of the rear wheels has reduced compared to the horizontal configuration because of the smaller size of the area of high pressure on the front of the rear wheels. The bogie is no longer aligned with the flow which results in an increase in the drag coefficient. The drag of the rear axles has doubled compared to the horizontal configuration since they are exposed to the higher velocity flow. The toe up configuration has changed the drag coefficient of some of the components compared to the previous horizontal configuration but the standard deviation has not changed significantly. Only the rear wheels show a clear decrease in the standard deviation of the drag coefficient due to the clean flow over the lower half of the wheel.

toe up	Cd ($\times 10^{-2}$)		Cs ($\times 10^{-2}$)		Cl ($\times 10^{-2}$)	
component	mean	std	mean	std	mean	std
bogie	5.58	0.22	0.07	1.44	4.24	0.91
front axle rhs	1.66	0.09	0.00	0.00	-0.10	0.13
front axle lhs	1.63	0.07	0.00	0.00	-0.09	0.13
front wheel rhs	15.26	1.39	8.14	1.83	-7.63	0.97
front wheel lhs	16.42	1.62	-8.54	1.55	-7.95	0.72
rear axle rhs	2.33	0.39	0.01	0.00	0.52	1.13
rear axle lhs	2.21	0.36	-0.01	0.00	0.46	1.05
rear wheel rhs	16.59	1.31	1.61	2.65	0.58	3.60
rear wheel lhs	16.38	1.40	0.45	3.08	-0.83	2.15
strut	43.46	1.86	0.67	12.05	0.01	0.01
MLG	121.53	3.49	2.39	14.30	-10.79	5.64

TABLE 4.2: Mean and std of the aerodynamic force coefficients of the simplified toe up configuration.

The side force on the front wheels points outwards just as for the horizontal configuration due to the area of low pressure on the forward outside edge of the front wheels. The side force coefficient of both the rear wheels is positive which is unexpected, an opposite sign of the mean side force coefficient is expected because of the symmetry of the landing gear geometry. The sideforce coefficients of the rear wheels are relatively low and this inconsistency would probably disappear with a longer sampling time. The other components have low side force coefficients either due to symmetry or due the fact that the shear stress generates smaller force than pressure differences. The strut is again responsible for the large fluctuations in side force due to the vortex shedding in the wake and the turbulent flow passing along the lower part of the strut. The unsteadiness of the side force of both the front and rear wheels has reduced compared to the horizontal configuration. The front wheel in the toe up configuration generates only two strong vortices and the lower half of the rear wheel is in the undisturbed flow which explains the reduced level of the side force fluctuations. Although the flow field in the centre of the landing gear has changed compared to the horizontal configuration the standard deviation of the side force coefficient of the bogie has the same value as for the horizontal configuration.

The toe up configuration gives the bogie an angle of attack to the incoming flow which causes it to generate lift as can be seen in table 4.2. The different separation pattern on the top and bottom of the front wheel changes the pressure distribution on the aft part of the wheel creating a significant amount of down force. The lift coefficients of the rear wheels are of opposite sign which is the same type of inconsistency as seen in the side force coefficients and should disappear with a longer sampling time. The downforce generated by the front wheels is dominant over the lift contribution of all the other components which results in a downforce for the whole simplified landing gear in the toe up configuration. The fluctuations in the lift coefficient are small for the front axles and front wheels which are in the undisturbed flow and large for the rear axles and rear wheels which are in the wake of the forward components. The variation in the lift coefficient of the bogie is lower compared to the horizontal configuration since it is not surrounded by four strong streamwise vortices.

4.3 Toe down configuration

This section describes the aerodynamic results of the CFD simulation of the simplified main landing gear in the 10° toe down configuration. Toe down configuration means that the front wheels have moved down compared to the horizontal configuration. This

section has the same structure as the previous two sections starting with the flow features followed by the unsteady pressure distribution and the aerodynamic forces.

4.3.1 Flow features

The surface flow features of the time averaged flow field on the front wheel of the toe down configuration (Figure 4.22) are almost a vertically mirrored copy of the flow features on the front wheel of the toe up configuration (Figure 4.13). The flow features on the forward half of the front wheel are the same as seen in the previous two configurations and the significant flow features are found on the aft half of the wheel. The inside and outside surface of the front wheel (Figures 4.22a and 4.22b) show that the flow separates from the sides of the front wheel before it reaches the downstream edge. This results in a separation line across the width of the wheel tread as can be seen in Figure 4.22f. This flow separation at the bottom of the front wheel leads to a region of recirculating flow as shown by the attachment point in the surface LIC pattern on the lower aft face of the front wheel (Figure 4.22d).

The flow features on the top of the front wheel in Figure 4.22e show the by now familiar curved surface LIC pattern indicating the formation of a streamwise vortex pair. The induced velocity of these streamwise vortices helps the the flow to stay attached down along the centreline of the front wheel until it encounters the flow recirculation zone at the bottom of the wheel. The main difference in the surface flow features on the front wheel between the toe up and toe down configuration is the shorter recirculation zone behind the front axle for the toe down configuration.

Similar to what happens for the front wheel, the time averaged flow features on the rear wheel of the toe down configuration (Figure 4.23) are almost a vertically mirrored copy of the flow features on the rear wheel of the toe up configuration (Figure 4.14). The toe down configuration moves the upper half of the rear wheel into the relatively clean flow which results in a surface LIC pattern similar to that of the upper half of the front wheel. The front face of the rear wheel (Figure 4.23c) shows an attachment line which runs from the middle of the wheel to the outside lower edge. This indicates that a large part of the flow that reaches the lower half of the rear wheel moves towards the centre of the landing gear. The surface LIC pattern on the aft face of the rear wheel (Figure 4.23d) shows strong curvature at the lower outside corner which indicates the formation of a vortex. The flow at the top of the rear wheel (Figure 4.23e) separates from the surface relatively early which can be seen by the sudden change in direction of the shear stress vectors combined with an increase in the pressure coefficient.

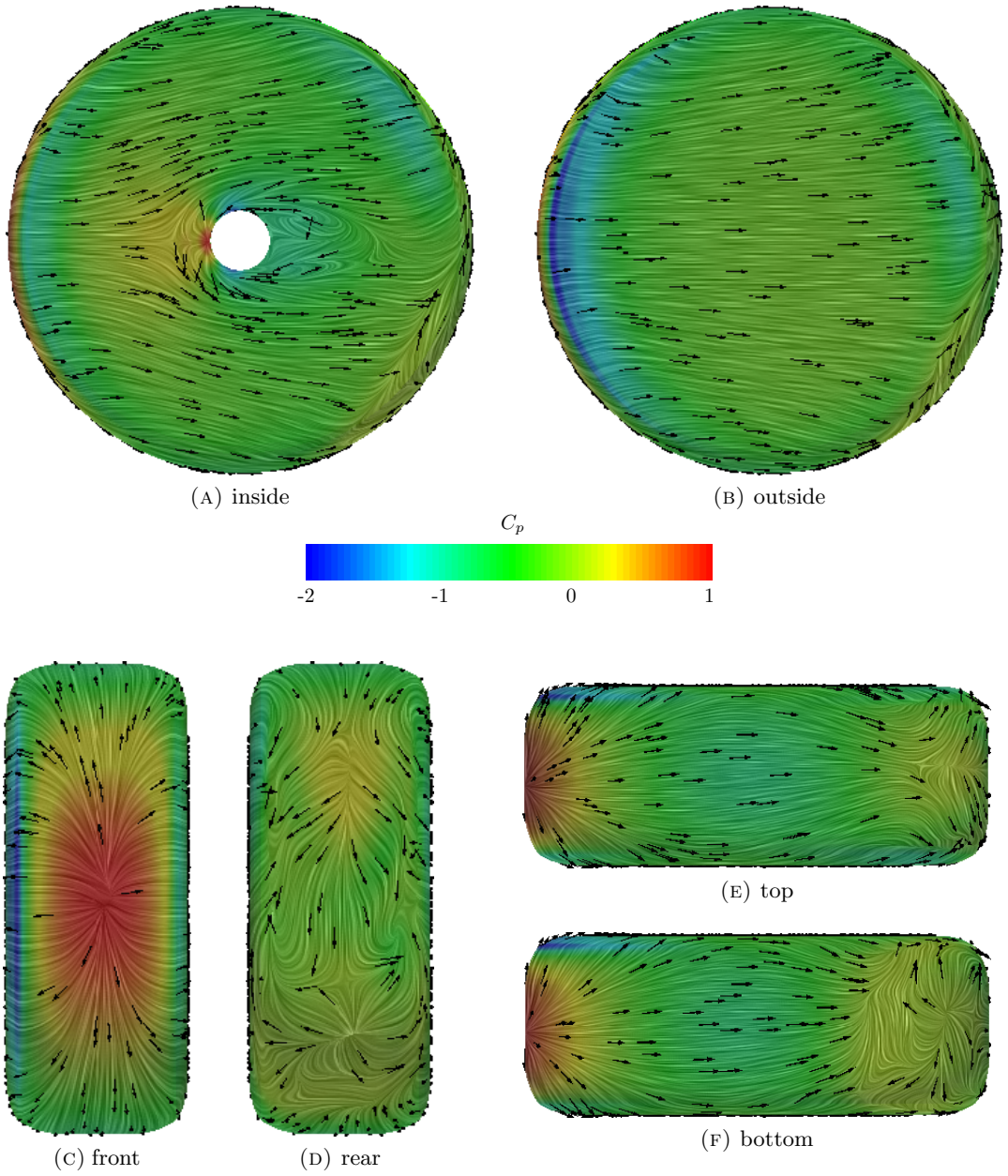

(A) inside (B) outside

(C) front (D) rear

(E) top

(F) bottom

FIGURE 4.22: Surface flow features of the time averaged flow field on the forward wheel of the simplified toe down configuration.

The toe down configuration means that the top of the bogie is facing the incoming flow. This results in an attachment line from the front of the bogie along the centre of the surface to the base of the strut as can be seen in Figure 4.24a. The increase in pressure towards the bogie to strut junction causes the flow to split towards the sides of the bogie. Part of the flow that moves from the top of the bogie to the sides merges with the recirculation zone behind the front axle as shown in the side view (Figure 4.24b). The increased pressure on the top aft half of the bogie pushes the flow towards the side of the bogie but this effect is not as strong as on the forward half of the bogie due to the reduced flow velocity in the wake of the strut.

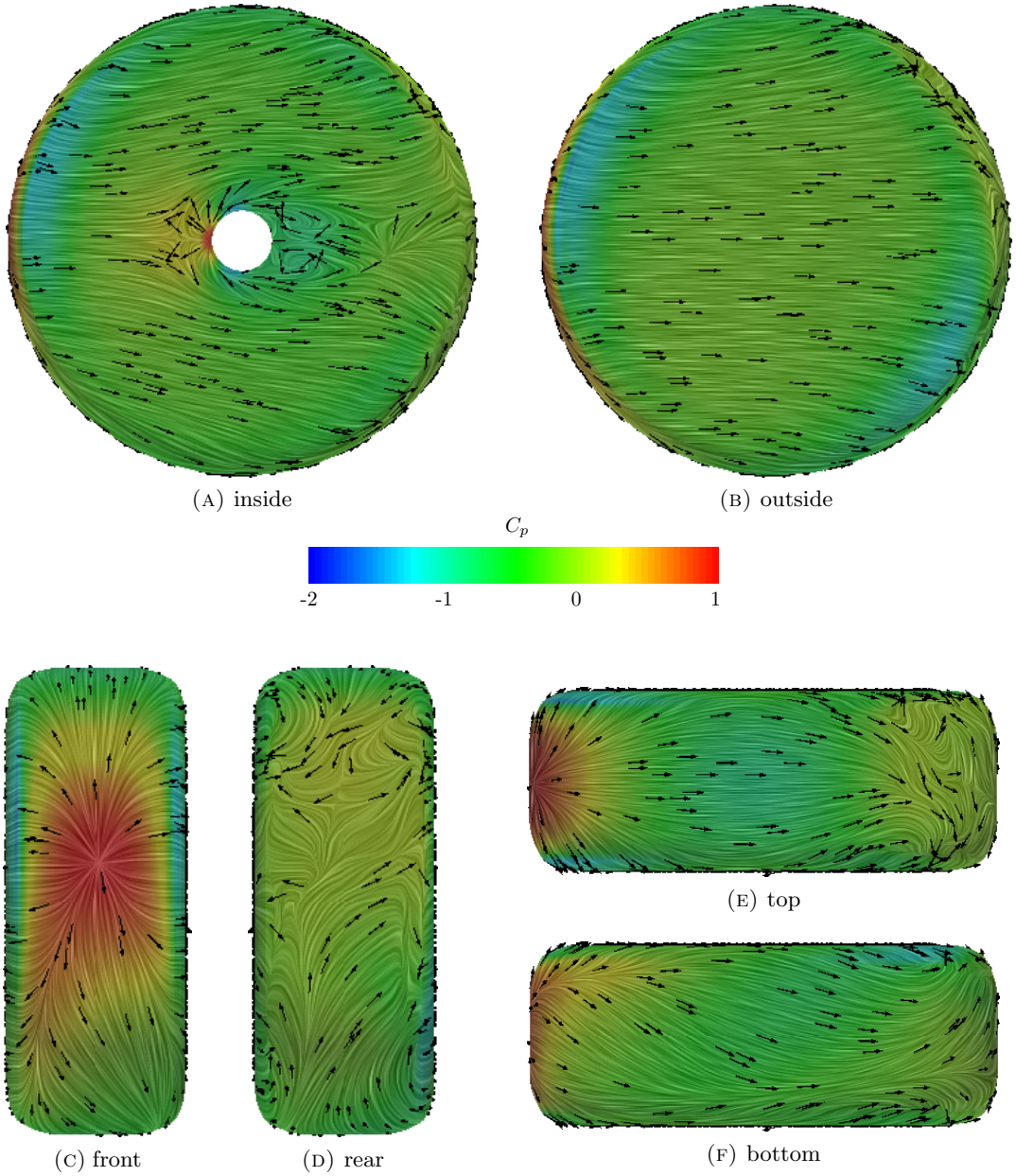

(A) inside (B) outside

(C) front (D) rear (E) top (F) bottom

FIGURE 4.23: Surface flow features of the time averaged flow field on the rear wheel of the simplified toe down configuration.

The bottom view of the bogie in Figure 4.24c shows an attachment point at approximately one third of the bogie length downstream of the front edge. The direction of the shear stress vectors forward of this attachment point are opposite to the flow direction which indicates the presence of a region of recirculating flow. This recirculation zone is generated by the flow separating of the sharp lower bogie edge and merging with the wake of the front axles. The pressure from the attachment point to the rear bogie edge decreases resulting in a pressure gradient which helps the flow to stick to the bottom surface of the bogie all the way to the downstream edge as shown by the surface LIC pattern.

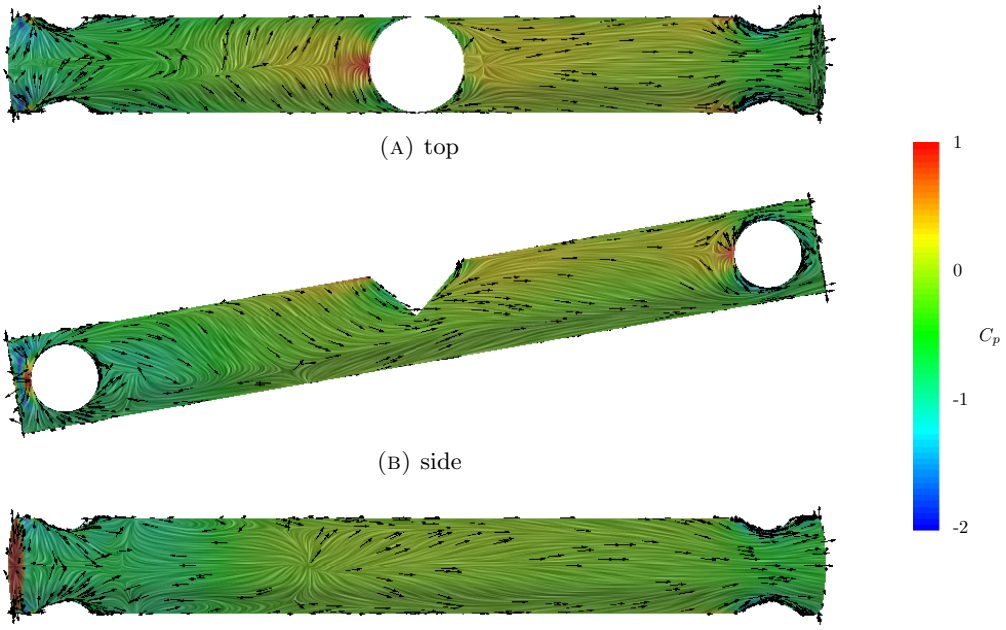

(A) top

(B) side

(C) bottom

FIGURE 4.24: Surface flow features of the time averaged flow field on the bogie of the simplified toe down configuration.

The time averaged surface flow features around the lower half of the strut of the toe down configuration (Figure 4.25) look similar to those of the horizontal and toe up configurations. There is an attachment line in the high pressure area on the front face of the strut (Figure 4.25a) followed by an acceleration of the flow resulting in an area of low pressure on the side of the strut (Figure 4.25b). The flow separates just downstream of the widest point of the strut which generates a region of recirculating flow in the wake as shown by the upstream pointing shear stress vectors at the rear face of the strut (Figure 4.25c).

The location of the streamwise vortices of the time averaged flow field at the aft end of the front wheels in Figure 4.26a is almost a vertically mirrored copy of Figure 4.17a of the toe up configuration. The main difference between these two figures is the absence of the vortex pair near the surface of the bogie for the toe down configuration. This is because the flow recirculation zone at the front of the bogie is not forced sideways by the strut in the toe down configuration. Figure 4.26b at the mid plane of the landing gear shows that the strong vortex pairs from the top of the front wheels have moved down and towards the centre of the landing gear following the local direction of the time averaged flow field. The area of high vorticity in the figure has increased but this is again due to the fact that the vortex core is not perpendicular to the plane of observation.

The last figure 4.26c shows the location of the vortices at a plane through the centre of the rear axles and wheels. It is clear that the vortices have continued their downwards trajectory and pass below the rear wheels. This again is an almost vertically mirrored

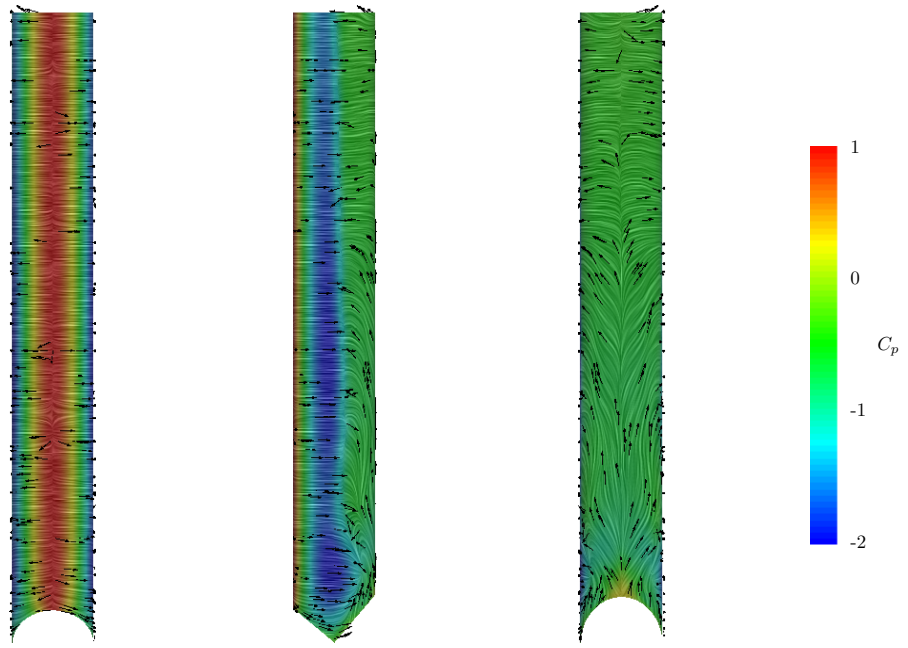

(A) front (B) side (C) rear

FIGURE 4.25: Surface flow features of the time averaged flow field on the lower half of the strut of the simplified toe down configuration.

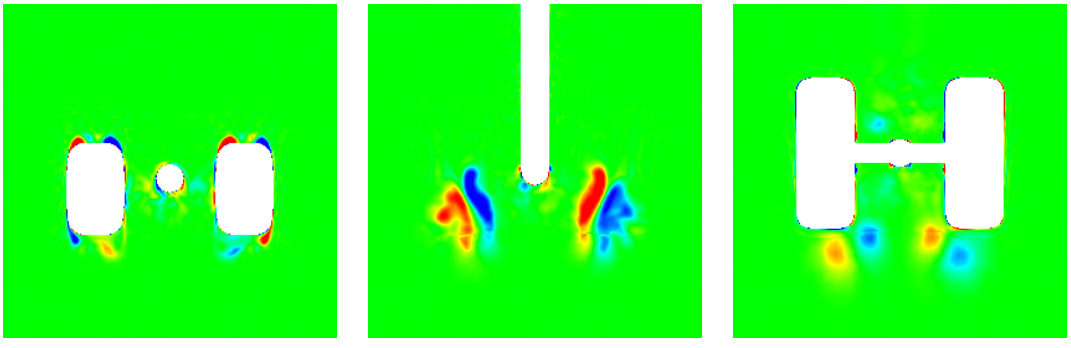

(A) upstream (B) centre (C) downstream

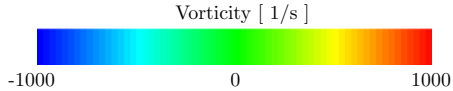

FIGURE 4.26: Streamwise vorticity of the time averaged flow field around the simplified toe down configuration, upstream = aft part of the front wheels, centre = centre of the MLG, downstream = centre of the rear wheels.

copy of Figure 4.17c of the toe up configuration. The main difference between these figures is that for the toe down configuration both vortex cores pass below the rear wheel while for the toe up configuration only one of the two vortex cores passes above the rear wheel while the other vortex passes on the inside of the rear wheel. It is assumed that this difference is caused by the wake from the strut which restricts the upward trajectory of the vortices of the toe up configuration. The trajectory of the streamwise vortices of the toe down configuration is not restricted and this results in them passing at a larger distance from the rear wheels.

4.3.2 Unsteady surface pressure distribution

The time averaged flow features around the front wheel of the toe up and toe down configurations show a lot of similarity but this is not the case for the unsteady pressure distribution which shows some clear differences. The front wheel is in the undisturbed flow which results in a low level of unsteadiness on the forward half of the wheel. The peaks in the unsteady pressure level are located on the aft half of the front wheel as can be seen in Figure 4.27. The turbulent wake behind the front axle creates an area of high pressure fluctuations on the inside surface of the front wheel. The strength and distribution of the peaks behind the front axle in Figure 4.27a is not symmetric as it is for the other two configurations with a stronger peak at the bottom and a weaker peak at the top of the wake. The peak at the bottom is closer to the front axle while the weaker peak at the top is a little further downstream. Both peaks are closer to the front axle compared to the toe up configuration and this agrees with the location of the shorter recirculation zone as shown in Figure 4.22a of the flow features section. Figure 4.27a clearly shows how the early flow separation on the lower half of the inside surface of the wheel leads to an increase in the unsteady pressure level. The same happens at the lower downstream edge on the outside surface of the front wheel in figure 4.27a.

The highest unsteady pressure level is visible just below the middle of the rear view of the front wheel in Figure 4.27d. This is where the induced flow from the top of the wheel encounters the recirculation zone at the bottom of the wheel. The interaction between these two different flows leads to large pressure fluctuations at the surface of the wheel. The aft face also shows an increased unsteady pressure level at the inside edge of the front wheel which is where the turbulent wake from the front axle passes over the wheel edge.

The toe down configuration moves the top of the rear wheel away from the wake of the forward components which leads to relatively low unsteady pressure level on the top of the rear wheel (Figure 4.28e). The strut also generates a wake and Figure 4.28a shows

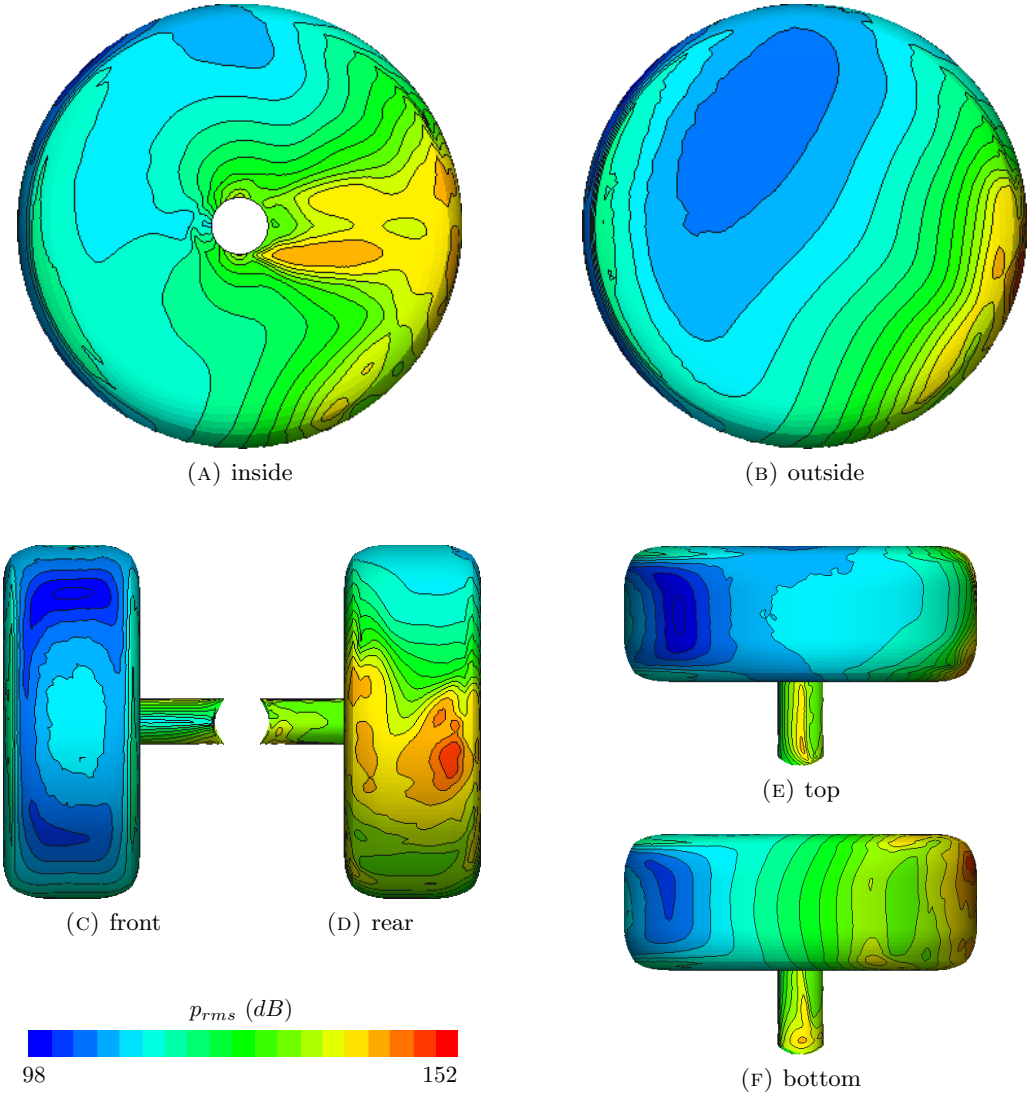

FIGURE 4.27: Unsteady surface pressure level on the forward wheel and axle of the simplified toe down configuration.

an increase in the unsteady surface pressure levels at the top forward edge of the rear wheel. The strong streamwise vortices pass below the rear wheel and axle and they are further away from the surface of the wheels compared to the other two configurations which results in lower unsteady pressure peaks on the bottom of the rear wheels and axles (Figure 4.28f). The highest unsteady pressure levels are generated by the wake of the rear axle on the inside surface of the rear wheel as can be seen in Figure 4.28a.

The top of the bogie of the toe down configuration in Figure 4.29a shows a low unsteady pressure level due to the attached undisturbed flow over the front half of the bogie as shown in the flow features section. The side view of the bogie (Figure 4.29b) shows a peak in the unsteady pressure level as a result of the wake of the front axle. The front lower half of the bogie in Figure 4.29c shows a slightly elevated unsteady pressure level

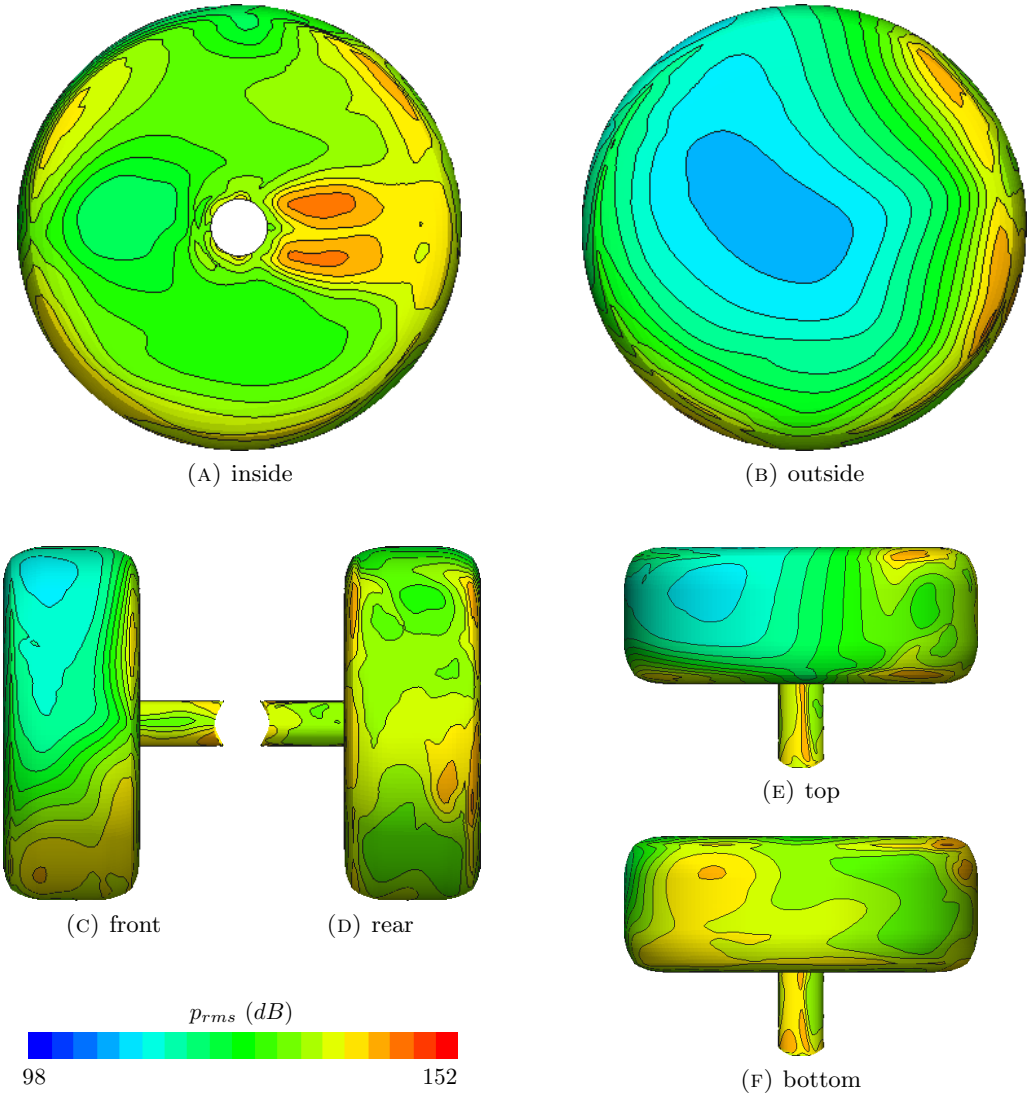

FIGURE 4.28: Unsteady surface pressure level on the rear wheel and axle of the simplified toe down configuration.

due to separated recirculating flow generated by the sharp bogie edge and front axles. The flow velocity in this recirculation zone is low which reduces the level of the pressure fluctuations. The flow over the aft lower half of the bogie is attached which results in a low unsteady pressure level compared to the horizontal and toe up configurations.

The toe down configuration leads to a relatively smooth bogie to strut junction which combined with the attached flow on top of the bogie leads to a relatively low unsteady pressure level on the front face of the strut (Figure 4.30a). The toe down configuration moves the forward components away from the strut which means that a smaller part of the strut is exposed to the wake compared to the other two configurations. This is confirmed by the small area of the unsteady pressure peak visible in the side and rear view in Figures 4.30b and 4.30c.

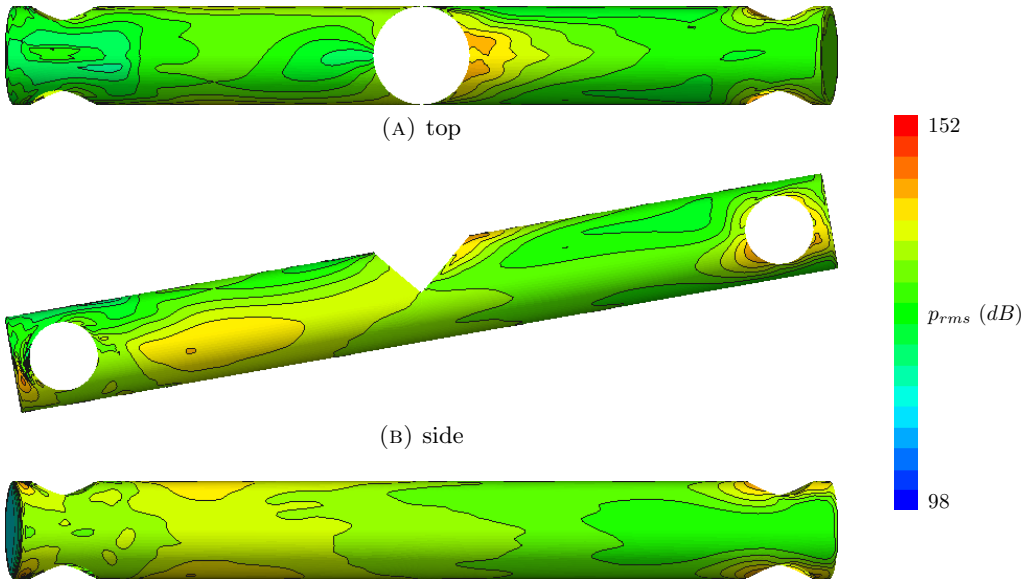

(A) top

(B) side

(C) bottom

FIGURE 4.29: Unsteady surface pressure level on the bogie of the simplified toe down configuration.

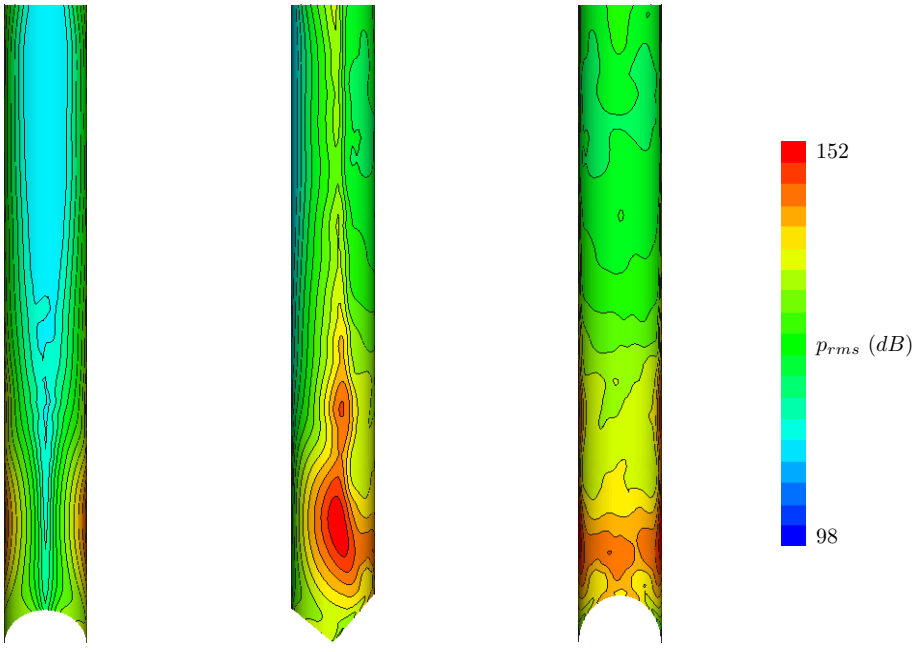

(A) front (B) side (C) rear

FIGURE 4.30: Unsteady surface pressure level on the lower half of the strut of the simplified toe down configuration.

4.3.3 Aerodynamic forces

The drag coefficients of the different components of the toe down configuration (table 4.3) are almost the same as those of the toe up configuration (table 4.2) with the exception of the front axles. Both the mean and standard deviation of the drag coefficient of the front axles has increased compared to the toe up configuration. The mean drag of the front axles has increased to the same level as the rear axles but the fluctuations of the drag of the front axles are still a lot lower due to the relatively clean inflow conditions.

toe down	Cd ($\times 10^{-2}$)		Cs ($\times 10^{-2}$)		Cl ($\times 10^{-2}$)	
component	mean	std	mean	std	mean	std
bogie	5.80	0.20	-0.40	0.93	-5.06	0.75
front axle rhs	2.21	0.14	0.00	0.00	0.15	0.27
front axle lhs	2.24	0.19	0.00	0.00	-0.03	0.39
front wheel rhs	15.42	1.43	6.66	1.24	6.66	0.83
front wheel lhs	15.76	1.63	-5.82	1.65	6.86	1.05
rear axle rhs	2.27	0.27	-0.01	0.00	-0.16	0.84
rear axle lhs	2.17	0.29	0.01	0.00	-0.21	0.83
rear wheel rhs	16.48	1.54	-0.21	2.75	-1.13	2.20
rear wheel lhs	15.49	1.54	0.08	3.20	-0.82	2.67
strut	42.80	1.52	0.40	8.68	0.06	0.01
MLG	120.64	2.53	0.72	9.42	6.31	3.70

TABLE 4.3: Mean and std of the aerodynamic force coefficients of the simplified toe down configuration.

The front wheels of the toe down configuration are the only components which generate a significant amount of side force and it points away from the centre of the landing gear. This is the same as for the previous two configurations due to the area of low pressure at the outside forward edge of the front wheel. The standard deviation of the side force coefficient of the strut has reduced due to the fact that a smaller part of the strut is exposed to the turbulent wake of the upstream components. The strong streamwise vortices are further away from the landing gear geometry compared to the other two configurations which results in smaller fluctuations in the side force.

The negative angle of attack of the bogie of the toe down configuration causes it to generate a down force. The front wheels generate a significant amount of lift due to the difference in the flow separation pattern on the top and bottom of the wheel. This is the exact opposite of what happens in the toe up configuration. The rear wheels generate a small down force and the contribution of the other components is so small it can be neglected. The fluctuating lift of the forward components has increased but the level on the aft components has decreased more resulting in a lower level of the fluctuating lift for the complete landing gear compared to both the horizontal and toe up configurations.

4.4 Summary and discussion

The main flow features of the time averaged flow field around the simplified landing gear configurations are the strong streamwise vortices which are generated by the flow separation on the front wheels. Similar streamwise vortices are seen in a study of the aerodynamics of a single wheel near the ground by McManus [71] and also in the flow field around the downstream part of the Ahmed car body [72]. A schematic of the vortex generation at the shoulder of the wheel is shown in Figure 4.31. The difference in the direction of the flow over the side of the wheel (dark blue vector) and over the top of the wheel (red vector) results in a vortex (green helix). This vortex entrains the fast freestream flow from the top of the wheel (light blue vector) and pushes this flow to the side (cyan vector) at the centre of the wheel. The schematic only shows the formation of a single vortex but this process happens at both the inside and outside shoulder of the wheel resulting in a vortex pair. The strength of the vortices on the inside and outside of the wheel are not equal due to the presence of the axle. The axle generates a more diverging flow over the inside surface of the wheel. This results in a larger difference in direction between the two flows which increases the strength of the vortex closest to the centre of the landing gear.

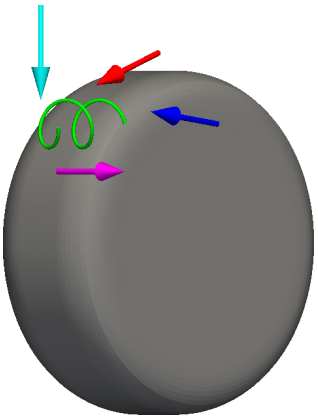

FIGURE 4.31: Schematic of vortex formation at the shoulder of the front wheel (looking upstream).

The description until now is based on the generation of a vortex pair at the top or bottom of an isolated wheel but the situation around the front wheels of the main landing gear is a little different due to the influence of the rear wheels. The horizontal landing gear configuration is almost symmetric so the effect of the rear wheel is the same on both the top and bottom of the front wheel. This results in two vortex pairs or four vortices being generated at each front wheel. The vortices entrain the freestream flow from the top and bottom of the wheel and push this flow sideways both to the centre of the landing gear and to the outside. The strong vortices from the inside edge of the front wheel move to the centre of the landing gear following the direction of the time averaged flow

field while the weaker vortices from the outside edge of the front wheel are pushed away from the centre of the landing gear to the outside of the rear wheel.

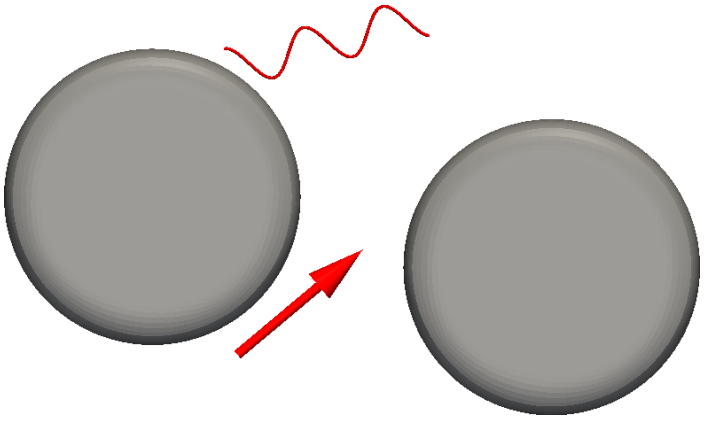

FIGURE 4.32: Schematic of flow separation on the front wheel due to rotation of the bogie.

The toe up and toe down configurations both have an asymmetric placement of the wheels which has an important effect on the vortex generation at the shoulders of the front wheels. Part of the rear wheel is exposed to the freestream which results in an area of high pressure on the front face of the rear wheel. The flow over the front wheel encounters this area of high pressure and gets forced through the gap between the two wheels as indicated by the red arrow in Figure 4.32. The effect of entrainment of high velocity flow by the vortex pair is increased by the blockage of the rear wheel. This results in the displacement of the wake behind the front wheel to the opposite side. The displaced wake changes the pressure distribution on the other side of the front wheel which leads to early flow separation (as indicated by the wave in figure 4.32) along the complete width of the wheel thread. This type of flow separation generates a turbulent wake but no strong streamwise vortex pair.

The presence of a strong streamwise vortex pair on a single side of the front wheel means that the entrainment of high velocity flow also happens from this side which has a lot of influence on the flow over the downstream part of the landing gear. For the toe up configuration the flow from the bottom of the front wheels gets sucked upward through the gap in between the wheels to the centre of the landing gear where it runs into the wake behind the strut which limits the further upward movement of the flow. The opposite happens for the toe down configuration where the flow gets entrained from the top of the front wheels and moves down and to the centre of the landing gear. However there is nothing to change the flow direction at the bottom of the landing gear so the downward movement continues.

The trajectory of the strong streamwise vortices of the time averaged flow determines where the turbulent structures transported by the flow interact with the solid surface

of the landing gear resulting in pressure fluctuations. The time averaged flow features around the horizontal configuration show that the flow from both the top and bottom of the front wheel gets pushed to the centre of the landing gear. This leads to a high unsteady pressure level on the aft half of the bogie and the rear axles. The results of the toe up simulation show that the flow from the bottom of the front wheels interacts with the top of the rear wheels and axles. The simulation of the toe down configuration shows that the flow from the top of the front wheels moves down and passes below the rear wheels reducing the interaction compared to the other two configurations.

The aerodynamic forces of the three configurations show some interesting results. The total drag coefficient of the three configurations is similar but the drag distribution between the components differs. The drag coefficient of the rear wheels is the highest for the horizontal configuration due to the large area of high pressure on the front of the rear wheel. The rear wheels of the toe up and toe down configurations are more exposed to the freestream but the drag coefficient of the rear wheels is lower. The opposite happens to the drag coefficient of the bogie and rear axles which mean there is almost no change in the total drag of the landing gear.

The symmetry of the three landing gear geometries results in a low mean side force coefficient of the complete landing gear. The main components which generate a side force are the front wheels but their contributions cancel out. The strut is the component which generates the largest unsteady side force. The level of the unsteady side force of the strut of the horizontal and toe up configurations is similar. The unsteady side force of strut of the toe down configuration is significantly lower since a smaller part of the strut in this configuration is exposed to the wake of the forward components.

The lift coefficient of the landing gear is the most affected by the differences in the time averaged flow features of the three configurations. The horizontal configuration is nearly symmetric in the vertical direction and this results in low lift coefficients of the different components. The different flow separation pattern on the front wheels of the toe up and toe down configurations changes the pressure distribution. This results in a downforce for the front wheels of the toe up configuration and lift for the front wheels of the toe down configuration. Although this effect is partially compensated by the contribution of the bogie, the total lift of the complete landing gear is still dominated by the force on the front wheels. The unsteady lift of the three configurations is similar and does not seem to be affected much by the changes in the flow features.

Chapter 5

Acoustics of the simplified main landing gear

This chapter describes the acoustic results of the three simplified landing gear configurations. The first section shows the strength of the dipole source term on the surface of the landing gear which has been calculated from the sampled surface pressure signal. The following two sections describe the far field noise levels which have been generated using Fluents FW-H solver. The far field results are presented in two ways: overhead noise spectra and noise directivity contours. The overhead spectra show the frequency content of the noise generated by the different components of the landing gear while the directivity contours show the overall sound pressure level at different observer locations.

5.1 Magnitude of the dipole source term

The magnitude of the dipole source term in the FW-H equation is proportional to the Root Mean Square of the derivative of the surface pressure with respect to time [70],[73].

$$Dipole\,Source\,Strength \sim \left(\frac{\partial p}{\partial t}\right)_{RMS}. \tag{5.1}$$

The magnitude of the dipole source term on the surface of the landing gear has been calculated from the sampled surface pressure data. The unit of the dipole source strength term in equation 5.1 is pressure per second [Pa/s] which is not very intuitive to work with. The magnitude of the dipole source term has therefore been multiplied with the time step Δt of the CFD simulation ($2.5 \cdot 10^{-5}$ s) and then converted to dB using the reference pressure $2.0 \cdot 10^{-5}$ Pa. The magnitude of the dipole source term on the surface

of the components of the horizontal landing gear configuration has been plotted in 3 dB bands in figures 5.1 to 5.4.

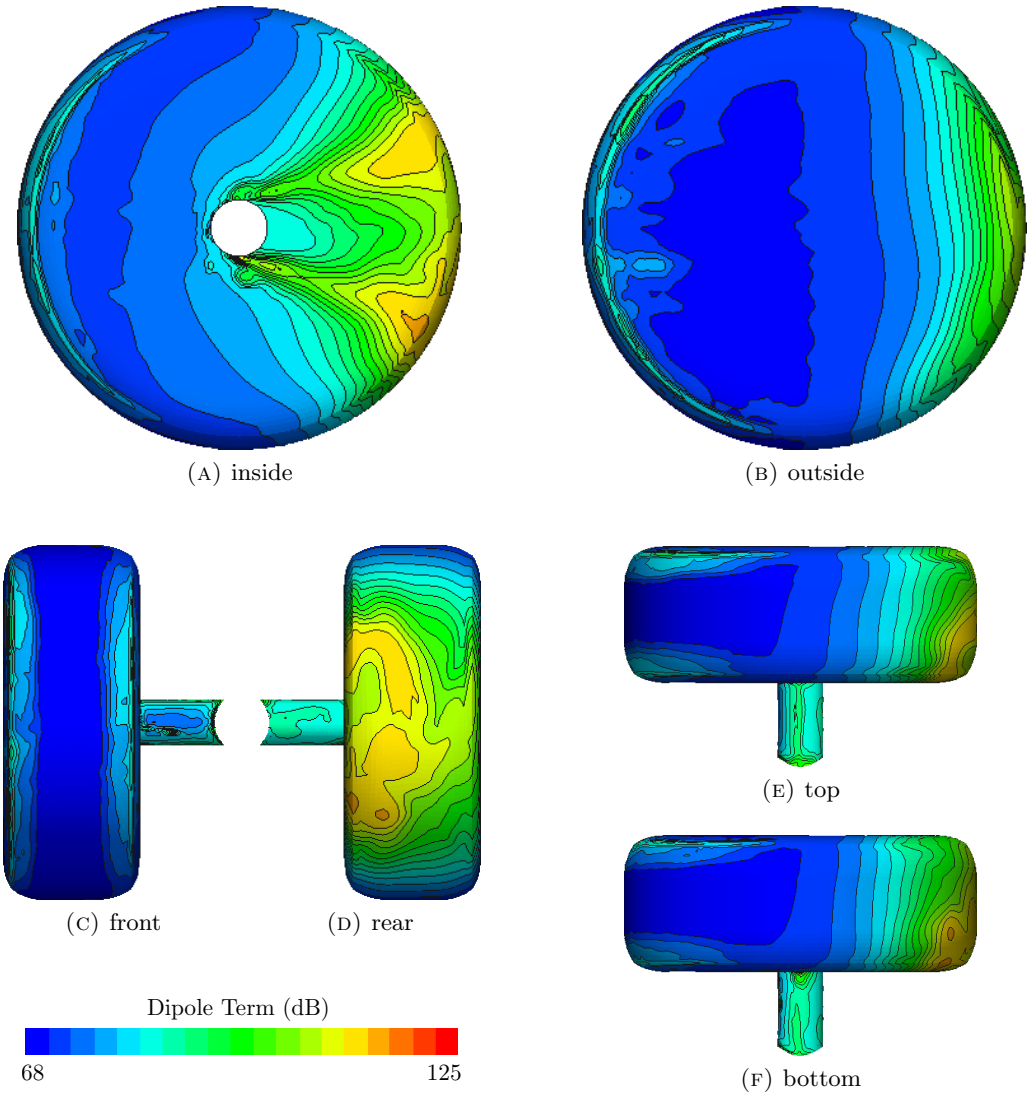

FIGURE 5.1: Magnitude of the dipole source term on the forward wheel and axle of the simplified horizontal configuration.

These dipole source term figures (5.1 to 5.4) show a very strong similarity to the unsteady surface pressure level figures (4.9 to 4.12) in section 4.1.2 of the previous chapter. The levels are different but the distribution of maxima and minima and shape of the contours is very similar. This is no coincidence as the magnitude of the dipole source term is closely related to the unsteady pressure level as will be shown next.

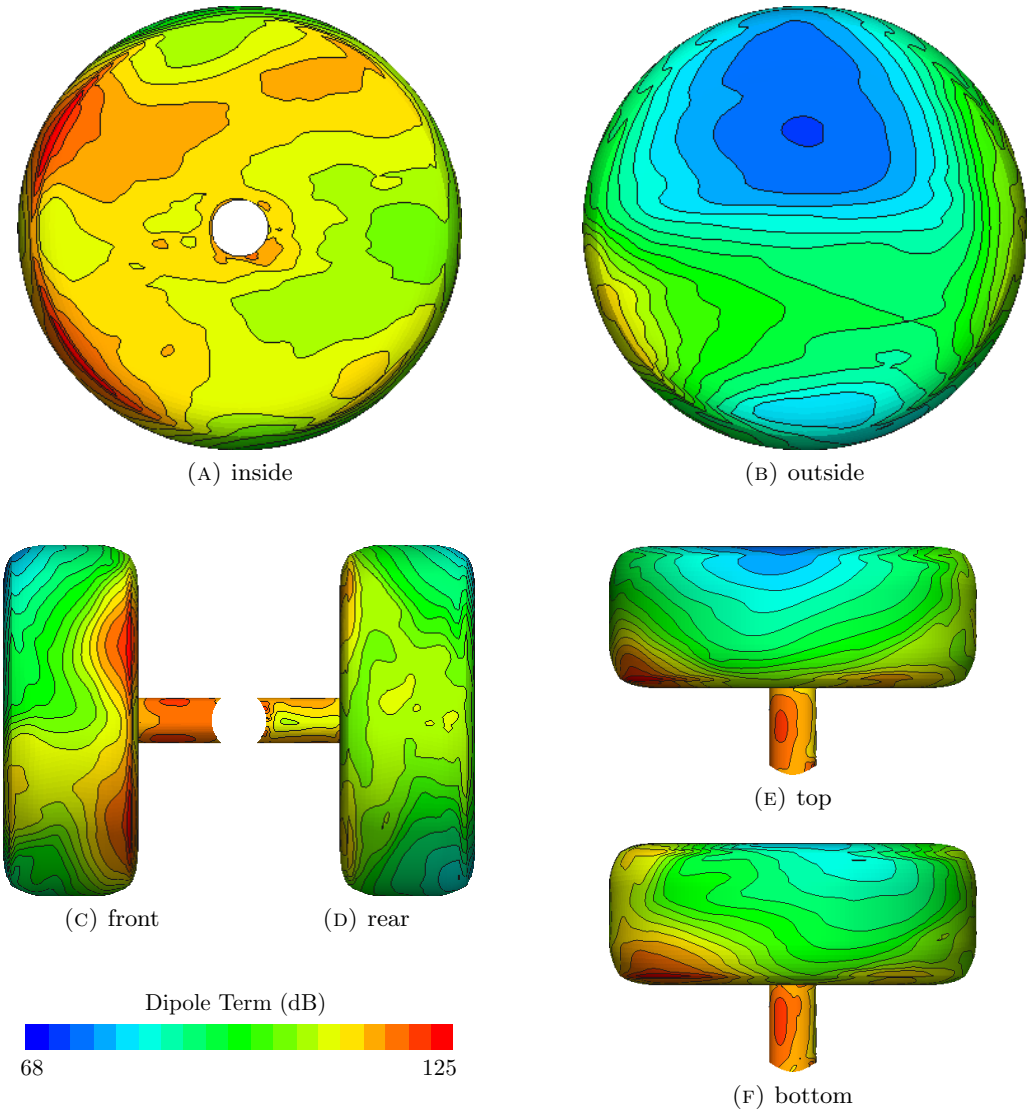

FIGURE 5.2: Magnitude of the dipole source term on the rear wheel and axle of the simplified horizontal configuration.

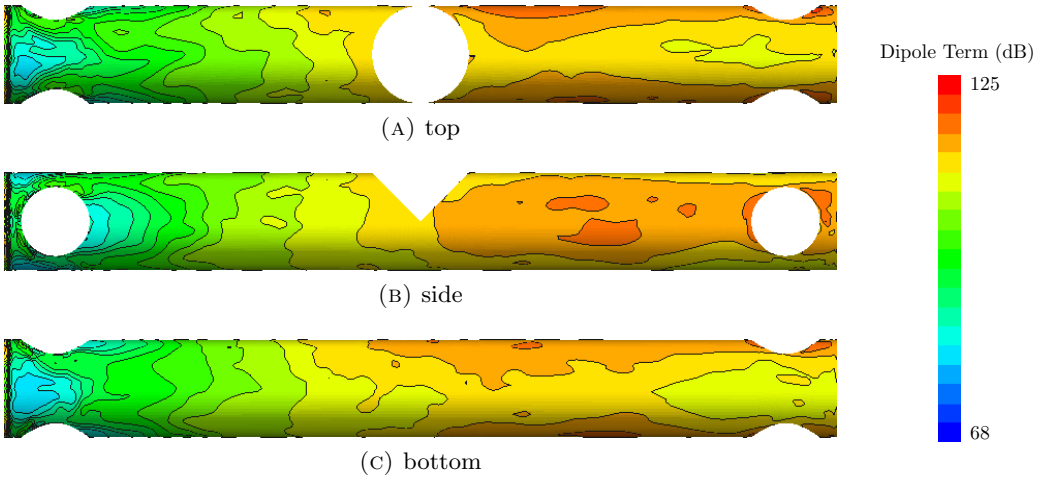

FIGURE 5.3: Magnitude of the dipole source term on the bogie of the simplified horizontal configuration.

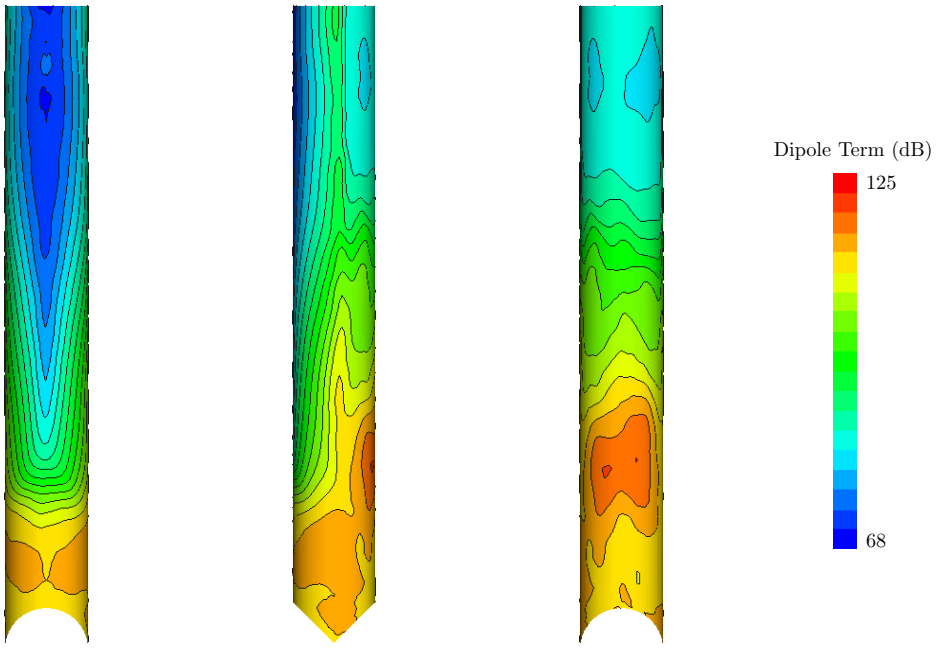

(A) front (B) side (C) rear

FIGURE 5.4: Magnitude of the dipole source term on the lower half of the strut of the simplified horizontal configuration.

The Root Mean Square of the surface pressure can be determined from the sampled time data using equation 3.26 which results in the following equation:

$$p_{RMS} = \sqrt{\frac{1}{n}\sum_{i=1}^{n}(p_i - \bar{p})^2}. \tag{5.2}$$

The pressure (p_i) can be split in an averaged ($\bar{p}$) and a fluctuating (p_i') component following a similar approach as during the derivation of the Reynolds averaged equations in section 3.3:

$$p_i = \bar{p} + p_i'. \tag{5.3}$$

Substituting 5.3 into 5.2 results in equation 5.4 which gives the Root Mean Square of the surface pressure based on the fluctuating component,

$$p_{RMS} = \sqrt{\frac{1}{n}\sum_{i=1}^{n}(p_i')^2}. \tag{5.4}$$

Equation 3.26 can also be used to determine the Root Mean Square of the derivative of the pressure with respect to time:

$$\left(\frac{\partial p}{\partial t}\right)_{RMS} = \sqrt{\frac{1}{n}\sum_{i=1}^{n}\left[\left(\frac{\partial p}{\partial t}\right)_i - \left(\overline{\frac{\partial p}{\partial t}}\right)\right]^2}. \tag{5.5}$$

The average of the derivative of the pressure with respect to time is zero since the data sampling is done while the transient effects have disappeared and the flow is stationary.

$$\left(\overline{\frac{\partial p}{\partial t}}\right) = 0 \tag{5.6}$$

The derivative of the pressure can be approximated numerically by a first order forward differencing as shown in equation 5.7:

$$\left(\frac{\partial p}{\partial t}\right)_i = \frac{p_{i+1} - p_i}{\Delta t} = \frac{p'_{i+1} - p'_i}{\Delta t}, \tag{5.7}$$

which can then be substituted in equation 5.5 resulting in the following equation:

$$\left(\frac{\partial p}{\partial t}\right)_{RMS} = \frac{1}{\Delta t}\sqrt{\frac{1}{m}\sum_{i=1}^{m}\left[(p'_{i+1})^2 + (p'_i)^2 - 2\,p'_{i+1}\,p'_i\right]}, \tag{5.8}$$

where m = n-1 since the calculation of the derivative has reduced the length of the sample by one. The two leading (squared) terms on the right hand side of equation 5.8 clearly show that the magnitude of the dipole source strength is directly related to the unsteady surface pressure level (equation 5.4). The last term on the right hand side in equation 5.8 can be either positive or negative depending on the sign of consecutive pressure fluctuations and its contribution is therefore smaller than that of the leading terms. The fact that the leading terms of the magnitude of the dipole source strength are directly related to the unsteady pressure level makes it superfluous to show all the dipole source strength figures here since they are very similar to the unsteady pressure level figures of the previous chapter. So instead the dipole source strength figures of the components of the toe up and toe down configurations have been added to section B.1 and B.2 of appendix B.

5.2 Overhead spectra

The overhead spectra have been calculated from the far field pressure signal at the ground plane, 100 wheel diameters below the landing gear. The unsteady surface pressure data has been sampled at each time step ($\Delta t = 2.5 \times 10^{-5} s$) of the CFD simulation and this

results in the same time step for the far field noise signal generated by the FW-H solver. Sampling data with that time step would result in a theoretical maximum frequency of the far field noise signal of 20 kHz however the noise signal is not only limited by the time step but also by the spacing of the grid used in the CFD simulation. The incompressible flow assumption has been used in the CFD simulations which means that the pressure fluctuations at the surface of the landing gear are purely generated by the unsteady flow structures that pass along the surface. The average cell size on the surface of the landing gear is between 4 and 5 mm and combined with the free stream velocity of 40 m/s this results in a time of approximately $1.1 \times 10^{-4} s$ for the flow to pass the length of a single cell. Figure 5.5 shows a surface LIC plot of the instantaneous velocity field near the surface of the bogie with the grid overlayed and the two visible eddies are approximately 4 cells long. So it takes an eddy approximately $4.4 \times 10^{-4} s$ to pass a point on the surface of landing gear which results in a frequency of 2.2 kHz. The frequency range of the following overhead third octave band noise spectra figures have therefore been limited to 2 kHz.

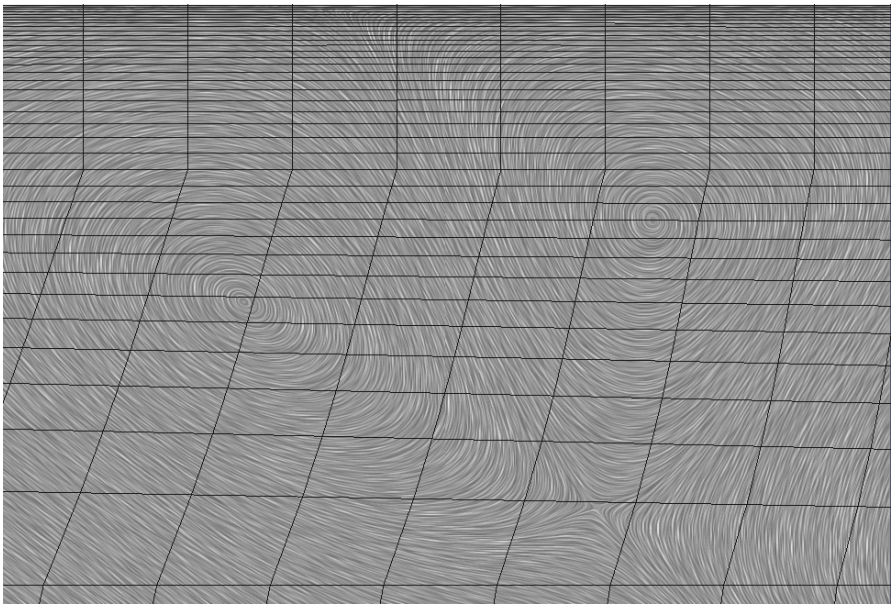

FIGURE 5.5: Overlay of the grid and surface LIC plot of instantaneous velocity field highlighting the relative size of the resolved flow structures near the bogie surface.

The overhead spectrum of the simplified horizontal landing gear configuration is shown in Figure 5.6 and it is clear that the bogie and rear axles are the major contributors to the overhead noise. Both the bogie and rear axles are in the turbulent wake of the upstream components resulting in high levels of unsteady surface pressure as shown in section 4.1.2 of the previous chapter. The FW-H solver calculates the noise radiation to the far field using the surface pressure signal but the direction of the surface normal is just as important as the unsteady surface pressure level. The noise radiated by the pressure fluctuations on a surface reaches a maximum when the observer is positioned in

the same direction as the surface normal. The far field noise level reduces with increasing angle between the direction of the observer and the surface normal vector. The phase of the pressure signal is also important since signals from different parts of the landing gear with the same phase will amplify while signals with opposite phase will cancel each other out. However turbulence is a 'random' process and this will in general average out the effect of the phase of the different signals. The aft half of the bogie shows a high level of unsteady surface pressure which combined with a relatively large surface area facing the ground causes it to be the major overhead noise source. The unsteady pressure level on the surface of the rear axles is even higher than that of the bogie but they only have a small surface area resulting in the second largest contribution to the overhead noise level.

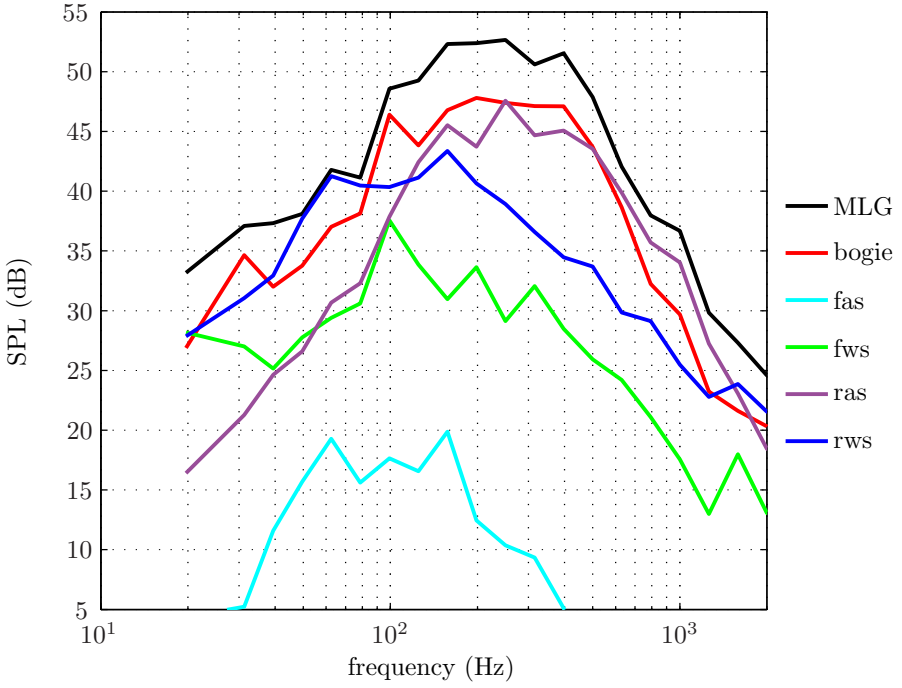

FIGURE 5.6: Overhead third octave band spectrum of the simplified horizontal configuration.

The rear wheels have a large surface area facing the ground but the lower unsteady surface pressure level at the bottom of the wheels makes them the next largest contributor to the overhead noise level. The front wheels and front axles generate low levels of far field noise since they are in the undisturbed inflow resulting in a low level of pressure fluctuations at the surface. The front wheels do have peaks in the unsteady surface pressure level on the inside and outside surface due to the wake of the front axles and flow separation. The surface normal on the sides of the wheels is parallel to the ground and these areas do not contribute much to the overhead noise level. The small surface area of the front axles combined with the low level of pressure fluctuations results in the lowest far field noise level off all the components. The aerodynamic results in the

previous chapter show a high level of unsteady surface pressure on the lower half of the strut. However the surface normal vector of the strut is perpendicular to the direction of the overhead observer which results in a noise level that is too low to show up in the spectrum in Figure 5.6.

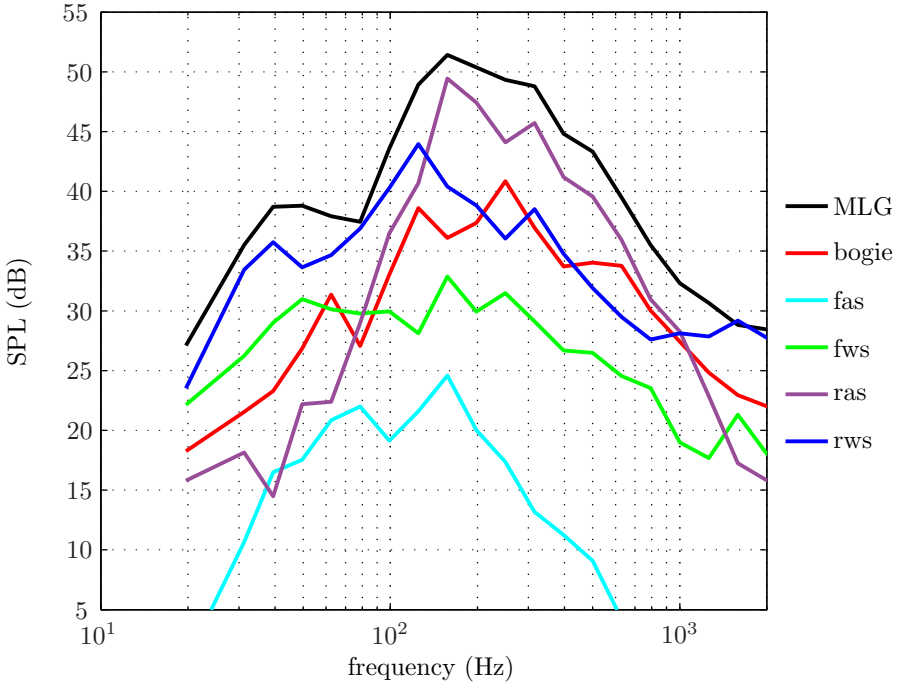

FIGURE 5.7: Overhead third octave band spectrum of the simplified toe up configuration.

The overhead noise spectrum generated by the flow around the simplified landing gear in toe up configuration in Figure 5.7 shows a lower noise level than the overhead spectrum of the horizontal configuration in Figure 5.6. A comparison of the two spectra clearly shows that the change in the noise level generated by the bogie is responsible for this difference. The noise level generated by the bogie, which is the major noise source for the horizontal configuration, has dropped below the level of the rear axles and rear wheels for the toe up configuration. The aerodynamic results of the toe up configuration in section 4.2 show that the flow is attached on the bottom surface of the bogie which results in a low unsteady surface pressure level and thus a low overhead noise level.

The turbulent flow results in a high level of unsteady pressure on the surface of the rear axles which makes them the major overhead noise source for the toe up configuration. Most of the turbulent flow passes over the top of the rear wheels such that the far field noise level of the rear wheels in the toe up configuration does not differ much from the horizontal configuration. The front wheels and front axles are again the quietest components due to the undisturbed inflow. The noise from the front wheels has reduced while the noise from the front axles has increased compared to the levels of the horizontal configuration.

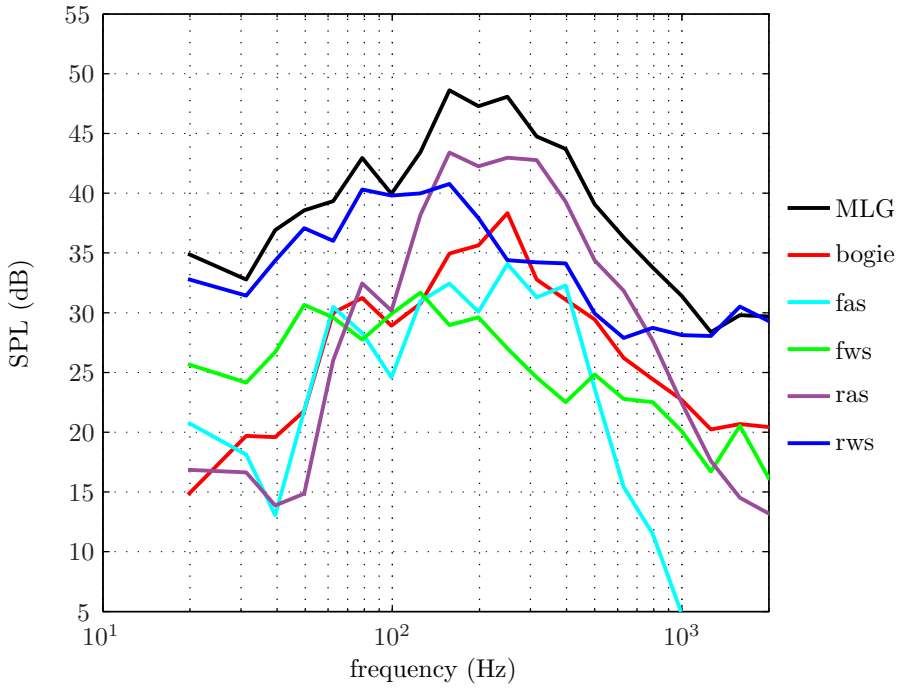

FIGURE 5.8: Overhead third octave band spectrum of the simplified toe down configuration.

The overhead spectrum of the main landing gear in toe down configuration in Figure 5.8 shows the lowest overhead noise level of the three simplified landing gear configurations. The rear axles and rear wheels are still the two main contributors to the overhead noise but their noise level has reduced compared to the other two configurations. The previous chapter describes how the turbulent flow passes at a greater distance from the rear axles and rear wheels for this configuration and this reduces the level of the surface pressure fluctuations and thus the far field noise level.

The bogie is the third contributor to the overhead noise level just as for the toe up configuration but its noise level is significantly lower than in the other two configurations. The flow separates at the sharp front edge of the bogie which creates a flow circulation zone at the bottom of the bogie. The low velocity of the flow in the circulation zone results in a low level of the pressure fluctuations and thus a reduced overhead noise level.

The overhead noise level generated by the front axles has gone up by a significant amount compared to the other two configurations and contributes more to the overhead noise level than the front wheels. The aerodynamic results show a peak in the unsteady pressure distribution close to the axle to bogie junction and this peak is not present in the results of the other two configurations. The increased local flow velocity at the axle to bogie junction enhances the strength of the turbulent fluctuations in the separated flow coming from the sharp bogie edge.

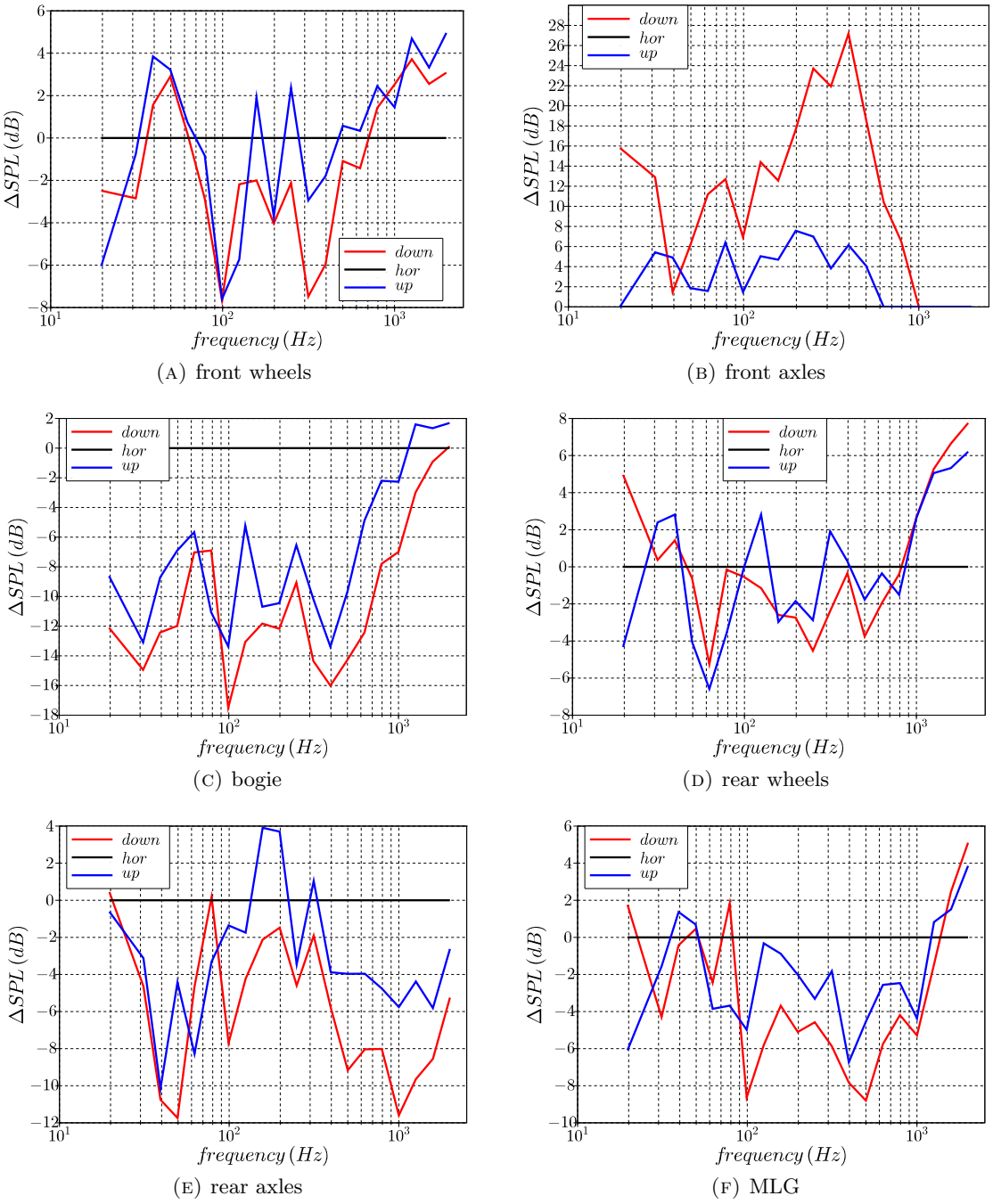

(A) front wheels

(B) front axles

(C) bogie

(D) rear wheels

(E) rear axles

(F) MLG

FIGURE 5.9: Relative overhead third octave band noise level of the different components of the simplified landing gear compared to that of the horizontal configuration.

Figure 5.9 shows the relative overhead noise levels of the components of the three configurations which have been calculated by subtracting the overhead noise level of the horizontal configuration. The relative contribution of the horizontal configuration compared to itself is always zero but has been included in the figures to highlight the reference level. The trend of the relative noise level of the toe up and toe down configuration for each component is quite similar but the level of the toe down configuration is in general lower than the toe up configuration. The front axles (Figure 5.9b) are the only exception with a much larger relative noise level of the toe down configuration than that of the toe up configuration. The bogie of both the toe up and toe down configuration in figure 5.9c have a very low relative noise level which emphasises again how noisy the bogie of the horizontal configuration is.

5.3 Noise directivity

The overall sound pressure level is calculated on a plane 100 wheel diameters below the centre of the landing gear and the results are presented in the form of noise directivity contours. The distance from the centre of the main landing gear to the observers on the plane differs and this has been compensated for in the calculated overall sound pressure levels as described in the post-processing section (3.11) of the research methodology chapter (3). The noise directivity depends both on the shape of the component emitting the noise and the unsteady pressure levels at the surface. This section will compare the noise directivity contours generated by the simplified landing gear components in the three different configurations.

5.3.1 Front wheels

The noise directivity contours of the front wheels in Figure 5.10 show a similar shape but the far field noise level of the front wheels in the horizontal configuration is approximately 2 dB louder than the other two configurations. The far field noise level generated by the front wheels is the lowest directly below the landing gear and increases in all other directions. The noise level increases faster to the sides than in the upstream and downstream direction as can be seen by the difference in the spacing between the contours.

The unsteady pressure distribution figures in the previous chapter show peaks in the unsteady pressure level on the inside of the front wheels where the wake from the front axle moves along the surface of the wheel. The surface normal vector on the inside of the front wheel points to the side which explains why the noise level increases more to

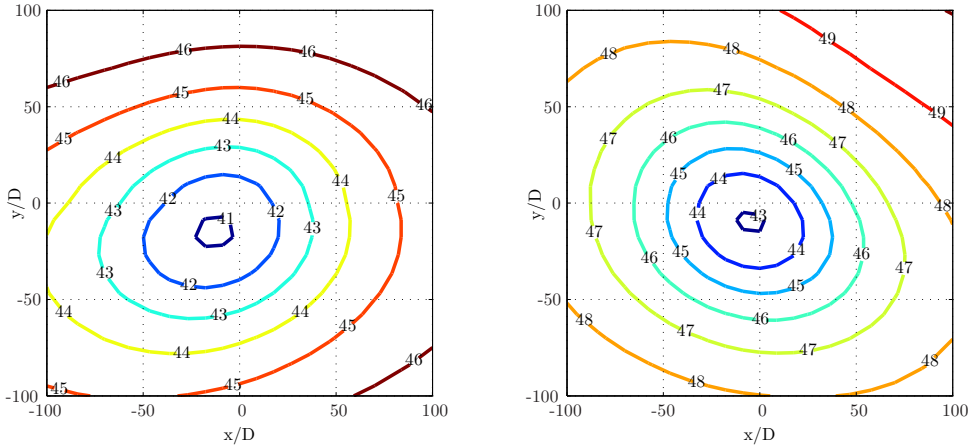

(A) toe up

(B) horizontal

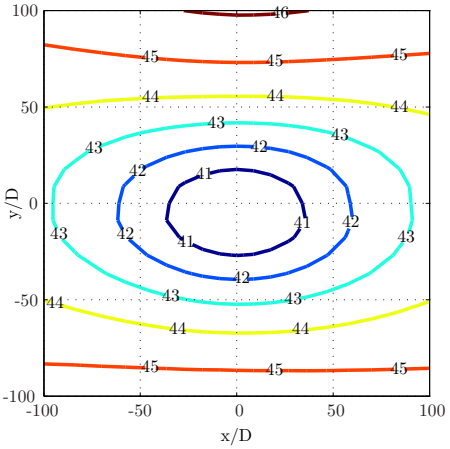

(C) toe down

FIGURE 5.10: Noise directivity contours of the front wheels of the simplified landing gear configurations. (OASPL in dB)

the sides than it does in the upstream and downstream direction. The noise directivity contours of the front wheels of the three configurations are not completely symmetric in the transverse direction. The previous chapter has shown that the aerodynamic force coefficients of the components on the right and left hand side of the landing gear are not equal either. Running the CFD simulations for longer would increase the sample size and should lead to more symmetric results but is not feasible with the available resources for this study.

The noise directivity contours of the Overall Sound Pressure Level (OASPL) in Figure 5.10 show the sound pressure level of the complete noise signal which does not distinguish between the noise at different frequencies. The noise directivity plots could be repeated for the individual third octave bands but this would lead to a large number of figures. Instead a low (49.6 Hz), mid (250 Hz) and high frequency (1000 Hz) third octave band have been chosen to show the frequency content of the far field noise. The noise levels

at these frequencies have been plotted on the longitudinal and transverse centreline of the observer plane such that all three landing gear configurations can be shown in two figures. The observer plane extends 200 wheel diameters in the longitudinal and transverse directions which is equivalent to angles of + and - 45 degrees. A correction, as described in the post processing section (3.11), has been applied to the noise signal to adjust for the difference in distance between the centre of the landing gear and the observer.

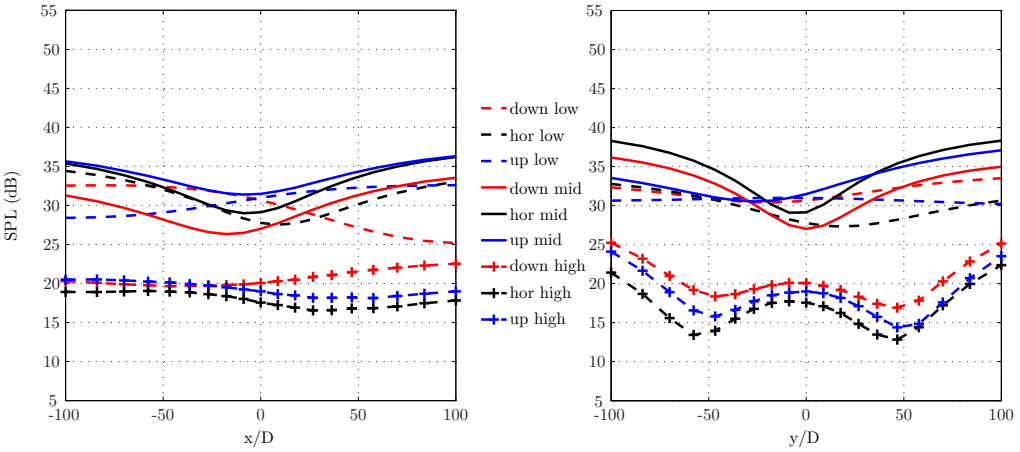

(A) longitudinal (B) transverse

FIGURE 5.11: Low, mid and high frequency noise levels generated by the front wheels of the simplified landing gear on the longitudinal and transverse centreline of the observer plane. (low = 49.6 Hz, mid = 250 Hz and high = 1000 Hz third octave band)

The mid and low frequency noise level of the front wheels is much higher than the high frequency noise level as shown in Figure 5.11. The front wheels of the simplified landing gear are relatively large and smooth and located in the clean undisturbed flow which explains the low level of the high frequency noise. The longitudinal centreline plot in Figure 5.11a shows an interesting behaviour for the front wheel of the toe down configuration which does not follow the same trend as the other two configurations. The front wheels of the toe up and horizontal configuration show that the mid frequency noise level is higher than the low frequency noise level along the whole longitudinal centreline. However the front wheels of the toe down configuration show that the low frequency noise is dominant in the upstream direction and the mid frequency noise in the downstream direction. The front wheels of the toe down configuration also show an increase in the high frequency noise in the downstream direction while the other two configurations show a decrease of the high frequency noise. The flow features around the front wheels of the horizontal and toe up configurations both show strong streamwise vortices at bottom of the wheel (Figures 4.4f and 4.13f) but the flow features of the toe down configuration (Figure 4.22f) shows a large area of flow separation. This large area of flow separation at the bottom of the front wheel in the toe down configuration

is assumed to be responsible for the increase in the high frequency noise level in the downstream direction.

The noise levels of the front wheels on the transverse centreline in Figure 5.11b are not symmetric which has already been shown by the OASPL contours in Figure 5.10. The mid frequency noise shows a single dip in the noise level directly below the landing gear while the high frequency noise shows two separate dips. This does not show up in the OASPL contour Figures since the high frequency noise level is much lower than the noise level of the mid and low frequencies.

5.3.2 Front axles

Figure 5.12 shows that there are large differences in the far field noise levels generated by the front axles. The front axles of the toe down configuration are the loudest at 41 dB followed by the toe up configuration at 30.5 dB and the horizontal configuration at 26.5 dB. Each axle consists of a cylinder with its axis perpendicular to the mean flow direction, a configuration which normally generates a dipole type noise source. The orientation of the axle to the flow results in one of the lobes of the dipole pointing towards the ground. This is confirmed by the directivity contours which all show a peak in the noise level below the landing gear.

The peak in the far field noise level is directly below the landing gear for the horizontal configuration but has moved a little upstream for the toe up configuration and a little downstream for the toe down configuration. An investigation of the flow field around the front axle shows that the local flow direction around the axles is not always parallel to the freestream. The flow near the front axles in the horizontal configuration is almost horizontal which results in a peak in the noise level directly below the landing gear. The toe up configuration of the main landing gear leads to a slightly downward local flow direction at the front axles which results in a rotation of the dipole such that the noise peak moves upstream. The opposite happens for the toe down configuration: the mean local flow direction around the front axles is slightly upward resulting in a downstream displacement of the far field noise peak.

The noise directivity contours generated by the front axles of the toe down configuration are nearly circular but the shape of the contours of the other two configurations differ near the longitudinal centreline. This difference becomes more pronounced with a lower far field noise level indicating that it is caused by a relatively weak flow feature. The front axle is a low aspect ratio cylinder connected to the bogie and wheel which means that the flow near the ends of the axle is disturbed. These flow disturbances at both

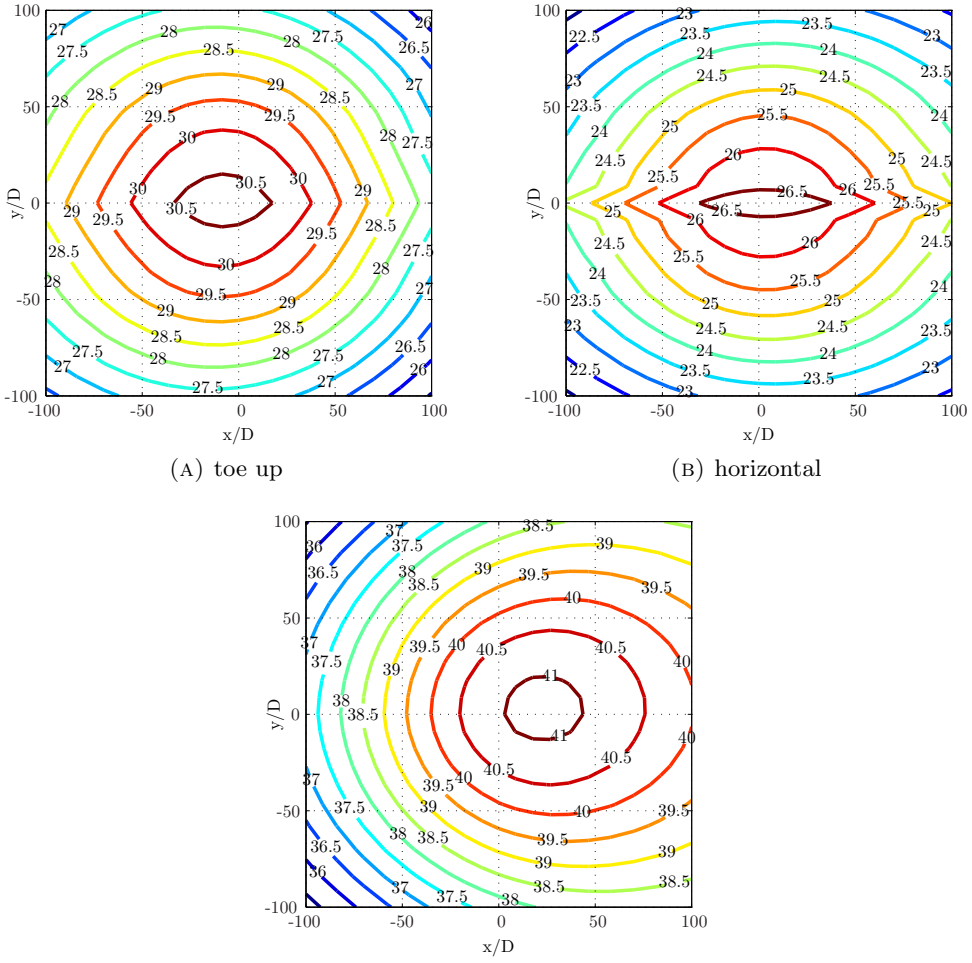

(A) toe up

(B) horizontal

(C) toe down

FIGURE 5.12: Noise directivity contours of the front axles of the simplified landing gear configurations. (OASPL in dB)

ends of the front axle are expected to be responsible for the non circular noise contour near the longitudinal centreline.

The longitudinal and transverse centreline plots in Figure 5.13 show that there is almost no high frequency noise generated by the front axles which agrees with the overhead spectra in section 5.2. The noise levels of the front axles show large differences between the three configurations. The order is the same for the low and mid frequencies with the front axles of the toe down configuration being the noisiest, followed by toe up and the front axles of the horizontal configuration are the quietest. The contribution of the different frequencies per configuration does differ however: the toe down is dominated by the mid frequency noise while the low frequency noise is dominant for the horizontal configuration. The contribution of low and mid frequencies is similar for the front axles of the toe up configuration. The axles of the toe down configuration are the only ones which show high frequency noise on the longitudinal centreline in Figure 5.13a. The

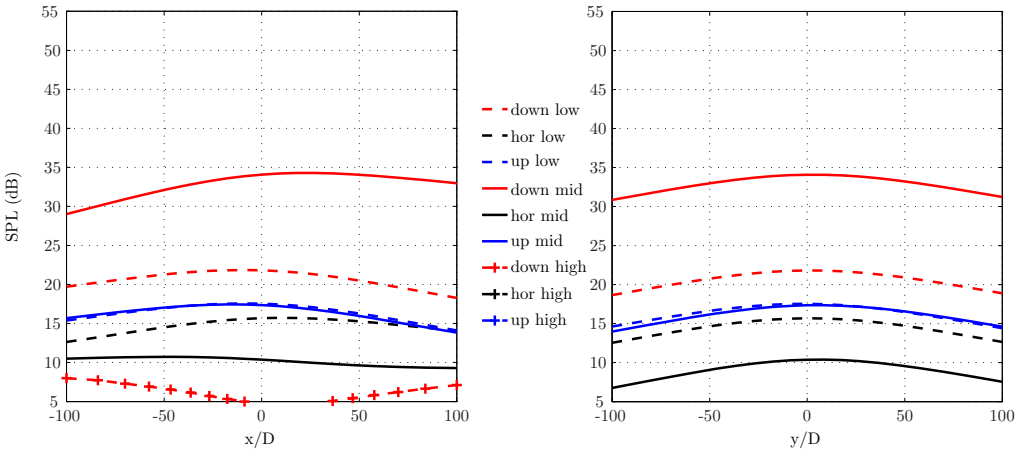

(A) longitudinal (B) transverse

FIGURE 5.13: Low, mid and high frequency noise levels generated by the front axles of the simplified landing gear on the longitudinal and transverse centreline of the observer plane.(low = 49.6 Hz, mid = 250 Hz and high = 1000 Hz third octave band)

high frequency noise does not follow the same behaviour as the other frequencies and shows a dip below the landing gear while the low and mid frequencies show a small increase. This high frequency noise only shows up in the longitudinal centreline and not the transverse centreline in Figure 5.13b. It is expected that the flow disturbances at ends of the front axle are responsible for this high frequency noise along the longitudinal centreline.

5.3.3 Bogie

The noise directivity contours generated by the bogie in Figure 5.14 show the largest difference in the far field noise level between the three configurations: 11.5 dB. Not only the noise levels but the shape of the contours are different as well. The bogie consists of a cylinder that is aligned with the freestream flow direction for the horizontal configuration which results in a large surface area facing the ground. The surface normal vectors of the bogie in the horizontal configuration point down and to the sides such that the highest far field noise levels are suspected in these directions. The noise directivity contours of the bogie in the horizontal configuration are shaped as an elongated ellipsoid with the major axis in the transverse direction. The distribution of the contours is not symmetric with the peak located below the landing gear and to the left hand side looking upstream. This is consistent with the asymmetric unsteady pressure distribution on the surface of the bogie as shown in Figure 4.11. The unsteady surface pressure reaches a peak on both sides of the bogie but the noise directivity contour shows only a single peak below the landing gear. This effect is caused by the curved surface of the bogie which means that the acoustic signal of both sides of the bogie can reach the area below the landing

gear enhancing the noise level. The rest of the observer plane can only be reached by the acoustic signal from a single side of the bogie which results in a lower far field noise level.

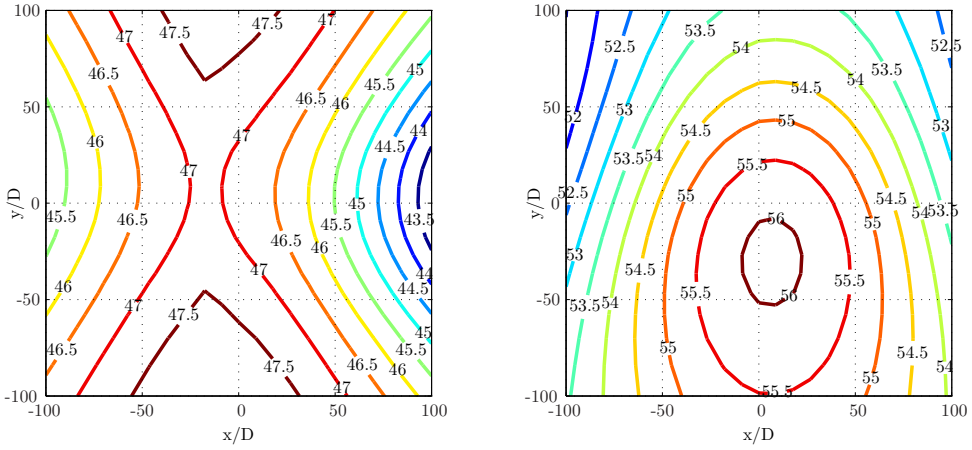

(A) toe up (B) horizontal

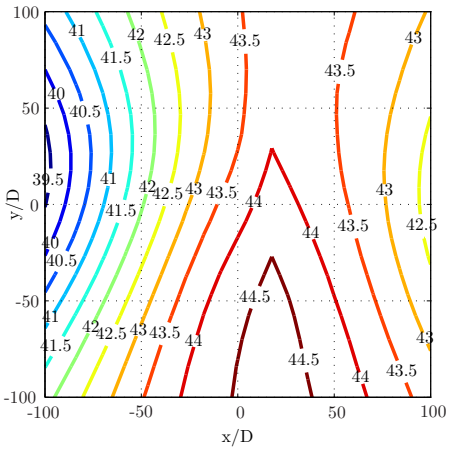

(C) toe down

FIGURE 5.14: Noise directivity contours of the bogie of the simplified landing gear configurations. (OASPL in dB)

The toe up configuration of the bogie changes the direction of the surface normal vectors and this leads to an upstream shift of the far field noise peaks as shown in Figure 5.14a. The unsteady surface pressure level on the surface of the bogie in the toe up configuration is low on bottom but has peaks on the top forward half of the bogie as shown in Figure 4.20. These unsteady pressure peaks radiate noise to the sides but because they are on the top half of the bogie there is no area on the observer plane where the noise level gets enhanced as is the case for the horizontal configuration. This results in noise peaks in the transverse direction and a slightly lower far field noise level directly below the landing gear.

Figure 5.14c shows that the peak in the far field noise level has shifted downstream for the bogie of the toe down configuration due to the change in direction of the surface normal vectors. The unsteady surface pressure distribution in Figure 4.29 shows two peaks at the lower forward half of the bogie just behind the front axles. The level of these unsteady surface pressure peaks is a lot lower than for the other two configurations. The asymmetric unsteady pressure distribution on the surface of the bogie results in a corresponding asymmetric far field noise contour with a peak in the noise level on the left hand side looking upstream.

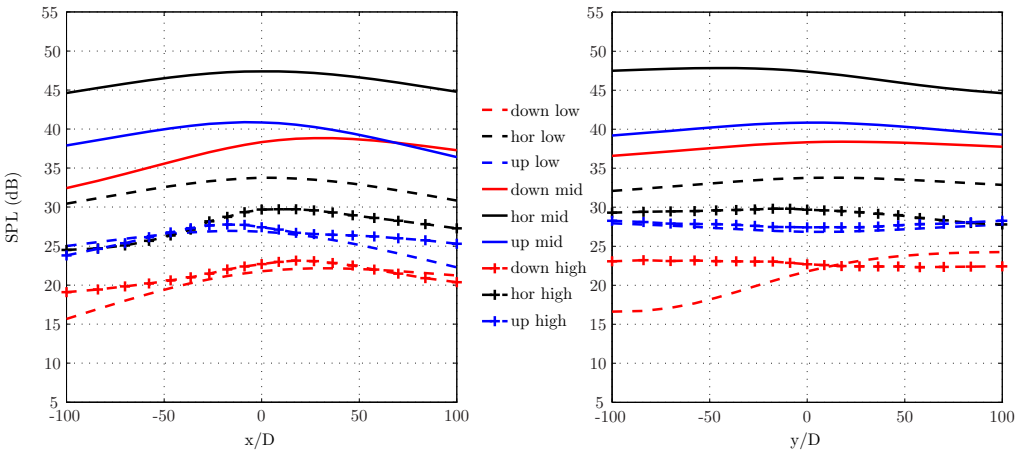

(A) longitudinal (B) transverse

FIGURE 5.15: Low, mid and high frequency noise levels generated by the bogie of the simplified landing gear on the longitudinal and transverse centreline of the observer plane.(low = 49.6 Hz, mid = 250 Hz and high = 1000 Hz third octave band)

The noise levels generated by the bogie in longitudinal and transverse direction in Figure 5.15 show that the contribution of the mid frequency is significantly higher than the low and high frequencies. The bogie of the toe up and down configurations show an approximately equal level for the low and high frequency noise. This is not the case for the horizontal bogie which shows a larger contribution from the low frequency noise than the high frequency noise. The peak in the noise levels on the longitudinal centreline in Figure 5.15a shifts with the bogie inclination angle: it is below the landing gear for the horizontal bogie, moves upstream for the toe up configuration and downstream for the toe down configuration. The noise levels in the transverse direction in Figure 5.15b are reasonable flat. The order of the different configurations is the same for each frequency: the horizontal bogie is the noisiest followed by the bogie of the toe up configuration while the bogie of the toe down configuration is the quietest.

5.3.4 Rear wheels

The rear wheels in the horizontal configuration show a high level of unsteady pressure on the forward inside edge of the wheel (Figure 4.10) where the turbulent flow passes the surface at high velocity. This results in a noise directivity contour (Figure 5.16b) which shows the peaks in far field noise level to the sides, upstream of the landing gear and the lowest noise level downstream and below the landing gear.

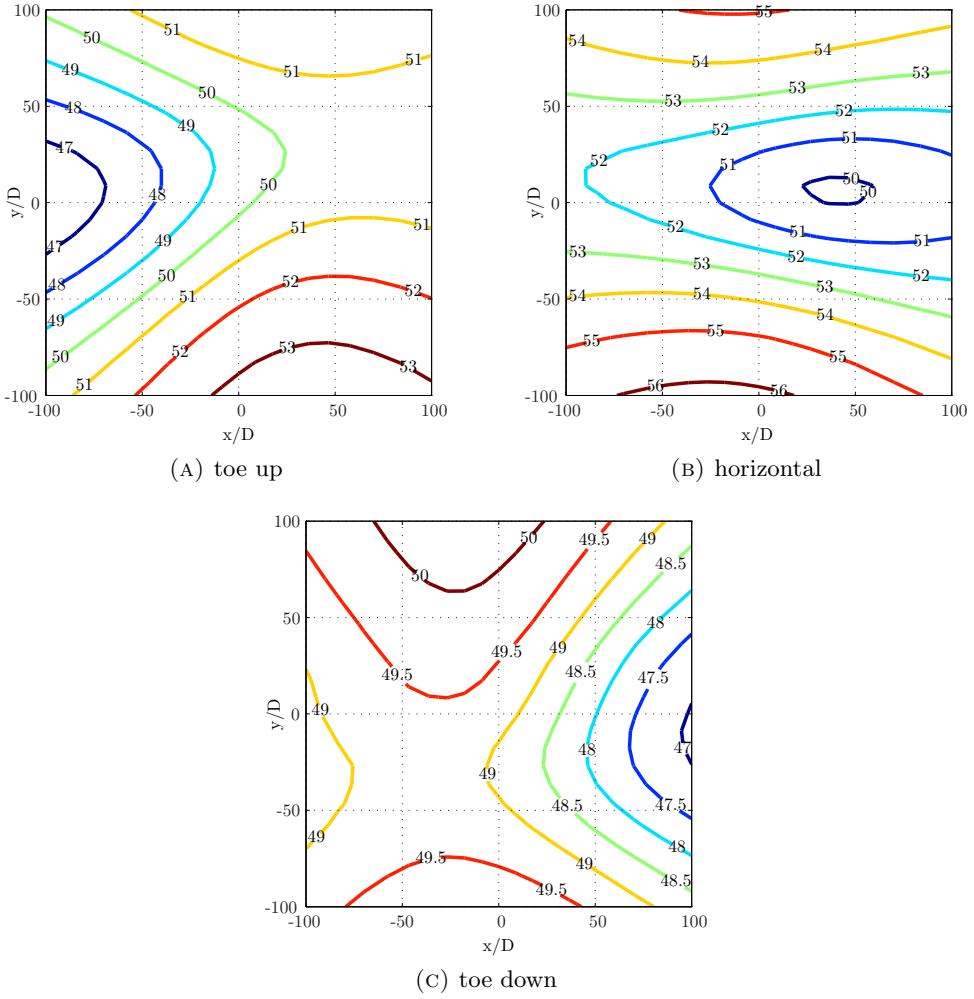

(A) toe up

(B) horizontal

(C) toe down

FIGURE 5.16: Noise directivity contours of the rear wheels of the simplified landing gear configurations. (OASPL in dB)

Most of the turbulent flow passes over the top of the rear wheels in the toe up configuration which results in a relative low level of unsteady pressure on the bottom half of the rear wheels. There are peaks in the unsteady surface pressure level on the inside surface of the rear wheel at the location of the wake of the rear axle as can be seen in Figure 4.19. The direction of the surface normal at these peaks means that the rear wheels radiate noise to the sides which is confirmed by the noise directivity contour in Figure

5.16a. The increased unsteady pressure level at the aft face of the rear wheel generated by the flow separation results in a downstream shift of the far field noise peaks.

The turbulent flow passes below the rear wheels of the toe down configuration which leads to a higher level of unsteady pressure on the forward bottom half of the rear wheels compared to the other configurations (Figure 4.28). The unsteady pressure level on the inside surface of the rear wheel is lower than the other two configurations which results in a directivity contour with noise peaks to the sides and upstream as can be seen in Figure 5.16a. The difference between the peak and minimum far field noise level of the rear wheels of the toe down configuration is only 3 dB while this is 6 dB for the other two configurations.

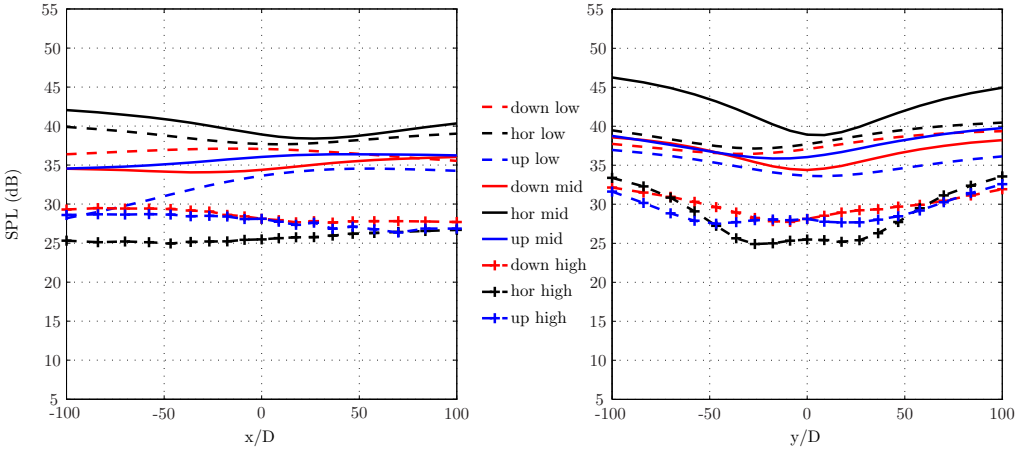

(A) longitudinal (B) transverse

FIGURE 5.17: Low, mid and high frequency noise levels generated by the rear wheels of the simplified landing gear on the longitudinal and transverse centreline of the observer plane.(low = 49.6 Hz, mid = 250 Hz and high = 1000 Hz third octave band)

Figure 5.17 shows the noise levels of the rear wheels on the longitudinal and transverse centreline of the observer plane. The noise levels have gone up compared to the front wheels in Figure 5.11 since the rear wheels are in the wake of the forward components. Most noise is generated by the mid and low frequencies while the contribution of the high frequency noise is less just as for the front wheels. The rear wheels of the toe down configuration stand out since their low frequency noise level is higher than the mid frequency noise while the mid frequency noise is dominant for the other two configurations. The mid and low frequency noise of the rear wheels on the transverse centreline in Figure 5.17b show a drop in the levels below the landing gear just as what happens for the front wheels in Figure 5.11b. The high frequency noise of the front wheels shows two drops in the noise level on the transverse centreline but this is not the case for high frequency noise of the rear wheels where the two separate drops in the noise level seem to have merged and form a single much wider area of low noise below the landing gear.

5.3.5 Rear axles

The noise contours generated by the rear axles of all three simplified configurations in Figure 5.18 show a circular shaped directivity pattern with the noise peak below the landing gear. The far field noise level drops off at other angles which is consistent with the dipole type noise source of a cylinder. The rear axles of the toe up configuration (Figure 5.18a) generate the highest far field noise level with the peak just downstream of the landing gear. The toe up rotation moves the rear axle away from the wake of the forward components but into the higher velocity flow. The unsteady pressure distribution on the bottom of the rear axle in Figure 4.18f shows a peak at the flow separation point just aft of the thickest part of the rear axle. This causes the downstream shift of the far field noise peak and a higher noise level in the downstream direction as can be seen by the increased distance between the contours.

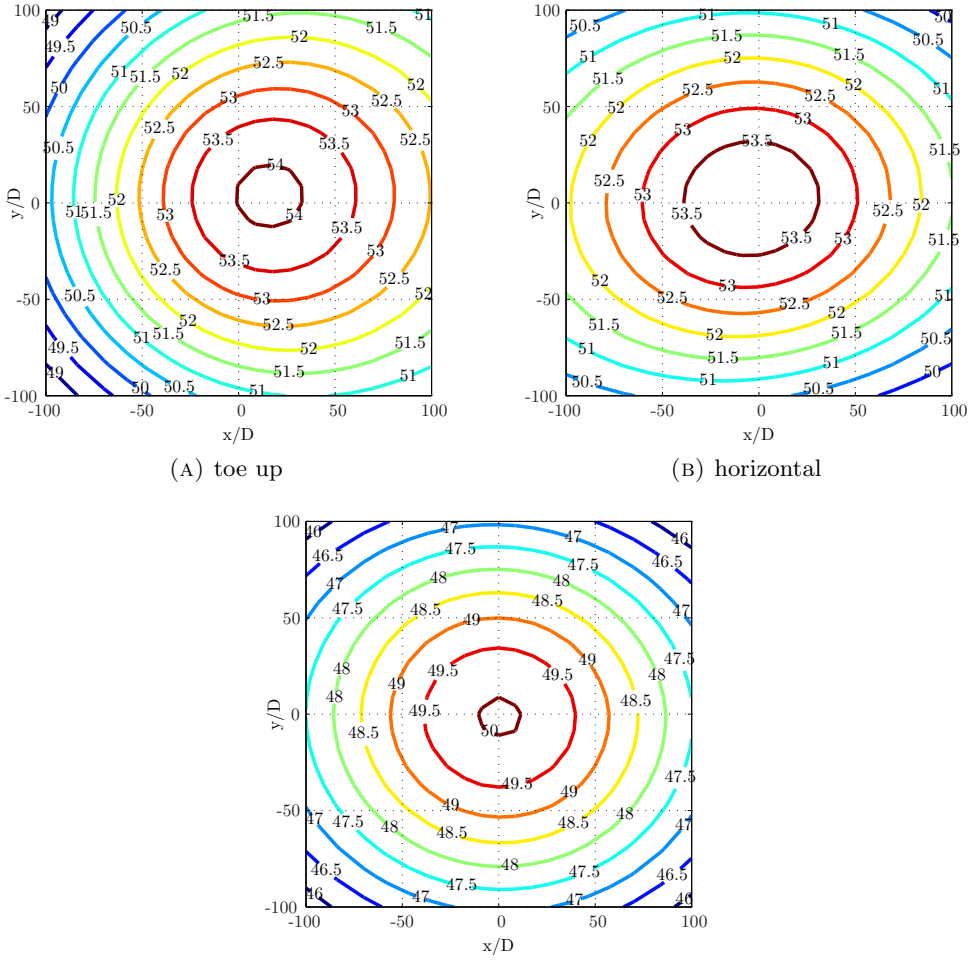

(A) toe up

(B) horizontal

(C) toe down

FIGURE 5.18: Noise directivity contours of the rear axles of the simplified landing gear configurations. (OASPL in dB)

The rear axles of the horizontal configuration (Figure 5.18b) generate a far field noise level similar to that of the toe up configuration but the location of the peak has shifted upstream of the landing gear. The aerodynamic features of the simplified horizontal configuration in section 4.1.1 show that the turbulent wake of the forward components is trapped between the rear wheels. This results in a high level of unsteady pressure on the surface of the rear axles. The peak in the unsteady surface pressure is towards the front of the rear axle (Figure 4.9f) which results in an increase of the far field noise level in the upstream direction and therefore an upstream shift of the far field noise peak.

The noise directivity figure of the rear axles in the toe down configuration (Figure 5.18c) shows a pattern of concentric circles with the peak noise level directly below the landing gear. The noise level on the whole observer plane is almost 4 dB lower than the far field noise level of the other two configurations. The rear axles are in the wake which has a reduced flow velocity and at a significant distance of the strong turbulent flow that passes below the rear wheels. This results in a lower unsteady surface pressure level (Figure 4.27f) and thus a lower far field noise level than the other two configurations.

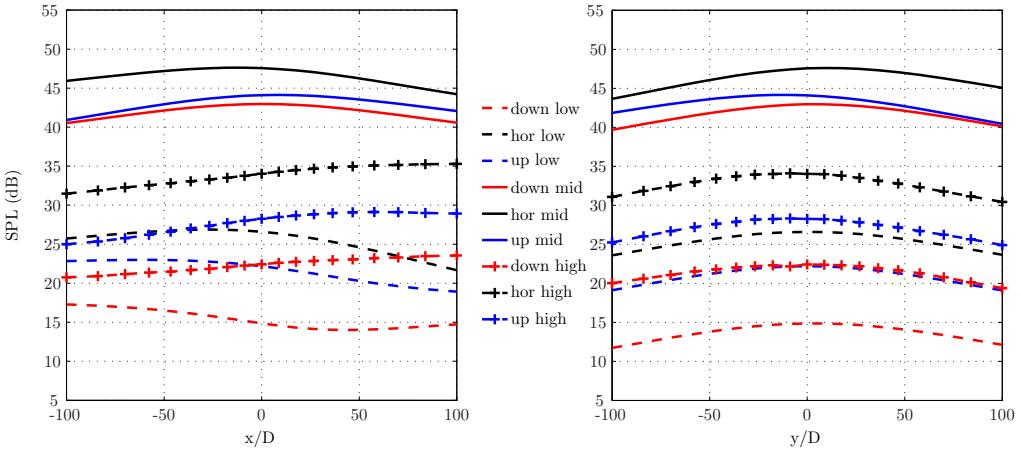

(A) longitudinal (B) transverse

FIGURE 5.19: Low, mid and high frequency noise levels generated by the rear axles of the simplified landing gear on the longitudinal and transverse centreline of the observer plane.(low = 49.6 Hz, mid = 250 Hz and high = 1000 Hz third octave band)

The longitudinal and transverse centreline plots in Figure 5.19 show that the mid frequency noise is dominant for all rear axle configurations. The rear axles are in the wake of the forward components so the noise level of all the frequencies has increased compared to the front axles in Figure 5.13. The axles are relatively small components of the landing gear and thus do not create much low frequency noise. The dominant mid frequency noise on the longitudinal centreline in Figure 5.19a shows a peak below the landing gear as expected from the OASPL contour figures. The high frequency noise of the rear axles shows a different behaviour with an increasing noise level in the downstream direction. The low frequency noise of the rear axles does not follow a clear trend

and is different for each configuration. The transverse centreline plot in Figure 5.19b shows that all frequencies follow the same trend and generate a noise peak below the landing gear and that the noise level drops off towards the sides.

5.3.6 Strut

The flow field around the strut of the simplified main landing gear can be divided into two parts: a clean inflow at the upper part of the strut and the turbulent inflow at the lower part of the strut. The upper part of the strut generates noise due to flow separation and vortex shedding while the lower part of the strut generates noise due to the turbulence of the forward components moving past the solid surface. Both of these flows result in high pressure fluctuations near the widest part of the strut which creates a dipole type noise source. This dipole type source radiates most of the noise in the transverse direction as shown in the noise directivity contours of all three configurations in Figure 5.20. The spectra in the previous section have shown that the overhead noise level generated by the strut approaches zero due to the orientation of the surface normal vector.

The far field noise level generated by the strut is directly related to the extend of the strut that is exposed to a turbulent inflow. The toe up configuration of the bogie moves the wake of the forward components up which means that a larger part of the strut is exposed to a turbulent inflow. This results in a large area of high unsteady surface pressure and thus a high far field noise level as shown in Figure 5.20a. The opposite happens for the strut of the toe down configuration which has a smaller part exposed to the turbulent inflow and thus generates a lower far field noise level (figure 5.20c). The far field noise level generated by the strut of the horizontal configuration sits in the middle of these two extremes. These results show that the noise generated by the turbulent inflow is dominant over the noise generated by flow separation and vortex shedding in this situation.

The transverse centreline plot of the noise level generated by the strut in Figure 5.21 shows a much higher noise level than the longitudinal centreline plot as expected from the OASPL contours in Figure 5.20. The mid frequency noise is again dominant and the centreline plots are very symmetric in both the transverse and longitudinal directions. A large part of the strut is in the undisturbed flow and only the lower part of the strut is in the wake of the forward component which results in a relatively small amount of high frequency noise. The toe up configuration has the largest part of the strut exposed to the wake and therefore generates the highest noise levels while the opposite is true for the strut of the toe down configuration. The mid frequency noise of the strut of the toe

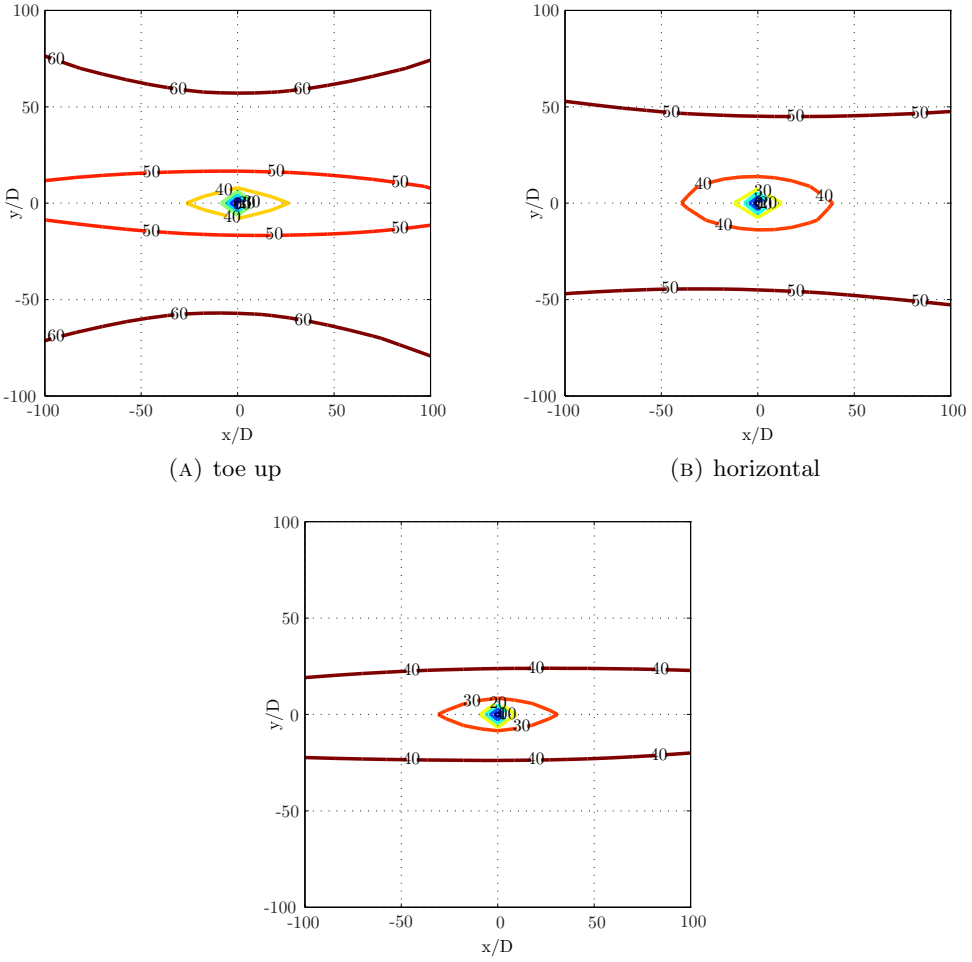

(A) toe up (B) horizontal

(C) toe down

FIGURE 5.20: Noise directivity contours of the strut of the simplified landing gear configurations. (OASPL in dB)

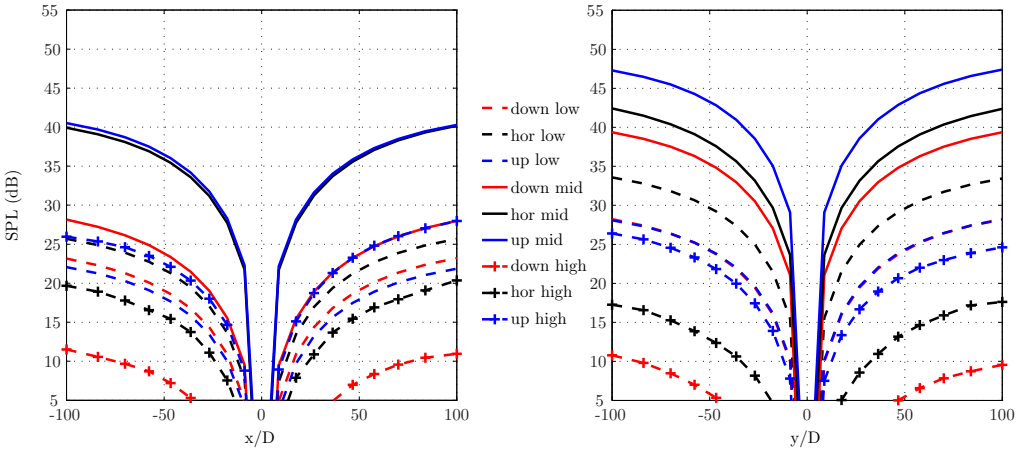

(A) longitudinal (B) transverse

FIGURE 5.21: Low, mid and high frequency noise levels generated by the strut of the simplified landing gear on the longitudinal and transverse centreline of the observer plane.(low = 49.6 Hz, mid = 250 Hz and high = 1000 Hz third octave band)

up configuration is the only exception to this trend and is lower than the mid frequency noise of the other configurations on both the longitudinal (Figure 5.21a) and transverse (Figure 5.21b) centrelines.

5.3.7 Complete landing gear

The noise generated by the main landing gear is a combination of the noise of the different components however it is not possible to simply add the noise levels due to the phase angle of the different acoustic signals. Instead a separate FW-H calculation has been done to determine the far field noise level generated by the complete main landing gear. The strut is the dominant noise source of the toe up configuration and the shape of the directivity pattern of the complete landing gear in Figure 5.22a is similar to that of the strut. The noise generated by the other components does increase the noise level near the transverse centreline and below the landing gear but is not enough to significantly change the shape of the noise directivity contours.

The far field noise level of the complete landing gear in the horizontal configuration is not dominated by the strut but its contribution is still significant. The bogie and rear axles of the horizontal configuration generate a high noise level directly below the landing gear while the rear wheels generate a relatively high noise level to the sides. The directivity pattern of the complete landing gear in Figure 5.22b still shows noise peaks to the sides and relatively quiet areas in the upstream and downstream direction but the difference between the minimum and maximum level is only 2 dB compared to more than 7 dB for the toe up configuration.

The contribution of the strut to the far field noise level generated by the complete landing gear in the toe down configuration is so low that it is no longer significant. The rear axles and rear wheels are the most important noise sources but the contribution of the bogie and front wheels can not be ignored either. The directivity pattern of the landing gear in toe down configuration also shows noise peaks to the sides and a difference between the peaks and the quiet regions of only 2 dB. The simplified main landing gear in toe down configuration is by far the quietest of the three configurations.

Figure 5.23 shows the noise levels of the complete simplified landing gear on the longitudinal and transverse centreline of the observer plane. The mid frequency noise is dominant for most of the components and also for the complete landing gear. The longitudinal plot in Figure 5.23a shows that the horizontal configuration generates the most noise followed by the toe up and then the toe down configurations which is the same order as shown by the OASPL contours in Figure 5.22. The transverse plot in Figure

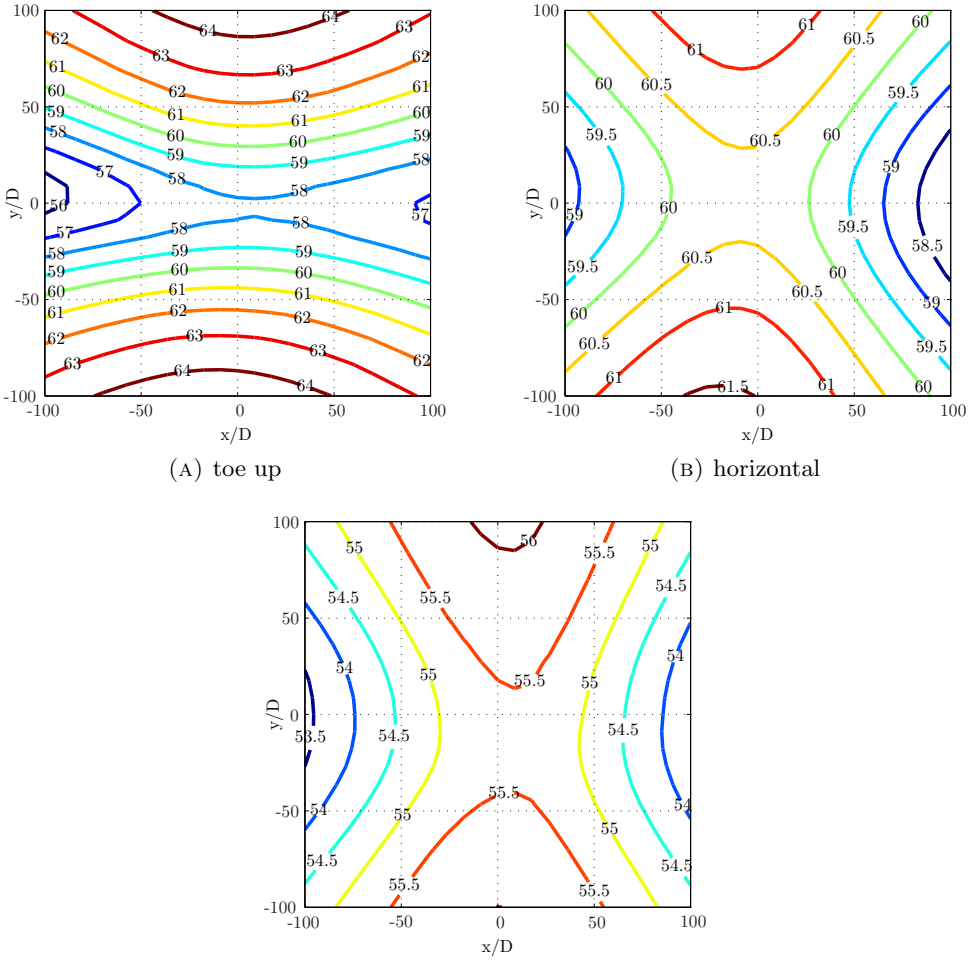

(A) toe up

(B) horizontal

(C) toe down

FIGURE 5.22: Noise directivity contours of the simplified landing gear configurations. (OASPL in dB)

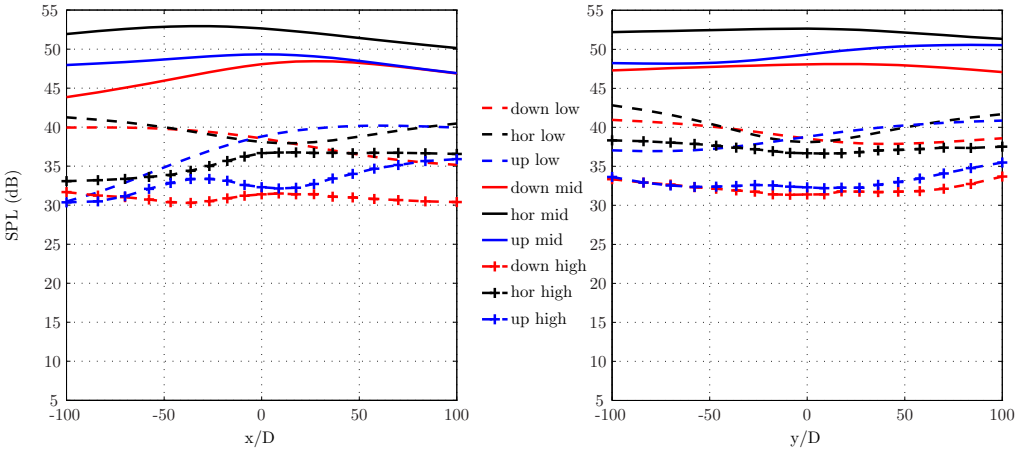

(A) longitudinal

(B) transverse

FIGURE 5.23: Low, mid and high frequency noise levels generated by the complete simplified landing gear on the longitudinal and transverse centreline of the observer plane.(low = 49.6 Hz, mid = 250 Hz and high = 1000 Hz third octave band)

5.23b also shows that the horizontal configuration is the noisiest while the OASPL contour in Figure 5.22 shows that the toe up configuration is generating the most noise. This means that the toe up configuration must generate more noise at a different third octave band than the ones shown in Figure 5.23 to increase the OASPL in the transverse direction to a higher level than that of the horizontal configuration.

5.4 Summary and discussion

The landing gear consists of multiple bluff bodies which generate a significant amount of separated flow and large turbulent wakes as shown in the previous chapter. The acoustic results show that the downstream components of the simplified landing gear are the dominant noise sources. This means that the turbulent wake interacting with a solid surface is a stronger noise mechanism than the noise generation by flow separation or vortex shedding in this situation. The magnitude of the dipole source term at the surface of the landing gear is closely related to the unsteady surface pressure distribution. The location of the peaks in the unsteady surface pressure distribution gives a good indication where the strongest interactions of the turbulent flow with the solid surface take place. The location of these peaks on the surface is linked to the trajectory of the strong streamwise vortices which are formed by the flow separation on the front wheels.

The simplified landing gear in toe up configuration is the loudest of the three simplified configurations based on the peak far field noise level on the observer plane. The toe up configuration of the bogie exposes a large area of the strut to the turbulent flow coming of the forward components which generates the far field noise peaks. The other components of this configuration do generate far field noise but their contribution is only significant in the overhead position and on the longitudinal centreline of the observer plane, directions in which the dipole type noise radiation of the strut is low.

The horizontal configuration of the simplified landing gear is the second loudest when considering the peak far field noise level on the whole observer plane but by far the noisiest configuration in the overhead position. The high overhead noise level is due to the large contribution of the bogie in this direction. Four strong streamwise vortices coming of the front wheels surround the aft half of the bogie and the induced velocity of these vortices pushes the turbulent flow to the surface of the bogie. This leads to large areas with a high unsteady pressure level on the sides of the bogie which radiate noise in the transverse and overhead direction. A smaller part of the strut is exposed to the turbulent flow in the horizontal configuration compared to the toe up configuration which reduces the amount of far field noise to the sides. The other components of the

horizontal landing gear generate similar noise levels as for the toe up configuration which leads to a more even noise level on the whole observer plane.

Both the overhead spectrum and the peak far field noise level of the toe down configuration clearly show that this is the quietest of the three simplified main landing gears. The toe down configuration moves the front wheels away from the strut resulting in a less disturbed inflow and therefore a large reduction of the dominant noise source. The strong streamwise vortices coming of the front wheels move downstream below the rear wheels and rear axles. This moves them further away from the landing gear geometry compared to the other two configurations. The increase in distance reduces the interaction of the turbulent flow with the solid surfaces and thus the far field noise levels. The combination of these two effects makes the toe down configuration of the simplified landing gear the quietest for any observer angle.

Chapter 6

Comparison of OpenFOAM and Fluent

The CFD simulations of the three simplified landing gear configurations have been run using commercial software package Fluent but the increase in the number of cells of the complex landing gear grids combined with license restrictions make it impossible to continue with this solver. The solver for the complex main landing gear simulations has therefore been changed to OpenFOAM, an open source CFD package, the details of which have been described in the numerical method section of the methodology chapter 3.8. Because of this change in software packages it has been decided to do a comparison before running the complex landing gear CFD simulations.

The toe up configuration of the simplified main landing gear is used for the comparison by doing a CFD simulation using OpenFOAM with the same grid and boundary conditions as used during the Fluent simulation. OpenFOAM does not include a FW-H solver so the surface pressure data collected during the CFD simulation has been converted to Fluents acoustic data format. This make it possible to use the Fluents FW-H solver for the far field acoustics, keeping the method consistent between the two simulations. This chapter describes the comparison of the aerodynamic and acoustic results of the OpenFOAM simulation with the results described in the previous two chapters generated using Fluent.

6.1 Aerodynamics

This section presents the aerodynamic results of the OpenFOAM CFD simulation of the simplified landing gear in toe up configuration and compares them with the Fluent results of chapter 4. The aerodynamic results have been post processed using the same method as before and the focus here is not on describing the important flow features but on identifying both the similarities and the differences in the flow field generated by the two CFD software packages. This section follows the same order as chapter 4 starting with the time averaged surface flow features followed by the unsteady surface pressure distribution and the aerodynamic force coefficients.

6.1.1 Flow features

The surface flow features on the front wheel are shown in Figure 6.1 and look similar to the Fluent results in Figure 4.13 however close inspection shows some small differences. The flow over the inside surface of the front wheel diverges more as it moves around the front axle in the OpenFOAM results as shown by the surface LIC pattern in Figure 6.1a. This more diverging flow pattern around the front axle to wheel junction indicates an earlier flow separation in OpenFOAM compared to the Fluent results. The same pattern of a slight upstream shift of the location of flow separation is seen on the top of the front wheel in Figure 6.1e. This earlier flow separation from the top of the wheel results in an upward shift of the flow attachment point in the flow recirculation zone on the aft face of the front wheel (Figure 6.1d).

Figure 6.2 shows a comparison of the time averaged pressure coefficient on the centreline of the front wheel between Fluent and OpenFOAM. Although the shape of the two curves is similar it clearly shows differences at the top and rear of the front wheel. The flow in the OpenFOAM simulation does not reach the same low pressure level at the top of the wheel indicating a lower local velocity. This results in earlier flow separation and less pressure recovery at the rear of the wheel compared to the Fluent results. The combination of earlier flow separation and reduced pressure recovery will increase the drag on the front wheel compared to the Fluent results.

Figure 6.3 shows the surface flow features on the bogie which compare well with the previous results in Figure 4.15. The only difference in the flow features can be seen at the front half of the bogie in side view (Figure 6.3b). The general flow features are the same but the flow in front of the strut has a stronger vertical component. This results in a narrower flow recirculation zone behind the front axle and a downward shift of the surface LIC pattern compared to the Fluent results.

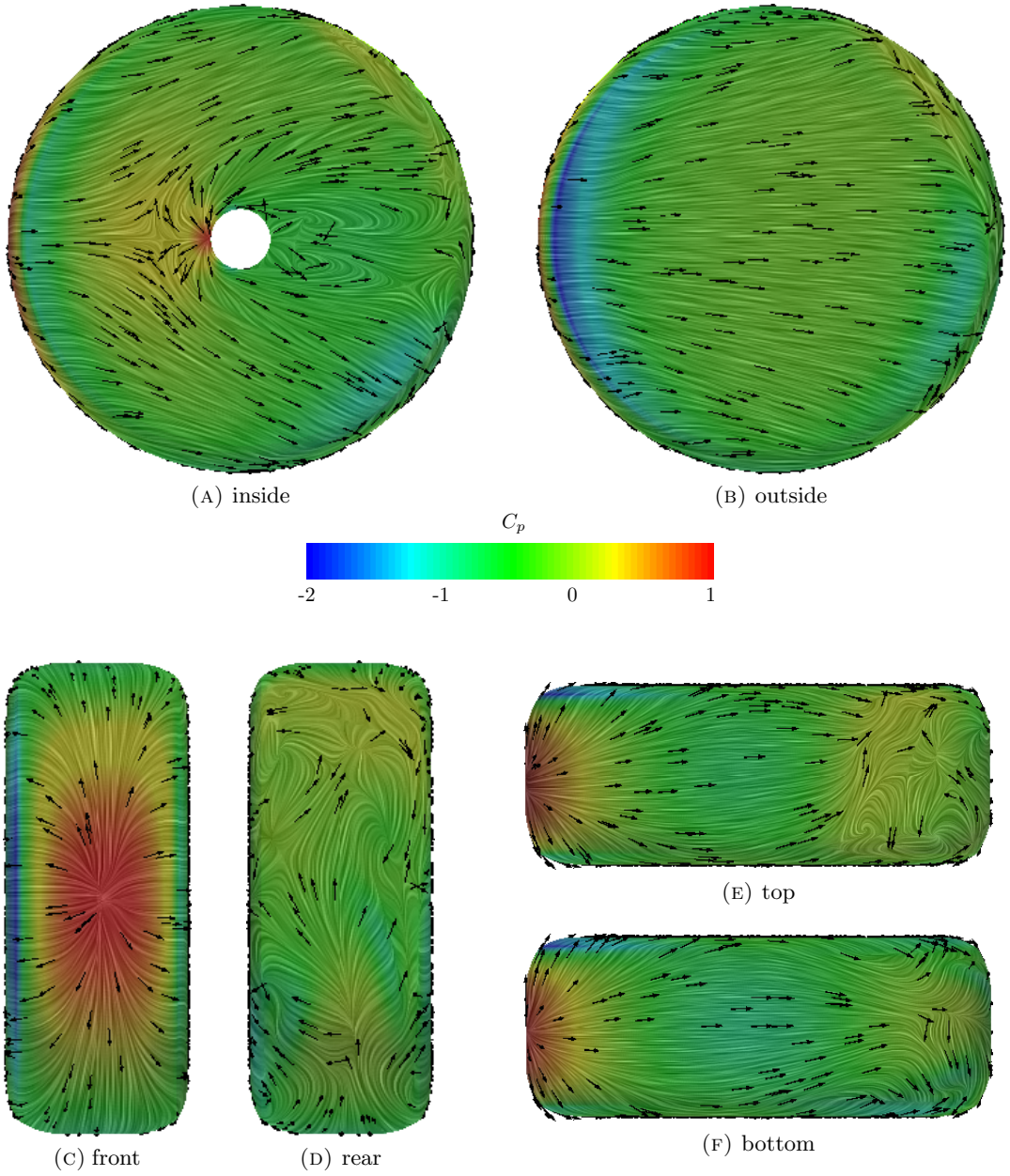

(A) inside (B) outside

(C) front (D) rear (E) top (F) bottom

FIGURE 6.1: Surface flow features of the time averaged flow field on the forward wheel of the simplified toe up configuration computed using OpenFOAM.

The surface flow features on the rear wheel of the toe up configuration look similar between OpenFOAM (Figure 6.4) and Fluent (Figure 4.13) but there are again some subtle differences. The flow at the the rear axle to wheel junction diverges more resulting in a wider wake region behind the rear axle for the OpenFOAM results. The top shoulder on the outside of the rear wheel in Figure 6.1d does not show the strong curved surface LIC pattern (which indicates the formation of a vortex) that is visible in the Fluent results in Figure 4.13d. The absence of this vortex results in a different flow separation pattern on the top of the rear wheel (Figure 6.1e) which also changes the surface LIC pattern in the wake at the top of the rear face (Figure 6.1d).

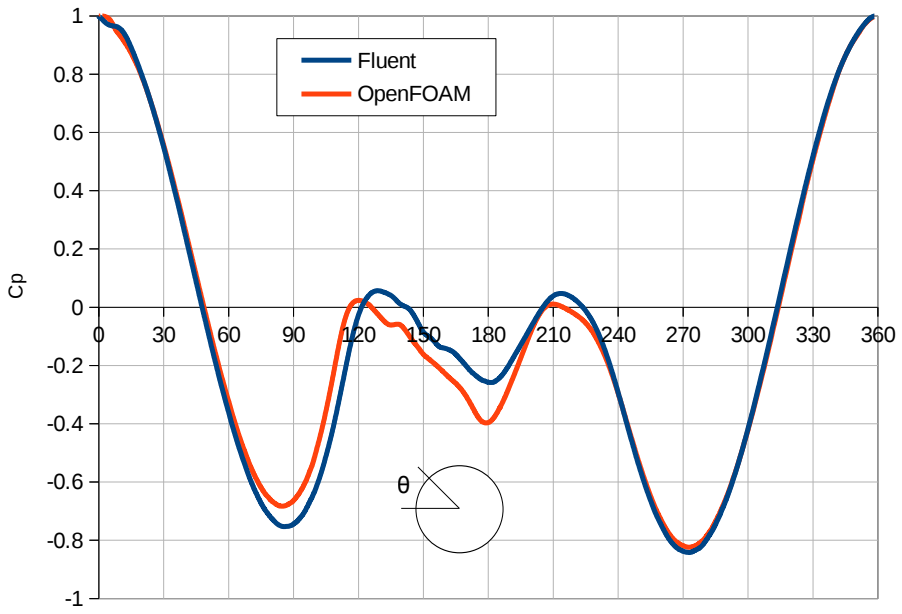

FIGURE 6.2: Comparison of the time averaged pressure coefficient on centreline of the front wheel of the simple toe up configuration between Fluent and OpenFOAM.

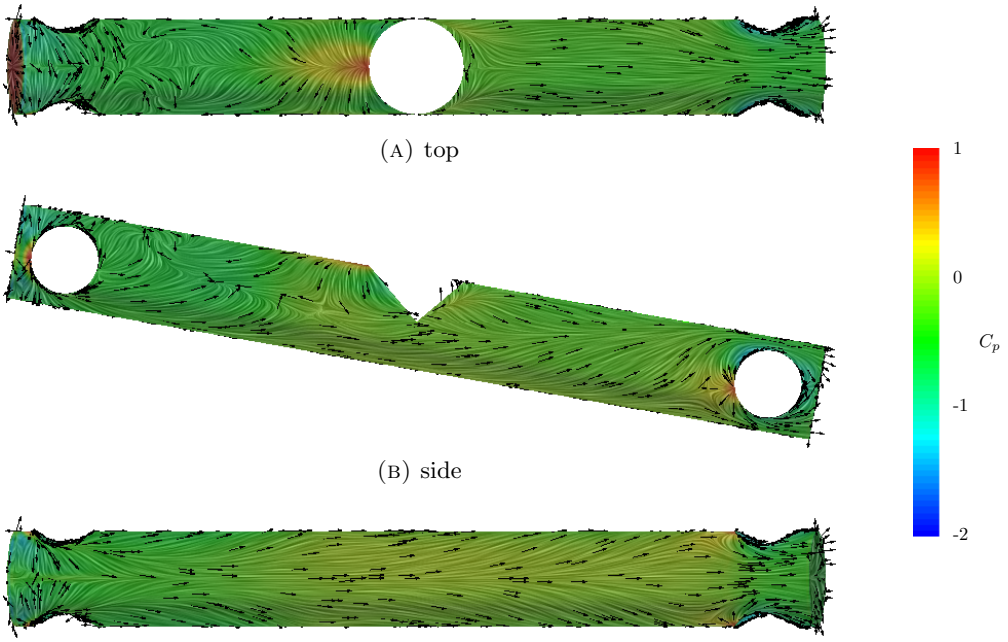

(A) top

(B) side

(C) bottom

FIGURE 6.3: Surface flow features of the time averaged flow field on the bogie of the simplified toe up configuration computed using OpenFOAM.

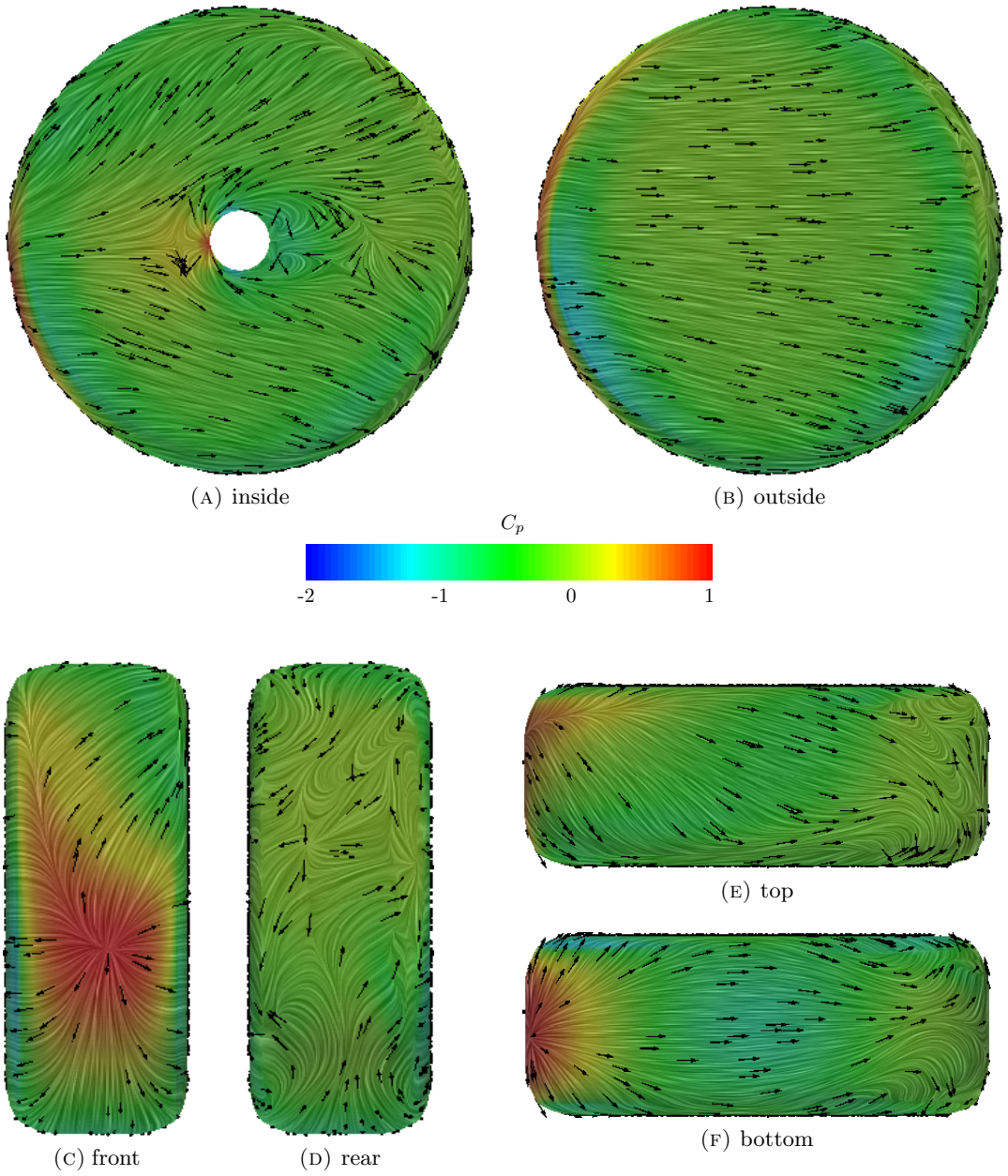

(A) inside (B) outside

(C) front (D) rear

(E) top

(F) bottom

FIGURE 6.4: Surface flow features of the time averaged flow field on the rear wheel of the simplified toe up configuration computed using OpenFOAM.

The comparison of the time averaged pressure coefficient on the centreline of the rear wheel between Fluent and OpenFOAM in Figure 6.5 shows the same trend as the comparison of the front wheel in Figure 6.2. The OpenFOAM results show a reduced pressure recovery at the rear of the wheel compared to the Fluent results. The lower pressure at the rear of the wheel will lead to an increase in the wheel drag of the OpenFOAM results compared to the Fluent simulation.

The flow features on the strut, in Figure 6.6, look similar to the Fluent results in Figure 4.16. The main difference is the less pronounced area of low pressure on the side of the

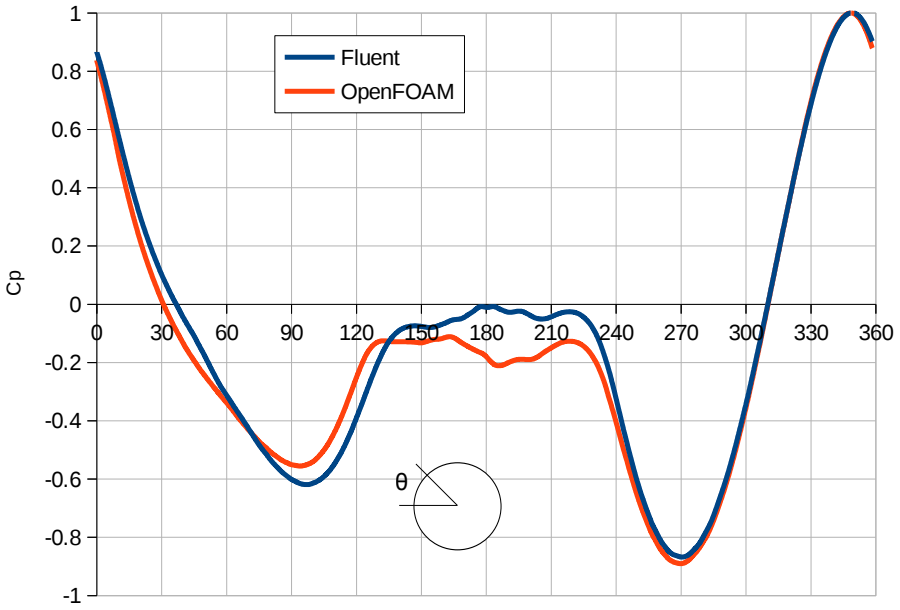

FIGURE 6.5: Comparison of the time averaged pressure coefficient on the centreline of the rear wheel of the simple toe up configuration between Fluent and OpenFOAM.

strut in the OpenFOAM results, indicating a lower local flow velocity. There also is a small area of low pressure on the aft face of the strut (Figure 6.6c) which is less visible in the Fluent results (Figure 4.16c).

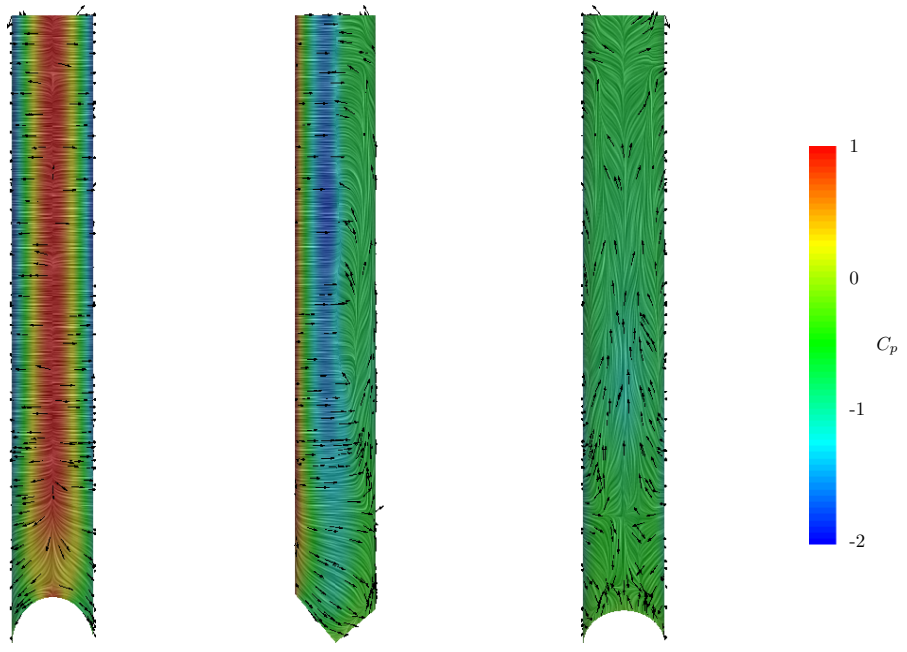

(A) front (B) side (C) rear

FIGURE 6.6: Surface flow features of the time averaged flow field on the lower half of the strut of the simplified toe up configuration computed using OpenFOAM.

The streamwise vorticity plots of the two simulations of the toe up configuration of the simplified landing gear (Figures 6.7 and 4.17) look similar. Both figures show the strong

attached vortices at the bottom of the front wheels and weaker separated vortices at the top of the front wheels. The vorticity plots at the centre plane of the landing gear show some differences, the location of the strong vortices is similar but the shape is different. The vortices close to the bogie in the Fluent results consist of two separate areas while these areas have merged into a single large structure in the OpenFOAM results. The location of the vortex cores in the downstream plane through the centre of the rear wheels and axles is almost identical but the OpenFOAM results show a reduced strength of the streamwise vortices.

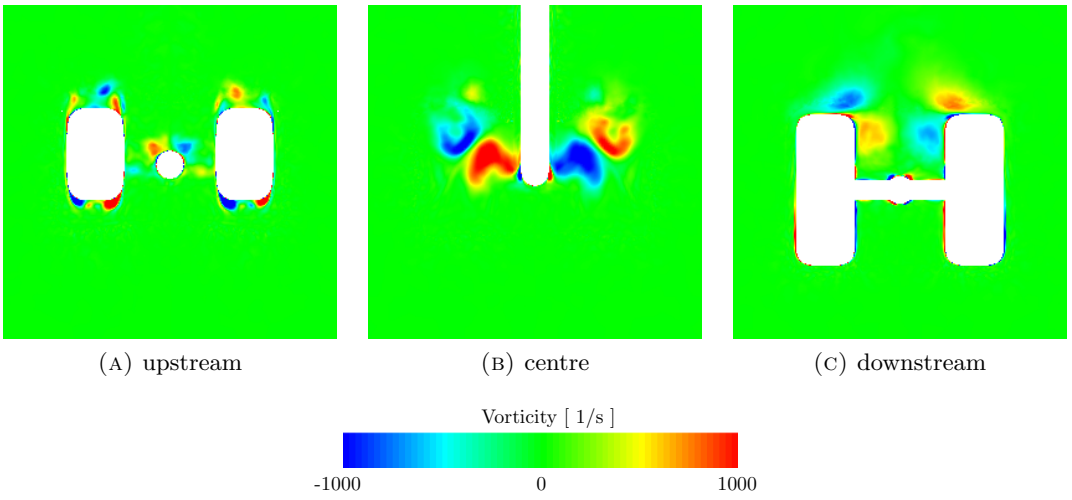

(A) upstream (B) centre (C) downstream

FIGURE 6.7: Streamwise vorticity of the time averaged flow field around the simplified toe up configuration computed using OpenFOAM, upstream = aft part of the front wheels, centre = centre of the MLG, downstream = centre of the rear wheels.

6.1.2 Unsteady surface pressure distribution

The previous section has shown that there is reasonable agreement of the time averaged flow features, the large flow features are similar but there are differences in the strength and location. The acoustics depend on the pressure fluctuations at the surface and these unsteady surface pressure levels will be compared in this section. Figure 6.8 shows the unsteady pressure distribution on the surface of the front wheel and axle computed using OpenFOAM which shows a lot of similarity to the Fluent results in Figure 4.18. The shape of the contours in the two figures is almost the same but the unsteady pressure levels are higher in the OpenFOAM results. The inside surface of the front wheel in Figure 6.8a shows that the two peaks in the unsteady pressure distribution downstream of the front axle are slightly further apart. This agrees with the more diverging surface LIC pattern visible in the surface flow features in Figure 6.1a. The unsteadiness in the wake of the front axle is higher in the OpenFOAM results and this carries over to the

aft face of the front wheel resulting in a larger area of high unsteady pressure compared to the Fluent results.

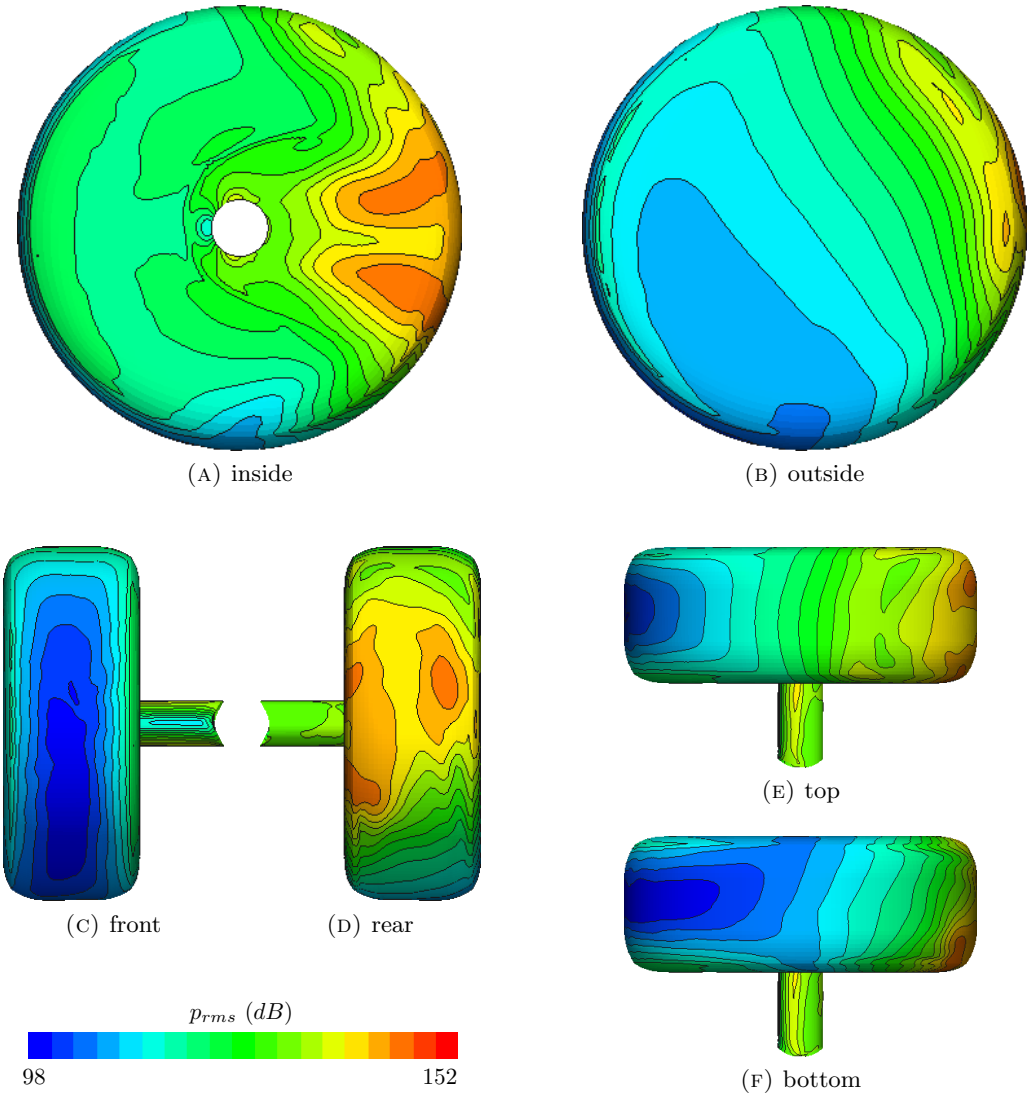

(A) inside (B) outside

(C) front (D) rear

(E) top

(F) bottom

FIGURE 6.8: Unsteady surface pressure level on the forward wheel and axle of the simplified toe up configuration computed using OpenFOAM.

The same trend as shown for the front wheel and front axle is present on the rear wheel and rear axle, the shape of the unsteady surface pressure contours is similar but the levels are different between the two CFD solvers. The OpenFOAM results in Figure 6.9 show a higher unsteady surface pressure level compared to the Fluent results in Figure 4.19. The most pronounced difference is visible on the top half of the inside surface of the rear wheel and on the surface of the rear axle where the unsteady pressure levels have moved up by one 3 dB band.

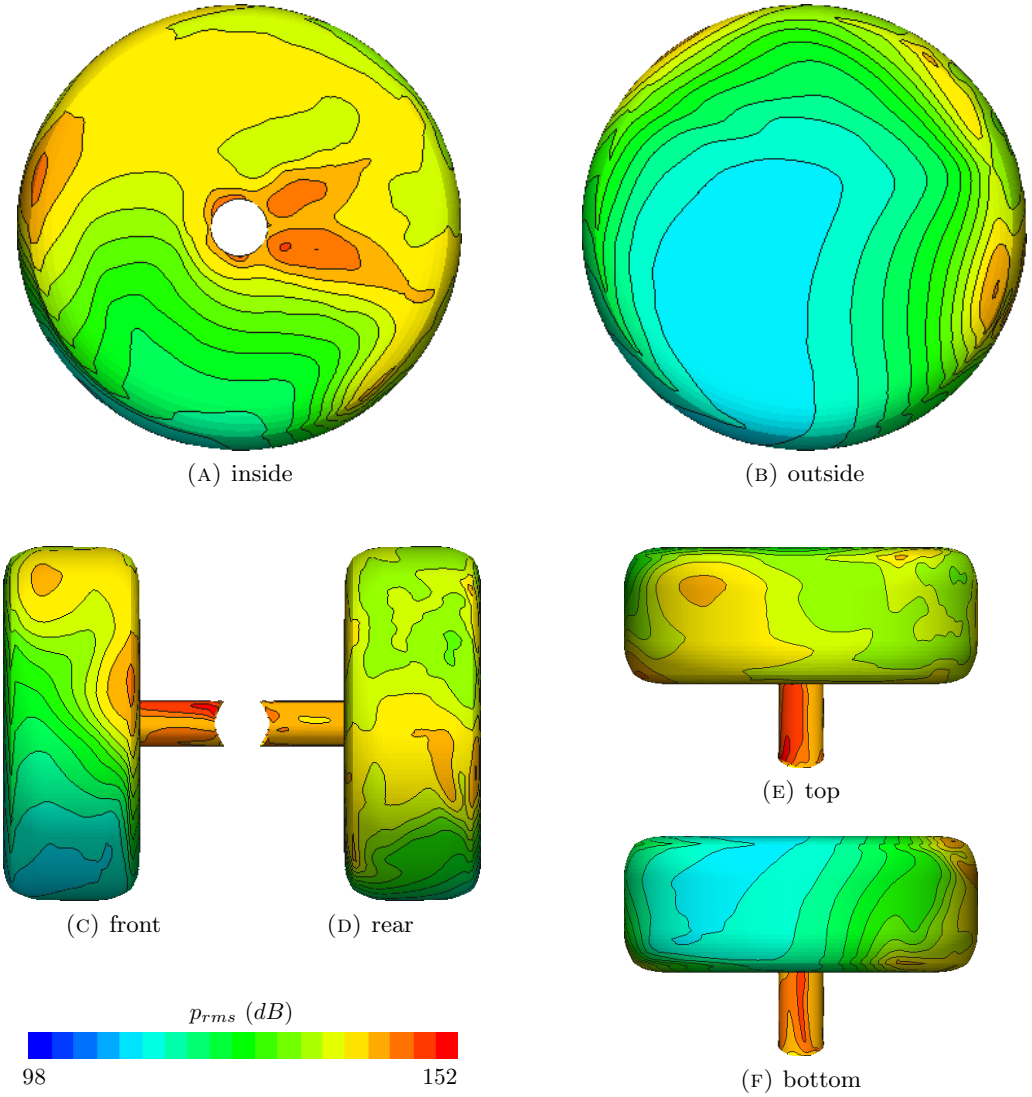

FIGURE 6.9: Unsteady surface pressure level on the rear wheel and axle of the simplified toe up configuration computed using OpenFOAM.

The unsteady pressure level on the surface of the bogie (Figure 6.10) and strut (Figure 6.11) follow the same trend as the wheels and axles: the shape of the contours is similar between the two CFD solvers but the level is approximately 3 dB higher in the OpenFOAM results.

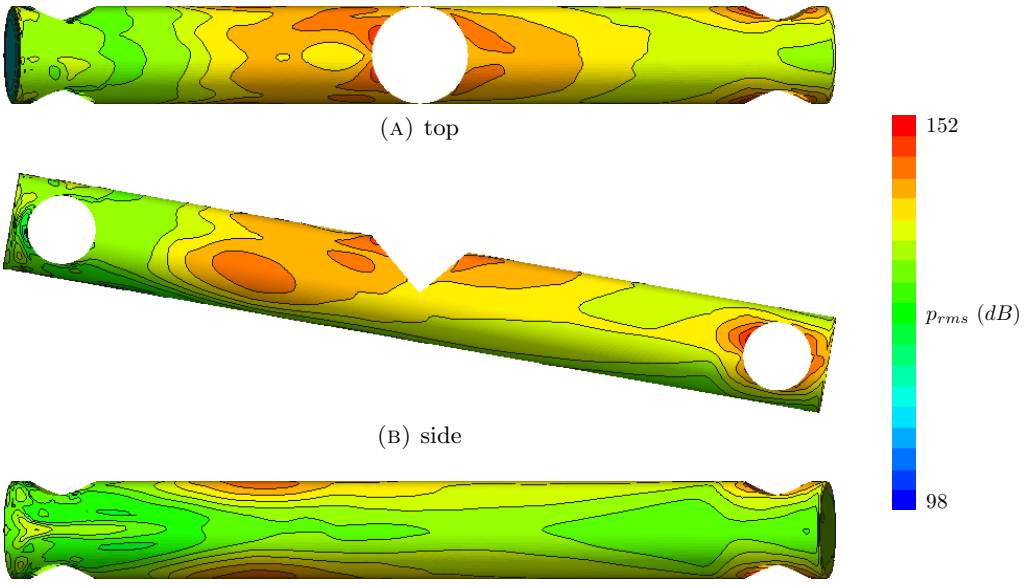

(A) top

(B) side

(C) bottom

FIGURE 6.10: Unsteady surface pressure level on the bogie of the simplified toe up configuration computed using OpenFOAM.

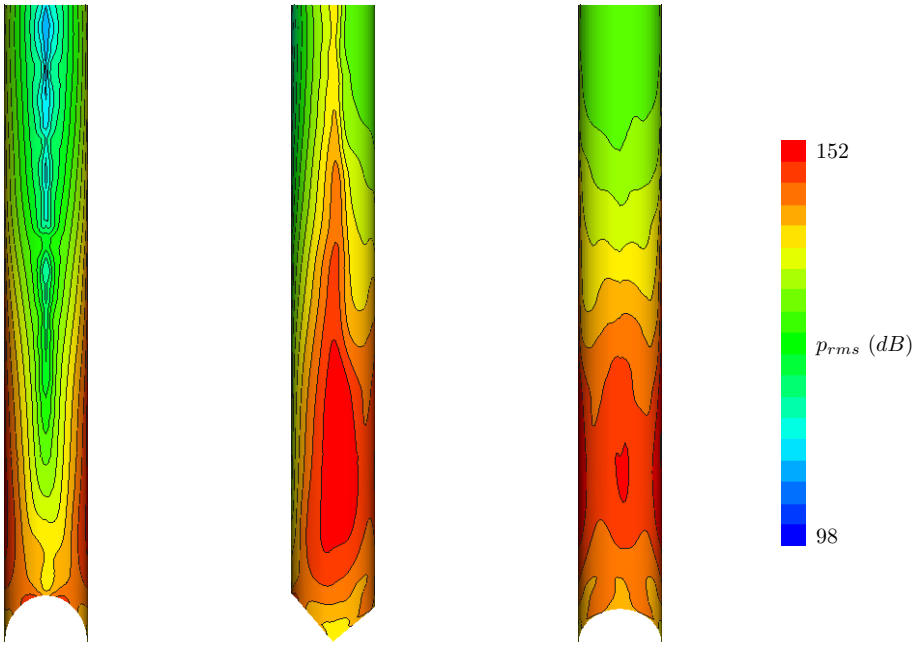

(A) front (B) side (C) rear

FIGURE 6.11: Unsteady surface pressure level on the lower half of the strut of the simplified toe up configuration computed using OpenFOAM.

6.1.3 Aerodynamic forces

The previous two sections show reasonable similarity of the time averaged flow features but there are differences in the exact location and strength of the flow features between the two solvers. The unsteady surface pressure distribution is very similar between the two solvers but the level is approximately 3 dB higher in the OpenFOAM results. The aerodynamic drag of a bluff body is in general dominated by pressure differences so the earlier flow separation and reduced pressure recovery of the OpenFOAM results will lead to a higher time averaged drag than the Fluent results as confirmed by the results in table 6.1. The Δ columns show the difference between OpenFOAM and Fluent and both the average drag as the standard deviation of the drag are higher in OpenFOAM. The higher unsteady surface pressure level of the OpenFOAM results, as shown in the previous section, causes the higher standard deviation of the drag coefficient compared to Fluent. The drag coefficient of the front wheels and axles is approximately 20 % higher than the Fluent results which is rather disappointing considering the time averaged flow features of the simulations are quite similar.

	Cd ($\times 10^{-2}$)			
component	mean	Δ	std	Δ
bogie	5.62	0.04	0.29	0.07
front axle rhs	2.11	0.45	0.09	0.00
front axle lhs	2.11	0.48	0.10	0.03
front wheel rhs	18.11	2.85	1.55	0.16
front wheel lhs	17.92	1.50	1.62	0.00
rear axle rhs	2.16	-0.17	0.55	0.16
rear axle lhs	2.25	0.04	0.58	0.22
rear wheel rhs	17.70	1.11	1.73	0.42
rear wheel lhs	16.63	0.25	1.53	0.13
strut	44.91	1.45	3.04	1.18
MLG	129.52	7.99	4.19	0.70

TABLE 6.1: Mean and std of the drag coefficients of the simplified toe up configuration computed using OpenFOAM. The Δ columns show the difference between the OpenFOAM and Fluent results.

The mean sideforce coefficient of most of the landing gear components is close to zero due to the symmetry of the geometry and the only components which generate a significant amount of sideforce are the front and rear wheels. The OpenFOAM results in table 6.2 show a significantly larger side force coefficient for the front wheels compared to the Fluent results. A comparison of the mean pressure coefficient on the surface of the front wheel in Figures 4.13 and 6.1 shows two reasons for this difference. The OpenFOAM results show a larger area of high pressure on the inside of the wheel in front of the axle and also a lower pressure on the forward outside edge of the wheel. The mean sideforce coefficients of the rear wheels in the OpenFOAM results are not equal between the right

and left hand side. The same is true for the results of the Fluent simulation and this should improve with longer sampling. The higher level of unsteadiness in the results of the OpenFOAM simulation leads to an increase of the standard deviation of the sideforce coefficient compared to the Fluent results. The only exception to this trend is the strut because the increased unsteadiness of the flow disrupts the regular vortex shedding.

	Cs ($\times 10^{-2}$)			
component	mean	Δ	std	Δ
bogie	0.00	-0.07	2.09	0.65
front axle rhs	0.00	0.00	0.00	0.00
front axle lhs	0.00	0.00	0.00	0.00
front wheel rhs	11.52	3.38	2.41	0.58
front wheel lhs	-11.52	-2.98	2.41	0.86
rear axle rhs	-0.01	-0.02	0.00	0.00
rear axle lhs	0.01	0.02	0.00	0.00
rear wheel rhs	-0.08	-1.69	3.29	0.64
rear wheel lhs	1.77	1.32	3.63	0.55
strut	0.07	-0.60	10.15	-1.90
MLG	1.77	-0.62	12.21	-2.09

TABLE 6.2: Mean and std of the side force coefficients of the simplified toe up configuration computed using OpenFOAM. The Δ columns show the difference between the OpenFOAM and Fluent results.

The lift coefficients in table 6.3 show reasonable agreement between the Fluent and OpenFOAM results except for the rear wheels. The OpenFOAM results show a large difference in the lift coefficient between the rear wheels on the right and left hand side. The lift coefficients of the rear wheels in the Fluent simulation (table 4.2) are not equal either but the difference is smaller. The asymmetric pressure distribution on the rear wheels which causes the difference in sideforce also results in a difference in lift. The standard deviation of the lift coefficient is again higher for most components in the OpenFOAM simulation compared to Fluent which is the same trend as shown for the drag and side force coefficients.

The comparison of the time averaged flow features show a reasonable similarity between the results of the two solvers but small differences in the exact location and strength of the features have a large effect on the aerodynamic forces. The OpenFOAM simulation shows a higher level of unsteadiness in the flow which leads to earlier flow separation and slightly wider wakes on the upstream components. This changes the flow field that reaches the downstream components and makes a comparison of the aerodynamic force coefficients of the downstream components of the landing gear less straightforward. The comparison of the aerodynamic force coefficients of the two solvers is therefore worse than expected from looking at the time averaged flow features.

	Cl ($\times 10^{-2}$)			
component	mean	Δ	std	Δ
bogie	4.45	0.21	1.19	0.28
front axle rhs	0.02	0.12	0.14	0.01
front axle lhs	0.06	0.15	0.14	0.01
front wheel rhs	-8.38	-0.75	0.83	-0.14
front wheel lhs	-7.93	0.02	1.21	0.49
rear axle rhs	0.63	0.11	1.45	0.32
rear axle lhs	0.61	0.15	1.43	0.38
rear wheel rhs	-5.69	-6.27	1.92	-1.68
rear wheel lhs	2.63	3.46	2.04	-0.11
strut	0.01	0.00	0.01	0.00
MLG	-13.59	-2.80	4.70	-0.94

TABLE 6.3: Mean and std of the lift coefficients of the simplified toe up configuration computed using OpenFOAM. The Δ columns show the difference between the OpenFOAM and Fluent results.

6.2 Acoustics

The previous section shows a reasonable agreement of the time averaged flow features but a higher unsteady surface pressure level for the OpenFOAM simulation compared to Fluent results. The magnitude of the dipole source term is strongly related to the unsteady pressure level as shown in section 5.1. The dipole source strength figures of the OpenFOAM results are therefore not included here but have been added to section B.3 of appendix B instead. The FW-H solver uses the surface pressure history to calculate the far field noise level. The difference in the unsteady surface pressure level is therefore predicted to lead to a higher far field noise level of the OpenFOAM results. The overhead noise spectrum in Figure 6.12, which has been generated using the sampled surface pressure data of the OpenFOAM simulation, confirms this. The noise level is higher than the overhead spectrum of the Fluent simulation in Figure 5.7. The peak overhead noise level of the landing gear has gone up by approximately 3 dB similar to the difference in the unsteady surface pressure levels between the two solvers. Although the absolute overhead noise levels are different between the two solvers, the OpenFOAM results do show the same relative contribution of the different components to the overhead noise level as the Fluent results.

The far field noise directivity contours generated by the front wheels of the OpenFOAM simulation in Figure 6.13a are more ellipse shaped compared to the round noise directivity contours of the Fluent results in Figure 5.10a and also contain a shallow dip on the longitudinal centreline. The difference in the far field noise level between the OpenFOAM and Fluent results as shown in Figure 6.13b is between 1 and 3 dB. The aerodynamic results of the OpenFOAM simulation show more diverging flow around the

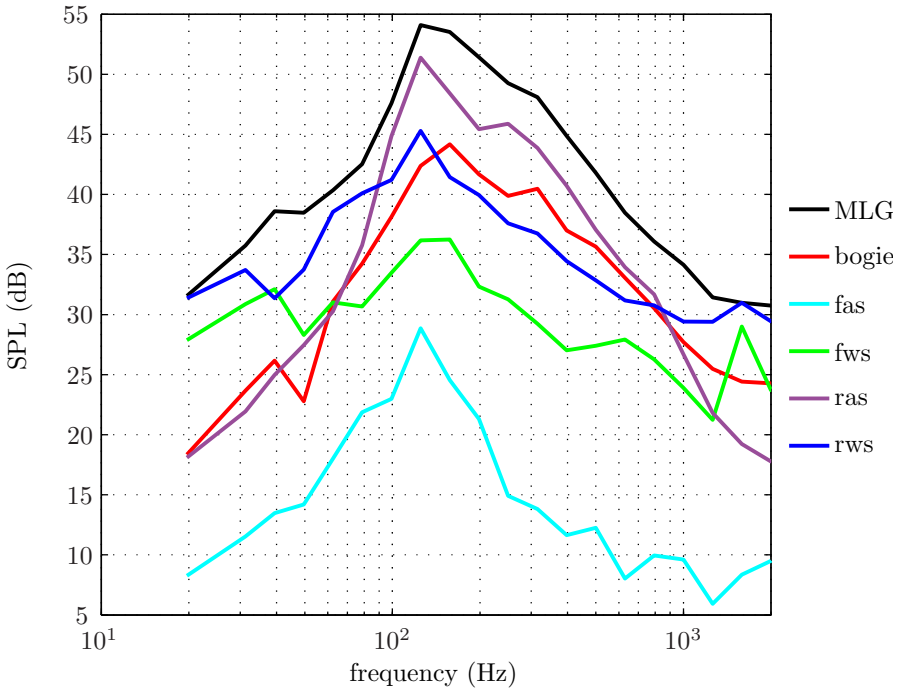

FIGURE 6.12: Overhead third octave band spectrum of the simplified toe up configuration computed using OpenFOAM.

front axle which results in a larger area of high unsteady pressure level on the inside surface of the front wheel (Figure 6.8) compared to the Fluent results (Figure 4.18). The unsteady surface pressure levels on the front and aft face of the front wheel are similar between the two solvers. This leads to an increase in the noise radiation below the landing gear and to the sides but a similar noise radiation in the upstream and downstream direction creating a more ellipse shaped noise directivity contour.

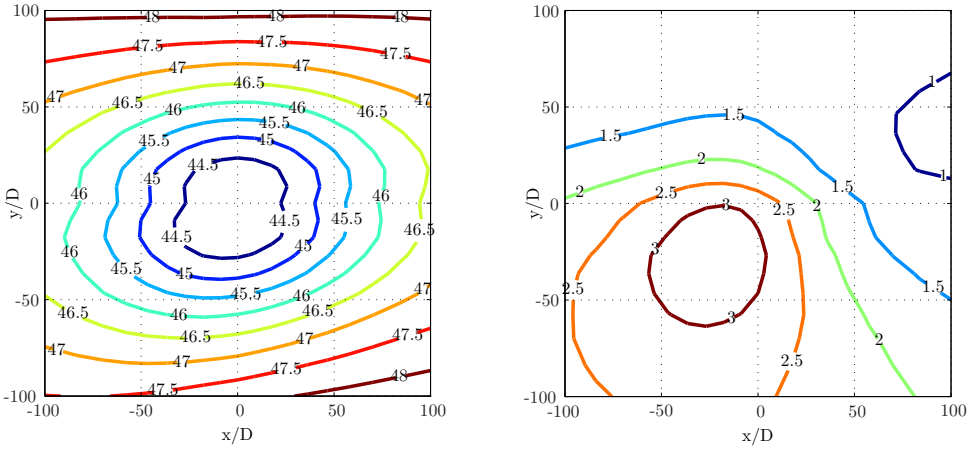

(A) front wheels

(B) Δ between OpenFOAM and Fluent

FIGURE 6.13: Noise directivity contours of the front wheels of the simplified toe up configuration computed using OpenFOAM. (OASPL in dB)

The front axles in the OpenFOAM simulation generate a far field noise directivity contour with a peak below the landing gear (see Figure 6.14a) similar to the Fluent results in Figure 5.12a. The difference between the two results (Figure 6.14b) is relatively constant over the observer plane at 2 to 3 dB. The shape of the directivity contours of the Fluent results are smooth without clear features while the OpenFOAM results show an increase in the noise level on the longitudinal centreline and also a set of lobes in the upstream direction at approximately + and - 45 degrees. The unsteady surface pressure distribution on the bottom of the axle in Figures 4.18f and 6.8f is different between the two solvers. The Fluent results show the unsteady pressure peak near the junction with bogie while the OpenFOAM results show the peak close to the junction with the wheel. The increased noise level on the longitudinal centreline in the upstream and downstream direction and the lobes in the noise contours of the OpenFOAM result are assumed to be a caused by aerodynamic interactions at the axle to wheel junction.

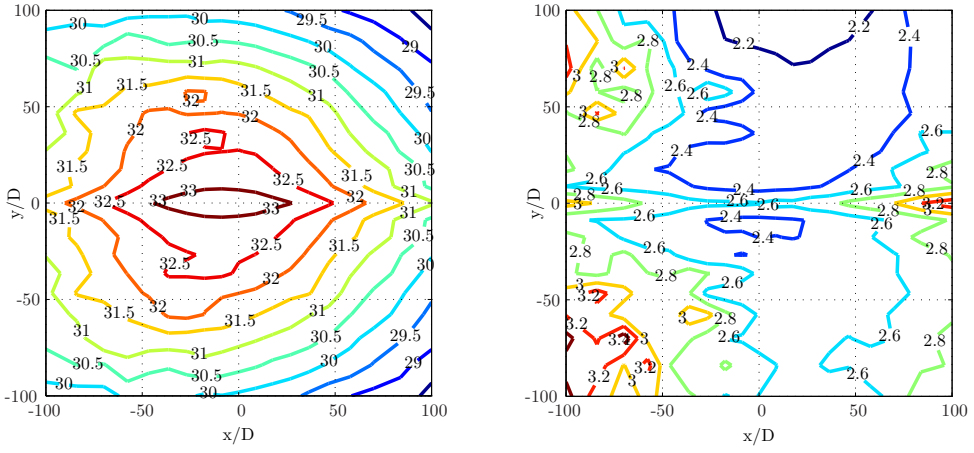

(A) front axles

(B) Δ between OpenFOAM and Fluent

FIGURE 6.14: Noise directivity contours of the front axles of the simplified toe up configuration computed using OpenFOAM. (OASPL in dB)

Figure 6.15a shows the far field noise directivity contours generated by the bogie in the OpenFOAM simulation and this is similar to the Fluent results in Figure 5.14a. The shape of the contours is more symmetric for the Fluent results but the location of the far field noise peaks and quiet areas is the same. Figure 6.15b shows that the far field noise level generated by the bogie in the OpenFOAM simulation is on average 3 dB higher over the whole observer plane which agrees with the 3 dB higher unsteady pressure level on the surface of the bogie as shown in Figure 6.10 of the previous section.

The noise directivity pattern generated by the rear wheels is similar for the two simulations as shown by Figures 5.16a and 6.16a. The noise directivity pattern of the Fluent simulation is asymmetric in the transverse direction compared to the more symmetric directivity of the OpenFOAM results which carries over to the difference plot in Figure

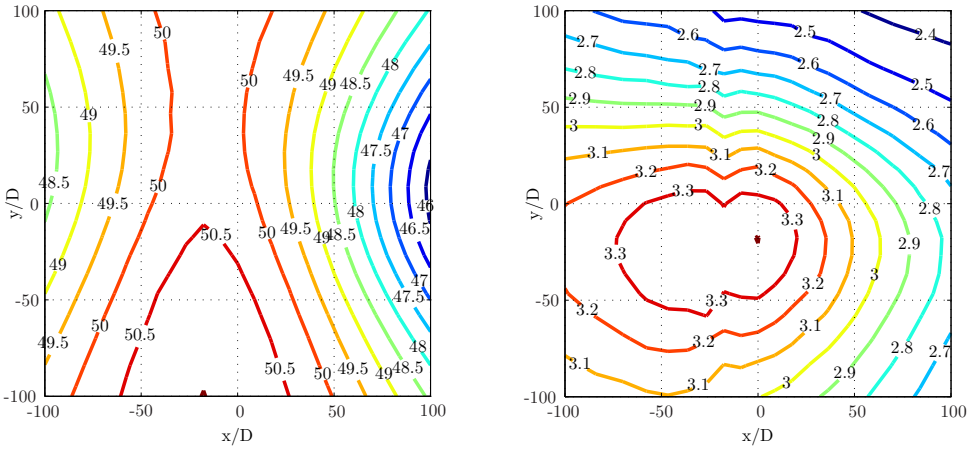

(A) bogie

(B) Δ between OpenFOAM and Fluent

FIGURE 6.15: Noise directivity contours of the bogie of the simplified toe up configuration computed using OpenFOAM. (OASPL in dB)

6.16b. The average noise level over the observer plane is approximately 1 dB lower for the Fluent results. This corresponds to the lower unsteady surface pressure distribution on the rear wheel of the Fluent results as can be seen by comparing Figures 4.19 and 6.9.

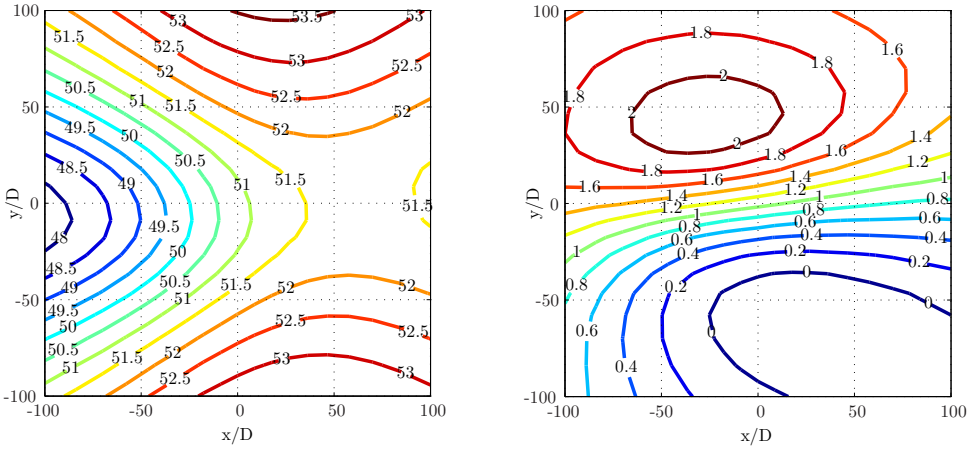

(A) rear wheels

(B) Δ between OpenFOAM and Fluent

FIGURE 6.16: Noise directivity contours of the rear wheels of the simplified toe up configuration computed using OpenFOAM. (OASPL in dB)

The rear axles in both simulations generate circular shaped noise contours as shown in Figures 5.18a and 6.17a which corresponds with the downward pointing lobe of a dipole source as expected for a cylinder. The average difference in the noise level over the whole observer plane is approximately 1.5 dB between the two simulations as shown in Figure 6.17b. The difference in the noise level increases in the downstream direction

which agrees with higher unsteady surface pressure on the rear of the axle as can be seen in Figures 4.19d and 6.9d.

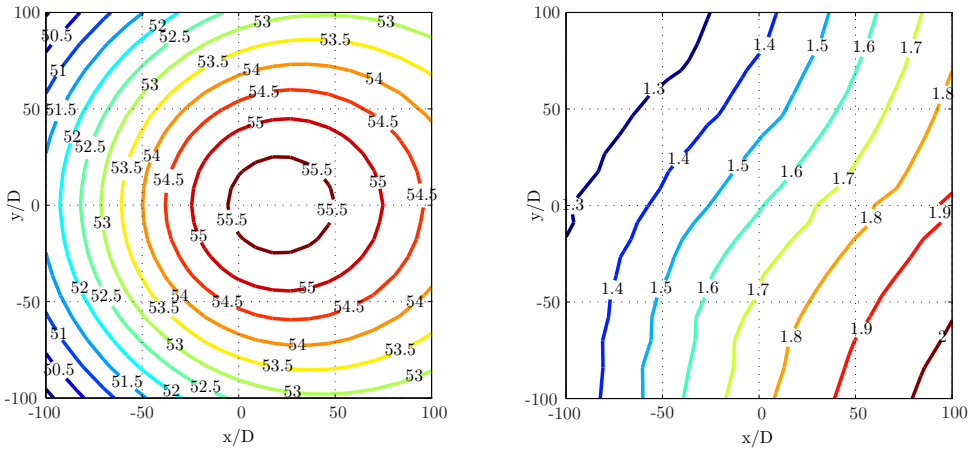

(A) rear axles

(B) Δ between OpenFOAM and Fluent

FIGURE 6.17: Noise directivity contours of the rear axles of the simplified toe up configuration computed using OpenFOAM. (OASPL in dB)

The strut is a cylinder and acts as a dipole source which results in two peaks in the far field noise levels to the sides. The noise level generated by the strut in the OpenFOAM simulation in Figure 6.18a is a higher than that of the Fluent simulation in Figure 5.20a. The noise directivity contour of the OpenFOAM results is a little asymmetric in the transverse direction and this is clearly visible in the difference plot of Figure 6.18b. The largest difference in the noise level is visible on the longitudinal centreline in both the upstream and downstream direction. This can be explained by the higher unsteady surface pressure level on the front and aft face of the strut close to the strut to bogie junction in the OpenFOAM results (Figure 6.11) compared to the Fluent results (Figure 4.21).

The far field noise levels generated by the different components of the landing gear in the OpenFOAM simulation are in general higher than the Fluent results but there is reasonably good agreement of the shape of the noise directivity patterns. The noise generated by the complete main landing gear is a sum of the noise of the individual components which results in the same trend as can be seen in Figures 5.22a and 6.19a. The directivity pattern of the complete landing gear is similar but the far field noise level is around 2 dB higher for the OpenFOAM simulation as shown in Figure 6.19b. The difference in the main landing gear noise directivity in Figure 6.19b is dominated by the loudest components, the strut and rear wheels. The asymmetry of the difference plot of the rear wheels in Figure 6.16b is also visible in the difference of the complete landing gear in Figure 6.19b.

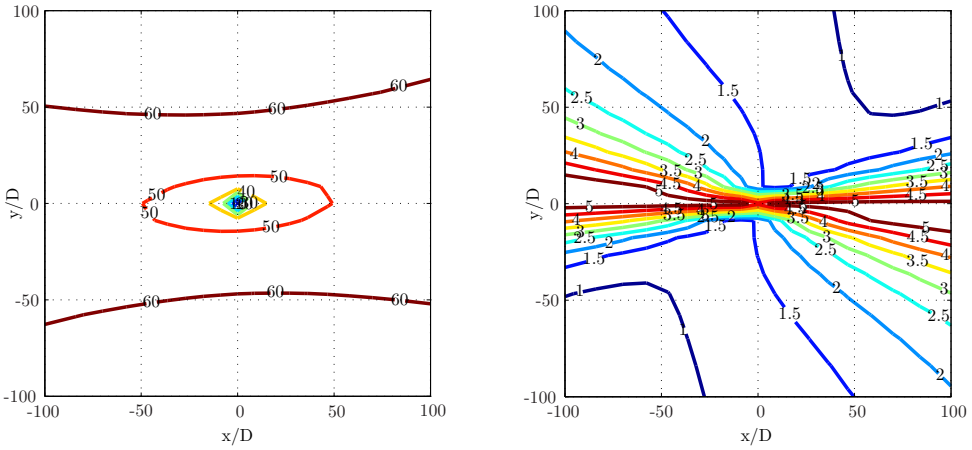

(A) strut (B) Δ between OpenFOAM and Fluent

FIGURE 6.18: Noise directivity contours of the strut of the simplified toe up configuration computed using OpenFOAM. (OASPL in dB)

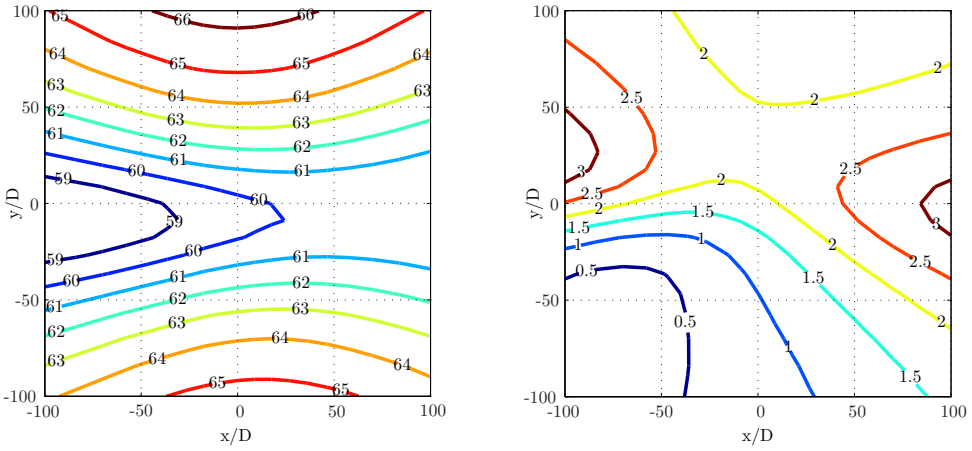

(A) MLG (B) Δ between OpenFOAM and Fluent

FIGURE 6.19: Noise directivity contours of the MLG of the simplified toe up configuration computed using OpenFOAM. (OASPL in dB)

6.3 Summary and discussion

The aerodynamic results of both CFD solvers, OpenFOAM and Fluent, show similar time averaged flow features around the simplified landing gear with relatively small differences in the location and strength of some of these flow features. The OpenFOAM results show earlier flow separation on the front wheels and front axles which results in a different size of some of the flow recirculation zones and a difference in the pressure recovery on the downstream side of these components.

The agreement of the unsteady pressure results on the surface of the landing gear is not as good as that of the time averaged flow features. Both CFD solvers show a

similar unsteady surface pressure distribution but there is a difference in the levels. The OpenFOAM results show a higher level of unsteadiness in the flow compared to the results of the Fluent simulation which leads to a higher unsteady surface pressure level and is also expected to be the reason for the earlier flow separation on the front wheels and axles.

The reasonable similarity of the time averaged flow features does not guarantee good agreement between the mean force coefficients of the two simulations. The difference in location of flow separation on the forward components results in changes to the wake and pressure distribution and thus the aerodynamic forces. The difference in the wake then affects the velocity field around the downstream components and the aerodynamic forces they generate. The results of the OpenFOAM simulation show a higher level of unsteadiness in the flow field which in general leads to an increase of the standard deviation of the force coefficients compared to the Fluent results.

The far field noise level is directly related to the history of the pressure signal at the surface of the landing gear. The difference in the unsteady surface pressure levels of the two simulations will lead to a difference in the far field noise level. The acoustic results of the FW-H solver show that the OpenFOAM simulation generates a far field noise level which is on average 2-3 dB higher than the noise level generated by the Fluent simulation. However, the relative contribution of the components to the far field noise is the same for both simulations and the shape of the noise directivity patterns on the observer plane is very similar.

A comparison of the flow field around the rudimentary four wheel main landing gear benchmark case using multiple CFD solvers by Spalart [63] has shown that there is a significant discrepancy in the aerodynamic results of the different CFD simulations. The agreement of the aerodynamic results of the two solvers here is reasonable which can be attributed to the use of the same grid and turbulence model. The setup of the two CFD solvers has been as close to identical as possible but even though both packages are based on the finite volume method there are differences in the used discretisation schemes and implementation of the methods. A full investigation of the differences is outside the scope of this study. Unfortunately it is not possible to determine which results (OpenFOAM or Fluent) are closer to reality since there is no experimental dataset of this exact landing gear geometry available. The switch to OpenFOAM for the complex landing gear simulations means that a direct comparison of the aerodynamic forces and far field noise levels generated by the simple and complex geometries will not be possible. It is however still possible to compare the important flow features and their effect on the far field noise levels and directivity.

Chapter 7

Uncertainty and error analysis

The CFD simulations done with Fluent and OpenFOAM show differences in the aerodynamic and acoustic results which leads to the following question: How accurate are the numerical results of the simulations compared to the real world situation that is being modelled? This issue has existed since CFD simulations started and multiple authors have since addressed it. Roache [74] has developed a method to quantify the uncertainty of CFD simulation results. The following terms are introduced by Roache [74]: verification as solving the equations right and validation as solving the right equations. Another way to make the distinction is to speak of numerical errors versus conceptual modelling errors.

Validation of the results of a simulation by comparing it with the real world can only be done after the numerical method used to solve the equations has been verified first. To verify the numerical method it is necessary to quantify the numerical error in the solution of the equations. The total numerical error of a simulation is a combination of different errors which are often related and therefore difficult to address separately. The behaviour of the total numerical error is assumed to be dominated by the discretisation error and depends directly on the grid resolution used for the simulation. Roache [74] uses this assumption to develop the Grid Convergence Index (GCI) which is based on generalized Richardson Extrapolation of discrete solutions on a 'family' of grids with different spacings / resolutions. An extrapolation of the results of the simulations on grids with different spacings is used to determine the continuum solution of the equations on an infinitely fine grid. The method assumes the convergence of the results is monotonic and all grids used for the extrapolation are fine enough to capture the important flow features. The last assumption is important since the grid refinement should only lead to a reduction of the numerical error and not result in significant changes in the flow field. The results of three simulations on different grid spacings are needed to determine the

order of the numerical method and to determine the continuum solution on the infinite fine grid spacing using extrapolation. The numerical error of the simulations is the difference between the result of the simulation and this extrapolated continuum solution. Roache suggests that a safe way to quantify the uncertainty in the results is to multiply this numerical error with a safety factor of 3.

The CGI method has been used on a large scale to quantify the accuracy of RANS simulations but does not work for Large Eddy Simulations (LES). The filter width in the LES turbulence model is directly linked to the grid spacing such that grid refinement leads to a different set of equations being solved. Detached Eddy Simulation combines RANS and LES and the switch between these two models is dependent on the grid spacing which also leads to a change of the equations when the grid is refined. This makes it impossible to use GCI on LES and DES to determine numerical error since the set of equations that are being solved are not kept constant. Spalart [75], who originally developed the concept of DES, has stated that one of the conceptual issues of the DES model is that it is not possible to show the numerical accuracy of the results. Although the standard CGI method does not work for LES / DES there have been efforts to quantify the errors in these type of CFD simulations as shown in the overview by Celik et al. [76]. However the methods are still under development and application of the methods to complex industrial problems may become very expensive.

The simple and complex landing gear CFD simulations of the current study have all been done on just one grid and an estimation of the numerical error and uncertainty is therefore not possible. The simulations have been done at the maximum grid resolution possible within the available computational resources at the time. The instantaneous vortical flow structures in Figures 4.1 and 8.1 show LES content in the flow near the landing gear geometry but the structures are relatively smooth which indicates that the grid resolution is not good enough to capture the very small flow scales. Both the time averaged flow data and far field noise data are not completely symmetric for the different simplified landing gear configurations which indicates that the sampling time should be increased. Similar issues have shown up in the CFD results of the BANC rudimentary landing gear [63] and unfortunately there is not much that can be done to improve this without a significant increase in computational costs / resources. This is not a very satisfying result but hopefully this will change in the near future when error estimation methods for DES improve and affordable computational resources increase.

Chapter 8

Aerodynamics of the complex main landing gear

This chapter describes the main aerodynamic features of the flow field around the three complex landing gear geometries. The complex geometry is based on the simple geometry but has additional components to better resemble an actual landing gear as shown in Figure 3.3. The following components have been added: a brake on the inside of the each wheel, an articulation link connecting the bogie to the front of the strut, a torque link downstream of the strut and a more realistic geometry of the strut including a yoke and swivel allowing the bogie to rotate. Figure 8.1 shows a snapshot of the instantaneous vortical flow structures around the complex horizontal landing gear and it is clear that the additional components generate a more disturbed flow field compared to the flow structures around the simple configuration in Figure 4.1.

Figure 8.2 show a comparison of the instantaneous and time averaged flow field on a transverse slice through the centre of the landing gear. The flow patterns of the instantaneous flow field (Figure 8.2a) are constantly changing and it is thus impossible to select a snapshot representative of the whole time series. The focus of the following sections is therefore on the main flow features of the time averaged flow field (Figure 8.2a). The current chapter follows the same order as the description of the aerodynamic results of the simple landing gear in chapter 4.

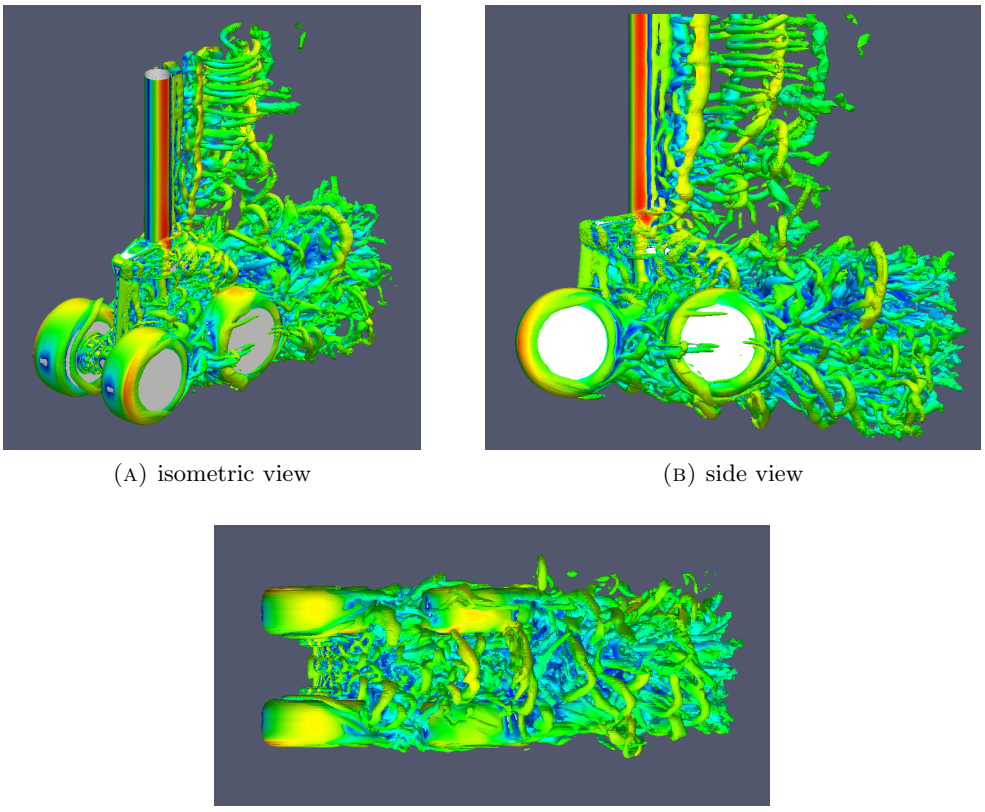

(A) isometric view

(B) side view

(C) bottom view

FIGURE 8.1: Isosurface of Q-criterion coloured by velocity magnitude highlighting the instantaneous vortical flow structures around the complex horizontal MLG.

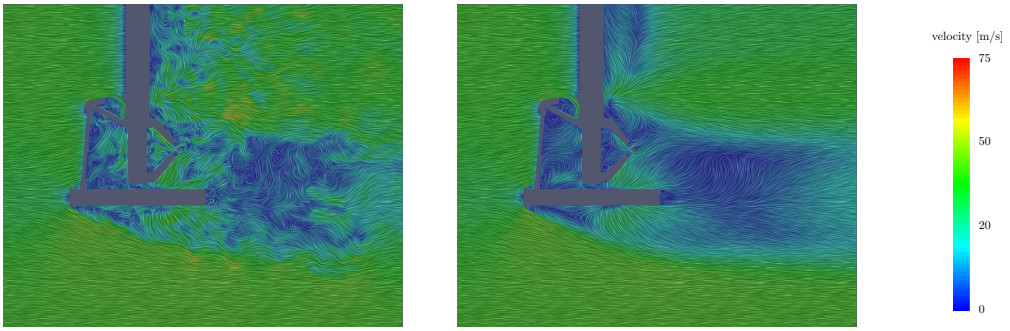

(A) instantaneous

(B) time averaged

FIGURE 8.2: Instantaneous and time averaged velocity on a transverse slice through the centre of the complex horizontal MLG.

8.1 Horizontal configuration

8.1.1 Flow features

The blockage at the centre of the complex landing gear is higher than that of the simplified geometry such that a larger part of the flow takes the path of least resistance and moves around the outside of the front wheels. This can be clearly seen in the surface LIC pattern on the front face of the front wheel (Figure 8.3c) which shows that the stagnation point is located closer to the centre of the landing gear compared to that of the simplified configuration (Figure 4.4c). The flow that moves to the outside of the front wheel accelerates around the edge resulting in a narrow band of low pressure. The surface LIC pattern on the outside surface of the wheel in Figure 8.3c is smooth indicating that the flow follows the surface until it reaches the downstream edge of the wheel where it separates. This is the same as what happens on the outside surface of the front wheel of the simplified landing gear configurations.

The surface of the brake unit on the inside of the front wheel has a complex shape with lots of curvature which results in a surface LIC pattern that is too disturbed to interpret and has therefore not been included in Figure 8.3a. The pressure increase towards the front of the brake unit results in area with upstream pointing shear stress vectors characteristic of a horse shoe vortex similar to the flow at the axle to wheel junction of the simple landing gear configuration. The brake unit forces the flow away from the centre of the wheel and the horse shoe vortex reaches the top and bottom edge of the wheel just aft of the half way point. The brake unit generates a turbulent wake however the surface LIC pattern on the inside of the front wheel downstream of the brake in Figure 8.3a is smooth. The brake unit consists of twelve small cylinders placed on top of two larger concentric disks which are connected to the wheel surface. These two concentric disks do not disturb the flow much resulting in a smooth surface LIC pattern downstream of the brake unit. The twelve small cylinders generate a strong turbulent wake but this is some distance away from the wheel surface such that it does not show up in the surface LIC pattern.

Figures 8.3e and 8.3f show the top and bottom surface of the front wheel and look similar to each other. The strong curvature of the surface LIC pattern indicates flow separation and the formation of a vortex pair at both the top and bottom of the wheel just as what happens in the simple horizontal configuration. The aft face of the front wheel in Figure 8.3d shows two short vertical attachment lines in between the vortex pairs. These attachment lines are located towards the outside of the wheel which shows that the vortices on the inside of the wheel are larger and stronger than the vortices on the outside of the front wheel. The difference in vortex strength is more pronounced

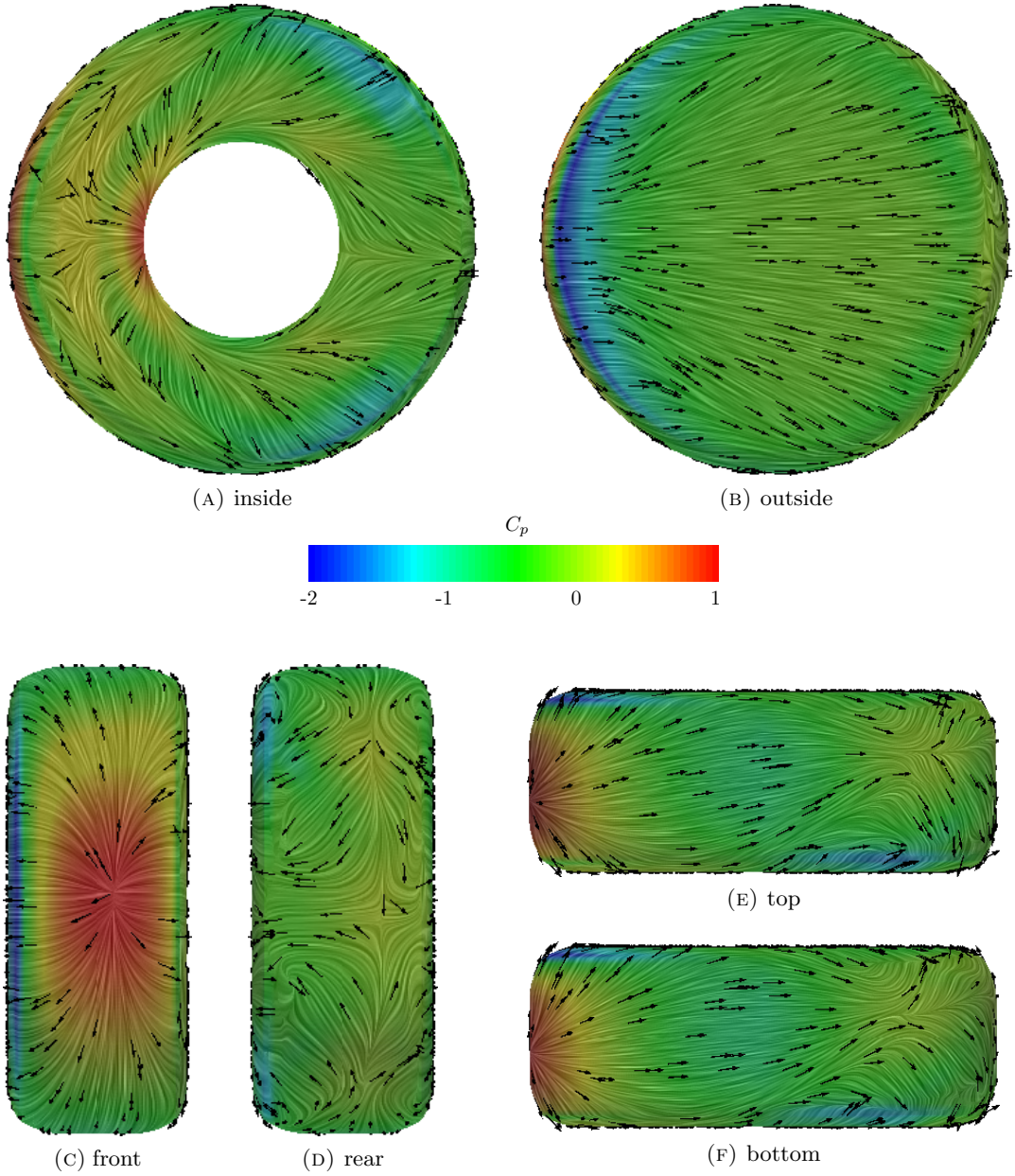

(A) inside (B) outside

(C) front (D) rear (E) top (F) bottom

FIGURE 8.3: Surface flow features of the time averaged flow field on the forward wheel of the complex horizontal configuration.

in the complex configuration compared to the simplified configuration and is a result of the addition of the brake unit to the wheel. The presence of the brake unit and axle generates a more diverging flow over the inside surface of the wheel which interacts with the flow over the top and bottom of the wheel resulting in more rotation and thus stronger vortices. The flow over the flat outside surface of the front wheel does not diverge as much from the free stream direction which results in less rotation in the flow and thus weaker vortices.

The flow separating from the surface of the front wheel results in the formation of

strong vortices and an area of separated flow on the aft face of the wheel. The surface LIC pattern in the separated region in Figure 8.3d is relatively smooth and shows the influence of the strong vortices on the local flow. The induced flow field of the strong vortices moves the flow from the top and bottom of the wheel towards the centre of the landing gear. This is the same flow feature as seen on the front wheel of the horizontal simplified configuration but the effect is more exaggerated due to the stronger vortices on the inside of the wheel.

The pressure distribution and surface LIC pattern on the front face of the rear wheel in Figure 8.4c looks similar to that of the simple horizontal configuration. The pressure near the attachment points is lower due to the reduced velocity around the complex landing gear. The two attachment points are close to the outside edge of the wheel indicating that most of the flow that reaches the rear wheel will move to the centre of the complex landing gear. The flow follows the front face of the rear wheel but separates from the surface at the inside wheel edge as can be seen by the upstream pointing wall shear stress vectors in front of the brake unit (Figure 8.4a). The absence of a pressure increase at the front of the rear brake unit is a clear sign of the lower flow velocity around the centre of the complex landing gear compared to the simple configuration.

Figures 8.4e and 8.4f are again similar and show the surface LIC pattern on the top and bottom surface of the rear wheel. The shear stress vectors are aligned with the free stream direction until the pressure increase at the aft part of the rear wheel leads to flow separation. The flat outside surface of the wheel in Figure 8.4b does not show any specific features indicating that the flow stays attached to the surface until it reaches the downstream edge of the wheel. The separated flow generates a complicated surface LIC pattern on the aft face of the rear wheel in Figure 8.4d. There are two small areas of strong curvature at the outside shoulders of the wheel where the flow over the flat outside surface merges with the flow over the top and bottom. The centre of the aft face also shows two spiralling patterns in the middle of the wake of the rear wheel. Both of these patterns indicate the formation of vortices.

The bogie of the complex horizontal configuration in Figure 8.5 shows a more disturbed surface LIC pattern compared to the simplified horizontal configuration but some of the same flow features can be distinguished. The top view in Figure 8.5a shows a small recirculation zone behind the attachment of the articulation link. There is a flow attachment point just in front of the middle of the bogie which is caused by the downwards deflected flow coming of the strut and yoke. Some of this flow turns upstream and forms a flow recirculation zone while the rest of the flow moves downstream through the gap between the yoke and the bogie. The upstream moving flow quickly loses momentum and separates from the surface at the separation point in between the articulation link

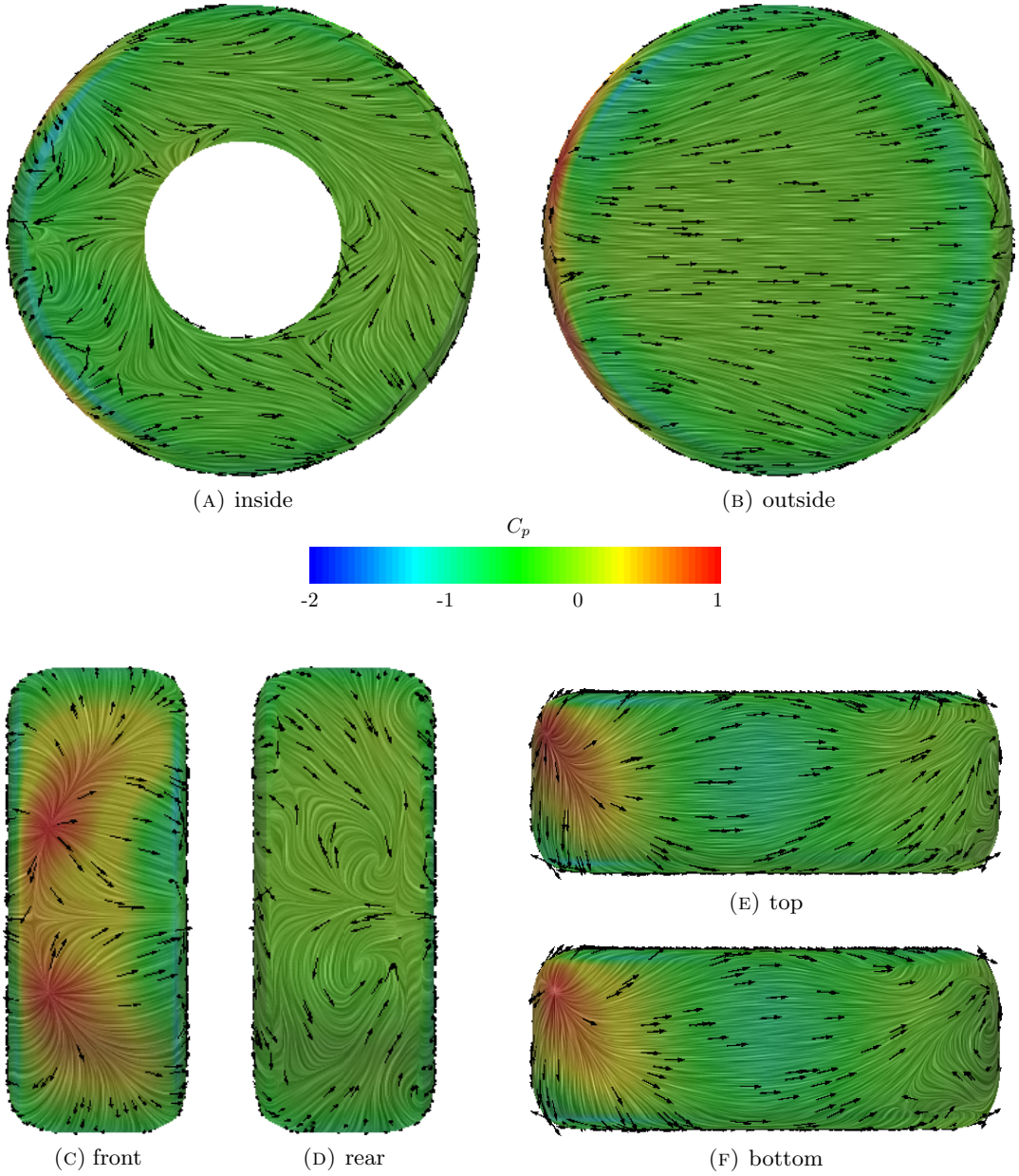

(A) inside (B) outside

(C) front (D) rear (E) top (F) bottom

FIGURE 8.4: Surface flow features of the time averaged flow field on the rear wheel of the complex horizontal configuration.

and the yoke. The side and bottom view of the front half of the bogie in Figures 8.5b and 8.5c show that there is a large area of reversed flow in between the front axle and the middle of the bogie which is caused by the wake of the front axle and looks similar to the simple case.

The surface LIC pattern on the aft half of the bogie looks similar to the surface LIC pattern on the bogie of the simple horizontal configuration. The side view in Figure 8.5b shows a clear attachment line which is formed under influence of the strong streamwise vortices. The attachment line is shorter and the local pressure coefficient is lower

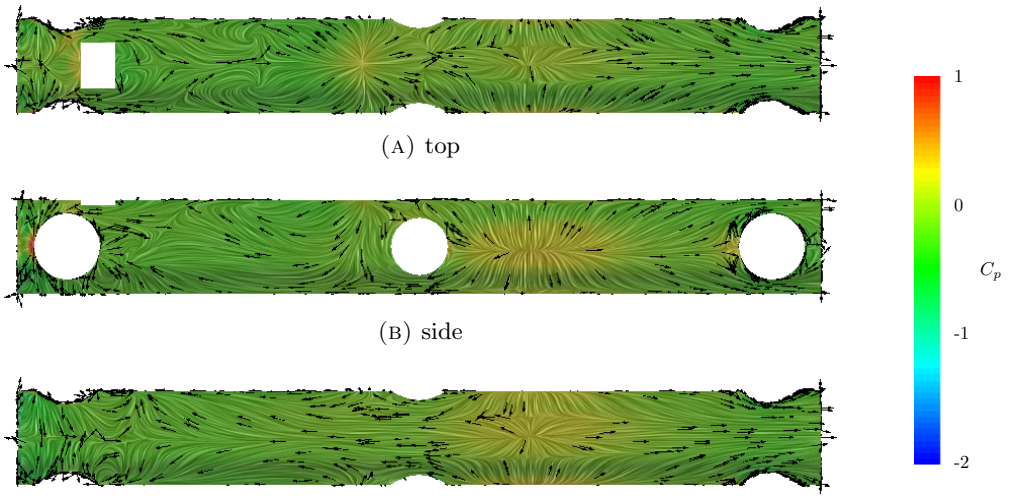

(A) top

(B) side

(C) bottom

FIGURE 8.5: Surface flow features of the time averaged flow field on the bogie of the complex horizontal configuration.

compared to the side of the bogie of the simple configuration. This is partly due to the reduced velocity at the centre of the landing gear but also indicates that the strength of the streamwise vortices is lower for the complex horizontal landing gear configuration.

The addition of the articulation link, yoke and torque link to the strut leads to a completely different geometry in the centre of the complex landing gear compared to the simple configuration. The forward position of the articulation link puts it in the undisturbed inflow resulting in high (stagnation) pressure on the front face as can be seen in Figure 8.6a. The articulation link has a square cross section and the sharp edges lead to immediate flow separation as shown by the upstream pointing wall shear stress vectors in the side view (Figure 8.6b). The turbulent wake generated by the articulation link moves downstream with the flow where it interacts with the strut and yoke. This results in two vertical attachment lines on the front face of the lower strut and two attachment points on the front of the yoke. The pressure increase near these attachment lines and points is relatively small due to the reduced velocity in the wake of the articulation link. The inclined front face of the yoke deflects the flow down as shown by the direction of the shear stress vectors and this agrees with the flow features on the top surface of the bogie.

The surface LIC pattern in the side view (Figure 8.6b) shows that the flow separates from the surface of the lower strut at approximately two thirds of the strut diameter. There is no pronounced area of low pressure on the side of the lower strut which shows that the mean flow velocity is relatively low near the centre of the landing gear. The flow attachment point on the flat side surface of the yoke is caused by the induced flow of the strong streamwise vortices coming of the front wheels. The top of the articulation

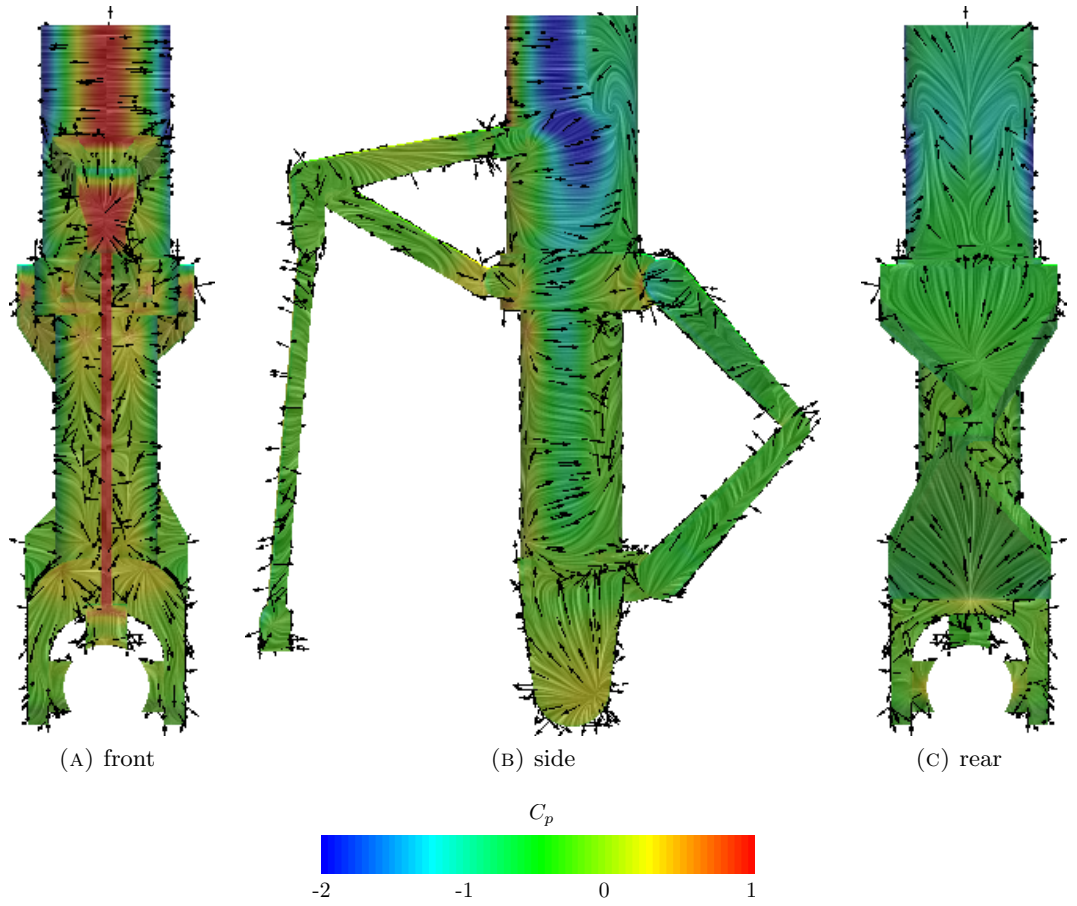

(A) front (B) side (C) rear

FIGURE 8.6: Surface flow features of the time averaged flow field on the lower half of the strut of the complex horizontal configuration.

link works as a ramp and guides the incoming flow around the strut. This results in a high local flow velocity on the side of the strut as can be seen by the large area of low pressure. The surface LIC pattern at this location shows that flow separation is delayed compared to the location of flow separation on the clean strut above it. The difference in location of flow separation on the curved surface of the strut leads to the formation of a streamwise vortex as can be seen by the strong curvature in the surface LIC pattern.

The torque link sits directly behind the strut and is almost completely covered by its wake which results in a complex surface LIC pattern. The rear view in Figure 8.6c shows a smooth surface LIC pattern on the lower half of the torque link with the shear stress vectors pointing downstream. This indicates that the flow follows the surface of the lower torque link in an upward direction due to the influence of the strong streamwise vortices. The top half of the torque link in the rear view shows an attachment point and upstream pointing shear stress vectors. These are characteristic of a flow recirculation zone in the wake behind the strut.

The surface flow features on the front wheel show the formation of strong streamwise

vortices similar to what happens in the flow around the simple landing gear configuration. Figure 8.7 shows the trajectory / development of these streamwise vortices as they move downstream with the flow. The plot at a plane through the aft part of the front wheel in Figure 8.7a shows four major vortices, one at each wheel shoulder, similar to the simple horizontal configuration (Figure 4.8a). The vortices on the inside of the front wheels are considerably larger than the ones on the outside. A small secondary vortex is visible above and below the large vortex on the inside of the wheel. This is the horse shoe vortex that originates from the front of the brake unit but has moved around the edge of the wheel.

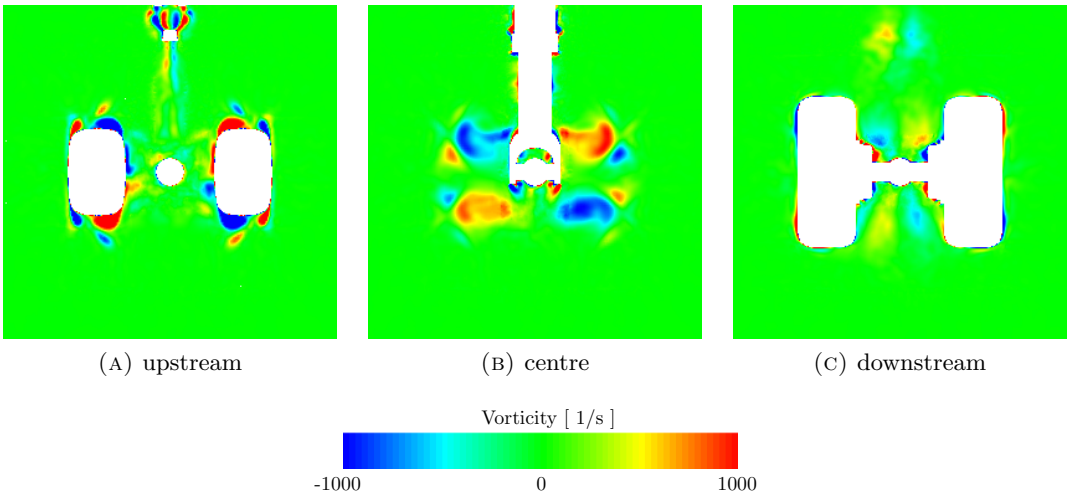

(A) upstream (B) centre (C) downstream

FIGURE 8.7: Streamwise vorticity of the time averaged flow field around the complex horizontal configuration, upstream = aft part of the front wheels, centre = centre of the MLG, downstream = centre of the rear wheels.

The streamwise vorticity plot at the centre plane of the complex landing gear in Figure 8.7b is similar to that of the simplified horizontal configuration (Figure 4.8b). There are four large areas of vorticity at the centre of the landing gear and four smaller vortices on the outside. The core of the streamwise vortex follows the local flow direction towards the centre of the landing gear. This means that the vortex cores are not perpendicular to the plane of the figure which makes them appear larger. The strength of the large vortices is lower than for the simplified configuration and the vortices are further apart due to the presence of the wider strut, yoke and torque link at the centre of the landing gear.

The four streamwise vortices from the centre of the landing gear are only barely visible in the vorticity plot at a plane through the rear axles and wheels in Figure 8.7c. The vortices coming off the front wheels interact with the turbulent wake behind the strut, yoke and torque link resulting in a quicker break down of the large flow structures. This creates smaller vortices / flow structures which are less stable and move around more such that they do not show up as clearly in the time averaged flow field. Two small

streamwise vortices are visible near the top of Figure 8.7c downstream of the articulation link. This agrees with the location of the strong curvature of the surface LIC pattern on the strut in Figure 8.6c.

8.1.2 Unsteady surface pressure distribution

This section shows the unsteady pressure distribution on the surface of the different components of the complex landing gear which is a good indication of where the far field noise is generated. The unsteady pressure distribution on the front wheel and brake unit of the horizontal complex configuration in Figure 8.8 looks similar to that of the simplified horizontal configuration in Figure 4.9. The clean inflow results in a low level of unsteadiness on the front of the wheel which increases further downstream. The flat outside surface of the wheel in Figure 8.8b shows the highest unsteady pressure level at the downstream edge where the flow separates from the wheel. The brake unit and axle disturb the flow over the inside of the wheel which creates a more diverging flow compared to the simple configuration. This results in a larger vertical separation of the two unsteady pressure peaks as can be seen in Figure 8.8a. The rear view of the front wheel in Figure 8.8d shows a relatively large area of increased unsteady pressure level at the location of the wake but no clear peaks or other features.

The front view of the rear wheel in Figure 8.9c shows four significant peaks in the unsteady pressure distribution. The two peaks on the inside edge of the rear wheel are in a similar position as for the simplified configuration (see Figure 4.10c) but slightly further apart. This agrees with the location of the strong streamwise vortices in Figure 8.7b of the previous section. The two smaller peaks are caused by the smaller vortices which move downstream along the outside surface of the rear wheel. These vortices create a band with increased unsteady pressure on the outside surface of the rear wheel as shown in Figure 8.9b.

The mean flow velocity near the centre of the complex landing gear configuration is lower compared to the simplified configuration due to the higher blockage. This results in a lower intensity of the pressure fluctuations on the inside surface of the rear wheel as can be seen by comparing Figures 4.10a and 8.9a. It also leads to a lower unsteady pressure level on the front face of the rear brake unit and rear axle even though they are completely immersed in the turbulent flow. The flow velocity in the wake of the rear brake unit is even lower and this results in a horizontal band of low unsteady pressure level downstream of the brake unit (Figure 8.9a).

The addition of the articulation link creates a wake at the front half of the bogie compared to the relatively clean flow towards the bogie of the simple configuration. The

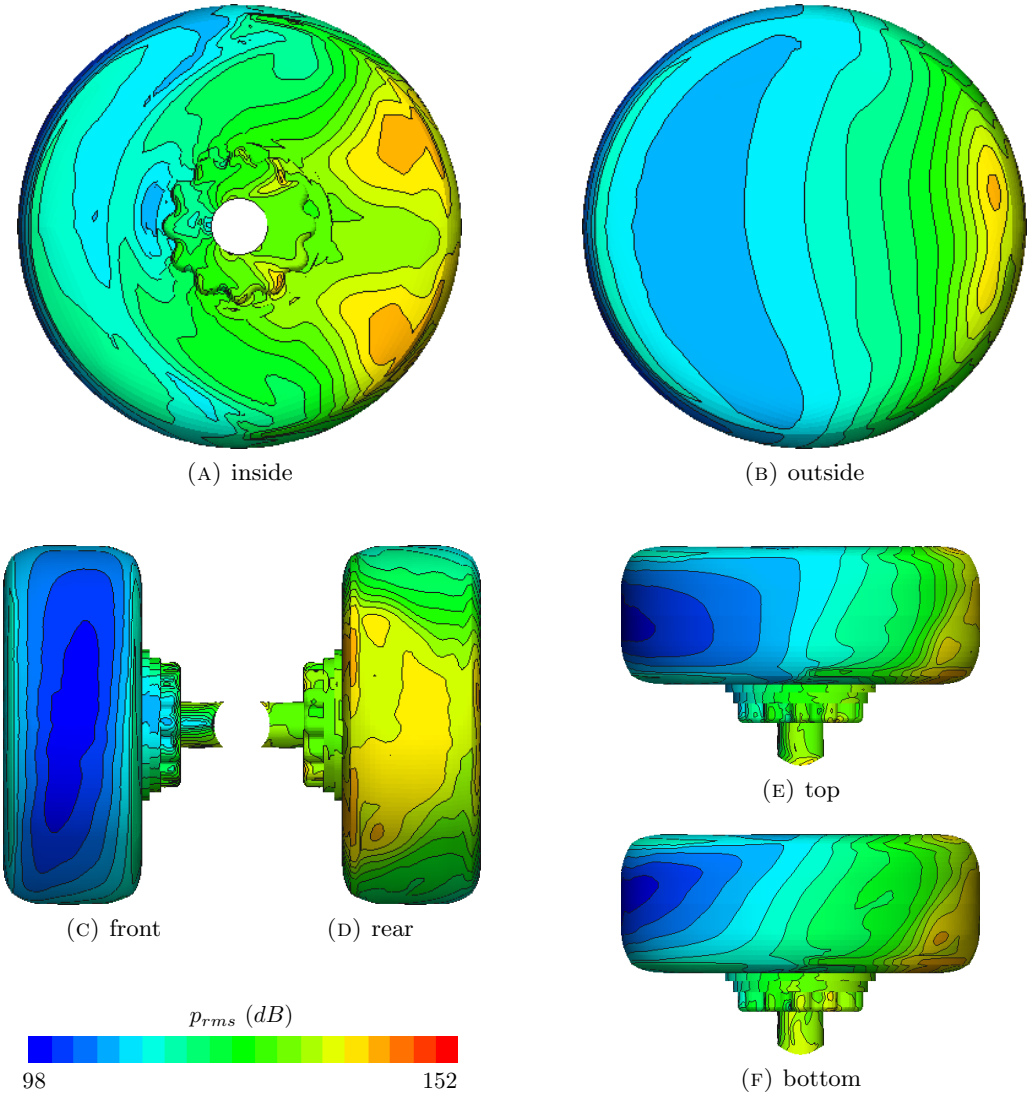

FIGURE 8.8: Unsteady surface pressure level on the forward wheel, brake and axle of the complex horizontal configuration.

surface LIC pattern in Figure 8.5 of the previous section shows large areas of upstream pointing shear stress vectors which indicate the presence of low velocity recirculating flow. The combination of these two effects leads to an increased but relatively constant unsteady pressure level on the front half of the bogie of the complex horizontal configuration (Figure 8.10). The top view of the bogie shows an increase in the unsteady pressure level just in front of the strut. This local increase is generated by the turbulent flow being deflected downwards by the yoke and impinging on the top of the bogie.

The flow over the aft half of the bogie of the complex horizontal configuration is dominated by the presence of the strong streamwise vortices. The induced velocity of these vortices pushes the turbulent flow into the side of the bogie resulting in a peak in the

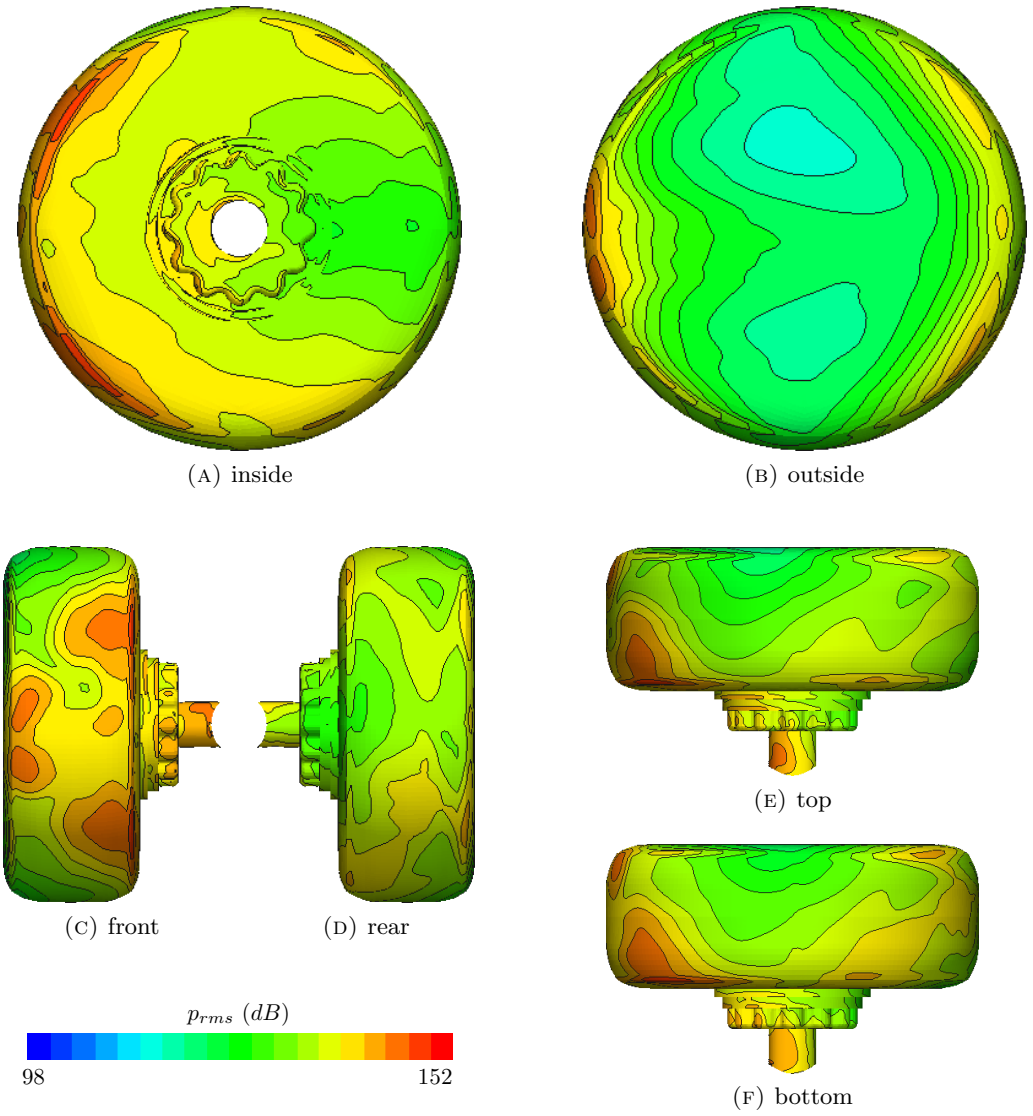

FIGURE 8.9: Unsteady surface pressure level on the rear wheel, brake and axle of the complex horizontal configuration.

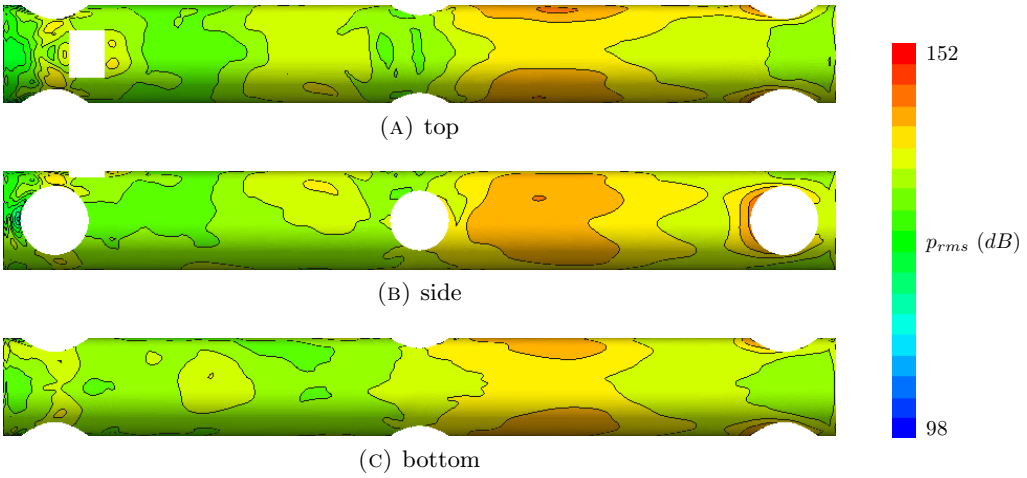

FIGURE 8.10: Unsteady surface pressure level on the bogie of the complex horizontal configuration.

unsteady pressure level (figure 8.10b). The location of the unsteady pressure peak coincides with the location of the attachment line in the surface LIC pattern (figure 8.5b). The strong vortices that generate this effect break down relatively quickly as shown by the streamwise vorticity plots in Figure 8.7. This restricts the unsteady pressure peak to the area just aft of the strut. The higher blockage of the complex geometry reduces the flow velocity near the centre of the landing gear. The lower mean velocity reduces the intensity of the pressure fluctuations which leads to lower unsteady pressure levels compared to the simplified horizontal configuration in Figure 4.11.

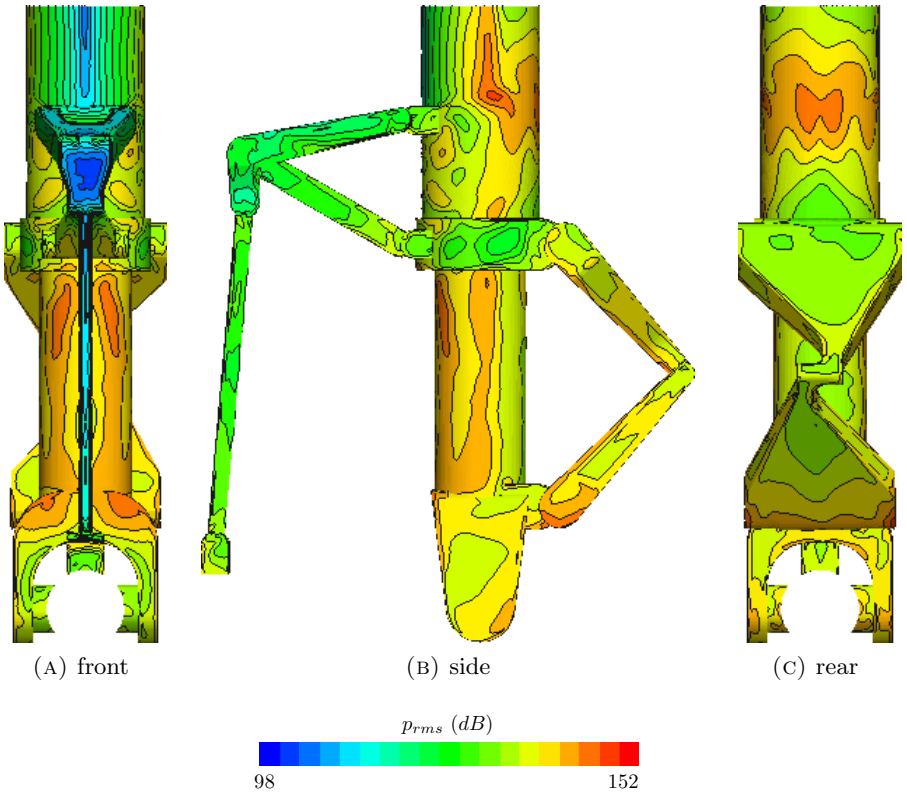

(A) front (B) side (C) rear

FIGURE 8.11: Unsteady surface pressure level on the lower half of the strut, articulation link and torque link of the complex horizontal configuration.

The addition of the articulation link, torque link and yoke to the strut has completely changed the flow field around the lower strut compared to the simplified configuration. The articulation link is far enough away from the wheels and brake units that it sits in the clean inflow which results in a low unsteady surface pressure level (Figure 8.11). However the articulation link does generate a turbulent wake which moves downstream and increases the pressure fluctuations on the other components. The front view in Figure 8.11a show peaks in the unsteady pressure level at the location of the flow attachment lines and points on the front of the strut and yoke. This shows that these peaks are generated by the turbulent flow of the articulation link impinging on the downstream

surfaces. The triangular section of the articulation link forces the flow down towards the lower strut which increases the unsteady pressure level even further.

The side view of the lower strut in Figure 8.11b shows a peak in the unsteady pressure level at the widest point of the strut where the flow reaches the highest velocity. The top of the articulation link guides the flow around the strut which increases the local flow velocity and leads to another peak in the unsteady pressure distribution. The flow separation forms two streamwise vortices as shown in the previous sections. This results in two peaks in the unsteady pressure distribution on the aft face of the strut in Figure 8.11c. The torque link is completely immersed in turbulent flow but the flow velocity in the wake is low which leads to an increased level of the unsteady pressure but no clear peaks. The highest level of unsteady pressure on the surface of the torque link is reached at the lower corners. These corners stick out from behind the strut and yoke into the higher velocity turbulent flow. The side of the yoke shows a small unsteady pressure peak at the bottom which is in line with the bogie. This peak is generated by impingement of turbulent flow due to the induced flow of the strong streamwise vortices.

8.1.3 Aerodynamic forces

The aerodynamic force coefficients of the different components of the complex horizontal landing gear configuration are shown in table 8.1 and will be discussed in this section. The strut is again responsible for the largest contribution to the drag of the landing gear due to its large frontal area just as for the simple horizontal configuration (see table 4.1). The frontal area of the strut has increased due to the larger diameter of the main cylinder and the addition of the yoke and this results in a higher drag coefficient compared to the simple configuration. This is partly compensated for by the reduced flow velocity in the wake of the articulation link which reduces the pressure coefficient and thus drag on the lower part of the strut. The wheels also generate a large amount of drag with a higher drag coefficient for the front wheels compared to the rear wheels. This is the opposite trend of what happens for the simple horizontal configuration. The mean flow velocity around the complex landing gear is lower than that of the simple landing gear. This results in a smaller area of high pressure on the front face of the rear wheel of the complex horizontal configuration compared to the simplified geometry. This leads to a reduction of the drag coefficient of the rear wheels and the reverse trend. The drag coefficient of the bogie is similar to that of the simple horizontal configuration since it mainly consists of the difference in pressure on the vertical front and rear face.

The articulation link has a small frontal area but it is completely exposed to the incoming flow which causes it to generate a relatively large amount of drag. The addition of the

horizontal	Cd ($\times 10^{-2}$)		Cs ($\times 10^{-2}$)		Cl ($\times 10^{-2}$)	
component	mean	std	mean	std	mean	std
articulation link	6.75	0.11	0.00	0.14	-2.81	0.18
bogie	4.03	0.11	0.12	0.98	1.40	1.82
front axle lhs	0.65	0.04	0.00	0.00	-0.01	0.10
front axle rhs	0.67	0.05	0.00	0.00	-0.03	0.10
front brake lhs	3.19	0.17	2.13	0.51	-0.08	0.21
front brake rhs	3.23	0.20	-2.20	0.55	-0.10	0.22
front wheel lhs	21.15	1.13	-23.35	1.92	-0.37	0.84
front wheel rhs	20.41	1.23	22.96	2.46	0.00	1.03
rear axle lhs	0.25	0.16	0.00	0.00	0.05	0.44
rear axle rhs	0.24	0.13	0.00	0.00	0.05	0.37
rear brake lhs	0.26	0.34	4.99	0.44	-0.21	0.50
rear brake rhs	0.26	0.31	-5.01	0.52	-0.29	0.41
rear wheel lhs	17.07	1.79	-5.50	3.22	0.58	1.90
rear wheel rhs	16.15	1.88	5.66	2.79	0.34	2.30
strut	45.60	1.45	-0.01	3.85	0.69	0.72
torque link	9.86	1.03	-0.24	1.01	2.69	1.01
MLG	149.76	3.58	-0.45	6.18	1.90	4.68

TABLE 8.1: Mean and std of the aerodynamic force coefficients of the complex horizontal configuration.

brake units has reduced the length of the axles and this reduces the drag coefficient compared to the simple configuration. The rear axles sit in the low velocity wake of the upstream components which results in a much lower drag coefficient than the front axles. The front brakes generate a significant amount of drag due to the stagnation pressure on the front face of the brake unit. The rear brakes however are in the low velocity wake of the forward components and therefore create only a small amount of drag. Most of the torque link is sheltered from the incoming flow but it still generates a significant amount of drag. The main contributor to this high drag coefficient is the area of low pressure on the aft surface of the torque link. The addition of components has increased the blockage of the complex landing gear which leads to a higher drag coefficient compared to the simple horizontal configuration.

The drag coefficient of a bluff body is in general relatively high and the fluctuations are therefore small compared to the mean values. The standard deviation of the drag coefficient of the components of the complex landing gear have a similar value as the equivalent components of the simple horizontal configuration. The fluctuations in the drag coefficient of the downstream components is significantly higher than their upstream counterparts due to the difference in the level of unsteadiness in the flow: undisturbed freestream versus turbulent wake.

A large number of components of the complex landing gear are symmetric which leads to low mean side force coefficients similar to what happens for the simple configuration.

The sideforce generated by the axles consists purely of the contribution of the shear stresses which for a bluff body are much smaller than the forces generated by pressure differences. The only components with a significant mean sideforce coefficient are the front and rear brakes and wheels. The side force generated by the front wheel points outwards just as for the simple configuration. This is due to the pressure difference between the area of low pressure on the outside surface of the wheel and the increased pressure in front of the brake unit on the inside surface of the wheel. The flow accelerates around the front brake unit which creates suction peaks at the top and bottom. The suction peaks result in a small inward pointing side force for the front brakes.

The freestream velocity flow over the outside surface of the rear wheel creates a lower pressure coefficient than the low velocity wake over the inside surface of the rear wheel. This pressure difference generates a relatively small outward pointing side force coefficient for the rear wheels. The side force coefficient of the rear brakes is more than double that of the front brakes. The low mean flow velocity in the wake reduces the pressure coefficient at the front of the brake unit. The flow still accelerates around the edges creating an area of low pressure. This results in a larger pressure difference and thus a larger sideforce coefficient than the front brakes. The geometry of the complex landing gear is almost symmetric and the contribution of the right and left hand side components cancel out against each other. The mean side force coefficient of the complete landing gear is therefor low.

The fluctuations in the side force coefficient of the components of the complex horizontal configuration are of a similar level as those of the simple horizontal configuration except for the strut. The flow around the strut has changed significantly due to the addition of the articulation link, torque link and yoke. The change in diameter of the main strut and the additional components disturb the flow which remove the regular vortex shedding. The mean flow velocity near the centre of the landing gear is reduced compared to the simple configuration which lowers the intensity of the pressure fluctuations on the side of the strut. The combination of these two effects leads to a reduction of the standard deviation of the side force coefficient of the strut of the complex geometry compared to the simple configuration.

The mean lift coefficient on the different landing gear components is in general small compared to drag and side force coefficients. The top of the articulation link is inclined to the freestream direction and acts as a ramp for the flow which causes it to generate a downforce. The area of low pressure on the top triangular surface of the torque link does not only create drag but also generates a lift force. The pressure coefficient on the surface of the bogie is relatively constant however there is an area of low pressure just aft of the junction with the articulation link. This results in a lift coefficient which is

a little higher than for the simple horizontal configuration. The addition of the yoke and other details to the strut has resulted in some surfaces with a normal vector in the vertical direction and this leads to a small lift force.

The standard deviation of the lift coefficient shows the same trend as the drag and side force coefficients: the downstream components experience significantly higher fluctuations than the upstream components due to fact they are in the turbulent wake of the upstream components. The coefficients have been normalised with a constant area and this means that large components such as the bogie and wheels also show large fluctuations in the lift coefficient. The only other component that stands out is the torque link which shows a relatively high standard deviation of the lift coefficient due to its location in the unsteady wake of the lower strut.

8.2 Toe up configuration

The aerodynamic results of the simple landing gear configurations show a clear relation between the bogie inclination angle and the location and type of flow separation on the front wheels. This leads to the formation of strong streamwise vortices which have a large influence on the flow around the downstream components. The flow field around the complex horizontal configuration in the previous section shows the same streamwise vortices as the simple horizontal configuration. The additional components have not changed the major flow features around the horizontal landing gear configuration. This section describes the aerodynamic results of the complex toe up configuration and will show if this trend continues.

8.2.1 Flow features

The surface flow features on the front wheel of the toe up configuration (Figure 8.12) are almost identical to those of the horizontal complex configuration (Figure 8.3) and show significant differences with the surface features on the front wheel of the simple toe up configuration (Figure 4.13). The addition of the brake unit leads to a more diverging flow on the inside surface of the front wheel (Figure 8.12a) such that this flow reaches the edge of the wheel further upstream than for the simple toe up configuration (Figure 4.13a). This means that the formation of the streamwise vortices starts further upstream before the flow experiences the adverse pressure gradient at the top and bottom of the wheel. The induced flow generated by the streamwise vortex pair at the top of the wheel (Figure 8.12e) avoids the sudden flow separation that is visible on the top of the front wheel of the simple toe up configuration (Figure 4.13e). The addition of the brake unit

has changed the flow behaviour around the front wheel compared to the simple toe up configuration. Instead the flow features are similar to those of the flow around the front wheel of the complex horizontal configuration.

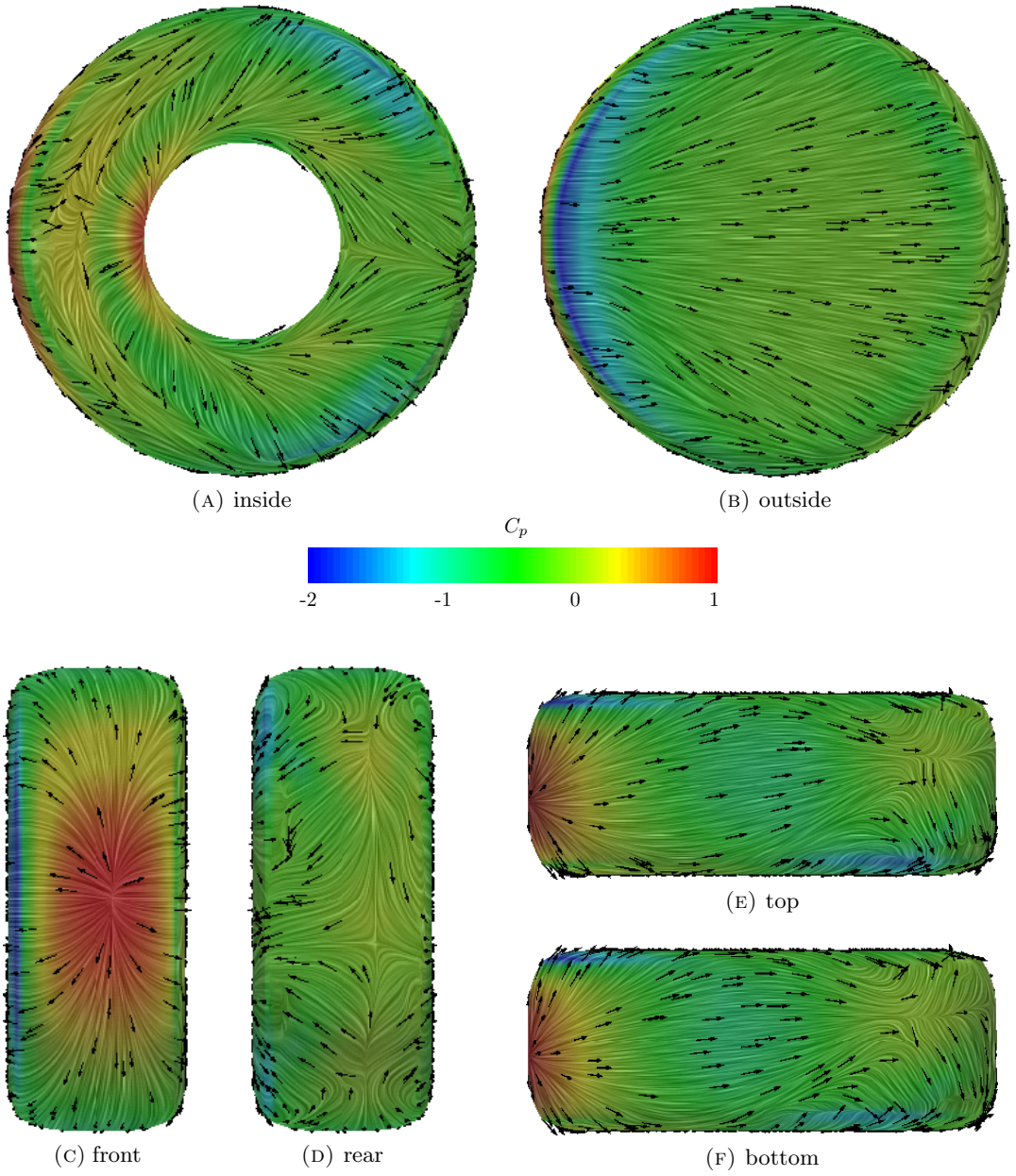

FIGURE 8.12: Surface flow features of the time averaged flow field on the forward wheel of the complex toe up configuration.

The surface LIC pattern on the front wheel of the complex toe up configuration shows the formation of four streamwise vortices per wheel, a strong vortex pair on the inside edge of the wheel and a weaker vortex pair at the outside edge of the front wheel. The main difference with the complex horizontal configuration is visible in the surface LIC pattern on the rear face of the front wheel in Figure 8.12d. The vortex pairs at the top and bottom of the front wheel generate an induced flow towards the centre of the

wheel. These induced flows meet below the middle of the wheel while this happens at the middle of the wheel for the horizontal complex configuration (Figure 8.12d). This means that for the complex toe up configuration the vortices at the top of the front wheel are stronger than the ones at the bottom.

The surface LIC pattern and pressure distribution on the rear wheel of the complex toe up configuration in Figure 8.13 shows a lot of similarities to that of the simple configuration in Figure 4.14. The area of high pressure on the front of the rear wheel (Figure 8.13c) shows two attachment points next to each other compared to a single attachment point on the front face of the rear wheel of the simple configuration (Figure 4.14c). The pressure coefficient on the front of the rear wheel is lower than for the simple configuration due to the reduced flow velocity around the complex landing gear configuration. The shape of the area of high pressure is similar to that of the simple toe up configuration but it has moved down the rear wheel. This seems to be related to the stronger downward induced flow generated by the streamwise vortices coming of the top of the front wheel. The surface LIC pattern shows a major flow attachment line close to the outside edge of the wheel which indicates that most of the flow that reaches the rear wheel is push up and towards the centre of the landing gear. The same flow behaviour is also seen for the simple toe up configuration but the effect is more pronounced for the complex configuration. The upward direction of the flow over the top half of the rear wheel is also clearly visible in the surface LIC pattern on the inside of the rear wheel (Figure 8.13a). The pressure increase at the front of the brake unit has shifted down just like the area of high pressure on the front of the wheel.

The front and inside surface of the rear wheel of the complex toe up configuration show some differences compared to the simple toe up configuration but the surface LIC pattern on the outside, top, bottom and rear face are nearly identical. The flat outside surface of the rear wheel in Figure 8.13f shows a smooth surface LIC pattern similar to the previous configurations. The flow follows the outside surface of the wheel until it reaches the downstream edge where it separates. The toe up configuration moves the bottom of the rear wheel into the clean flow and this leads to mean shear stress vectors which are parallel to the free stream direction. The complex surface LIC pattern on the aft face of the rear wheel in Figure 8.13d is characteristic of the separated flow in the wake.

Figure 8.14 shows the mean pressure coefficient and surface LIC pattern on the bogie of the complex toe up configuration which shows some similarities to that of the simple toe up configuration in Figure 4.15. The mean pressure coefficient on the surface of the bogie of the complex configuration is almost constant. This indicates that the mean flow velocity is relatively constant due to the increased mixing in the turbulent flow

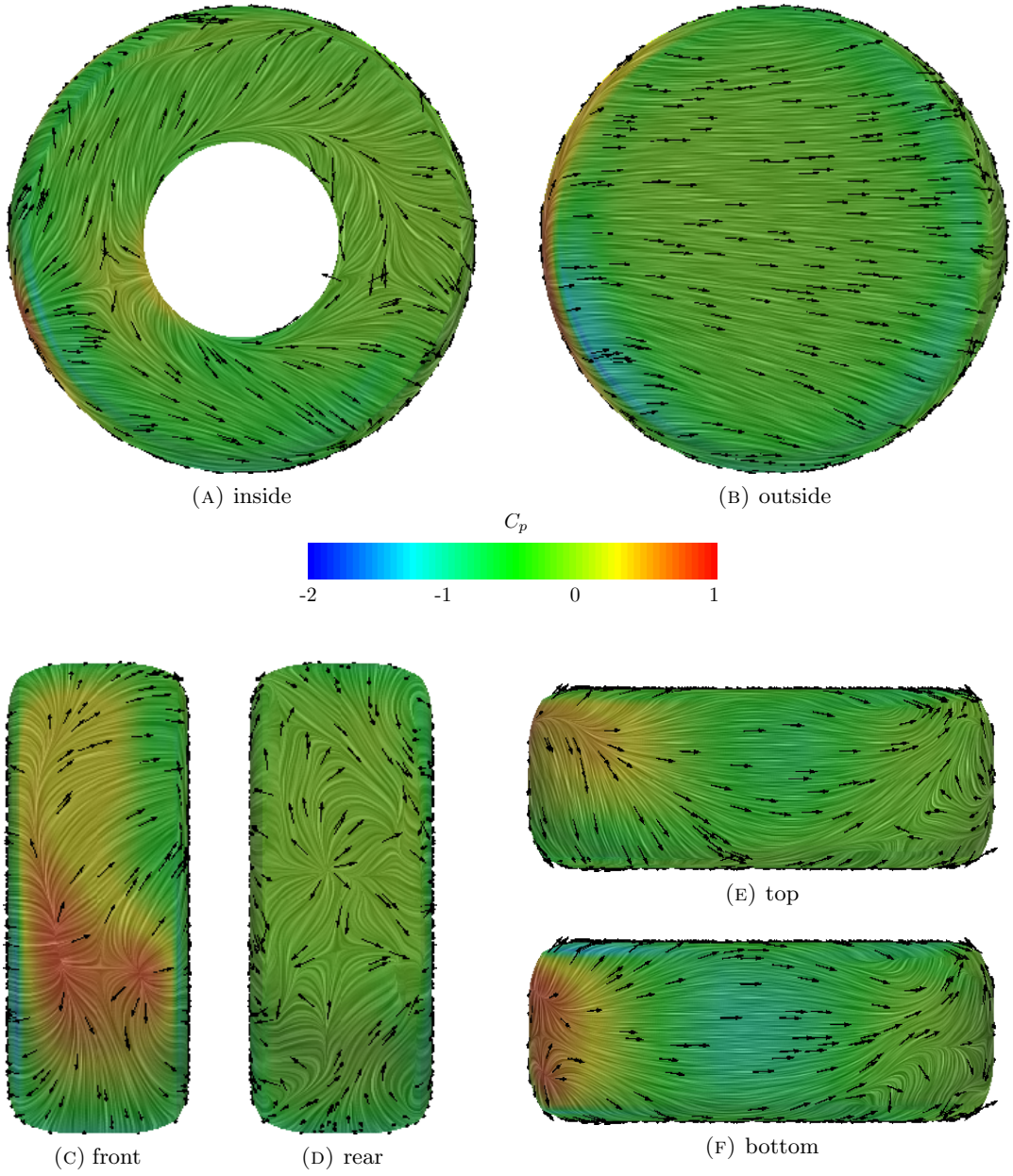

(A) inside (B) outside

(C) front (D) rear (E) top (F) bottom

FIGURE 8.13: Surface flow features of the time averaged flow field on the rear wheel of the complex toe up configuration.

near the centre of the complex landing gear. The bottom surface of the bogie faces the incoming flow resulting in attached flow along the complete surface as shown by the smooth surface LIC pattern in Figure 8.14c.

The side and top view of the bogie in Figures 8.14a and 8.14b show a complex surface LIC pattern. There is a large area of upstream pointing shear stress vectors on the front half of the bogie due to the presence of a flow recirculation zone. This zone is created by the flow separating from the sharp bogie edge and the wake from the articulation link and front axles. A flow attachment point is visible just aft of the yoke where the flow

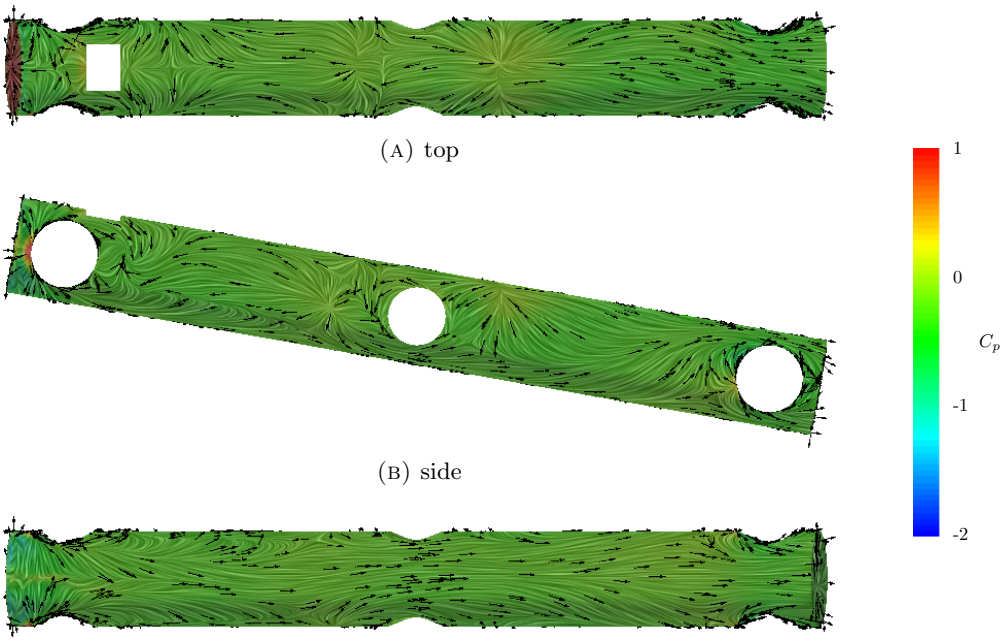

(A) top

(B) side

(C) bottom

FIGURE 8.14: Surface flow features of the time averaged flow field on the bogie of the complex toe up configuration.

gets pushed down into the top surface of the bogie by the induced flow of the streamwise vortices. The influence of these vortices becomes less further downstream as can be seen by the surface LIC pattern in the side view (Figure 8.14b). A large part of the flow at the lower half of the bogie turns upwards and moves over the top of the rear axle just as in the simple toe up configuration (Figure 4.15b).

The additional components have changed the geometry of the lower strut completely such that a comparison of the flow features with the simple configuration becomes pointless. Instead the surface flow features of the strut of the toe up configuration (Figure 8.15) are compared with those on the surface of the strut of the complex horizontal configuration (Figure 8.6). The toe up configuration changes the flow features near the centre of the landing gear but does not have any influence further up the strut as shown by the identical pressure distribution and surface LIC patterns in the top half of those two figures. The front face of the strut of the toe up configuration (Figure 8.15a) shows almost no pressure increase at the yoke and lower part of the strut due to the low flow velocity in the flow recirculation zone. This agrees with the upstream pointing shear stress vectors and constant mean pressure coefficient on the top of the bogie (Figure 8.14a).

The side view of the strut in Figure 8.15b shows a flow attachment point and area of increased pressure on the side of the yoke and lower part of the torque link. This is caused by the induced flow of the streamwise vortices coming of the front wheel. The

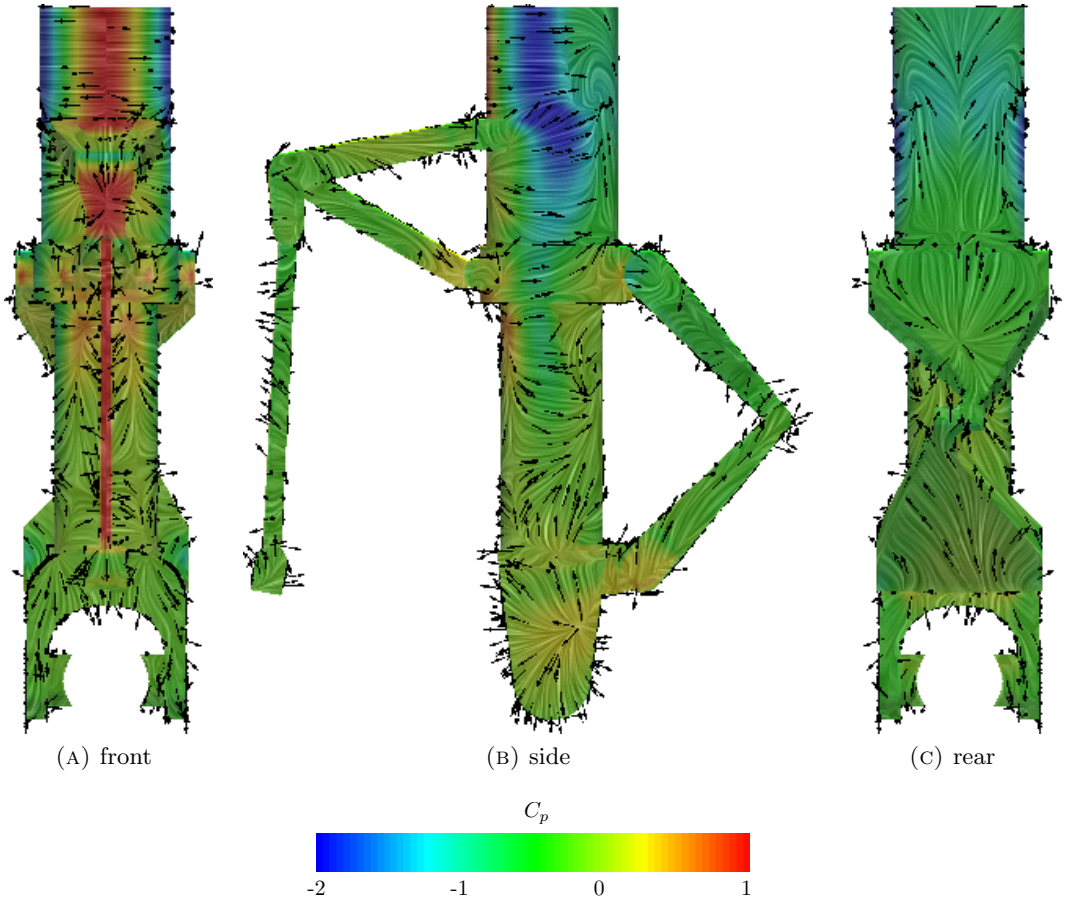

(A) front (B) side (C) rear

FIGURE 8.15: Surface flow features of the time averaged flow field on the lower half of the strut of the complex toe up configuration.

attachment point has moved further up the side of the yoke compared to the horizontal complex configuration (Figure 8.6b) due to the different trajectory of the streamwise vortices. The streamwise vortices follow the upward direction of the mean flow. The surface LIC pattern on the aft face of the strut (Figure 8.15c) is identical to that of the horizontal configuration (Figure 8.6c) and shows the formation of a vortex pair downstream of the top of the articulation link.

The flow features at the front part of the complex toe up configuration show a strong similarity to those of the complex horizontal configuration. The flow features at the aft part of the complex toe up configuration however look more like those of the simplified toe up configuration. This behaviour is confirmed by the streamwise vorticity plots of the time averaged flow in Figure 8.16. The first two vorticity plots (Figures 8.16a and 8.16b) look similar to the vorticity plots of the horizontal complex configuration (Figures 8.7a and 8.7b). The last vorticity plot (Figure 8.16c) however shows more similarities to the vorticity plot of the simple toe up configuration (Figure 4.17c).

The streamwise vorticity plot at a plane through the aft part of the front wheels (Figure

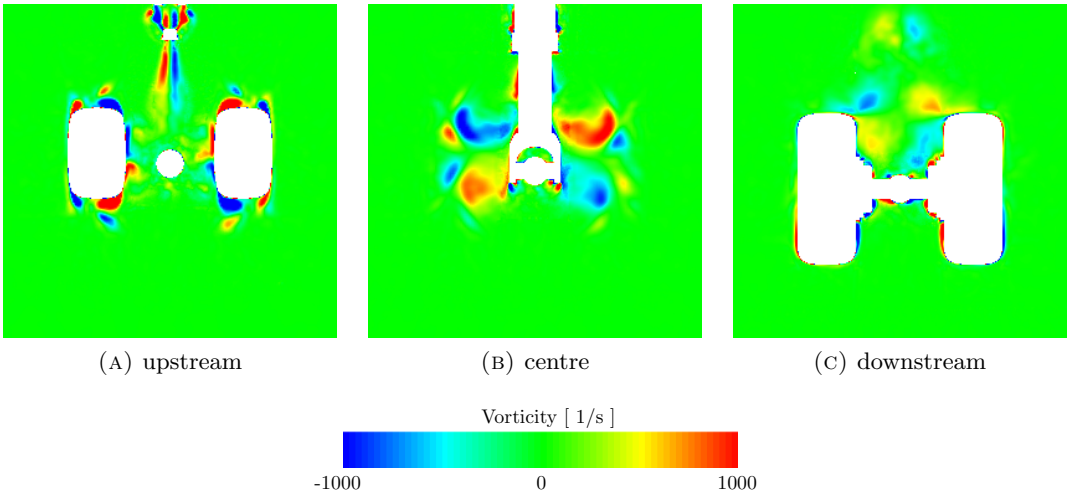

(A) upstream (B) centre (C) downstream

FIGURE 8.16: Streamwise vorticity of the time averaged flow field around the complex toe up configuration, upstream = aft part of the front wheels, centre = centre of the MLG, downstream = centre of the rear wheels.

8.16a) shows four main vortices at each wheel and two smaller vortex cores generated by the horse shoe vortex of the brake unit. The top centre of the figure shows the vorticity generated by the wake of the articulation link which starts to interact with the triangular structure that connects the articulation link to the main strut. The complex horizontal configuration in Figure 8.7a shows a similar patch of streamwise vorticity in that area but it has increased in strength for the complex toe up configuration.

Figure 8.16b shows the streamwise vorticity of the time averaged flow at a plane through the middle of the landing gear. The main vortices are still present but have moved together and up following the local flow direction. The four strong streamwise vortices move downstream and up with the local flow and pass over the top of the rear axle (see Figure 8.16c). The strength of the vortices in the last plot has reduced and this can be attributed to the interaction of the vortices with the turbulent wake downstream of the lower strut, yoke and torque link. The four streamwise vortices close to the top of the rear wheels (Figure 8.16c) look similar to the vortices of the simple toe up configuration (Figure 4.17c). However these vortices originate from a different location: the inside of the front wheels for the complex toe up configuration versus the bottom of the front wheels for the simple toe up configuration. The two vortex cores that are visible at the top of the last plot are the same as for the horizontal complex configuration in Figure 8.7c. These vortices are generated by the flow separation downstream of the articulation link to strut junction.

8.2.2 Unsteady surface pressure distribution

The features of the time averaged flow around the front wheel, brake unit and axle of the complex toe up configuration are similar to those of the complex horizontal configuration. The same is true for the unsteady surface pressure distribution as can be seen by comparing Figures 8.17 and 8.8. The general shape of the contours are similar and the level and location of the peaks are the same for the front wheels of the two different complex configurations. The only differences are the slightly lower unsteady pressure level on the front and the outside surface of the front wheel of the toe up configuration compared to the horizontal configuration.

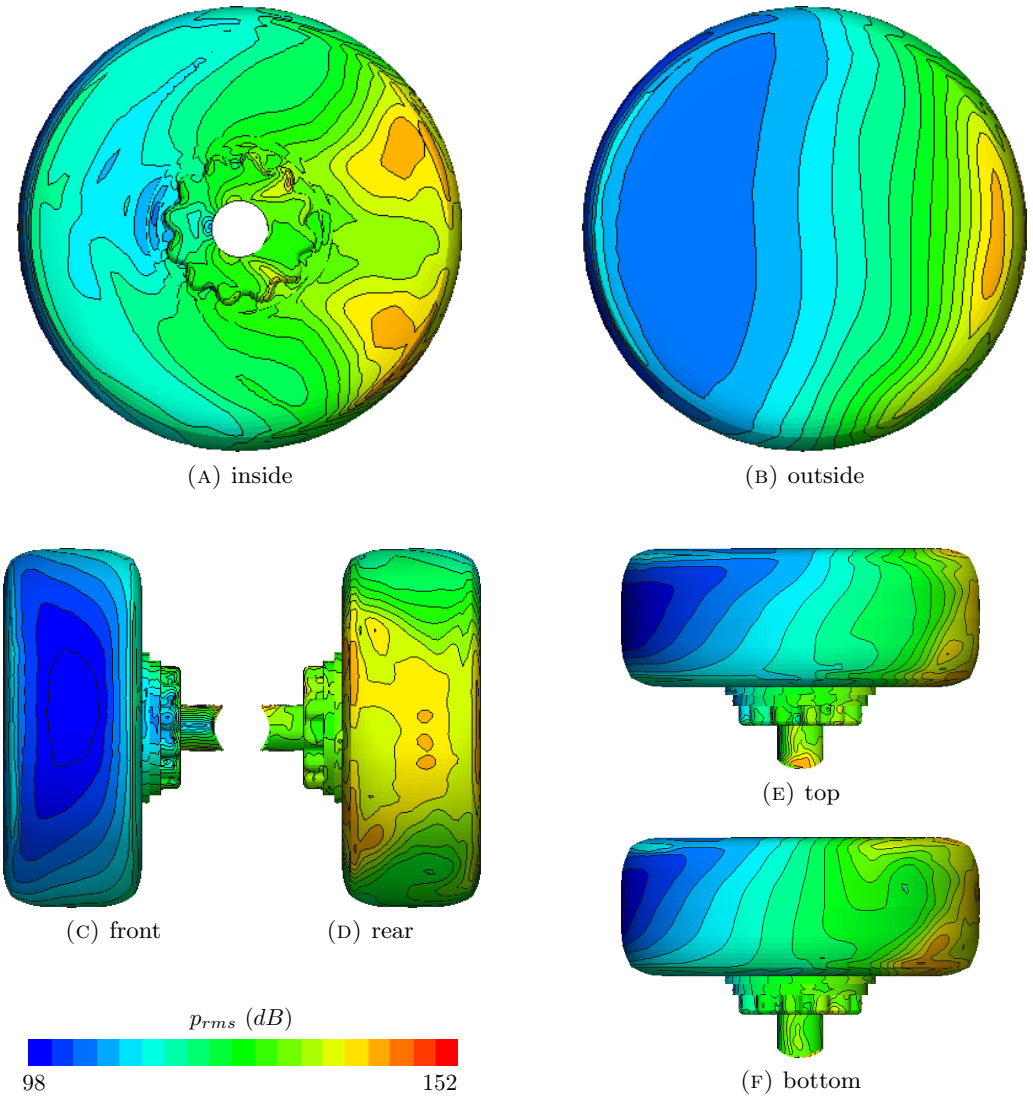

FIGURE 8.17: Unsteady surface pressure level on the forward wheel, brake and axle of the complex toe up configuration.

The unsteady pressure distribution is nearly identical for the front wheels and brake units of the complex horizontal and toe up configurations but the unsteady pressure

levels on the front axles do show some differences. The top view of the front axle in the toe up configuration (Figure 8.17e) shows a peak in the unsteady pressure level at the end of the axle where it joins the bogie. This peak is not present on the top of the front axle of the complex horizontal configuration in Figure 8.8e. The turbulent flow that comes of the sharp bogie edge and passes through the space in between the axle and the lower part of the articulation link is expected to be responsible for the peak.

The time averaged surface flow features on the rear wheel of the complex toe up configuration show some similarities with those of the simple toe up configuration but the important streamwise vortices originate from a different part of the front wheel. This is reflected in the unsteady pressure distribution on the rear wheel of the complex toe up configuration (Figure 8.18) which has peaks in different locations than the rear wheel of the simple toe up configuration (Figure 4.19). The streamwise vortices of the complex toe up configuration come from the inside edge of the front wheels and move to the centre of the landing gear before they start their upward trajectory over the top of the rear axles as shown in the vorticity plots (Figure 8.16) of the previous section. This delay in the upward motion of the vortices compared to the simple toe up configuration (Figure 4.17) changes the location of the interaction of the turbulent flow with the surface of the rear wheel. This is confirmed by the unsteady pressure peaks on the front face of the rear wheel in Figure 8.18c which have moved down compared to the simple toe up configuration (Figure 4.19c). The unsteady pressure peaks are not at the exact location of the attachment points shown in Figure 8.13c where the flow impinges on the surface but further downstream. The flow velocity at the attachment point is low which reduces the level of the pressure fluctuations. The flow velocity downstream of the attachment points increase which leads to stronger pressure fluctuations.

The surface LIC pattern on the inside of the rear wheel in Figure 8.13a shows how the flow that reaches the rear wheel moves around the inside edge of the wheel and towards the rear brake unit and axle. The turbulent fluctuations transported by the mean flow results in high unsteady pressure levels on the front of the brake unit and rear axle as can be seen in Figure 8.18a. Downstream of the brake unit and axle the unsteady pressure level is low due to the reduced flow velocity in the wake. The outside surface of the rear wheel (Figure 8.18b) shows a low level of the unsteady pressure except for the aft edge where flow separation leads to an increase of the unsteady surface pressure level.

The top view of the bogie in Figure 8.19a shows a low unsteady pressure level on the front half of the bogie except for two small areas at the junction of the bogie with the front axles. The flow velocity in the recirculation zone between the articulation link and strut is low which results in a low unsteady pressure level. The peak at the axle to bogie

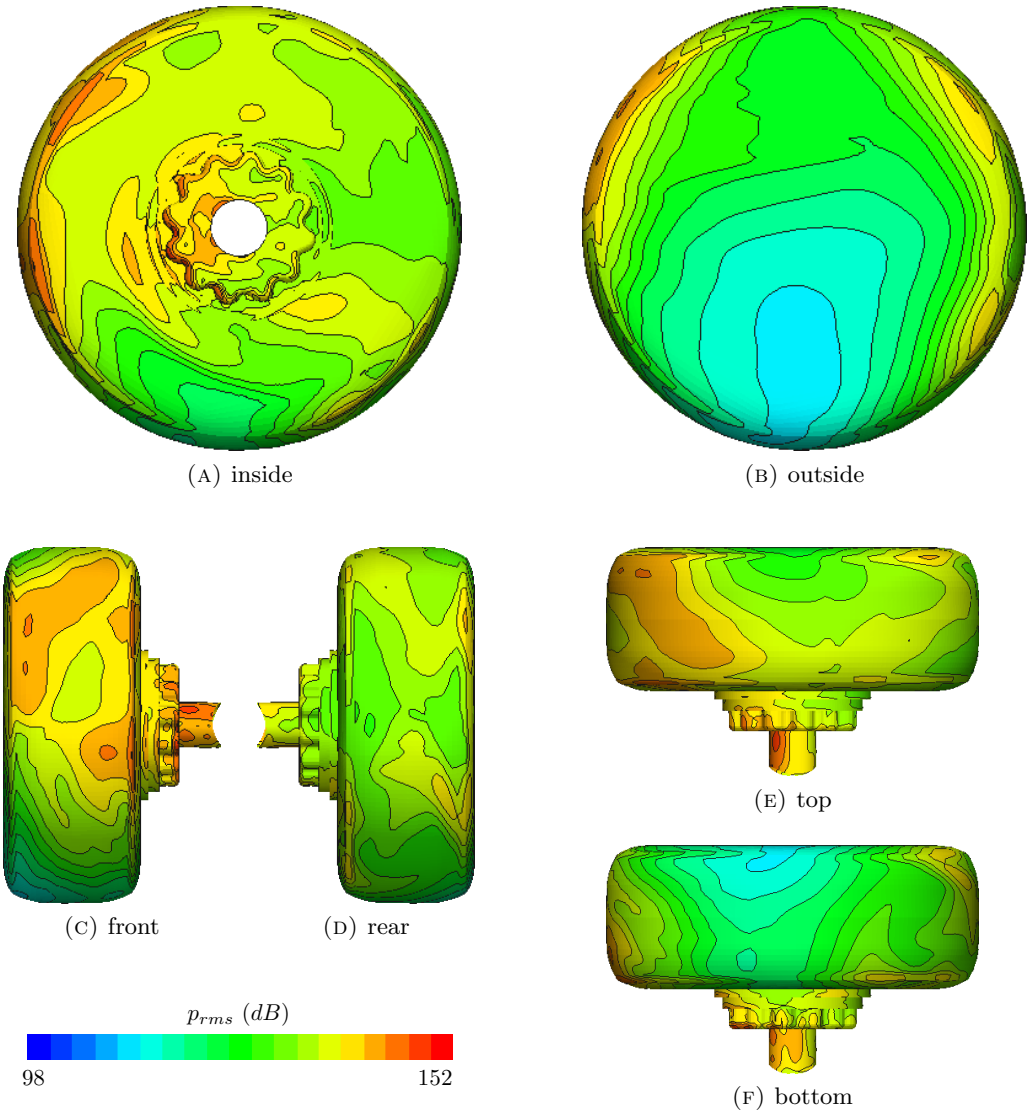

FIGURE 8.18: Unsteady surface pressure level on the rear wheel, brake and axle of the complex toe up configuration.

junction is the same peak that is visible on the top of the front axle in Figure 8.17e. This is generated by the separated turbulent flow from the sharp edge of the bogie which accelerate around the axle and lower part of the articulation link. A large peak in the unsteady pressure level is present on the top of the bogie just aft of the strut which is the same location as the flow attachment point in Figure 8.14a. The streamwise vortices coming of the front wheels pass over the top of the bogie at this point. The induced flow of the vortices pushes the turbulent flow down towards the surface of the bogie and this impinging turbulent flow creates a peak in the unsteady surface pressure level.

The previous section does not show any specific flow features on the bottom surface of the bogie but the unsteady pressure distribution (Figure 8.19c) does show two peaks. A comparison of the location of the peaks with the surface LIC pattern in Figure 8.14c

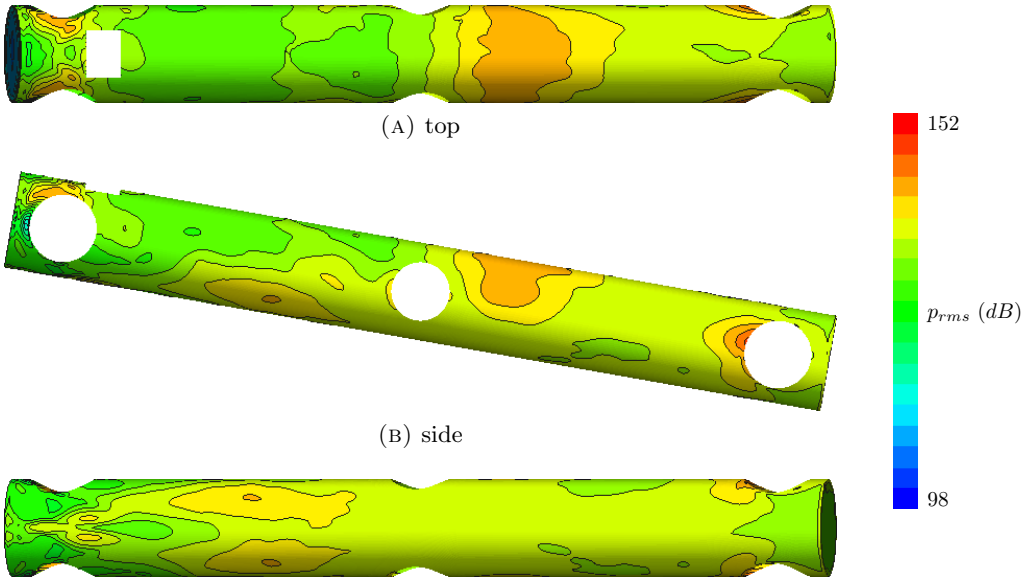

(A) top

(B) side

(C) bottom

FIGURE 8.19: Unsteady surface pressure level on the bogie of the complex toe up configuration.

shows that the peaks in the unsteady pressure are generated by the interaction between the attached flow at the bottom of the bogie and the recirculation zones downstream of the front axles. The unsteady pressure level on the bottom surface of the bogie downstream of the two peaks continues to be relatively high compared to the unsteady pressure levels of the simple toe up configuration in Figure 4.20c. This is due to the different trajectory of the strong streamwise vortices which stay below the level of the bogie for much longer before they move over the top of the rear axles as shown in Figure 8.16.

The toe up configuration of the bogie results in a change in the flow features around the lower part of the strut and yoke compared to the complex horizontal configuration. The same is true for the unsteady pressure distribution as can be seen by comparing Figures 8.20 and 8.11. The lower flow velocity in the recirculation zone at the top of the bogie reduces the unsteady pressure level on the front face of the yoke and bottom of the strut (Figure 8.20a) compared to the horizontal configuration (Figure 8.11a).

The side view of the strut in Figure 8.20b shows an increase of the unsteady pressure level on the side of the yoke and lower part of the torque link compared to the horizontal configuration. The location of this increase coincides with the flow attachment point shown in the time averaged surface flow features (Figure 8.15b). The induced flow of the streamwise vortices pushes turbulent flow to the centre of the landing gear which causes the increase in the unsteady surface pressure level. This area extends onto the aft face of the yoke and torque link in Figure 8.20c and also to the top of the bogie in Figure 8.19a. The toe up configuration of the bogie changes the trajectory of the

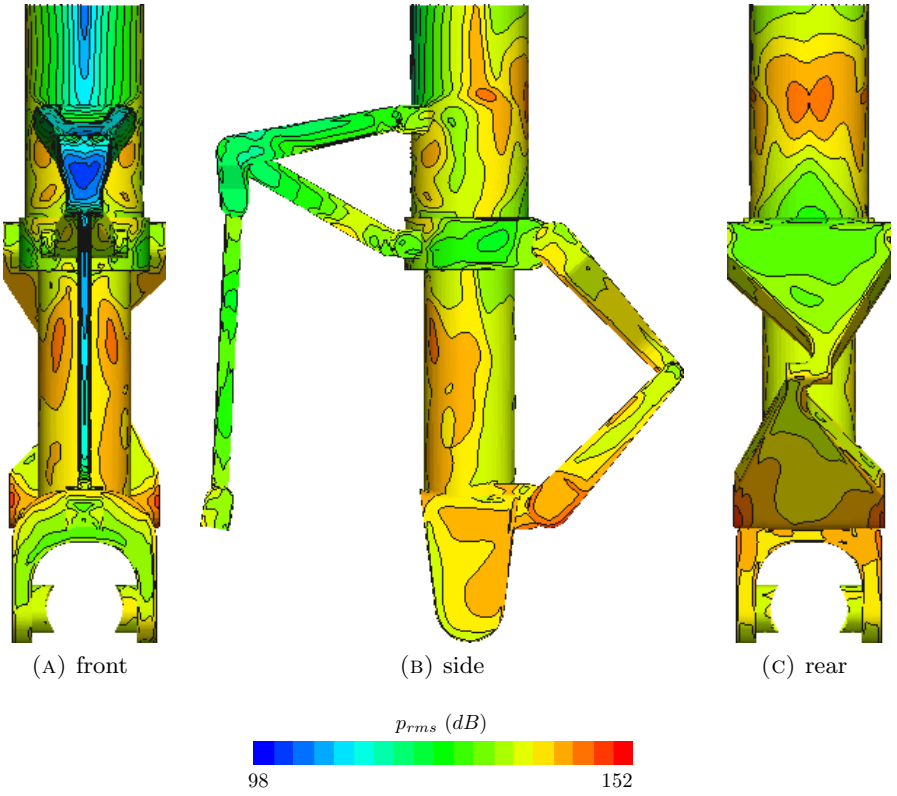

(A) front (B) side (C) rear

FIGURE 8.20: Unsteady surface pressure level on the lower half of the strut, articulation link and torque link of the complex toe up configuration.

streamwise vortices compared to the horizontal configuration which shifts the location of the turbulent flow impingement from the side of the bogie to the side of the yoke and bottom of the torque link instead. The flow field higher up the strut is similar to that of the complex horizontal configuration and the unsteady pressure distribution again shows two peaks downstream of the top of the articulation link where the flow separation results in the formation of a streamwise vortex pair as shown in Figure 8.16c.

8.2.3 Aerodynamic forces

Table 8.2 shows the aerodynamic force coefficients of the components of the complex toe up configuration. The drag coefficient of most components is comparable to that of the complex horizontal configuration in table 8.1. The strut remains the main source of drag since it has the largest frontal area but its drag coefficient has reduced due to the lower flow velocity near the bottom of the strut. The lower flow velocity at the bottom of the strut also leads to a significant reduction of the drag coefficient of the torque link compared to the horizontal configuration. The components that see the largest change in the drag coefficient compared to the horizontal configuration are the rear brakes. Their drag quadruples due to the fact that they are more exposed to the incoming flow

in the toe up configuration. The drag coefficient of the articulation link has dropped compared to the horizontal configuration. This reduction is partly caused by a change in the flow field but mainly due to the reduction in the length of the vertical square section. The toe up configuration increases the frontal area of the bogie but this does not lead to an increase of the drag coefficient compared to the horizontal configuration. This is due to the almost constant mean pressure coefficient on the surface of the bogie as shown in the flow features section. The frontal area of the complete landing gear in toe up configuration has increased as well compared to the horizontal configuration but the total drag coefficient shows a decrease. The two main components responsible for this reduction are the strut and torque link which are more sheltered from the incoming flow in the toe up configuration.

toe up	Cd ($\times 10^{-2}$)		Cs ($\times 10^{-2}$)		Cl ($\times 10^{-2}$)	
component	mean	std	mean	std	mean	std
articulation link	6.10	0.16	0.02	0.19	-2.56	0.25
bogie	4.09	0.22	-0.39	1.17	-0.95	1.15
front axle lhs	0.70	0.06	0.00	0.00	0.02	0.08
front axle rhs	0.71	0.05	0.00	0.00	0.03	0.09
front brake lhs	3.48	0.17	2.92	0.49	-0.24	0.18
front brake rhs	3.48	0.15	-2.97	0.46	-0.20	0.18
front wheel lhs	21.00	1.04	-22.23	3.05	2.72	1.83
front wheel rhs	19.97	0.99	20.90	2.19	0.89	1.38
rear axle lhs	0.27	0.17	0.00	0.00	0.19	0.31
rear axle rhs	0.35	0.18	0.00	0.00	0.10	0.38
rear brake lhs	0.95	0.33	6.05	0.62	0.07	0.46
rear brake rhs	1.05	0.35	-5.54	0.70	-0.12	0.56
rear wheel lhs	16.97	1.52	-8.61	2.80	-8.19	1.37
rear wheel rhs	15.05	1.18	11.19	3.14	-6.50	1.57
strut	42.61	1.59	0.08	3.51	-0.23	0.94
torque link	6.80	1.24	-0.32	0.87	4.48	1.08
MLG	143.12	2.73	1.11	5.70	-10.49	4.42

TABLE 8.2: Mean and std of the aerodynamic force coefficients of the complex toe up configuration.

The standard deviation of the drag coefficients of the components of the toe up configuration are similar to those of the horizontal configuration. The exception is the bogie whose value has doubled. The standard deviation of the drag of the horizontal bogie consists primarily of the pressure fluctuations on the front and aft face. The toe up rotation of the bogie means that the pressure fluctuations along the whole surface contribute to the fluctuations in the drag coefficient which explains the strong increase.

The mean side force coefficient of the components of the toe up configuration follow the same trend as for the horizontal configuration: the side force is small for the symmetric components and the only significant contribution comes from the wheels and brakes.

The mean flow features around the front wheel and front brake of two configurations are similar and this is reflected in the side force coefficients. The outward pointing side force of the rear wheels has almost doubled compared to the horizontal configuration. This is caused by the higher flow velocity around the bottom of the rear wheel which creates an area of low pressure on the outside surface of the wheel. The rear brakes are more exposed to the flow in the toe up configuration and this leads to an increase in the side force compared to the horizontal configuration. The standard deviation of the side force coefficients is similar to that of the horizontal configuration and only the values of the bogie and front wheels have increased a little.

The lift coefficient of the components of the toe up configuration in Table 8.2 show some considerable differences compared to the horizontal configuration in Table 8.1. The rear wheels generate a significant amount of downforce which does not happen for the complex horizontal configuration or for the simple toe up configuration (Table 4.2). An explanation can be found in the time averaged flow features on the rear wheel in Figure 8.13. The bottom of the wheel sits in the undisturbed freestream flow which results in a low pressure coefficient. The top of the wheel sits in the low velocity wake of the forward components which results in an increase of the pressure coefficient. This pressure difference between the top and bottom of the rear wheel is responsible for the downforce generation.

The pressure coefficient on the lower surface of the torque link has increased which means it creates more lift compared to the horizontal configuration. The changes in the lift coefficient of the other components are relatively small compared to the complex horizontal configuration. The large downforce of the rear wheels dominate the contribution of the other components which results in a downforce for the complete complex main landing gear in toe up configuration. The simple toe up configuration creates a similar amount of downforce as shown in table 4.2 but in that case the flow separation on the front wheels is responsible for the downforce generation. The unsteadiness of the lift coefficient of most components is similar to the values of the horizontal configuration with the exception of the front and rear wheels. The toe up rotation of the bogie has increased the standard deviation of the lift coefficient of the front wheels while that of the rear wheels has decreased compared to the horizontal configuration.

8.3 Toe down configuration

The previous section has shown that the addition of the brake unit to the front wheel leads to a change in the major flow features around the complex landing gear in the toe up configuration. The trend that has been found for the flow field around the

three simple landing gear configurations does not hold for the complex landing gear configurations. This section will describe the aerodynamic results of the complex toe down configuration and compare them with the results of both the simple toe down and the other two complex simulations.

8.3.1 Flow features

The time averaged flow features around the different landing gear configurations have been dominated by the formation of streamwise vortex pairs at the downstream edges of the front wheel. This is again the case for the complex toe down configuration but the pattern is different from the previous configurations as can be seen in Figure 8.21. The surface LIC pattern and pressure distribution as shown in the front and side views (Figures 8.21c, 8.21a and 8.21b) look similar to the front wheel of the other two complex configurations but there are clear differences in the flow features at the aft part of the front wheel.

The bottom view of the front wheel (Figure 8.21f) shows the strong curvature of the surface LIC pattern indicating the formation of a vortex pair. The top view of the front wheel however (Figure 8.21e) shows the confused surface LIC pattern across the width of the wheel tread and increase in pressure, characteristic of separated flow. The flow separation across the top and streamwise vortex pair at the bottom of the front wheel is exactly the opposite of what happens at the front wheel of the simple toe down configuration (Figure 4.22). This flow feature is also different from the two other complex configurations where the diverging flow around the brake unit results in strong streamwise vortex pairs at both the top and bottom of the front wheel (Figures 8.3 and 8.12).

The time averaged flow features on the surface of the rear wheel of the complex toe down configuration (Figure 8.22) are completely different from the previous configurations due to the change in the flow features at the front wheels. The surface LIC pattern on the front face of the rear wheel in Figure 8.22c shows two areas of flow attachment. There is a large attachment line on the lower half of the rear wheel near the outside edge and a smaller attachment point on the upper half of the rear wheel towards the inner edge. The surface LIC pattern shows a diagonal line in between the two attachment points which separates the two flow regimes. The flow pattern at the top of the rear wheel is generated by the separated flow from the top of the front wheel and the surface LIC pattern shows how the majority of this flow passes over the top and outside of the rear wheel. The flow pattern on the bottom of the rear wheel is generated by the streamwise vortex pair coming of the bottom of the front wheel. The surface LIC pattern on the

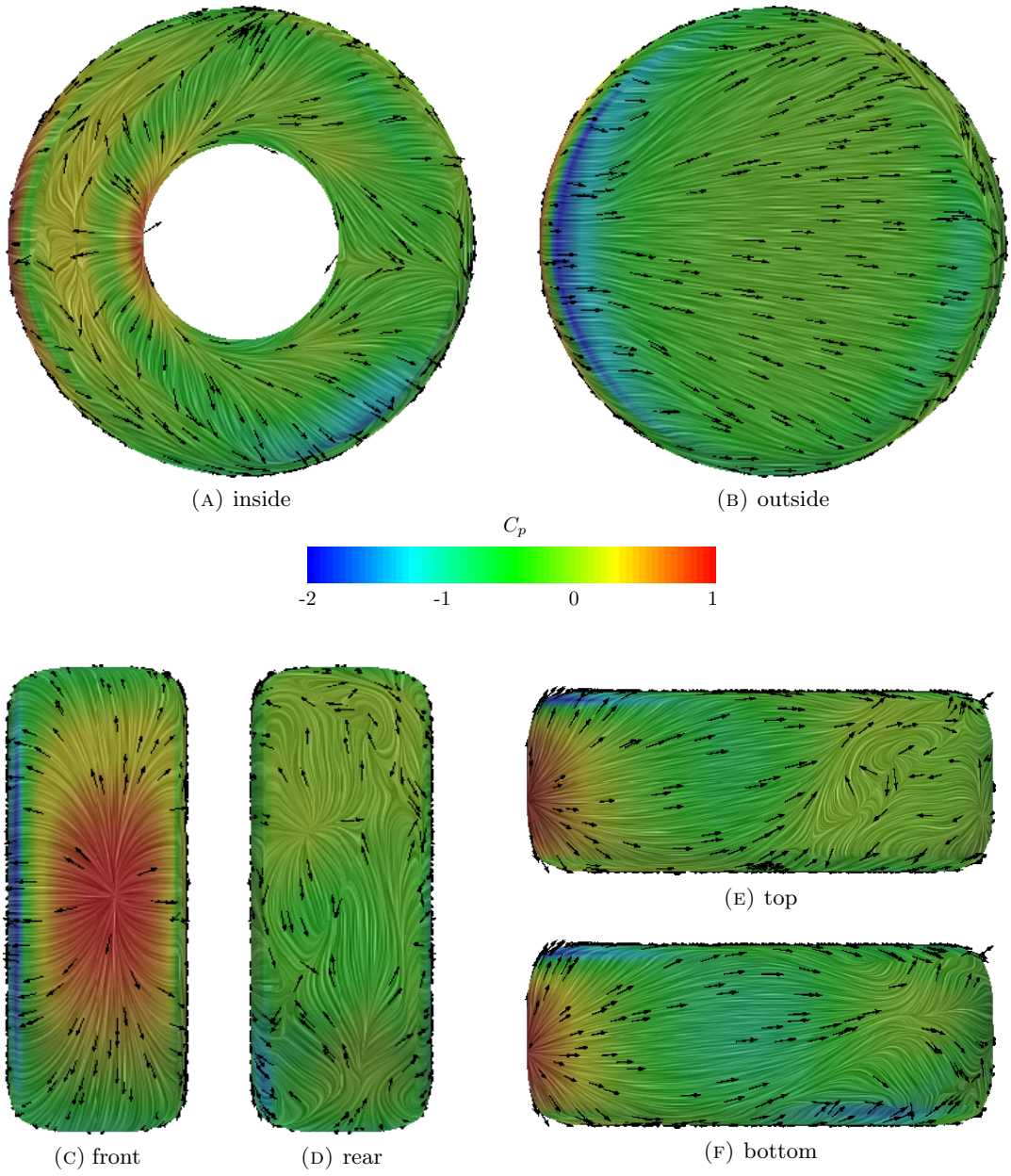

(A) inside (B) outside

(C) front (D) rear (E) top (F) bottom

FIGURE 8.21: Surface flow features of the time averaged flow field on the forward wheel of the complex toe down configuration.

lower half of the rear wheel shows that the flow changes direction towards the centre of the landing gear.

The surface LIC pattern on the inside of the rear wheel in Figure 8.22a shows the effect of the two different flow regimes. The top of the inside surface of the rear wheel shows a diverging surface LIC pattern as the turbulent flow moves around the brake unit. The bottom of the inside surface of the rear wheel shows an almost vertical direction of the shear stress vectors due to the induced flow of the strong streamwise vortex passing along the inside of the rear wheel. The top view of the rear wheel in Figure 8.22e shows

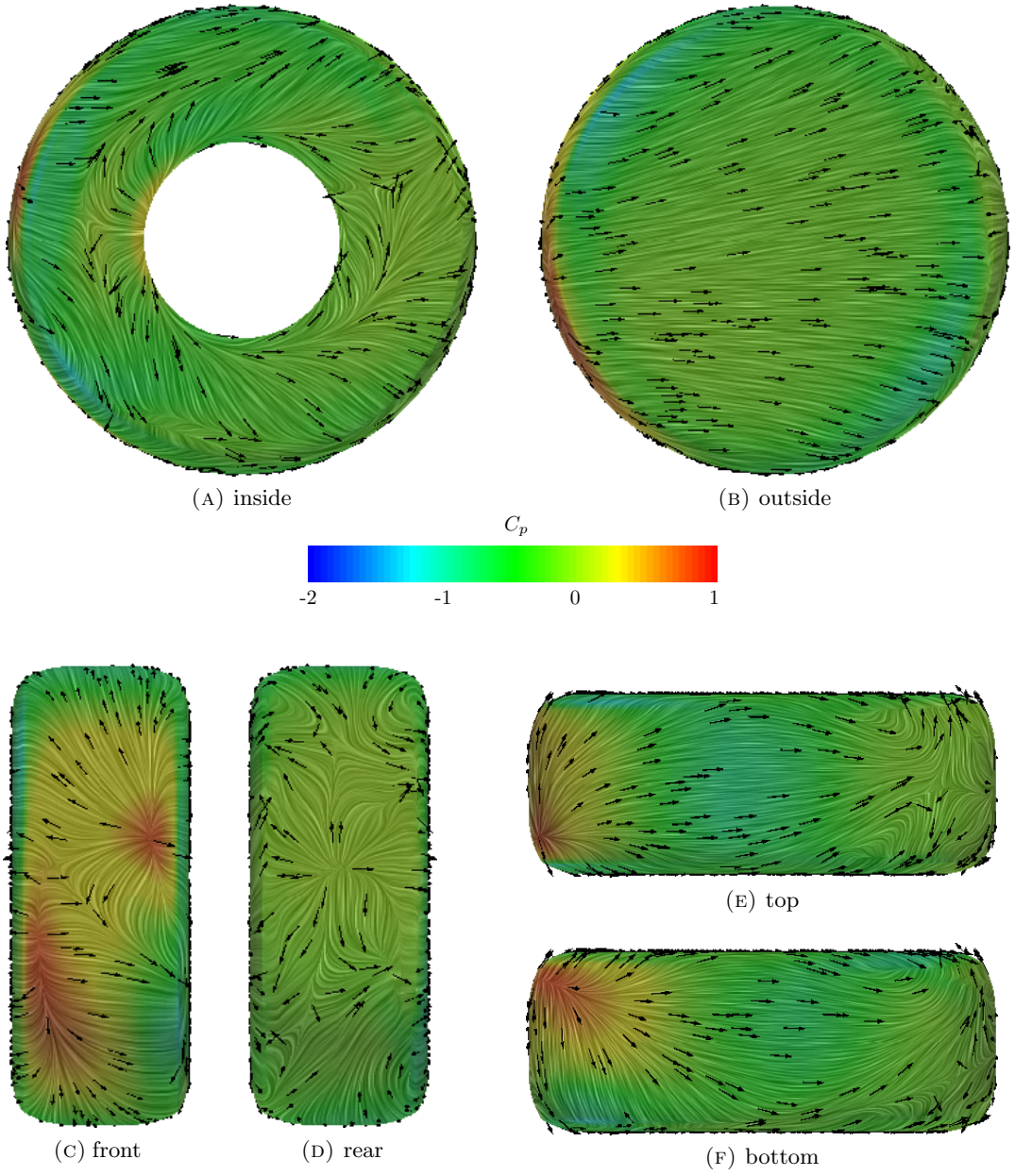

(A) inside (B) outside

(C) front (D) rear (E) top (F) bottom

FIGURE 8.22: Surface flow features of the time averaged flow field on the rear wheel of the complex toe down configuration.

that the flow follows the freestream direction along the wheel until it separates from the wheel. There are two small areas of high curvature visible at the location of flow separation which indicate the formation of a small vortex pair. The bottom view in Figure 8.22f shows a different flow behaviour with the flow moving towards the centre of the landing gear on the front half of the wheel but moving away from the centre on the aft half of the wheel. The confused surface LIC pattern on the aft face of the rear wheel in Figure 8.22d shows an attachment point in the middle which is characteristic of flow recirculation in the separated wake.

The front and rear wheel of the complex toe down configuration show completely different time averaged flow features compared to the previous configurations. However the surface flow features on the bogie of the complex toe down configuration (Figure 8.23) show at least some similarities with those on the bogie of the simple toe down configuration (Figure 4.24). The top view of the bogie in Figure 8.23a shows a small recirculation zone behind the attachment of the articulation link. This is followed by an attachment line and pressure increase which looks similar to the area in front of the strut of the simple toe down configuration in Figure 4.24a. The surface LIC pattern on the side of the bogie in Figure 8.23b shows a large flow recirculation zone behind the front axle followed by an area of vertical shear stress vectors due to the downwards deflected flow of the strut and yoke.

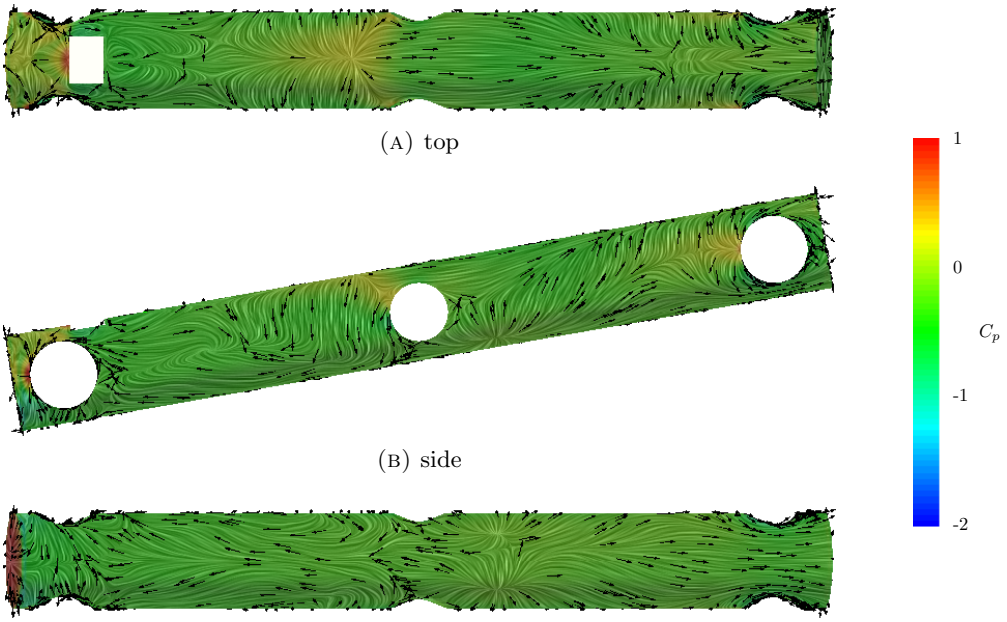

(A) top

(B) side

(C) bottom

FIGURE 8.23: Surface flow features of the time averaged flow field on the bogie of the complex toe down configuration.

The aft half of the bogie downstream of the strut shows the shear stress vectors pointing upwards due to the induced flow of the strong streamwise vortices. The pressure coefficient increases towards the front of the rear axle and the surface LIC pattern shows how the flow splits to move around the rear axle. The bottom view of the bogie in Figure 8.23c shows upstream pointing shear stress vectors on the forward half of the bogie which indicates the presence of a large flow recirculation zone. This is similar to the flow on the bottom of the bogie of the simple toe down configuration in Figure 4.24c. The bottom view of the bogie also shows two attachment points just aft of the strut as a result of the induced flow of the strong streamwise vortices. The surface LIC pattern downstream of these attachment points is smooth indicating that the flow continues to follow the surface of the bogie until it reaches the sharp aft edge where it separates.

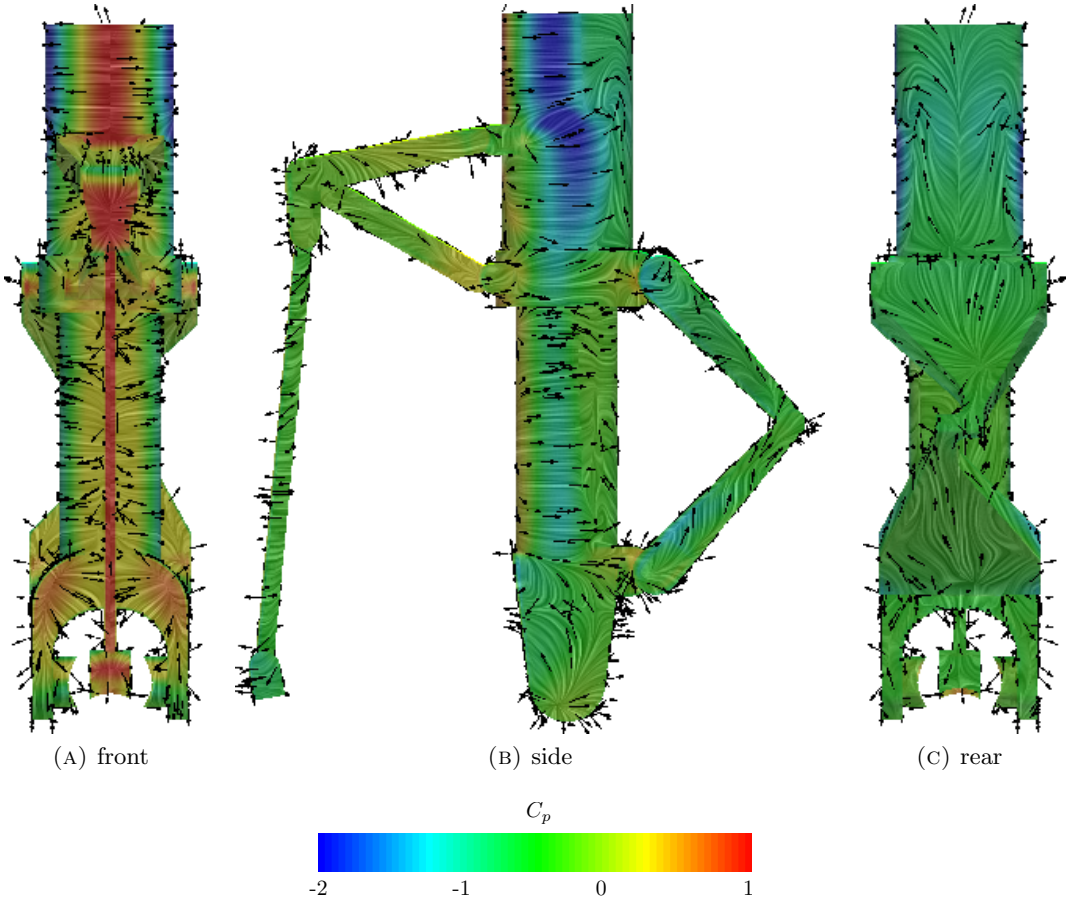

(A) front (B) side (C) rear

FIGURE 8.24: Surface flow features of the time averaged flow field on the lower half of the strut of the complex toe down configuration.

The flow features on the surface of the strut of the complex toe down configuration in Figure 8.24 shows some clear differences compared to strut of the previous two complex configurations (Figures 8.6 and 8.15). The toe down configuration of the bogie opens up the path of the flow to the centre of the landing gear which exposes the centre of the landing gear to the freestream flow. This leads to an increase of the local flow velocity near the centre of the complex toe down configuration compared to the other two complex configurations. The pressure coefficient on the front of the strut of the toe down configuration in Figure 8.24a is much higher than that of the horizontal or toe up configurations in Figures 8.6a and 8.15a. The higher local flow velocity also changes the wake behind the articulation link which results in a single attachment line on front of the strut in Figure 8.24a compared to two attachment lines for both of the other complex configurations. The surface LIC pattern shows two attachment points on the front of the yoke and a downward direction of the shear stress vectors which agrees with the attachment line and pressure increase on the top of the bogie in Figure 8.23a. The side and rear view of the strut (Figures 8.24b and 8.24c) look similar to the other two complex configurations. There is a flow attachment point on the side of the yoke

generated by the streamwise vortices and the curved surface LIC pattern on the rear face of the strut points at the formation of a streamwise vortex pair.

The time averaged surface flow features on the front and rear wheels of the complex toe down configuration show a completely different behaviour of the streamwise vortices compared to the previous landing gear configurations. This is confirmed by the streamwise vorticity plots of the time averaged flow field in Figure 8.25. Three vortices are generated at the bottom of each front wheel as shown in Figure 8.25a: a large vortex at the inside edge, a smaller vortex at the outside edge and below them the horse shoe vortex generated by the front brake unit. The top of the front wheel shows an area of vorticity further away from the wheel which is generated by the flow separating from the wheel surface. The location of the strong streamwise vortices at the front wheel of the complex toe down configuration is the opposite of the simple toe down configuration in Figure 4.26a where the strong vortices are generated at the top of the front wheel and the flow separates from the bottom.

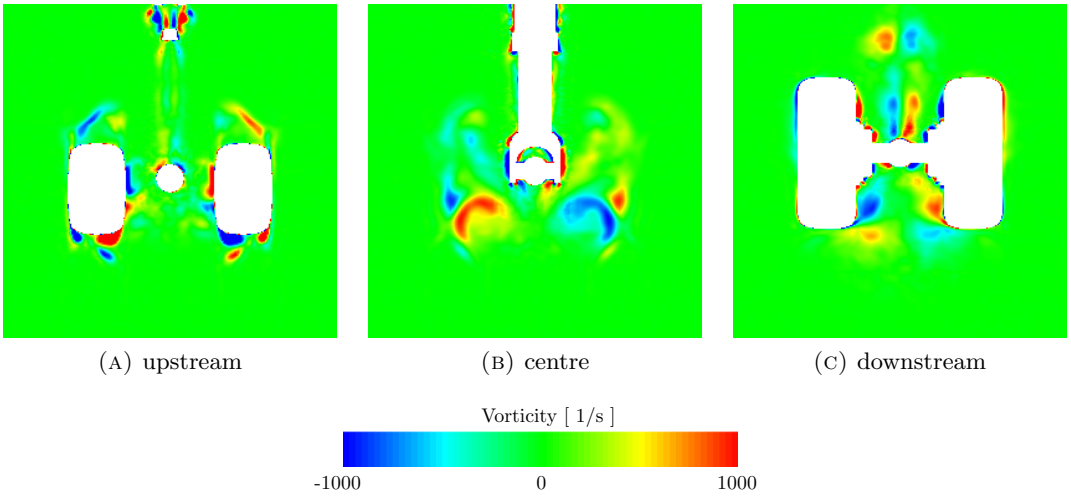

(A) upstream (B) centre (C) downstream

FIGURE 8.25: Streamwise vorticity of the time averaged flow field around the complex toe down configuration, upstream = aft part of the front wheels, centre = centre of the MLG, downstream = centre of the rear wheels.

The strong streamwise vortex pair generated at the bottom of the front wheel moves and rotates with the flow towards the centre of the landing gear as shown in Figure 8.25b. The plane through the centre of the rear axles and wheels in Figure 8.25c shows that the strong vortices have rotated even further and pass below and in between the rear wheels. This last figure looks similar to corresponding figure of the simple toe down configuration (Figure 4.26c) but the origin of the strong streamwise vortices is completely different. Figure 8.25c shows two areas of opposite vorticity just above the rear axles and bogie which are generated by the flow around the torque link which are not present in the other complex configurations.

8.3.2 Unsteady surface pressure distribution

The major features of the time averaged flow around the front wheel of the complex toe down configuration have changed compared to those of the two other complex configurations. However the unsteady surface pressure distribution in Figure 8.26 does show a lot of similarities to the results of the other complex configurations (Figures 8.26 and 8.17). The main differences are visible on the inside and top surface of the front wheel (Figures 8.26a and 8.26e) where the flow separation does not lead to the formation of a streamwise vortex pair. The flow separation across the width of the wheel leads to an increase in the unsteady surface pressure levels at the top of the front wheel compared to the other complex configurations.

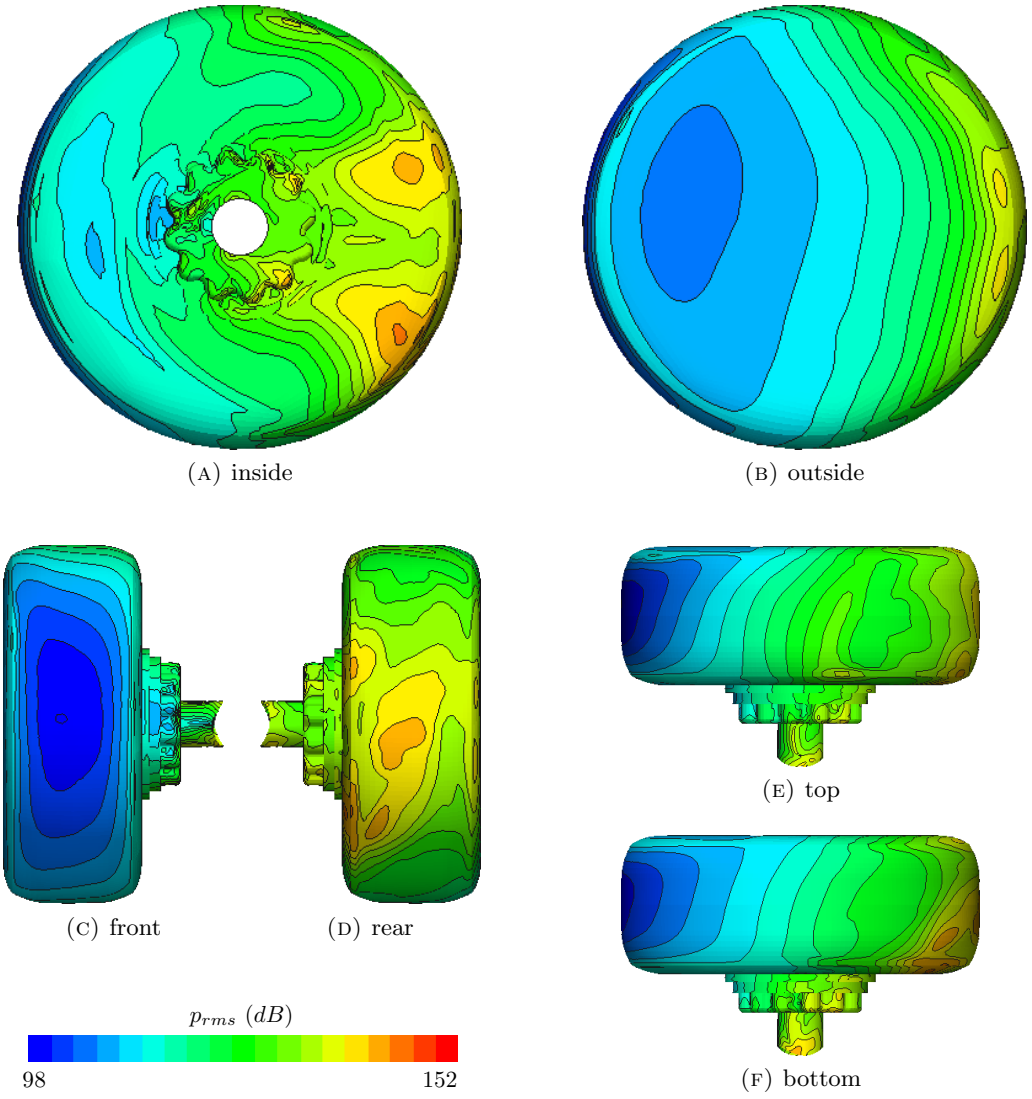

(A) inside (B) outside

(C) front (D) rear

(E) top

(F) bottom

FIGURE 8.26: Unsteady surface pressure level on the forward wheel, brake and axle of the complex toe down configuration.

The inside surface of the front wheel (Figure 8.26a) shows two peaks in the unsteady pressure level downstream of the brake unit similar to the other complex configurations but the peak at the top of the wheel has moved down and reduced in strength. There is no streamwise vortex to interact with the wake of the brake unit at the top of the front wheel and this causes the reduction of the unsteady pressure level. The vortex at the bottom of the front wheel does interact with the wake from the brake unit which leads to a higher unsteady pressure level.

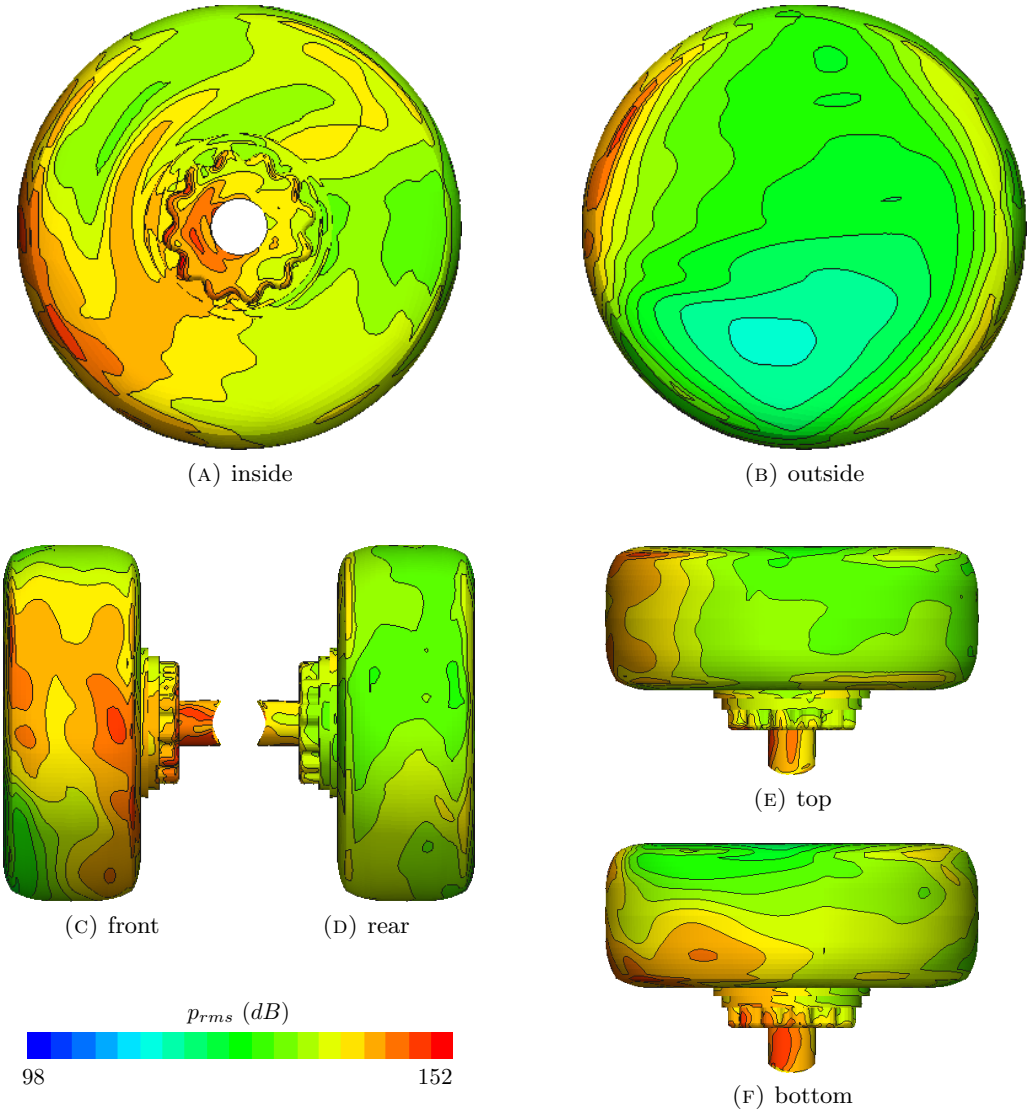

(A) inside (B) outside (C) front (D) rear (E) top (F) bottom

FIGURE 8.27: Unsteady surface pressure level on the rear wheel, brake and axle of the complex toe down configuration.

The features of the time averaged flow around the rear wheel of the complex toe down configuration are different than all the other configurations which also leads to a different unsteady pressure distribution (Figure 8.27). The separated turbulent flow from the top of the front wheel moves downstream and impinges on the front of the rear wheel. This

results in a high unsteady pressure level on the top half of the front face as shown in Figure 8.27c. A large part of this turbulent wake moves around the outside of the rear wheel and leads to an increase of the unsteady pressure level on the top half of the outside surface of the rear wheel (Figure 8.27b).

The flow over the lower half of the rear wheel is dominated by the streamwise vortices coming of the bottom of the front wheel as shown in Figure 8.25. These strong streamwise vortices follow the local flow direction towards the centre of the landing gear. This creates a high level of unsteady pressure on the lower inside edge and bottom of the wheel (Figures 8.27a and 8.27f) where the strong streamwise vortices pass along the surface of the rear wheel. The streamwise vortices move further downstream with the flow in between the rear wheels just below the rear brake unit and axle. This results in high unsteady pressure levels on the lower half of the inside surface of the rear wheel, the rear brake unit and the bottom of the rear axle. The low local flow velocity in the turbulent wake behind the rear wheel results in a low intensity of the pressure fluctuations and therefore no peaks or features in the unsteady pressure distribution on the rear face of the rear wheel (Figure 8.27d).

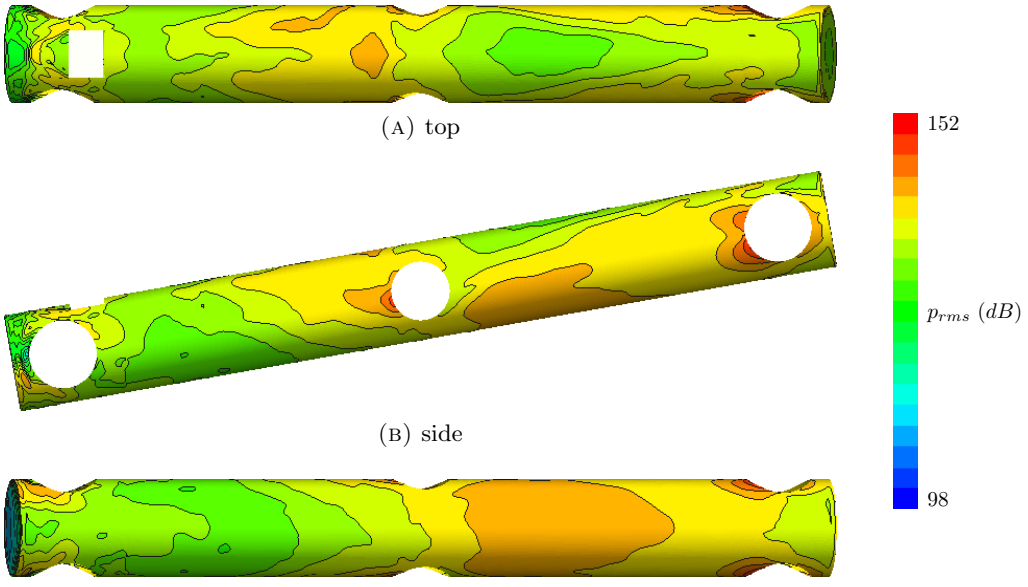

(A) top

(B) side

(C) bottom

FIGURE 8.28: Unsteady surface pressure level on the bogie of the complex toe down configuration.

The flow features section shows how the turbulent wake from the articulation link gets deflected downwards by the lower strut and yoke such that it impinges on the top of the bogie. This leads to an area of increased unsteady pressure level on the top surface of the bogie (Figure 8.28a) and this area continues on the sides of the bogie with a small peak just in front of the swivel (Figure 8.28b). The bottom surface of the bogie in Figure 8.28c shows a low unsteady pressure level on the front half of the bogie due to presence of

the flow recirculation zone generated by the flow separation of the sharp bogie edge and the wake of the front axles. However the aft half of the bogie shows a large peak in the unsteady pressure distribution which coincides with the location of the two attachment points in Figure 8.23c. The induced flow of the strong streamwise vortices moves the turbulent flow towards the surface of the bogie and this flow impingement generates a high unsteady pressure level on the bottom of the bogie. The turbulent flow continues downstream along the surface of the bogie where it encounters the rear axles which generates another peak in the unsteady pressure level at the bogie to rear axle junction (Figure 8.28b).

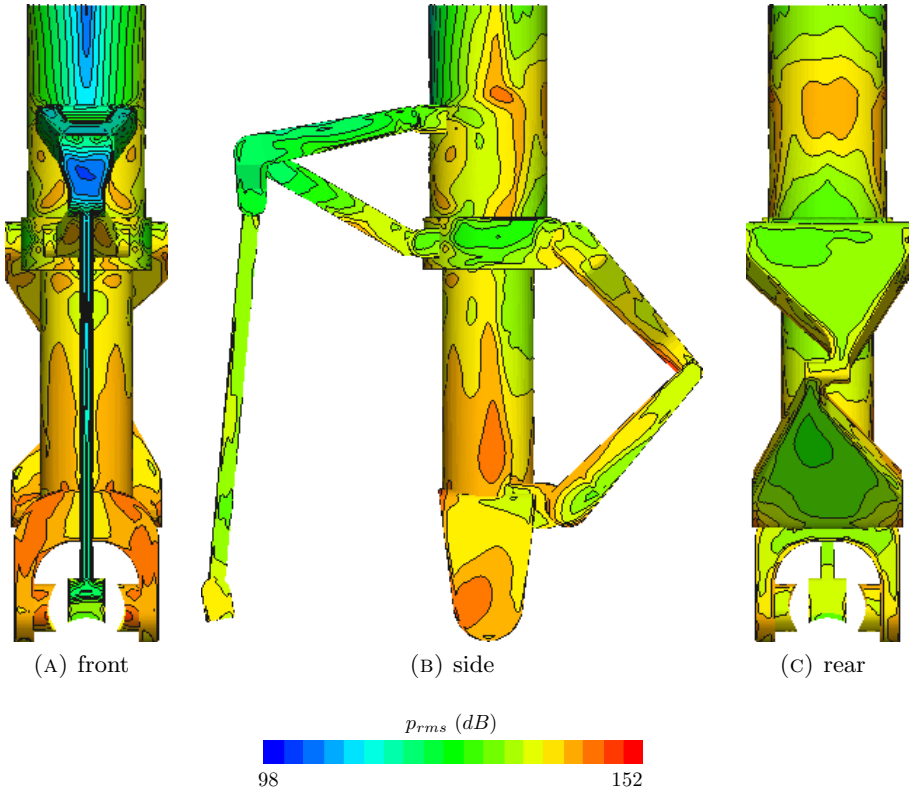

(A) front (B) side (C) rear

FIGURE 8.29: Unsteady surface pressure level on the lower half of the strut, articulation link and torque link of the complex toe down configuration.

The toe down configuration of the bogie opens up the path of the flow to the centre of the landing gear and this results in a higher local flow velocity compared to the other two complex configurations. The turbulent wake of the articulation link is transported by this higher velocity local flow which leads to an increase of the unsteady pressure level on the front of the yoke and strut (Figure 8.29a) compared to the other two complex configurations. The turbulent flow then accelerates around the side of the lower strut which creates another peak in the unsteady surface pressure at the widest point of the strut. The side of the yoke in Figure 8.29b also shows a peak in the unsteady pressure level at the same location as the flow attachment point in Figure 8.24b. The turbulent

flow impinges on the surface of the yoke due to the induced flow of the strong streamwise vortices. All three complex configurations show the same unsteady pressure peak on the rear of the strut at the top of the articulation link as seen in Figure 8.24c. The toe down configuration does not force the flow up as much as the other two configurations which results in a lower unsteady pressure level of these peaks compared to the other two configurations (Figures 8.6c and 8.15c).

8.3.3 Aerodynamic forces

The time averaged flow features around the complex toe down configuration differ significantly from to the other two complex configurations and this will have an effect on the aerodynamic forces. Table 8.3 shows the mean and standard deviation of the force coefficients of the components of the complex toe down configuration. A comparison with the results of the other two complex configurations (Tables 8.1 and 8.2) shows that the toe down configuration generates the highest drag of the three complex main landing gear. The toe down rotation of the bogie opens up the path of the flow to the centre of the landing gear which results in a higher local flow velocity compared to the other two configurations. This leads to a higher pressure coefficient on the front of the lower part of the strut, yoke and torque link as shown in Figure 8.24a and thus a significant increase of the drag coefficient of these components.

The change in the streamwise vortices at the front wheels does not lead to a significant change in the drag coefficient compared to the other configurations since the drag is mainly determined by the large area of high pressure on the front face of the wheel which is the same for all three configurations. The drag coefficient of the rear wheels on the other hand does get affected by the change in the flow features and has dropped due to a smaller area of high pressure on the front of the rear wheels. The articulation link of the toe down configuration is the longest of the three configurations and therefore has the highest drag coefficient. The difference with the other two configurations is larger than expected and will also be influenced by the increase of the local flow velocity. Not only the mean drag coefficient of most components in the complex toe down configuration has increased but the standard deviation is higher as well compared to the other two complex configurations. The higher flow velocity in the centre of the landing gear compared to the other configurations leads to stronger pressure fluctuations and thus a higher standard deviation of the drag coefficient.

The change in the time averaged flow features around the front wheel of the complex toe down configuration does not affect the drag compared to the other two configurations but it does lead to an increase in the outward pointing side force. The mean pressure

toe down	Cd ($\times 10^{-2}$)		Cs ($\times 10^{-2}$)		Cl ($\times 10^{-2}$)	
component	mean	std	mean	std	mean	std
articulation link	8.24	0.36	0.00	0.25	-1.78	0.37
bogie	4.50	0.29	-0.23	1.33	-1.11	1.36
front axle lhs	0.85	0.07	0.00	0.00	-0.04	0.11
front axle rhs	0.88	0.07	0.00	0.00	-0.13	0.11
front brake lhs	4.02	0.20	3.55	0.50	-0.26	0.22
front brake rhs	4.04	0.23	-3.64	0.43	-0.35	0.22
front wheel lhs	20.30	1.54	-26.21	1.55	-10.15	1.32
front wheel rhs	20.57	1.48	26.39	1.30	-10.37	1.34
rear axle lhs	0.61	0.21	0.00	0.00	-0.13	0.54
rear axle rhs	0.61	0.19	0.00	0.00	-0.17	0.51
rear brake lhs	1.38	0.36	6.41	0.82	-0.17	0.56
rear brake rhs	1.39	0.37	-6.21	0.90	-0.09	0.67
rear wheel lhs	12.91	1.87	-4.07	3.54	3.95	1.90
rear wheel rhs	12.66	2.14	4.75	3.97	3.57	2.08
strut	51.53	1.48	-0.02	4.26	-0.49	0.79
torque link	11.68	1.17	-0.12	0.89	-0.23	0.84
MLG	156.17	3.33	0.61	7.35	-17.96	5.18

TABLE 8.3: Mean and std of the aerodynamic force coefficients of the complex toe down configuration.

coefficient on the inside of the front wheel in Figure 8.21a shows that there is no area of low pressure at the top of the wheel due to the absence of the streamwise vortices. This effect increases the outward pointing sideforce coefficient compared to the other two complex configurations. The increase in the flow velocity at the centre of the landing gear results in a lower pressure coefficient on the surface of the front brakes and therefore a larger inward pointing side force. The flow features around the rear wheels have changed significantly compared to the other two complex configurations. This results in the lowest rear wheel sideforce coefficient of the three complex configurations due to the absence of the area of low pressure at the outside surface of the rear wheel. The side force coefficient of the rear brake follows the same trend as the front brake and has increased compared to the other two configurations due to the higher flow velocity in the centre of the landing gear. The side force generated by the components on the right and left hand side of the landing gear cancel out and the mean side force coefficient of the complete toe down configuration is close to zero as expected from a nearly symmetric geometry.

The standard deviation of the side force coefficients of the toe down configuration are the highest of the three complex configurations. This is attributed to the higher mean flow velocity and therefore larger pressure fluctuations near the centre of the landing gear. The exception to this trend are the front wheels and front brakes since these components experience undisturbed inflow conditions. The single streamwise vortex pair at each front

wheel will also lead to a reduction of the fluctuations in the aerodynamic forces of this component compared to the other configurations.

The flow separation across the top of the front wheel of the toe down configuration results in an increase of the pressure coefficient (see Figure 8.21e) and this generates a significant downforce compared to the other two complex configurations. The toe down configuration moves the top of the rear wheels away from the wake and into the faster flow which results in a low pressure coefficient on the top of the wheels. The high pressure area near the attachment point on the lower part of the rear wheel continues on the bottom surface. This leads to pressure difference between the top and bottom surface which generates a lift force on the rear wheels. This is the opposite of what happens with the rear wheel in the complex toe up configuration. The lift coefficient of the other components is relatively small and within the same range as the values for the complex horizontal and toe up configurations. The only component which stands out is the torque link which generates a slight downforce in the toe down configuration while it created lift in the other two configurations. An inspection of the pressure distribution shows almost no change on the top of the torque link. However the higher flow velocity past the bottom surface of the torque link results in a lower pressure and thus a downforce. The total complex toe down configuration generates a relatively large downforce compared to the other two complex configurations and this is all due to the change in the flow separation mechanism on the top of the front wheels.

The standard deviation of the lift coefficient of the complex toe down configuration show the same trend as the other two complex configurations. The standard deviation of the downstream components is higher than their upstream counterparts due to the increased level of turbulent fluctuations in the flow that reaches the component. The level of the standard deviation of the lift coefficient of the components of the complex toe down configuration is comparable with the levels of the other two complex configurations.

8.4 Summary and discussion

The aerodynamic results of the three simple landing gear configurations in chapter 4 show a clear relationship between the bogie angle and the time averaged flow features around the landing gear. The aerodynamic results in this chapter have shown that the same relationship is not present for the complex landing gear configurations. The streamwise vortices generated by the flow around the front wheels are again the dominant flow feature of the landing gear but their behaviour does not follow the same trend as for the simple configurations. The generation of these strong streamwise vortices at the front wheels does not follow a trend but is different for each complex configuration.

The time averaged flow features around the complex horizontal configuration do follow the same trend as the simple horizontal configuration with four vortices per front wheel, a strong pair on the inside and a weaker pair on the outside. The strong vortices from the inside of the front wheels move downstream parallel to the bogie and pass along the inside of the rear wheels. The additional components in the centre of the landing gear disturb the flow which results in a faster break down of the large flow structures compared to the simple horizontal configuration. This causes the streamwise vortices to reduce in strength quicker and restricts their effect to a smaller area.

The time averaged flow features around the front wheels of the complex toe up configuration do not show the same behaviour as the simple toe up configuration but instead show some strong similarities to the complex horizontal configuration. There are four streamwise vortices generated at each front wheel and the stronger ones at the inside of the wheel move to the centre of the landing gear just as what happens for the complex horizontal configuration. These vortices follow the mean flow direction downstream and pass over the top of the rear axles. So although the vortices originate from a different location on the front wheels they end up at the same downstream location as for the simple toe up configuration.

The complex toe down configuration does not follow the same trend as the simple toe down configuration and the time averaged flow features are also different from the other two complex configurations. The flow still forms streamwise vortices at the front wheel but they are only present at the bottom of the front wheel. The flow over the top of the wheel separates along the complete width of the wheel tread. This is the exact opposite of what happens with the flow around the front wheel of the simple toe down configuration. The separated flow from the top of the front wheel moves downstream and impinges on the top of the rear wheels. The streamwise vortices at the bottom of the front wheel move downstream with the mean flow and end up in the centre of the landing gear in between the rear wheels and below the rear axles. This downstream location of the vortex cores is similar to the location where the streamwise vortices of the simple toe down configuration end up but the origin of these vortices is completely different.

The different trajectory of the streamwise vortices compared to the simple configurations does change the location where the turbulent flow interacts with the complex geometry and thus the unsteady surface pressure distribution. The addition of the articulation link also has a large influence on the unsteady pressure distribution of the complex landing gear configurations. The wake from the articulation link increases the unsteadiness of the flow that reaches the strut and other components in the centre of the landing gear. The impingement of this turbulent wake generates local unsteady surface pressure peaks

which are an important source of far field noise. This effect is most clearly shown by the complex toe down configuration where the access of the flow to the centre of the landing gear is less restricted by the blockage by the front wheels. This increases the local flow velocity compared to the other two complex configurations and results in the highest level of the unsteady surface pressure on the lower strut.

The different flow features around the complex configurations have changed the aerodynamic force coefficients compared to the simple configurations. The effects are specific and different for each configuration and therefore not summarised here. The general trend shows an increased standard deviation of the force coefficients of the downstream components compared to their upstream counterparts due to the higher level of unsteadiness in the flow that reaches the component.

The addition of the brakes, articulation link, torque link and yoke has changed the geometry of the landing gear such that it is no longer as symmetric in the vertical direction as the simple landing gear configuration. This means that the trend between the bogie angle and flow features that exists for the simple configuration does not continue to hold for the complex configuration. The major flow features around the complex landing gear are different for each configuration and there is no clear relationship between bogie angle and the formation of the strong streamwise vortices. This shows that it is difficult to make predictions of the flow behaviour around complex configurations based on the results of a simplified geometry.

Chapter 9

Acoustics of the complex main landing gear

The far field noise levels generated by the three complex main landing gear configurations are described in this chapter which uses the same structure as chapter 5, describing the acoustic results of the simplified landing gear configurations. The strength of the dipole source term has been calculated for the different complex landing gear configurations but the figures are not shown here since they are again similar to the unsteady surface pressure level figures in the previous chapter. The dipole source term figures of the complex landing gear configurations have therefore been added to appendix C instead. This means that the overhead noise spectra are discussed first, followed by the far field noise directivity contours of the different landing gear components.

The addition of the brake units, torque link, articulation link, yoke and swivel has changed the geometry of the landing gear compared to the simple configuration. This makes a direct comparison of the acoustic results with those of the simple landing gear configurations difficult. Instead of describing the noise contribution of each individual component of the complex configuration some of the components have been added together such that there is a better similarity with the simple configuration. The wheels plus brakes are treated as an integrated unit and the yoke and swivel are considered to be parts of the strut which leaves only the articulation link and torque link without a counterpart in the simple configuration.

9.1 Overhead spectra

The overhead spectrum of the complex horizontal configuration in Figure 9.1 shows the characteristic haystack shape but has a lower peak noise level compared to the simple horizontal configuration in Figure 5.6. The frequency range of the noise spectrum has been limited to 2 kHz just as for the simple configuration in section 5.2 even though the number of grid points in the CFD simulation of the complex geometry is approximately three times that of the simple simulations. The number of grid points has increased due to larger domain size and the need to cover the additional components with a dense grid layer. The size of the grid blocks covering the wake of the landing gear have also been extended further downstream compared to the simple configuration. However the mean cell size in the proximity of the complex configurations is similar to that of the grid of the simple configurations. This results in the same size of the resolved flow structures and thus the same frequency range of the far field noise.

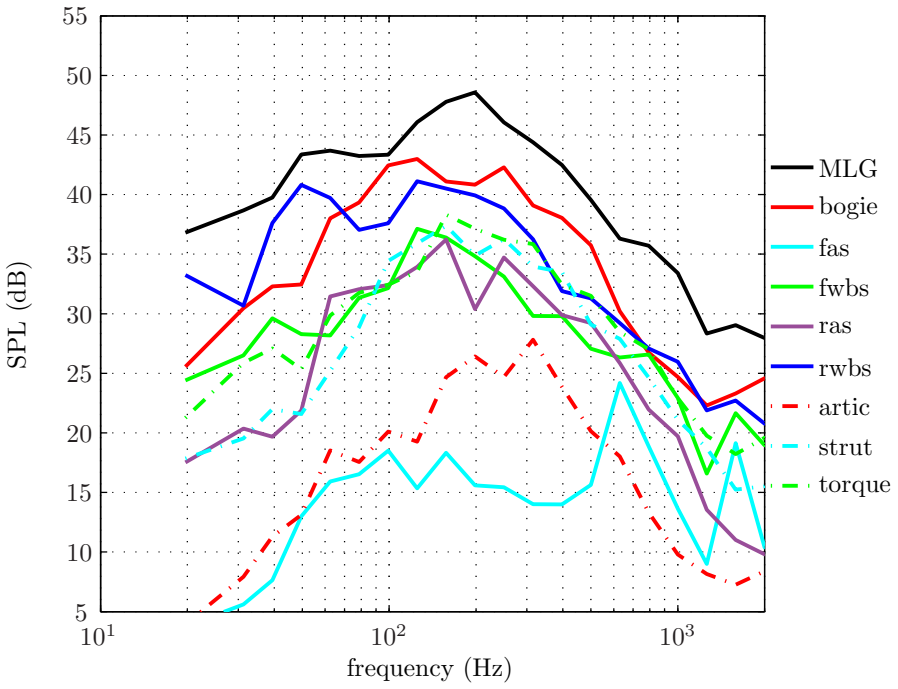

FIGURE 9.1: Overhead third octave band spectrum of the complex horizontal configuration.

The main flow features around the complex horizontal configuration show similarities with the simple horizontal configuration and this is also the case for the spectrum of the overhead noise. The bogie is again the dominant noise source in the overhead position, closely followed by the rear wheels and brakes which are also an important noise source of the simple configuration. The overhead noise level generated by the rear axles has reduced significantly compared to the simple horizontal configuration and there are two reasons for this. The surface area of the axles has reduced due to the addition of the brake

units and the higher blockage of the complex geometry results in a lower flow velocity near the centre of the landing gear reducing the strength of the pressure fluctuations.

The overhead noise generated by the strut, torque link and the front wheels plus brakes reaches the same level as the rear axles which means their contribution is significant but does not dominate the spectrum. The strut of the simple configurations does not generate any noise in the overhead direction due to the fact that the surface normal vector is perpendicular to the direction of the observer. This is no longer the case for the complex configuration due to the addition of the yoke and swivel. The yoke and swivel are in the same strong turbulent flow near the centre of the landing gear as the bogie. Their surface area is small but the high level of unsteady surface pressure still creates a significant amount far field noise. The torque link is sheltered from the flow by the lower part of the strut but the unsteady surface pressure level on the lower part is still relatively high due to the effect of the streamwise vortices. This leads to an overhead noise level similar to that of the strut and rear axles. The front wheels and brakes are in the relatively clean inflow and their contribution to the overhead noise is similar as for the simple horizontal configuration.

The articulation link is located in the clean inflow and has a small surface area such that it generates only a small amount of overhead noise. The frequency range of the noise generated by the front axles has increased compared to the simple configuration. This is most likely caused by the addition of the brake unit which disturbs the flow that reaches the axle in the complex configuration. The unsteadiness of the inflow may have increased but the surface area of the axles has decreased and the front axles are therefore still the quietest components of the horizontal complex landing gear configuration.

Figure 9.2 shows the spectrum of the overhead noise generated by the complex toe up configuration and this has a lower peak level than the spectrum of the complex horizontal configuration (Figure 9.1). This is the same trend as seen for the simple configuration in chapter 5. The drop of the noise level can again be attributed to the noise reduction of the bogie compared to the complex horizontal configuration. The noise reduction of the bogie leaves the rear wheels plus brake units as the dominant noise source of the complex toe up configuration in the overhead direction. The noise level of the bogie may have dropped compared to the horizontal configuration but it is still a significant noise sources. The torque link of the complex toe up configuration generates more noise than it does in the horizontal configuration such that it generates the same noise level as the bogie. The overhead noise spectrum generated by the other components has a similar level and frequency range as for the complex horizontal configuration in Figure 9.1.

The flow features around the complex toe down configuration are significantly different from the other two complex configurations and this leads to an increase of the overhead

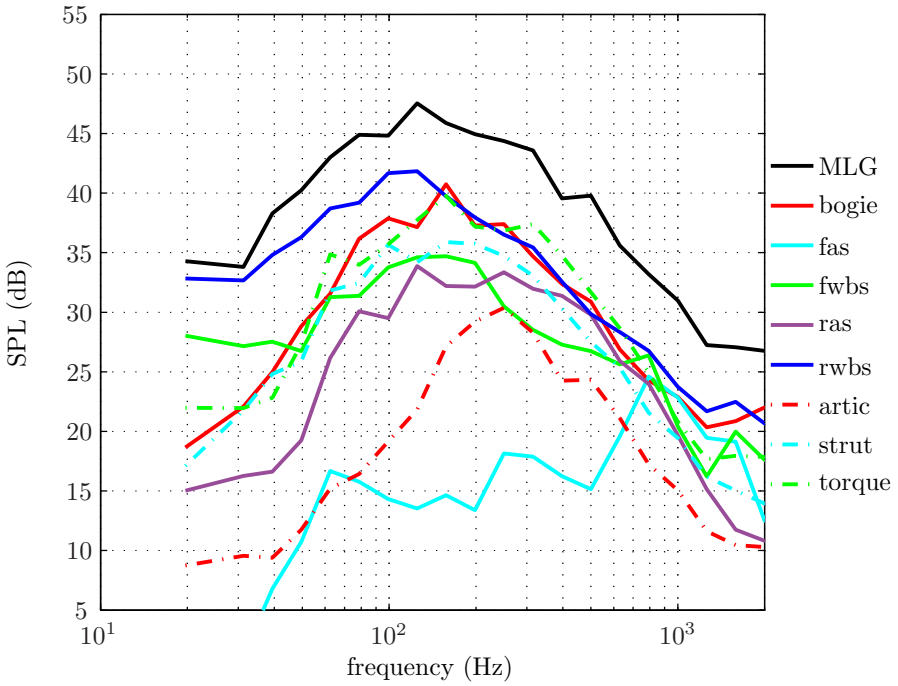

FIGURE 9.2: Overhead third octave band spectrum of the complex toe up configuration.

noise level as can be seen by the spectrum in Figure 9.3. The higher noise level of the complex toe down configuration compared to the other two complex configurations in the overhead direction is the opposite of the trend seen for the simple landing gear configurations. The simple toe down configuration is by far the quietest of the three simple landing gear configurations.

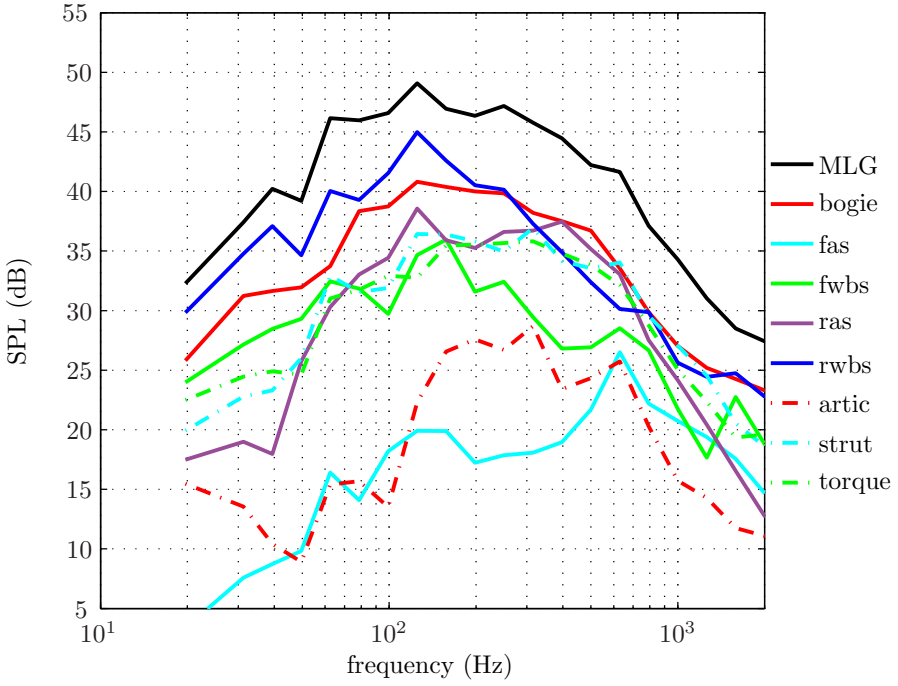

FIGURE 9.3: Overhead third octave band spectrum of the complex toe down configuration.

The rear wheels plus brakes are the dominant noise source in the overhead direction just as for the complex toe up configuration. The contribution of the bogie is again significant followed by the rear axles which generate more noise in the toe down configuration compared to the other two complex configurations. The toe down configuration of the complex landing gear results in a higher flow velocity in the centre of the landing gear which increases the unsteady pressure level on the downstream components such as the rear axles. The noise level of the torque link has reduced compared to the other complex configurations which is due to the fact that the strong streamwise vortices pass at a larger distance from the surface. The front axles and articulation link are again the quietest components just as for the other two complex configurations due to the combination of the undisturbed inflow conditions and the small surface area of the components.

Figures 9.4 and 9.5 show the relative overhead third octave band noise spectra of the components of the complex landing gear configurations with respect to the complex horizontal configuration. The relative noise spectrum of the horizontal configuration to itself is always zero but the curve has been included in the figures to highlight the reference level. The relative overhead noise level of the simplified landing gear in Figure 5.9 shows that for the different components the trend of toe up and toe down are similar with the level of the toe down configuration in general lower than that of the toe up configuration. This is not the case for the components of the complex landing gear, the relative noise level of the components in toe up and toe down configuration in Figures 9.4 and 9.4 show similarities but the relative noise level of the toe down configuration is equal to or higher than that of the toe up configuration.

There are a few components of the complex landing gear for which the similarities between the relative noise level of toe up and down do not hold for at least a part of the frequency range. The front axles in Figure 9.4b show similar relative noise levels for the low and high end of spectrum but the toe down configuration is much noisier in the middle of frequency range. The rear wheels plus brakes and the strut in Figures 9.4d and 9.5b both show similar relative noise levels of the toe up and down configurations for the lower half of the frequency range but an increase of the relative noise level of the toe down configuration for the upper half of the frequency range. The relative noise level of the bogie in toe down configuration in Figure 9.4e shows a drop in the middle of the frequency range which is not present for the toe up configuration. The torque link in Figure 9.5c is the component which stands out since it shows completely different relative noise levels for the toe up and toe down configurations. It is the only component of the complex landing gear for which the relative noise level of the toe up configuration is dominant over the toe down configuration for a significant part of the frequency range.

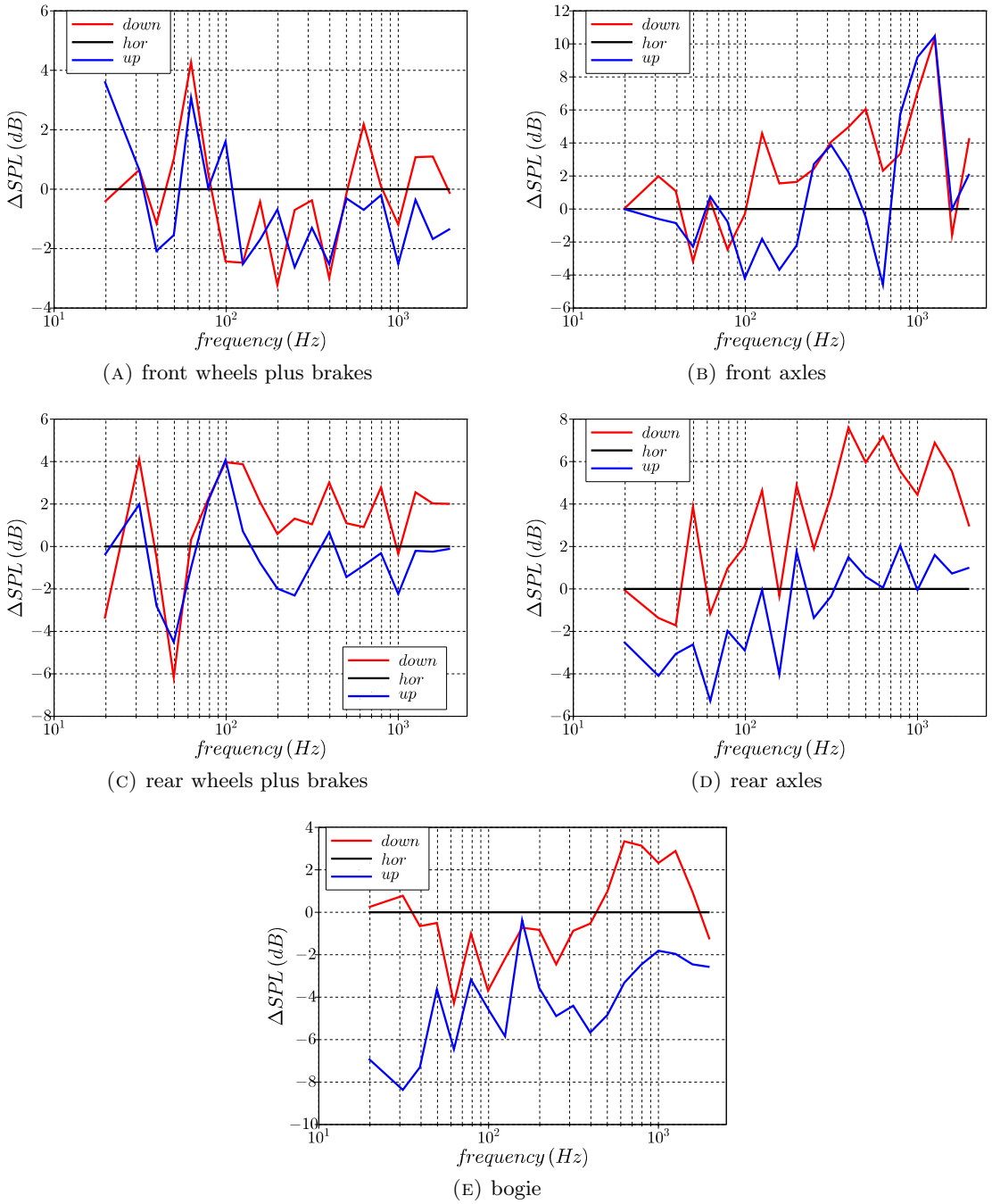

(A) front wheels plus brakes

(B) front axles

(C) rear wheels plus brakes

(D) rear axles

(E) bogie

FIGURE 9.4: Relative overhead third octave band noise level of the wheels plus brakes, axles and bogie of the complex landing gear compared to that of the horizontal configuration.

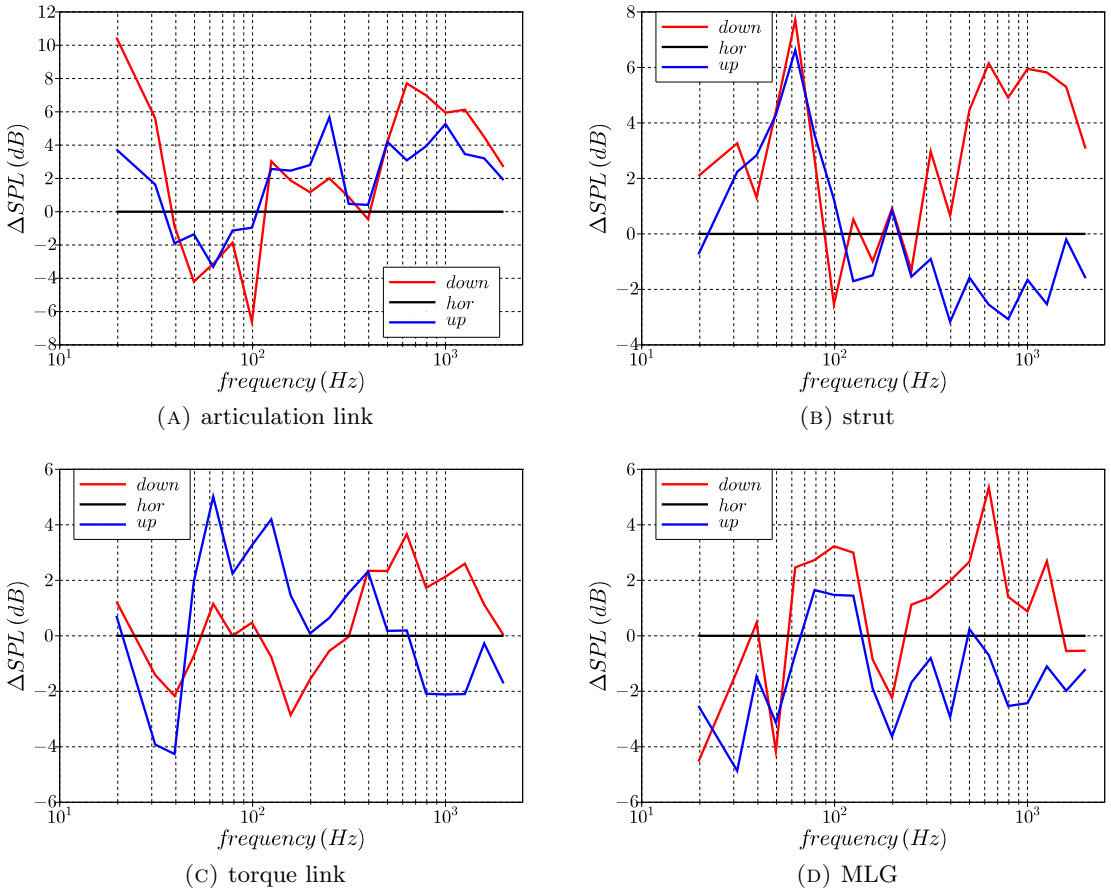

(A) articulation link (B) strut

(C) torque link (D) MLG

FIGURE 9.5: Relative overhead third octave band noise level of the different components of the complex landing gear compared to that of the horizontal configuration.

9.2 Noise directivity

The previous section has shown a different trend of the far field noise level in the overhead position of the complex configurations compared to the simple landing gear configurations. However the overhead spectra are based on the far field noise levels in a single observer location. This section will compare the noise levels and directivity pattern of the different components on a plane below the landing gear and will therefore give a more complete overview of the acoustics of the complex landing gear configurations.

9.2.1 Front wheels and brakes

The noise directivity contours of the front wheels and brakes in Figure 9.6 show a similar noise level for all three complex configurations: approximately 44 dB in the quiet zone below the landing gear and 47 dB at the peaks towards the sides. This agrees with the aerodynamic results of the previous chapter which show almost identical flow features

and unsteady pressure distributions on the lower half of the front wheels and brakes of the three configurations. The directivity pattern with a quiet zone below the landing gear and the peak noise level to the sides is similar to the noise directivity pattern of the front wheels of the simple configurations (Figure 5.10). This shape of this pattern is caused by the two peaks in the unsteady pressure distribution on the large flat inside surface of the front wheels.

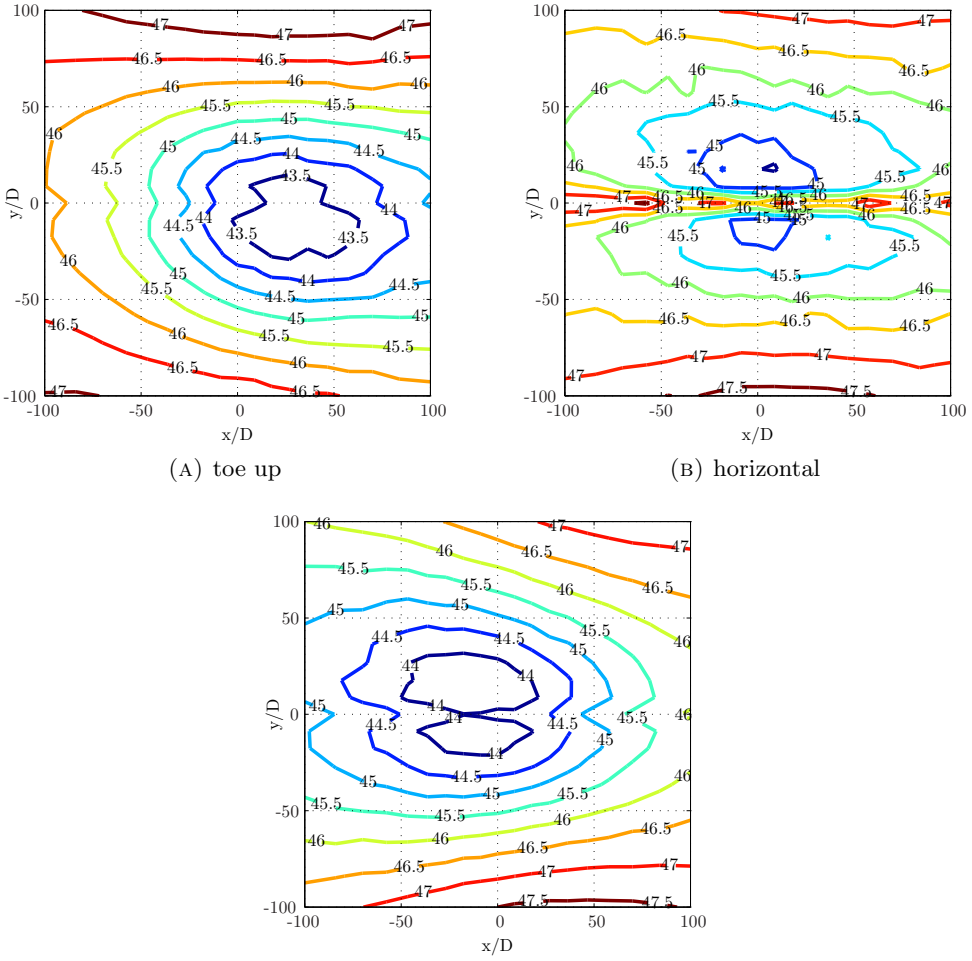

(A) toe up

(B) horizontal

(C) toe down

FIGURE 9.6: Noise directivity contours of the front wheels and brakes of the complex landing gear configurations. (OASPL in dB)

The noise directivity contours of the front wheels plus brakes are not as smooth as those of the front wheels of the simple configurations which is caused by the addition of the brakes. The complex curved shape of the brake units mean that it does not radiate a constant amount of noise in all directions which disturbs the smooth noise pattern generated by the front wheels. The front wheels of the three simple configurations all generate a quiet zone directly below the landing gear. However the location of this quiet zone of the complex configurations varies with bogie inclination angle: it moves downstream for the toe up configuration and upstream for the toe down configuration.

The noise contour generated by the front wheels plus brakes of the horizontal configuration in Figure 9.6b shows a narrow longitudinal band of increased noise level below the landing gear separating the quiet zone into two ellipse shaped regions. The contours of the toe down configuration (Figure 9.6c) shows that the two ellipses are touching and they have merged into a single area for the toe up configuration (Figure 9.6a). The unsteady pressure distribution on the bottom of the front wheels and brakes of all three configurations (Figures 8.8, 8.17 and 8.26) is similar and does not explain this change in the noise contours. The effect is most likely caused by a change in the interaction between the noise generated by the wheels plus brakes on the right and left hand side of the landing gear.

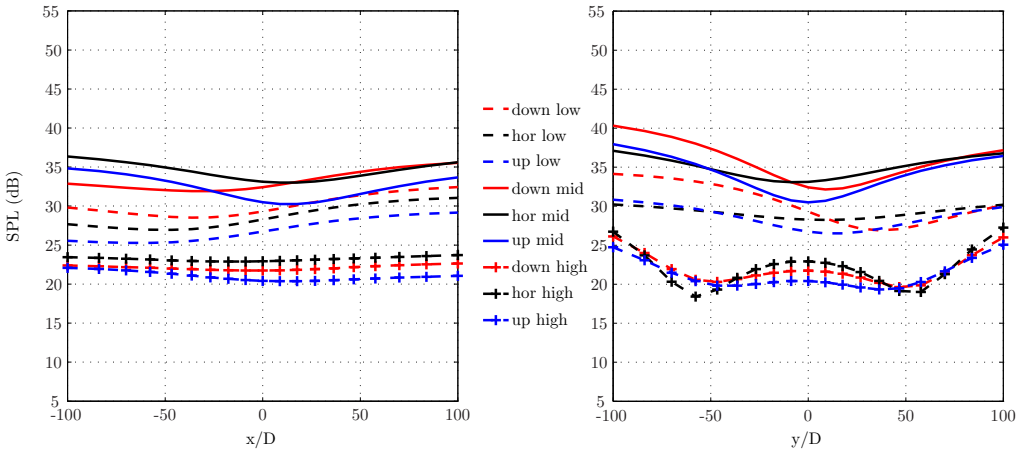

(A) longitudinal (B) transverse

FIGURE 9.7: Low, mid and high frequency noise levels generated by the front wheels and brakes of the complex landing gear on the longitudinal and transverse centreline of the observer plane.(low = 49.6 Hz, mid = 250 Hz and high = 1000 Hz third octave band)

The noise directivity contours of the Overall Sound Pressure Level (OASPL) in Figure 9.6 show the sound pressure level of the complete noise signal which does not distinguish between the noise at different frequencies. The noise levels at a low (49.6 Hz), mid (250 Hz) and high frequency (1000 Hz) third octave band have been plotted on the longitudinal and transverse centreline of the observer plane to show the frequency content of the far field noise just has been done for the simplified landing gear results in Chapter 5. Figure 9.7 shows the noise of the front wheels plus brakes on the longitudinal and transverse centreline of the observer plane. The mid frequency noise on the longitudinal centreline in Figure 9.7a shows a small reduction in the noise level below the landing gear but the location of the dip in the mid frequency noise levels has moved downstream compared to that of the simple landing gear in Figure 5.11a. The low frequency noise level of all three complex configurations is consistent: constant upstream of the landing gear and increases slowly in the downstream direction. The high frequency noise along

the longitudinal centreline is constant for the three complex configurations while it shows more variation for the simple configurations.

The noise level on the transverse centreline in Figure 9.7b is not completely symmetric but is very similar that of the simplified landing gear in Figure 5.11b: the mid frequency noise level shows a single dip below the landing gear while the high frequency noise level curve shows a double dip. This double dip of the high frequency noise in transverse direction is also visible in the directivity contours in Figure 9.6 while that is not the case for the directivity contours of the simple configurations in Figure 5.10.

9.2.2 Front axles

The front axles of the complex landing gear configuration are shorter than those of the simple configurations due to the addition of the brake unit to the inside of the wheels. This has an effect on the noise directivity pattern and noise levels which are shown in Figure 9.8. The front axles of the simple configuration in Figure 5.12 generate a characteristic dipole type noise source with a peak below the landing gear and circular shaped contours. The front axles of the complex configurations are so short that the disturbed flow near the ends becomes more important and they do not behave like a long cylinder anymore. This changes the noise directivity pattern of the complex configurations compared to dipole type noise of the front axles of the simple configurations.

The noise contour of the front axles of all three configurations in Figure 9.8 show a noise peak in a relatively narrow longitudinal area below the landing gear. The noise level generated by the front axles in the transverse direction reduces quickly. The noise level of the all the front axles is low but that of the toe down configuration is slightly higher than the other two configurations. This agrees with the peak in the unsteady pressure distribution at the bogie to axle junction (Figure 8.26f) which is not present in the unsteady pressure distribution of the other two configurations (Figures 8.8f and 8.17f).

Figure 9.9 shows the longitudinal and transverse centreline noise of the front axles of the complex landing gear. The high frequency noise level is dominant for the front axles of the complex landing gear while it is almost non existent for the front axles of the simple landing gear in Figure 5.11. The addition of the brake unit on the inside of the wheels of the complex configuration disturbs the flow and this is assumed to create the increase in the high frequency noise level of the front axles in the complex configurations compared to the simplified configurations. The front axles of the complex toe up and down configurations in Figures 9.9a and 9.9b show similar curves with the high frequency noise level being the loudest followed by the mid frequency and then the low frequency

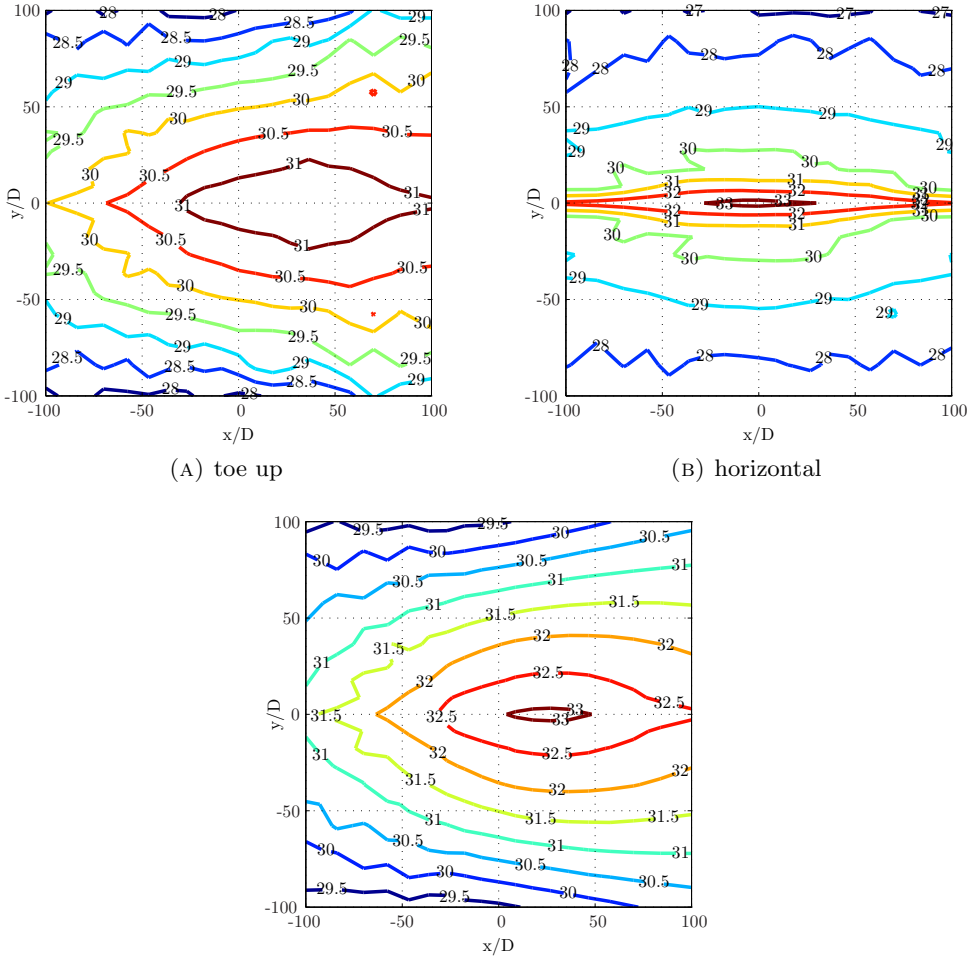

(A) toe up (B) horizontal

(C) toe down

FIGURE 9.8: Noise directivity contours of the front axles of the complex landing gear configurations. (OASPL in dB)

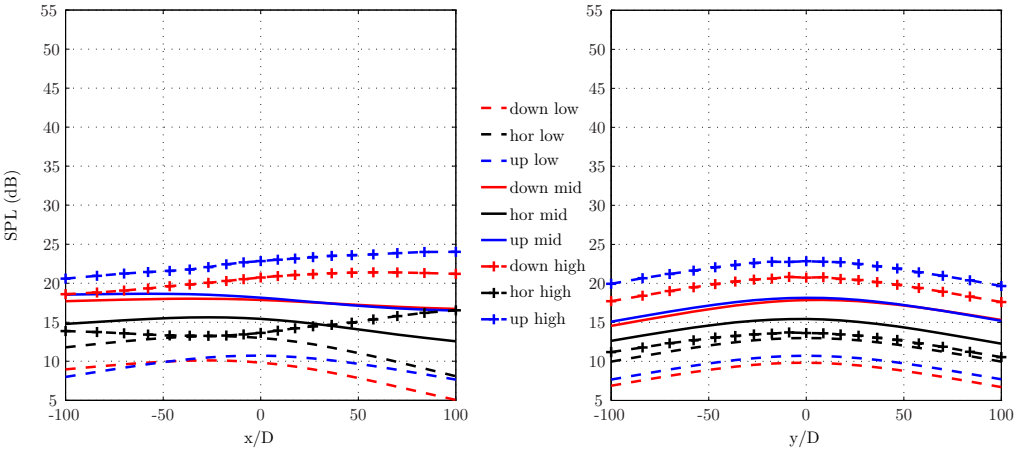

(A) longitudinal (B) transverse

FIGURE 9.9: Low, mid and high frequency noise levels generated by the front axles of the complex landing gear on the longitudinal and transverse centreline of the observer plane.(low = 49.6 Hz, mid = 250 Hz and high = 1000 Hz third octave band)

noise level. The front axles of the complex horizontal configuration stand out since the they do not follow the same order as the other two configurations.

9.2.3 Articulation link

Figure 9.10 shows the noise directivity contours generated by the articulation link and both the shape and levels differ for each configuration. The wake from the vertical beam of the articulation link impinges on the solid top surface which generates most of the far field noise. This triangular shaped top surface is inclined to the mean flow direction which explains the increase in the noise level in the upstream direction. The turbulent flow that moves past a sharp edge will cause the surfaces on both side of the edge to emit noise in the direction of the surface normal vector. The complex geometry of the articulation link has a lot of sharp edges and this results in distinct peaks in the far field noise contours.

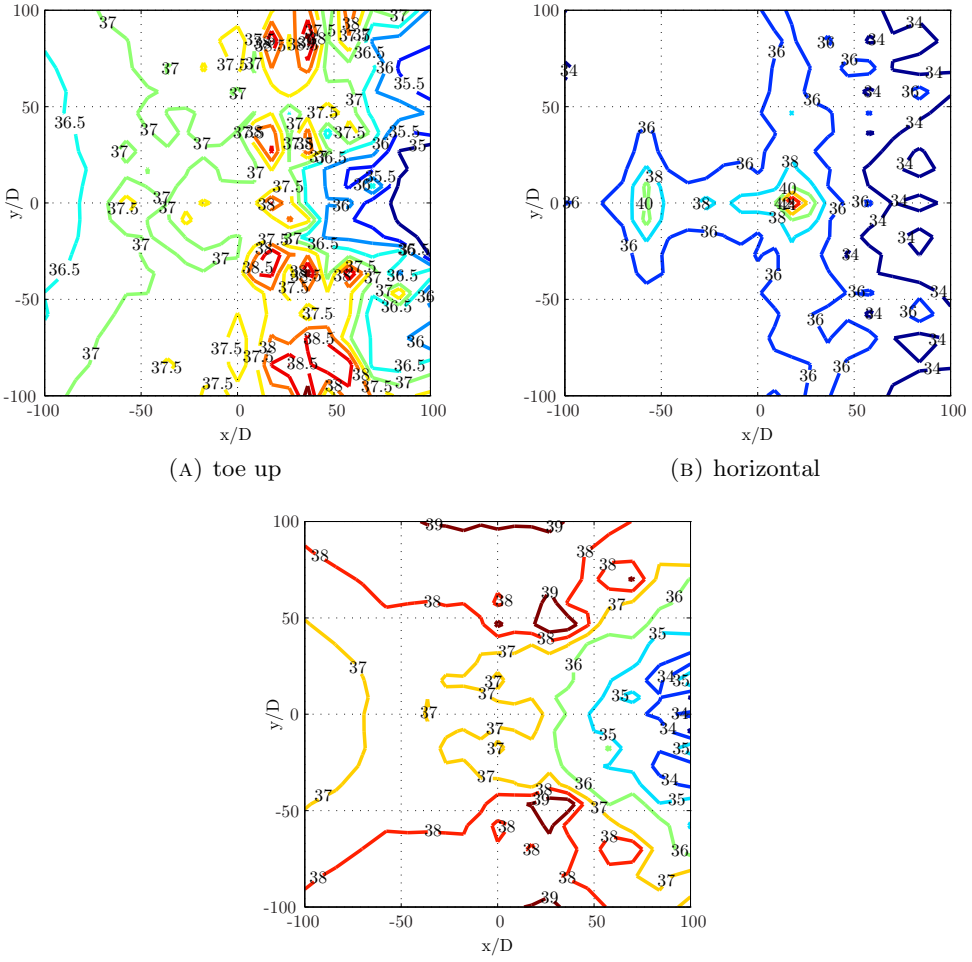

(A) toe up

(B) horizontal

(C) toe down

FIGURE 9.10: Noise directivity contours of the articulation link of the complex landing gear configurations. (OASPL in dB)

The mid frequency noise level of the articulation link in both the longitudinal and transverse directions is much higher than the level of the low and high frequencies as shown in Figure 9.11. A large part of the articulation link consist of a long vertical square beam perpendicular to the flow similar to the orientation of the main strut. The dimension of this square beam in the direction of the flow is small but Figures 9.11a and 9.11b do not show a large amount of high frequency noise. Two possible explanations for this are as follows: the upstream position of the articulation link which puts it in the undisturbed clean inflow and the grid in the wake of the articulation link is not fine enough to capture the very small flow structures.

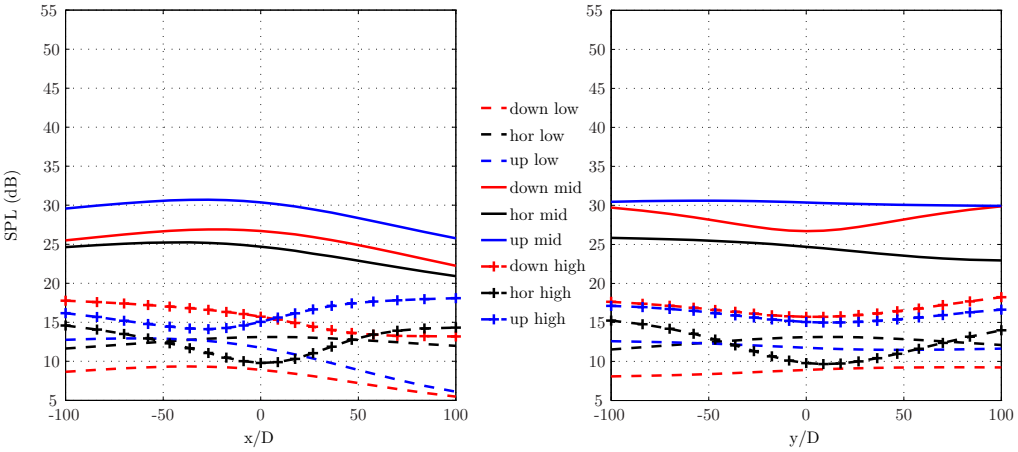

(A) longitudinal (B) transverse

FIGURE 9.11: Low, mid and high frequency noise levels generated by the articulation link of the complex landing gear on the longitudinal and transverse centreline of the observer plane.(low = 49.6 Hz, mid = 250 Hz and high = 1000 Hz third octave band)

9.2.4 Bogie

The noise directivity contours generated by the bogie of the complex landing gear configurations in Figure 9.12 show a similar location of the noise peaks as the bogie of the simple configurations in Figure 5.14. The bogie is a cylinder which, due to the orientation of the surface normal vectors, will radiate noise mainly directly below the landing gear and to the sides. This creates a band of high far field noise level perpendicular to the flow direction. The toe up configuration moves this band upstream and the toe down configuration moves this band downstream compared to the band generated by the bogie of the horizontal configuration.

The bogie of the horizontal complex configuration generates the highest far field noise level of the three configurations as shown in Figure 9.12. This is the same result as seen for the horizontal bogie of the simple configuration. The noise peak of the horizontal bogie in Figure 9.12b covers a much narrower band than the noise peak of the bogie of

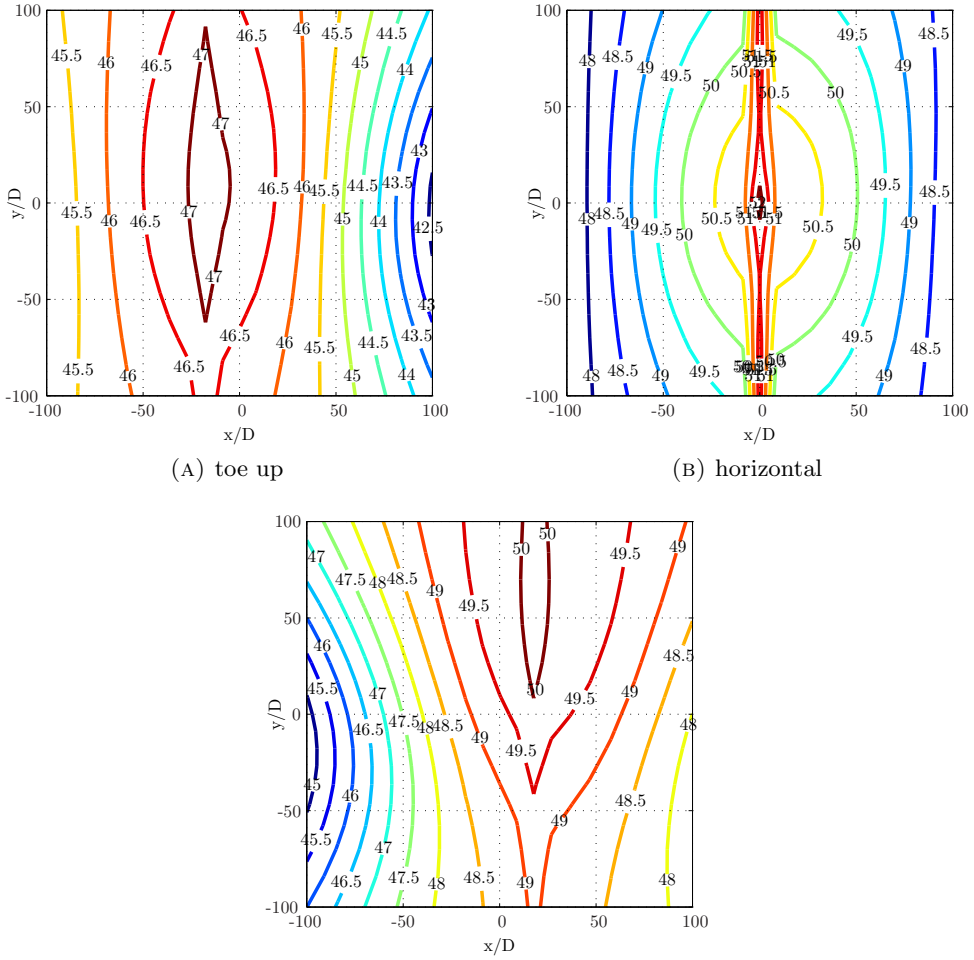

(A) toe up

(B) horizontal

(C) toe down

FIGURE 9.12: Noise directivity contours of the bogie of the complex landing gear configurations. (OASPL in dB)

the other two complex configurations (Figures 9.12a and 9.12c). The unsteady pressure distribution on the surface of the horizontal bogie (Figure 8.10) does not show any specific features. The narrow band in the contour plot is most likely generated by some sort of interaction between the unsteady pressure peaks on each side of the bogie (Figure 8.10b).

The bottom of the bogie of the complex toe down configuration (Figure 8.28c) shows a larger area of high unsteady surface pressure than the bogie of the complex horizontal configuration (Figure 8.10c). However this does not lead to a higher far field noise level as shown in Figure 9.12c. The bottom of the bogie of the complex toe up configuration (Figure 8.19c) shows the lowest unsteady pressure level of the three configurations and this does lead to the lowest far field noise level in Figure 9.12a.

Figure 9.13 shows that the mid frequency noise level of the bogie on the longitudinal and transverse centreline is the noisiest followed by the low and high frequencies. The

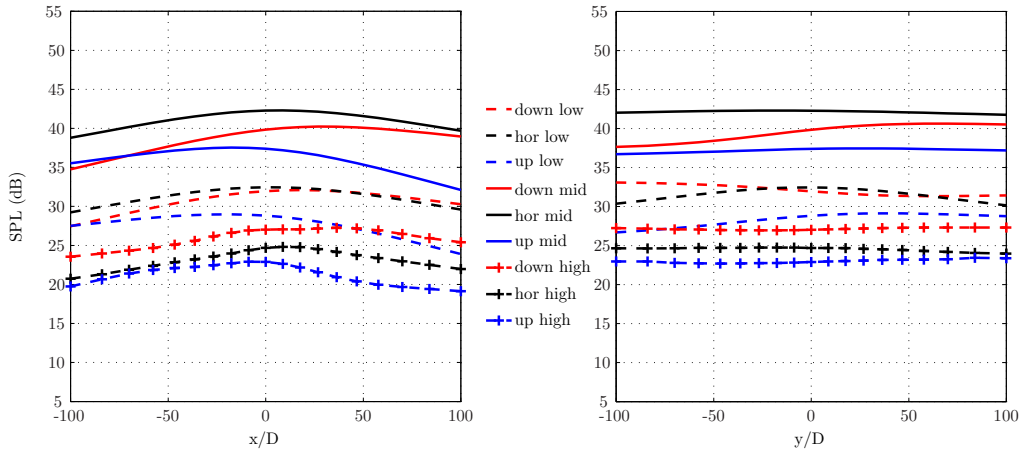

(A) longitudinal (B) transverse

FIGURE 9.13: Low, mid and high frequency noise levels generated by the bogie of the complex landing gear on the longitudinal and transverse centreline of the observer plane.(low = 49.6 Hz, mid = 250 Hz and high = 1000 Hz third octave band)

noise level in the transverse direction (Figure 9.13b) is almost constant but the noise level in the longitudinal direction (Figure 9.13a) shows a small peak below the landing gear. This peak shifts upstream for toe up configuration and downstream for the toe down configuration just as what happens for the bogie of the simplified landing gear in Figure 5.15. The horizontal configuration of the bogie is again the noisiest but the difference with the other two configurations is smaller compared to simplified landing gear. The toe down configuration of the bogie of the complex landing gear is noisier than the toe up configuration and also noisier than the horizontal configuration for the high frequency noise while it is the quietest configuration for the simple landing gear.

9.2.5 Rear wheels and brakes

The noise directivity contours of the rear wheels and brakes (Figure 9.14) show similarities to the noise contours of the rear wheels of the simple configuration (Figure 5.16) with the far field noise peaks located to the sides of the observer plane. This is due to the geometry of the wheel with its large flat inside and outside surfaces radiating noise to the sides and the smaller surface of the curved wheel tread radiating noise downwards. The rear wheels and brakes of the complex toe up configuration (Figure 9.14a) are the quietest of the three complex configurations. The toe up configuration of the bogie moves the bottom of the rear wheels away from the wake of the upstream components which results in a low unsteady surface pressure level as shown in Figure 8.18f.

The rear wheels and brakes of the complex toe down configuration generate the highest far field noise level (Figure 9.14c) of the complex configurations. This is the opposite of

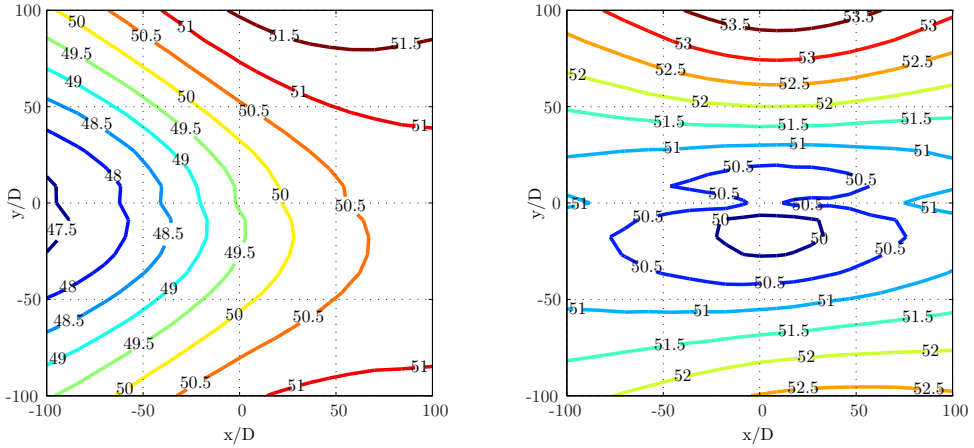

(A) toe up

(B) horizontal

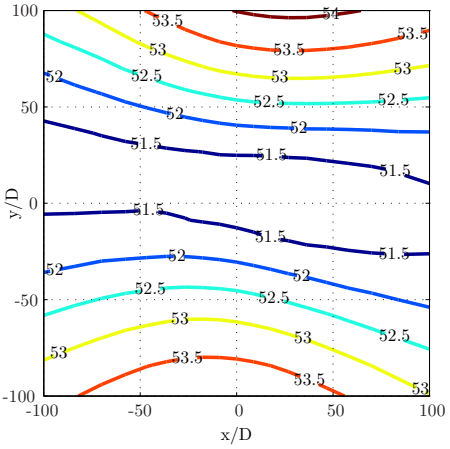

(C) toe down

FIGURE 9.14: Noise directivity contours of the rear wheels and brakes of the complex landing gear configurations. (OASPL in dB)

the trend for the rear wheels of the simple configurations in Figure 5.16. The reversal of the trend can attributed to the change in the flow features around the complex toe down configuration compared to the simple configuration. The flow separation at the bottom of the front wheel generates a pair of streamwise vortices that move downstream with the mean flow and pass in between the rear wheels (Figure 8.25c). These vortices are a lot closer to the surface of the rear wheels than the streamwise vortices of the simple toe down configuration in Figure 4.26c. This leads to a stronger interaction of the turbulent flow with the surface of the rear wheels and thus a higher unsteady pressure level (figure 8.27) which results in a higher far field noise level.

The far field noise level generated by the rear wheels and brakes of the complex horizontal configuration (Figure 9.14b) reaches almost the same peak level as that of the complex toe down configuration (Figure 9.14c) but the noise level in the quiet area below the landing gear is lower. The pair of streamwise vortices of the horizontal configuration

move downstream in between the rear wheels and generate a high unsteady pressure level on the forward inside edge of the rear wheel (figure 8.9) which explains the peak in the far field noise level to the sides. The unsteady pressure level on the bottom of the rear wheel of the complex horizontal configuration (Figure 8.9f) is lower than that of the complex toe down configuration (Figure 8.27f) and this results in the lower far field noise level in the quiet zone below the landing gear.

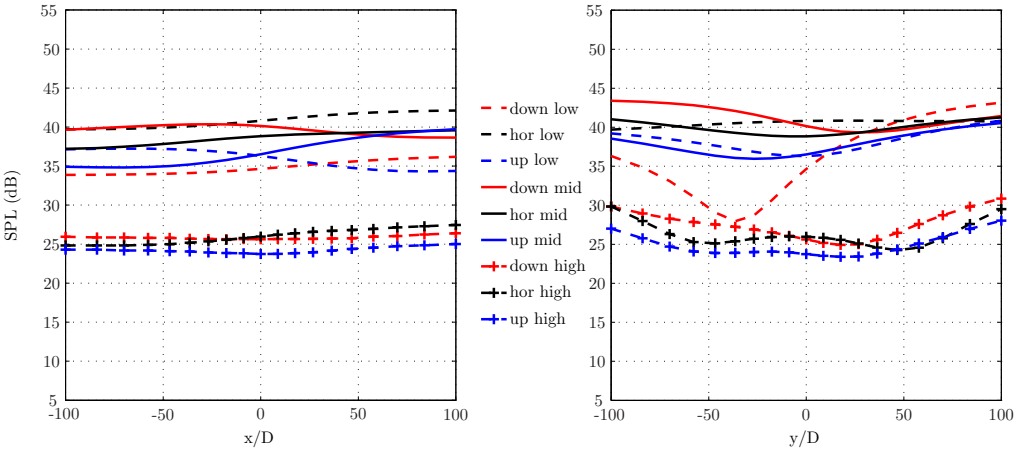

(A) longitudinal (B) transverse

FIGURE 9.15: Low, mid and high frequency noise levels generated by the rear wheel and brakes of the complex landing gear on the longitudinal and transverse centreline of the observer plane.(low = 49.6 Hz, mid = 250 Hz and high = 1000 Hz third octave band)

The noise levels of the rear wheels plus brakes on the longitudinal centreline in Figure 9.15a do not show a clear trend for the low and mid frequency noise levels which are different for each of the configurations. The high frequency noise of the three configurations does show the same trend which is a constant noise level in the upstream direction and a small increase in the downstream direction. The noise levels on the transverse centreline of the observer plane in Figure 9.15b show a large asymmetry for the low frequency noise of the rear wheels plus brakes of the toe down configuration. The mid and high frequency curves are not completely symmetric either but it is unclear why the asymmetry is so large for the low frequency noise curve. The high frequency noise curves show two drops close together forming a large area of lower noise level which is the same behaviour as seen for the rear wheels of the simplified landing gear in Figure 5.17b. These two areas of low noise below the landing gear are visible in the noise directivity contours of the horizontal configuration in Figure 9.14b but not in the directivity contours of the other two complex configurations.

9.2.6 Rear axles

The shape of the noise directivity contours generated by the rear axles of the complex configurations in Figure 9.16 is similar to that of the rear axles of the simple configurations in Figure 5.18. All configurations show a peak in the far field noise level directly below the landing gear. The noise levels of rear axles of the complex configuration are lower due to the smaller surface area of the axles and the reduced flow velocity around the centre of the complex configurations.

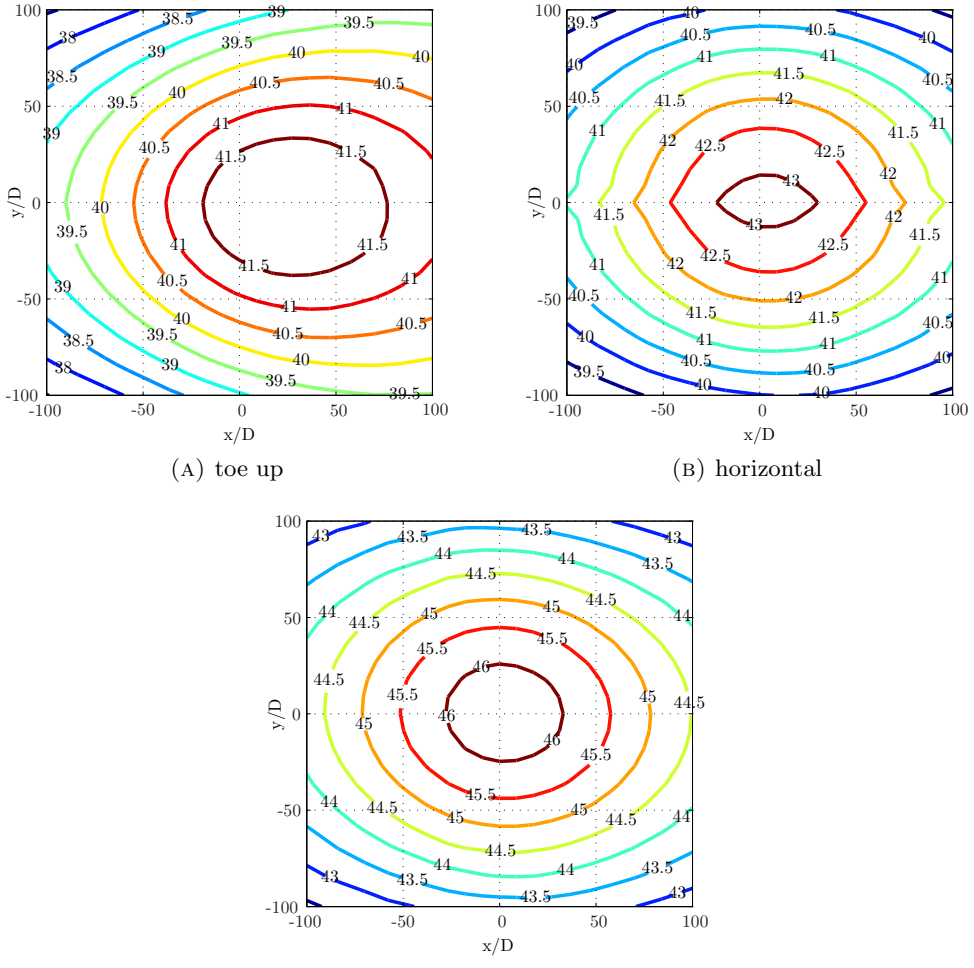

(A) toe up

(B) horizontal

(C) toe down

FIGURE 9.16: Noise directivity contours of the rear axles of the complex landing gear configurations. (OASPL in dB)

The order of the rear axles of the complex configurations is the exact opposite of the trend of the simple configurations: the rear axles of the complex toe down configuration are the noisiest and those of the toe up configuration are the quietest. This is the same trend as shown by the noise levels of the rear wheels plus brakes in the previous section. The change in the trend is due to the different flow features and agrees with the unsteady

surface pressure levels on the bottom of the rear axles (Figures 8.9f, 8.18f and 8.27f) which show the same trend.

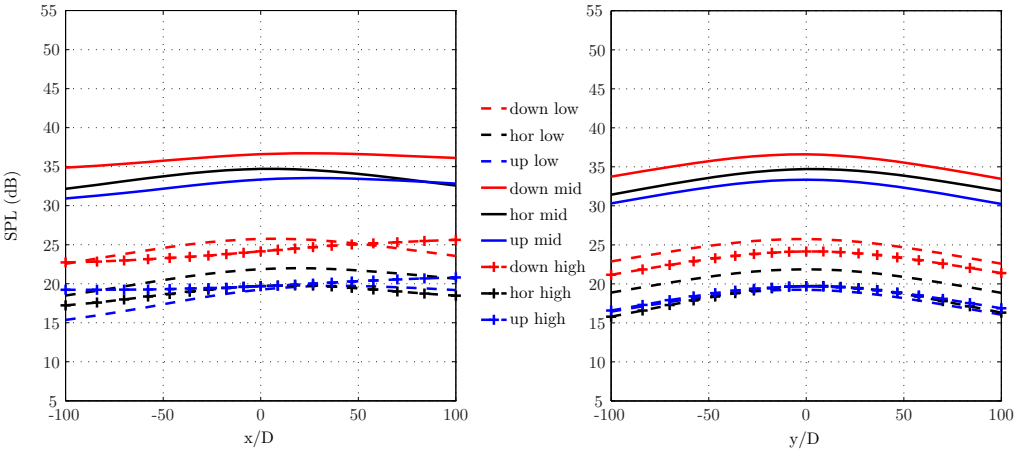

(A) longitudinal (B) transverse

FIGURE 9.17: Low, mid and high frequency noise levels generated by the rear axles of the complex landing gear on the longitudinal and transverse centreline of the observer plane.(low = 49.6 Hz, mid = 250 Hz and high = 1000 Hz third octave band)

Figure 9.17 shows the noise levels of the rear axles of the complex landing gear configurations on the longitudinal and transverse centreline of the observer plane and the mid frequency noise level is the loudest just as for the simplified landing gear in Figure 5.19. The low and mid frequency curves show a peak below the landing gear but the high frequency noise on the longitudinal centreline in Figure 9.17a shows an increasing noise level in the downstream direction just as what happens for high frequency noise of the rear axles of the simple configuration in Figure 5.19a. The difference between the low and high frequency noise levels of the complex configurations is much smaller than for the simple configurations. All frequencies show a peak below the landing gear and a drop off to the sides in the transverse centreline Figure 9.17b which is the same as seen for the rear axles of the simple configuration in Figure 5.19b.

9.2.7 Strut

The geometry of the strut of the complex configuration has changed considerably compared to that of the the simple configuration due to the addition of the yoke and swivel and increase of the diameter of the main strut. However it still acts as a dipole type noise source with far field noise peaks to the sides and a low noise level directly below the landing gear as shown in Figure 9.18. The peak noise level generated by the strut of the complex configurations has reduced compared to that of the simple configurations in Figure 5.20. The noise level in the quiet zone below the landing gear has increased considerably.

These changes in the noise levels can all be attributed to the different flow features around the complex strut as described in the previous chapter. The higher blockage at the centre of the landing gear reduces the flow velocity at the lower part of the strut which leads to lower unsteady surface pressure level compared to the simple configurations. This reduction of the unsteady surface pressure leads to a reduction of the far field noise peaks. The strut of the complex configuration has horizontal surfaces due to the addition of the yoke and the swivel which means that it will radiate noise in the downward direction. This increases the noise level in the quiet area below the landing gear compared to the simple configurations.

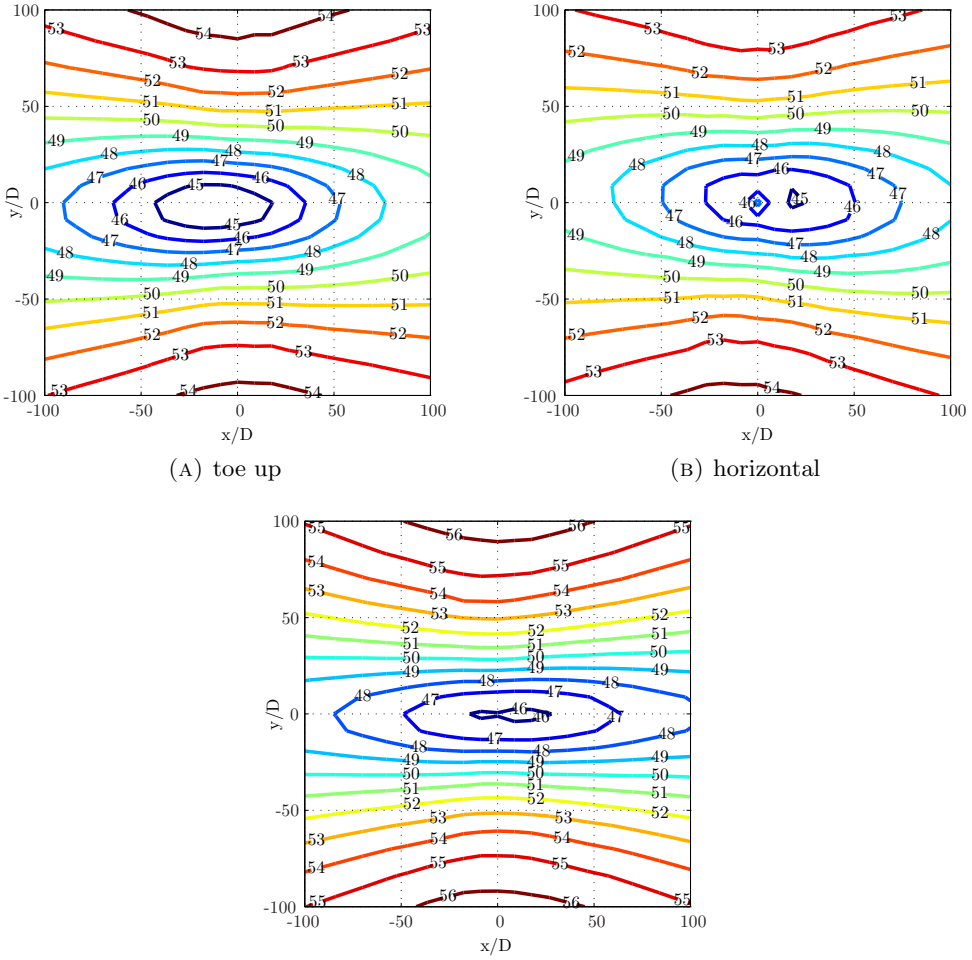

(A) toe up

(B) horizontal

(C) toe down

FIGURE 9.18: Noise directivity contours of the strut of the complex landing gear configurations. (OASPL in dB)

The noise level generated by the strut of the complex configurations is lower than that of the strut of the simple configurations but the relative noise level in the upstream and downstream directions has increased. The turbulent wake of the articulation link impinges on the front of the lower strut which leads to a peak in the unsteady surface pressure level. This causes an increase of the noise radiation in the up stream direction

compared to the simple configurations. The two streamwise vortices behind the top of the articulation link generate two peaks in the unsteady pressure distribution on the aft face of the strut. This increases the noise level in the downstream direction compared to the simple configurations.

The order of noise level of the strut of the complex configurations has reversed compared to the simple landing gear in chapter 5. The strut of the complex toe down configuration is the loudest and that of the toe up configuration the quietest. This is the same trend as the rear wheels plus brakes and also the rear axles in the previous two sections. The difference in the peak far field noise level of the three configurations is directly linked to the unsteady pressure level on the lower part of the complex strut. The toe down configuration has the highest unsteady pressure level on the side of the strut (Figure 8.29b) which leads to the highest far field noise level. The strut of the complex horizontal and toe up configurations in Figures 8.11b and 8.20b both show a similar unsteady pressure level on the side and this results in the same level of the far field noise peaks. The toe up configuration of the bogie shields the yoke and swivel from the incoming flow which reduces the noise level directly below the landing gear compared to that of the strut of the complex horizontal configuration.

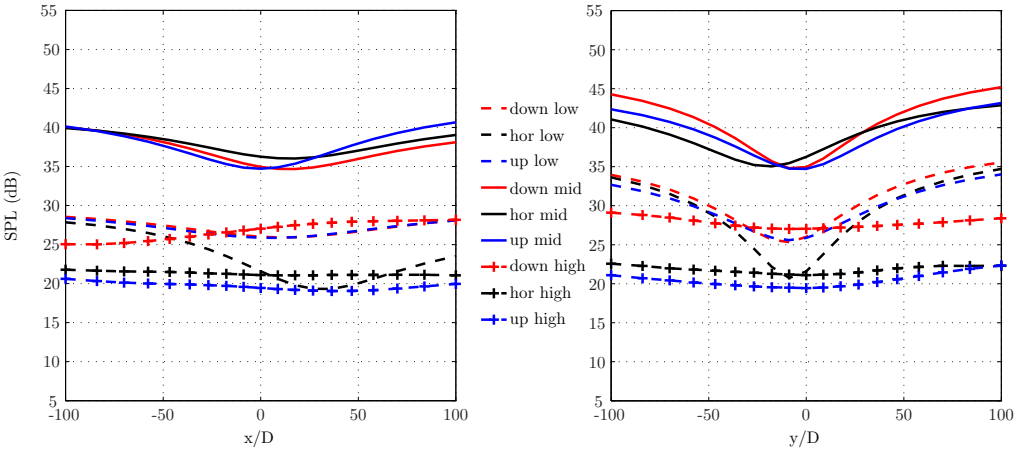

(A) longitudinal (B) transverse

FIGURE 9.19: Low, mid and high frequency noise levels generated by the strut of the complex landing gear on the longitudinal and transverse centreline of the observer plane.(low = 49.6 Hz, mid = 250 Hz and high = 1000 Hz third octave band)

The noise level of the strut on the longitudinal centreline in Figure 9.19a shows that the mid frequency is the noisiest with a drop in the noise level below the landing gear similar to noise level of the strut of the simple landing gear in Figure 5.21a. The drop in the mid frequency noise level is not as extreme as it is for the strut of the simple landing gear since the the addition of the yoke and swivel mean that the strut of the complex configurations has some surfaces directly facing the ground which is not the case for the strut of the simple configurations. The low frequency noise in the longitudinal direction

of the toe up and down configurations are almost the same with a small dip below the landing gear but the horizontal configuration is different with a significant drop in the low frequency noise level in the downstream direction. The high frequency noise level is constant for the horizontal and toe up configurations but the high frequency noise level of the toe down configuration stands out as it is much higher than the other two configurations and it also increases in downstream direction. The strut of the simple landing gear in Figure 5.21 does show large variations in the high frequency noise level due to the different amount of the lower strut that is exposed to the wake of the front wheels. The variation of the high frequency noise level of the strut of the complex configurations in Figure 9.19 is much smaller since the flow towards the lower strut is already disturbed by the articulation link for all three complex configurations.

The low and mid frequency noise levels of the strut in the transverse direction in Figure 9.19b also show a drop in the levels below the landing gear and the drop is more visible than in the longitudinal direction. The vertical orientation of the strut causes it to radiate noise in a dipole pattern to the sides which explains the more pronounced drop of the noise levels in the transverse direction. The high frequency noise curves show only a small reduction below the landing gear compared to the mid and low frequencies. The high frequency noise level of the strut in the complex toe down configuration stands out as it again has a much higher noise level than the other two configurations.

9.2.8 Torque link

There is no reference for the far field noise level generated by the torque link in Figure 9.20 since this component is not present in the simple landing gear configuration. The far field noise level generated by the torque link does not differ much between the three configurations but the shape of the directivity contour does. The torque link of the toe up configuration (Figure 9.20a) shows an asymmetric directivity pattern with only 1.2 dB difference between the minimum noise level to the sides and the maximum noise level in the upstream and downstream direction.

The noise directivity pattern of the torque link of the horizontal configuration is different with a quiet area below and slightly upstream of the landing gear. The far field noise level increases slowly in all other directions as can be seen in Figure 9.20b. A sharp increase in the noise level is visible in two small areas at the edge of the observer plane in the upstream and downstream directions. The noise directivity pattern of the torque link of the toe down configuration (Figure 9.20c) also shows a quiet area directly below the landing gear. The noise level of this configuration increases faster to the sides than it does in the up and down stream direction.

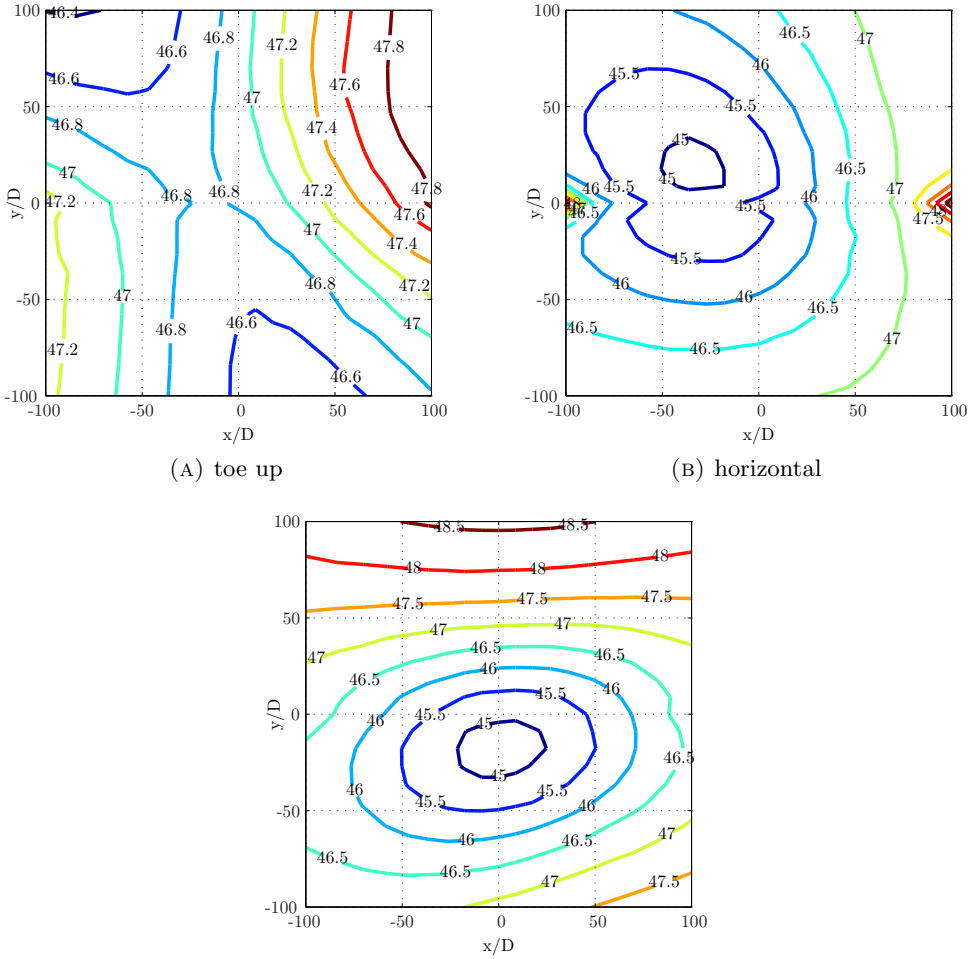

(A) toe up

(B) horizontal

(C) toe down

FIGURE 9.20: Noise directivity contours of the torque link of the complex landing gear configurations. (OASPL in dB)

Inspection of the unsteady pressure distribution on the surface of the torque link (Figures 8.11, 8.20 and 8.29) is difficult since the torque link is partly obscured by the lower strut. All three configurations show a peak in the unsteady pressure level on the corners of the lower half of the torque link. The corners stick out from behind the strut into the strong turbulent flow near the centre of the landing gear which causes the peaks. The shape of the torque link is quiet complex with lots of sharp edges and the turbulent flow moving past these edges results in local unsteady pressure peaks. The complex shape combined with an unsteady pressure distribution with multiple peaks make it impossible to give an exact explanation for the difference in the noise directivity pattern generated by the torque link of the three complex configurations.

The noise of the torque link along the longitudinal centreline in Figure 9.21a shows that the mid frequency noise level is the loudest for all three configurations. The noise level curves of all frequencies are very flat in the upstream direction but show different

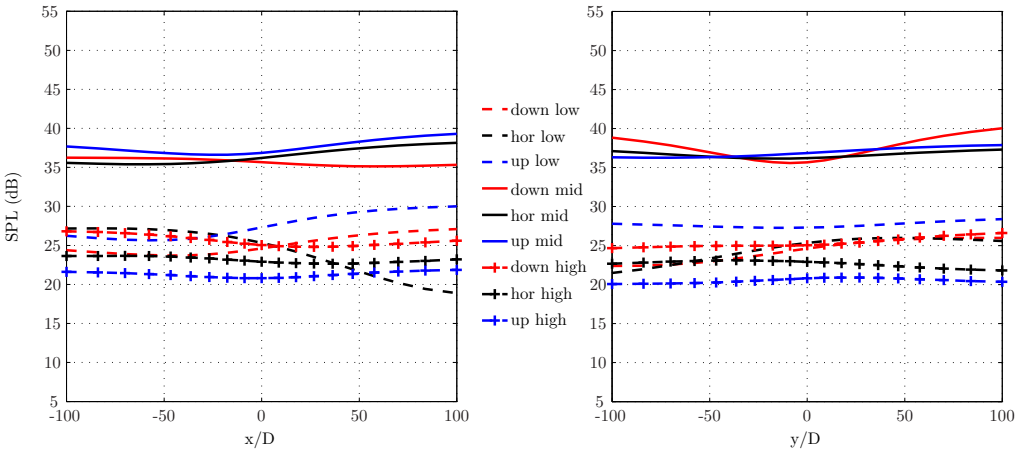

(A) longitudinal (B) transverse

FIGURE 9.21: Low, mid and high frequency noise levels generated by the torque link of the complex landing gear on the longitudinal and transverse centreline of the observer plane.(low = 49.6 Hz, mid = 250 Hz and high = 1000 Hz third octave band)

behaviour in the downstream direction. The low frequency curve of the torque link in the horizontal configuration stand out since it is the only one which shows a significant reduction of the noise level in the downstream direction. The noise level in the transverse direction in Figure 9.21b is constant for all frequencies and configurations except the mid frequency noise level of the toe down configuration which shows a drop in the noise level below the landing gear. The mid frequency noise level of all configurations is much higher than the low and high frequency noise levels but there is no trend in the order of the different configurations.

9.2.9 Complete landing gear

The noise directivity plots of the three complex landing gear configurations in Figure 9.22 show a pattern characteristic of a dipole type source with noise peaks to the sides and quiet areas in the up and downstream direction. The two dominant noise sources of the complex landing gear, the strut and the rear wheels plus brakes, both radiate noise in a dipole type pattern. The contribution of the bogie is clearly visible as a spike in the otherwise smooth contours of the noise directivity pattern of the complex horizontal landing gear configuration (Figure 9.22b).

The noise contribution of the other components is not large enough to show up in the directivity plot of the complete landing gear. The upstream components such as the articulation link, front axles and front wheels plus brakes are in the relatively clean flow and do not generate enough far field noise compared to the dominant sources. The torque link does generate a reasonable amount of far field noise but the level is relatively

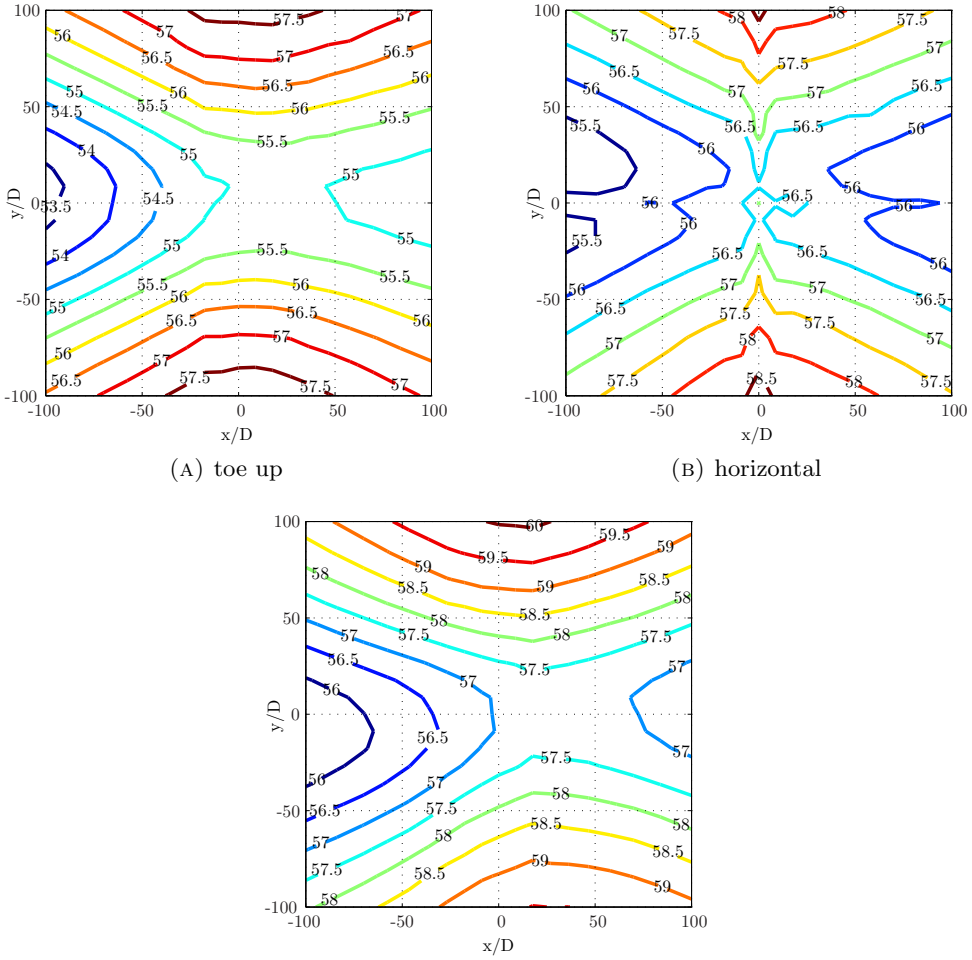

(A) toe up

(B) horizontal

(C) toe down

FIGURE 9.22: Noise directivity contours of the complex landing gear configurations. (OASPL in dB)

constant over the observer plane such that it does not change the shape of the contours. The rear axles are one of the dominant noise sources of the simple landing gear but this is no longer the case for the complex configuration. Their contribution to the far field noise has dropped well below that of the strut and rear wheels plus brakes.

The order of complex landing gear configurations based on the peak noise level on the observer plane is as follows: the toe down configuration is the loudest followed by the horizontal configuration and the toe up configuration which is the quietest. This is the exact opposite order compared to that of the simple landing gear configurations in chapter 5. The downstream components are responsible for most of the landing gear noise due to the high turbulence level of the flow. The additional components have changed the main flow features around the complex landing gear and this results in a different trend of the far field noise levels. The toe down configuration of the bogie leads to a higher flow velocity in the centre of the landing gear compared to the other two

complex configurations. Combining this increased flow velocity with the high turbulence levels due to a different flow separation pattern on the front wheels results in the highest far field noise level for the complex toe down configuration. The forward components of the complex toe up configuration block the high velocity flow to the centre of the landing gear which leads to the lowest far field noise levels of the complex configurations.

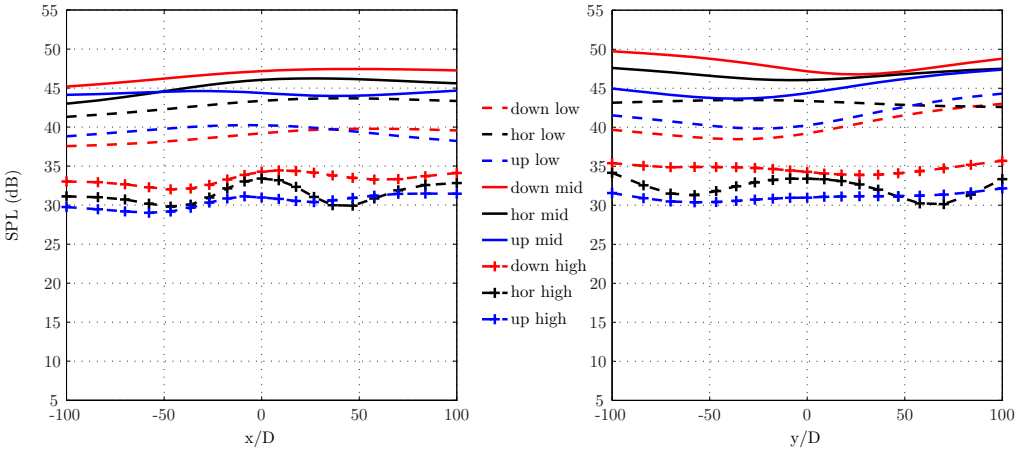

(A) longitudinal (B) transverse

FIGURE 9.23: Low, mid and high frequency noise levels generated by the complete complex landing gear on the longitudinal and transverse centreline of the observer plane.(low = 49.6 Hz, mid = 250 Hz and high = 1000 Hz third octave band)

Most of the components of the complex landing gear show a high level of the mid frequency noise and this is also the case for the complete landing gear in Figure 9.23. The difference between the low and mid frequency noise level of the complex landing gear is much smaller than that of the simple landing gear in Figure 5.23. The low and mid frequencies show a small peak in the noise level below the landing gear in the longitudinal direction (Figure 9.23a) but a small drop in the noise level below the landing gear in the transverse direction (Figure 9.23b). This opposite behaviour is due to the fact that the overhead position is a saddle point on the noise contour as shown in Figure 9.22. This is not the case for the high frequency noise level which varies more in both the longitudinal and transverse directions. The order of the mid and high frequency noise levels is the same with the complex toe down configuration being the loudest followed by the horizontal and toe up configurations. The low frequency noise level of the complex landing gear does not follow same trend and shows the lowest noise level for the toe down configuration.

9.3 Summary and discussion

The acoustic results of the complex landing gear configurations show that the peak overhead noise level has reduced compared to that of the simple landing gear configurations. This is mainly caused by the addition of the extra components which increase the blockage and therefore reduce the flow velocity near the centre of the landing gear. This results in less intense surface pressure fluctuations and thus a lower far field noise level compared to the simple landing gear configurations. Another effect of the added components is that they disturb the flow more which results in a faster break down of the large coherent flow structures. The faster break down of the large energetic flow structures also reduces the intensity of the surface pressure fluctuations.

The peak noise level has reduced but the frequency range of the far field noise of the complex configurations is the same as that of the simple configurations. The complex landing gear geometry has more details which should generate more small scale flow structures and thus a larger frequency range of the far field noise. The frequency range of the far field noise does not only depend on the size of the geometric details but also on the cell size of the grid used for the simulations. The number of cells in the grid of the complex CFD simulations is approximately three times that of the simple CFD simulations. However most of the extra cells are used in the boundary layer of the additional components and also in the extended size of the flow domain. The mean cell size outside the boundary layer but near the geometry is similar for the CFD simulations of both the simple and complex configurations. This results in the same size of the resolved flow structures and thus the same frequency range of the far field noise.

The addition of the components changes the flow field around the complex configurations compared to the simple configurations as shown in the previous chapter. The changes in the flow field also affect the far field noise directivity patterns and noise levels. The noise directivity pattern of the components is affected differently depending on the location of the component. The upstream components of the landing gear are in the undisturbed flow and generate a relatively low far field noise level. This means that the noise directivity pattern is more sensitive to changes in the flow features. The directivity patterns of the front wheels plus brakes and front axles of the complex configuration are different compared to the same components of the simple configuration. The downstream components are immersed in the turbulent flow and therefore generate a higher far field noise level. This makes the noise directivity pattern less sensitive to the changes in the flow features. The directivity patterns of the strut, rear wheels plus brakes and rear axles are similar to the patterns generated by their counterparts of the simple configuration. The downstream components are the dominant noise sources and

the noise directivity pattern of the complete complex landing gear therefore resembles that of the simple configuration.

The change in the flow features may not have much influence on the shape of the noise directivity pattern of the complex landing gear it does have a strong effect on the far field noise levels. The noise level generated by most components of the complex configurations has reduced compared to those of the simple configurations as already has been shown by the lower peak noise levels of the overhead spectra. Not only has the noise level been reduced but the order of the three complex configurations has completely changed compared to that of the simple landing gear. The toe down configuration is the quietest of the three simple landing gear but the noisiest configuration of the complex landing gear. The change in the flow separation pattern on the front wheels results in a different trajectory of the strong streamwise vortices. These vortices move past the bottom of the rear wheels plus brakes at a much shorter distance than for the simple toe down configuration. The articulation link at the front of the landing gear generates a wake which increases the turbulence levels of the flow that reaches the downstream components. The toe down configuration opens up the path of the high velocity freestream flow to the centre of the landing gear. The combination of these effects leads to an increase of the unsteady surface pressure levels and thus a higher far field noise level.

The toe up configuration is the noisiest of the three simple landing gears but turns out to be the quietest of the complex configurations. The increased blockage of the complex geometry reduces the flow velocity near the lower part of the strut which leads to a drop of the far field noise level compared to the simple configuration. Most of the turbulent flow passes over the top of the rear axles and rear wheels of the toe up configuration such that most noise is radiated away from the observer plane below the landing gear.

The flow features of the horizontal configuration show the most similarity between the simple and complex landing gears. This results in a peak far field noise level of the horizontal configuration that sits in between the other two configurations. The peak noise level of the complex horizontal landing gear may not stand out but the bogie of this configuration generates by far the most noise of the three configurations. The mean flow features of both the simple and complex horizontal configuration show that the bogie is surrounded by four strong streamwise vortices. The induced flow of these vortices pushes the turbulence into the sides of the bogie which results in the high unsteady surface pressure levels on the sides of the bogie. The combination of the unsteady pressure distribution and shape of the bogie lead to a high far field noise level in a narrow transverse band below the landing gear.

Chapter 10

Conclusions and recommendations

The aim of this research is to identify the important flow features around the bogie area of a main landing gear and the effect of the bogie inclination angle on these flow features. The second aim is to determine the location of the major noise sources on the landing gear surface and the relation between the flow features and the noise sources. The landing gear is a complex structure challenging the current simulation capabilities such that a two step approach has been used. The first part of the research is based on a simplified landing gear configuration and this has been changed to a more realistic complex landing gear configuration for the second part of the research. The conclusions in the next two sections summarise the findings of the research and are followed by further recommendations.

10.1 Simplified landing gear configurations

The flow field around the simplified landing gear configurations is dominated by the strong streamwise vortices that form at the downstream edge of the front wheels. There is a difference in flow direction over the sides of the front wheel and the flow along the tread of the wheel which results in the formation of streamwise vortices when the flows meet. The formation of these vortices depends strongly on the relative orientation of the front and rear wheels. The orientation of the wheels is symmetric for the horizontal configuration and this results in four strong streamwise vortices that move downstream parallel to the bogie. The orientation of the wheels is not symmetric for the toe up and toe down configurations which changes the vortex formation. The blockage of the flow by the presence of the rear wheel causes a pressure increase which changes the

flow direction along the aft part of the front wheel. This change in local flow direction increases the vortex strength on this side of the wheel and causes a displacement of the wake towards the opposite side of the front wheel. The displacement of the wake changes the pressure distribution on the opposite side of the front wheel and leads to flow separation across the tread of the wheel. The simplified landing gear geometry is not symmetric in the vertical direction due to the presence of the strut but this does not affect the vortex formation and flow separation on the front wheels. The results show a consistent trend for the simplified landing gear configurations. The vortex formation and flow separation pattern on the front wheels of the toe up and toe down configuration are almost mirror images.

The strong streamwise vortices generated at the front wheels of the simplified landing gear move downstream with the mean flow. The trajectory of the strong streamwise vortices determines where the turbulent flow interacts with the downstream components of the landing gear. The interaction of the turbulent flow with the solid geometry results in high unsteady surface pressure levels. The unsteady surface pressure distribution is a good indicator of where the noise is generated. The vortices of the horizontal configuration move downstream parallel to the bogie and are not influenced by the presence of the strut. The wake of the strut limits the upward trajectory of the streamwise vortices of the toe up configuration such that the vortices pass over the top of the rear axles in between the rear wheels. The downward trajectory of the streamwise vortices of the toe down configuration is not influenced by the wake of the strut and the vortices pass below the rear wheels. This changes the distance between the streamwise vortex cores and the aft part of the geometry for the toe up and toe down configurations. The unsteady surface pressure levels at the downstream part of the simplified landing gear are strongly related to this distance between the vortex cores and the geometry.

The overhead noise spectra of the simplified landing gear configurations show a characteristic haystack shape without any tonal features. The overhead spectra show that the far field noise is dominated by the contribution of the downstream components of the landing gear configurations. The bogie is the dominant overhead noise source of the horizontal configuration but is less important for the toe up and toe down configurations. The noise generated by the strut does not show up in the overhead spectra due to the 90° angle between the surface normal vectors and the direction of the observer. The peak noise levels of the overhead spectra is related to the trajectory of the strong streamwise vortices. The vortices of the horizontal configuration move downstream along the bogie and pass in between the rear wheels. This puts the vortices close to the bogie and rear axles which makes the horizontal configuration the noisiest of the three simplified landing gear in the overhead direction. The vortices of the toe down configuration move downstream below the rear wheels and the results in the largest distance between the

vortices and the geometry. This makes the toe down configuration the quietest in the overhead direction. The vortices of the toe up configuration pass over the top of the rear axles but still in between the rear wheels. The distance between the vortices and the geometry is further than for the horizontal configuration but closer than the toe down configuration. The peak noise level of the toe up configuration in the overhead direction sits in between the peak noise levels of the other two configurations.

The noise directivity contours of the components of the simplified configurations show a high noise level generated by the strut which does not show up in the overhead spectra. The strut is a cylinder and generates a dipole type noise source: noise peaks to the sides and a reduced noise level in the upstream and downstream directions. The noise level generated by the strut is directly related to the area of the lower strut that is exposed to the turbulent flow. The toe up configuration moves the front wheels up and therefore exposes a larger part of the strut to the turbulent wake. This makes the strut of the toe up configuration the noisiest of the three configurations. The opposite happens for the flow around the strut of the toe down configuration which therefore is the quietest of the three configurations. The rear wheels and rear axles are also important noise sources, the rear wheels generate noise peaks to the sides while the rear axles generate a far field noise peak directly below the landing gear. The bogie is an important noise source for the horizontal configuration and generates a noise peak below the landing gear. The noise contribution of the bogie for the other two configurations is much lower and generates noise peaks to the sides.

All three simplified landing gear configurations generate a dipole type noise directivity contour with noise peaks to the sides and a more quiet area in the upstream and downstream directions. The order of the simplified landing gear configurations is the same as that of the strut which is the dominant noise source. The toe up configuration of the simplified landing gear is the noisiest and the toe down configuration the quietest. The strut of the toe down configuration is no longer the dominant noise source since its noise level has fallen below the noise level of the rear wheels. However this does not change the directivity pattern of the toe down configuration since the now dominant rear wheels also radiate most noise to the sides.

10.2 Complex landing gear configurations

The mean flow features of the complex landing gear configurations also show the formation of strong streamwise vortices but their formation does not follow the same trend as seen for the simplified configurations. The addition of the articulation link, torque link and the more realistic geometry of the strut result in an increase of the blockage and

this makes the geometry more asymmetric in the vertical direction. This changes the vortex formation and flow separation process on the front wheels and breaks the trend seen for the flow features around the simplified configurations. The strong streamwise vortices of the complex horizontal and toe up configurations originate from the inside edge of the front wheels while those of the toe down configuration start from the bottom of the front wheels. The streamwise vortices of the complex configurations move downstream following the mean flow direction. This results in a position of the vortex cores at the downstream part of the complex landing gear configurations that is similar to that of the simplified configurations. The trajectory of the streamwise vortices of the complex horizontal configuration is the same as that of the simple horizontal configuration. However the trajectory of the streamwise vortices of both the complex toe up and toe down configurations is different compared to the equivalent simplified configuration. The change in the trajectory of the streamwise vortices results in different locations where the turbulent flow interacts with the solid geometry of the complex landing gear.

The additional components have increased the blockage of the complex landing gear configuration compared to the simplified configuration. The increased blockage forces a larger part of the flow around the outside of the complex landing gear. The resulting flow through the centre of the complex landing gear has a lower velocity compared to the simplified configurations. The additional components also increase the turbulence levels around the complex landing gear compared to the simplified configurations. The addition of the articulation link is particular important since it generates a turbulent wake which changes the flow conditions for the downstream components. The increased turbulence levels of the flow lead to a quicker break down of the large energetic flow structures. The combined effect is a reduction of the unsteady surface pressure levels of the complex configurations compared to the simplified configurations. The unsteady pressure levels near the centre of the complex landing gear differ between the three configurations. The complex toe up configuration shields the components in the centre of the landing gear from the high velocity flow which leads to a reduction of the unsteady surface pressure levels. The opposite happens for the complex toe down configuration which opens up the path to the centre of the landing gear resulting in a higher local flow velocity and therefore higher unsteady surface pressure levels.

The overhead noise spectra of the complex landing gear configurations show a lower noise level than those of the simplified configurations. The downstream components are again the main source of noise of the landing gear just as for the simplified configurations. The bogie is the dominant overhead noise source of the complex horizontal configuration but not for the other two complex configurations. The rear wheels plus brakes are the dominant noise source in the overhead direction of the toe up and toe down configurations and also generate a significant amount of noise in the complex horizontal configuration.

The rear axles are an important overhead noise source of the simple landing gear configurations but their contribution is low for the complex configurations. The surface area of the axles of the complex configuration has reduced due to the addition of the brake units which leads to a drop of the far field noise levels. The addition of the yoke and swivel to the strut means that it does generate noise in the overhead direction which was not the case for the simplified configurations.

The strut of the complex configuration generates less noise than it does for the simplified configurations but it remains the dominant noise source of the complex landing gear. The additional components have changed the geometry of the strut but it still generates a dipole type pattern. The rear wheels plus brakes also generate a significant amount of far field noise and they also produce a dipole type pattern. This is due to the relatively large surface area of the sides of the wheel compared to the smaller surface area of the wheel tread. The two dominant noise sources of the complex configurations generate dipole type directivity patterns which means the noise contours of the total complex landing gear configurations also shows a dipole type pattern. Most of the other components do not generate enough far field noise to influence the shape of the contours with the exception of the bogie of the complex horizontal configuration. The bogie of the horizontal configuration generates a narrow transverse band with a high noise level below the landing gear and this shows up as a spike in the otherwise smooth noise directivity contour of the complete complex landing gear. The directivity pattern of the complex configurations is similar to that of the simple configurations but the order of the configurations has changed. The complex toe down configuration is the noisiest and the toe up configuration the quietest which is the opposite trend compared to the simple configurations. This change in the order of the configurations follows from the change in the flow features and agrees with the unsteady pressure levels near the centre of the landing gear.

10.3 Recommendations

The results of the current study show the effect of the change in bogie angle on the flow features and far field noise levels of the main landing gear. Two main landing gear configurations with different levels of complexity have been used and the available resources have limited the number of bogie angle to three. The trajectory of the streamwise vortices show a strong dependency on the bogie angle and it would be useful to see how these flow features behave over a larger range of bogie angles.

The frequency range of the far field noise of the current study is limited due to the available computational resources which limit the number of grid points and sampling

time of the CFD simulations. An increase of the number of grid points would reduce the cell size near the landing gear and resolve more of the small scale flow structures. Resolving the smaller flow structures will increase the frequency range of the far field noise. The availability of computational resources continues to improve due to advances in technology and this will lead to higher resolution CFD simulations in the future.

The flow around the simple and complex main landing gear configurations show different trends of the important flow features with respect to the bogie angle. The difference in the flow features changed the far field noise levels which shows that it is not always possible to use the results of a simplified model to make predictions about more complex configurations. The computational costs of a CFD simulation of an actual landing gear geometry are still too high such that simplification of the landing gear geometry for CFD will continue to be necessary in the near future. Comparison of the results of these simplified models with wind tunnel experiments of actual geometries will be needed to make sure that the trends of the important flow features are the same.

Both the simplified and complex geometry generate strong streamwise vortices at the front wheels which have a large influence on the flow field around the downstream part of the main landing gear. The interaction of these vortices with the downstream components are an important source of noise. The formation of these strong vortices behind a bluff body such as a wheel will be difficult to avoid but a possible far field noise reduction can be achieved by changing the trajectory of the streamwise vortices and reducing their interaction with the downstream components.

Appendix A

OpenFOAM discretisation schemes

```
/*---------------------------*- C++ -*----------------------------*\
| =========                 |                                     |
| \\      /  F ield         | OpenFOAM: The Open Source CFD Toolbox   |
|  \\    /   O peration     | Version:  1.7.1                     |
|   \\  /    A nd           | Web:      www.OpenFOAM.com          |
|    \\/     M anipulation  |                                     |
\*-------------------------------------------------------------------*/
FoamFile
{
    version     2.0;
    format      ascii;
    class       dictionary;
    location    "system";
    object      fvSchemes;
}
// * * * * * * * * * * * * * * * * * * * * * * * * * * * * * * * * * * * * //

ddtSchemes
{
    default         backward;
}

gradSchemes
{
    default         Gauss linear;
    grad(p)         Gauss linear;
    grad(U)         Gauss linear;
}
```

```
divSchemes
{
    default                             none;
    div(phi,U)                          Gauss limitedLinearV 1;
    div(phi,nuTilda)                    Gauss limitedLinear 1;
    div((nuEff*dev(grad(U).T())))       Gauss linear;
}

laplacianSchemes
{
    default                             none;
    laplacian(nuEff,U)                  Gauss linear limited 0.5;
    laplacian((1|A(U)),p)               Gauss linear limited 0.5;
    laplacian(DnuTildaEff,nuTilda)      Gauss linear corrected;
    laplacian(1,p)                      Gauss linear corrected;
}

interpolationSchemes
{
    default         linear;
    interpolate(U)  linear;
}

snGradSchemes
{
    default         corrected;
}

fluxRequired
{
    default         no;
    p               ;
}


// ************************************************************************* //
```

Appendix B

Magnitude of the dipole source term of the simplified main landing gear

B.1 Toe up configuration

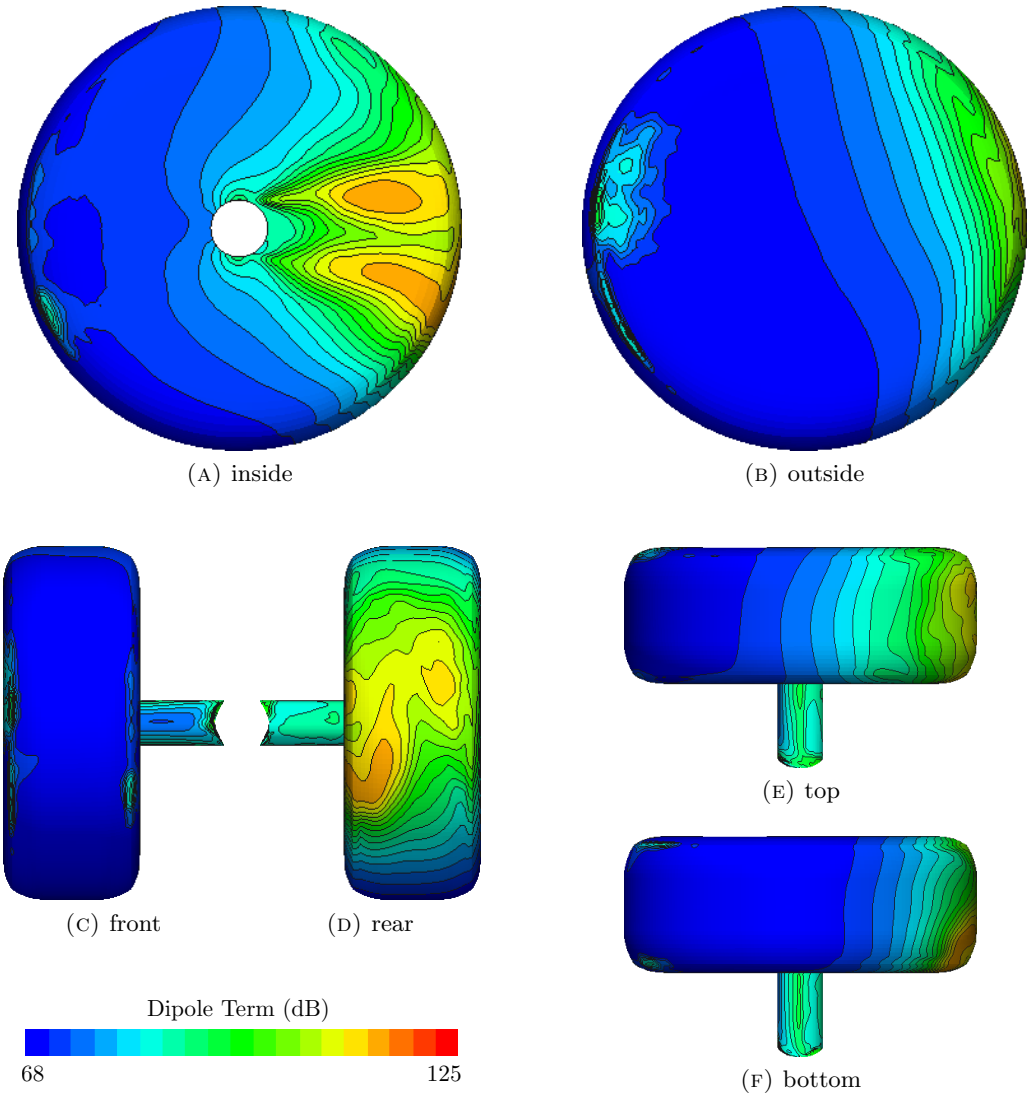

FIGURE B.1: Magnitude of the dipole source term on the forward wheel and axle of the simplified toe up configuration.

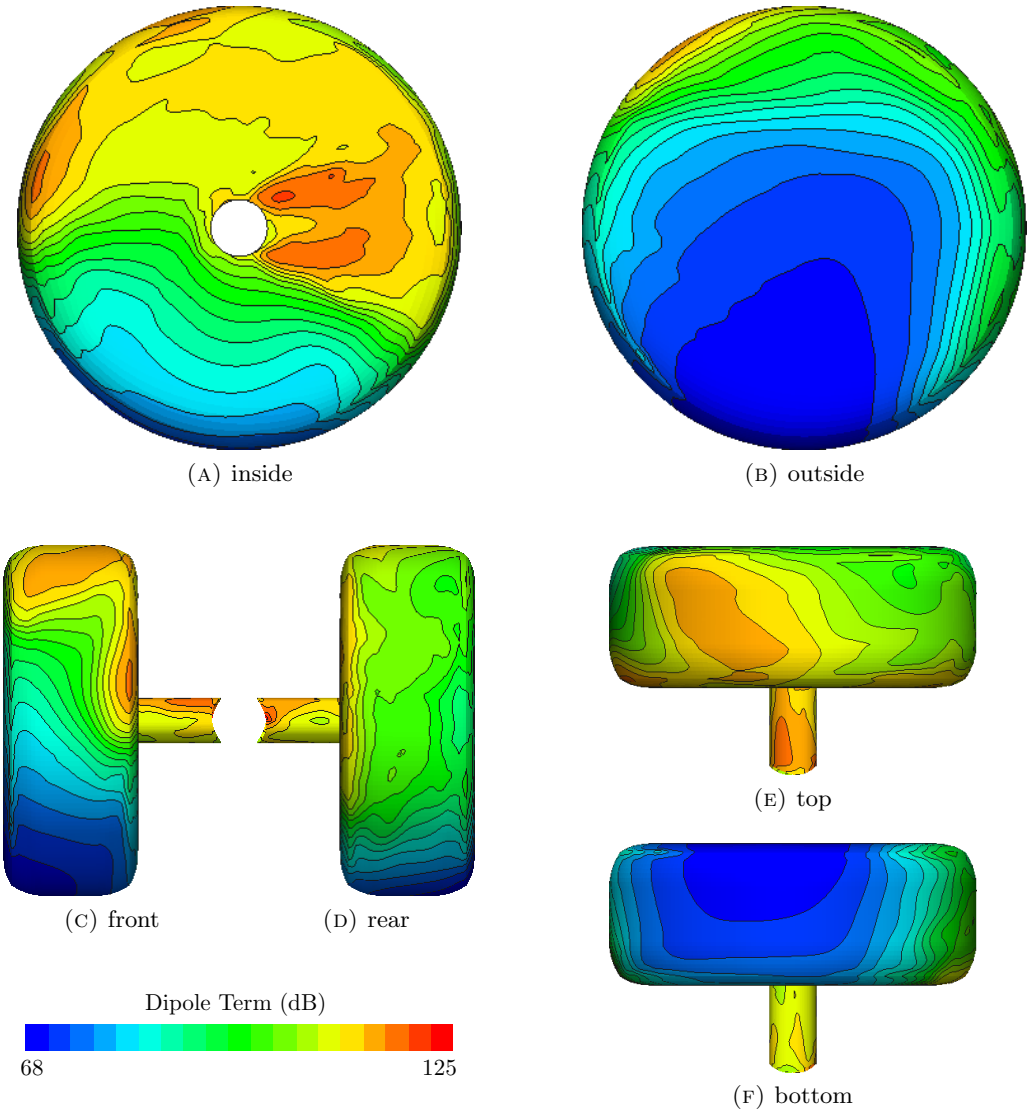

(A) inside (B) outside

(C) front (D) rear

(E) top

(F) bottom

FIGURE B.2: Magnitude of the dipole source term on the rear wheel and axle of the simplified toe up configuration.

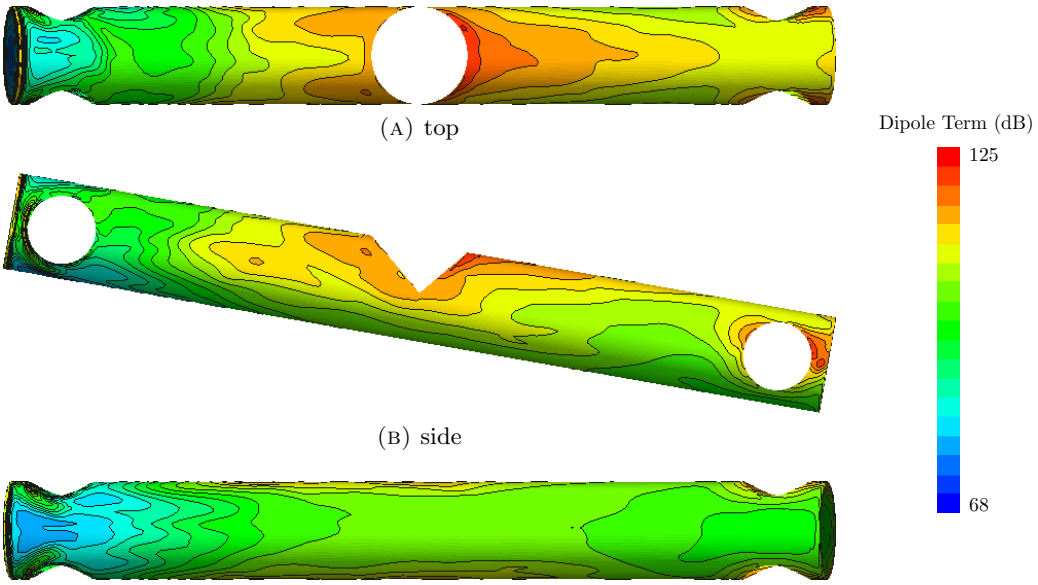

(A) top

(B) side

(C) bottom

FIGURE B.3: Magnitude of the dipole source term on the bogie of the simplified toe up configuration.

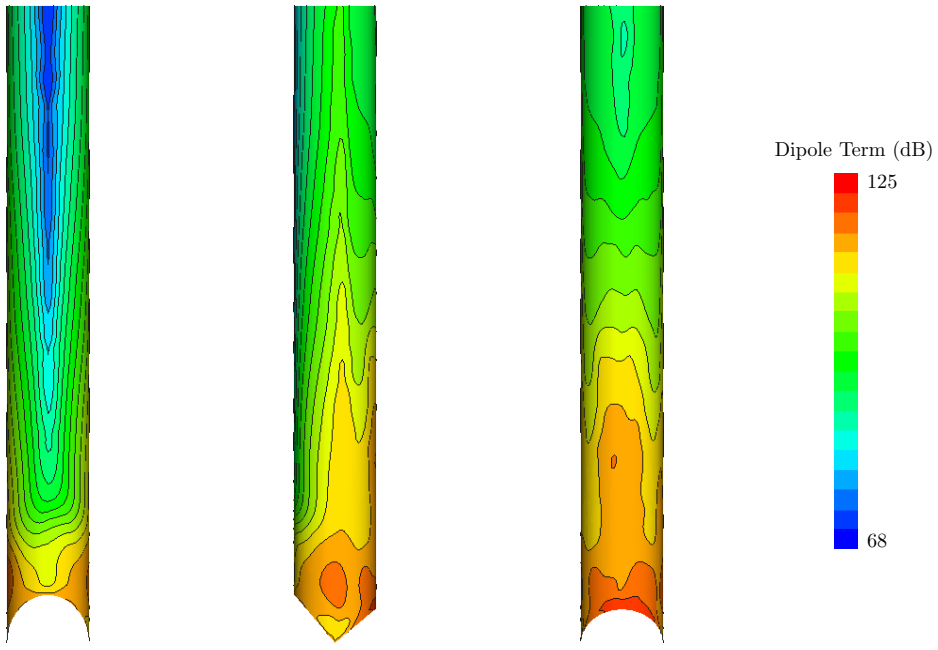

(A) front (B) side (C) rear

FIGURE B.4: Magnitude of the dipole source term on the lower half of the strut of the simplified toe up configuration.

B.2 Toe down configuration

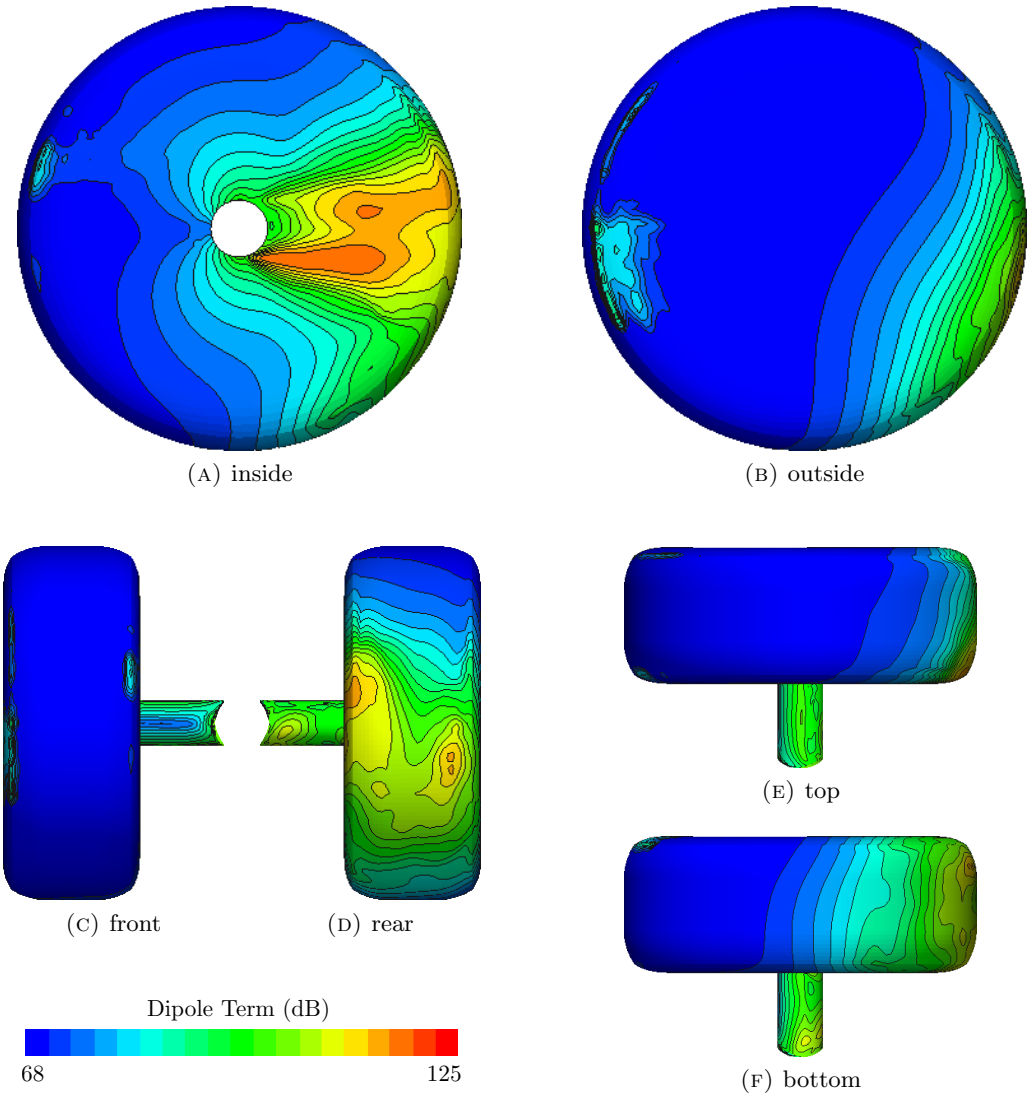

FIGURE B.5: Magnitude of the dipole source term on the forward wheel and axle of the simplified toe down configuration.

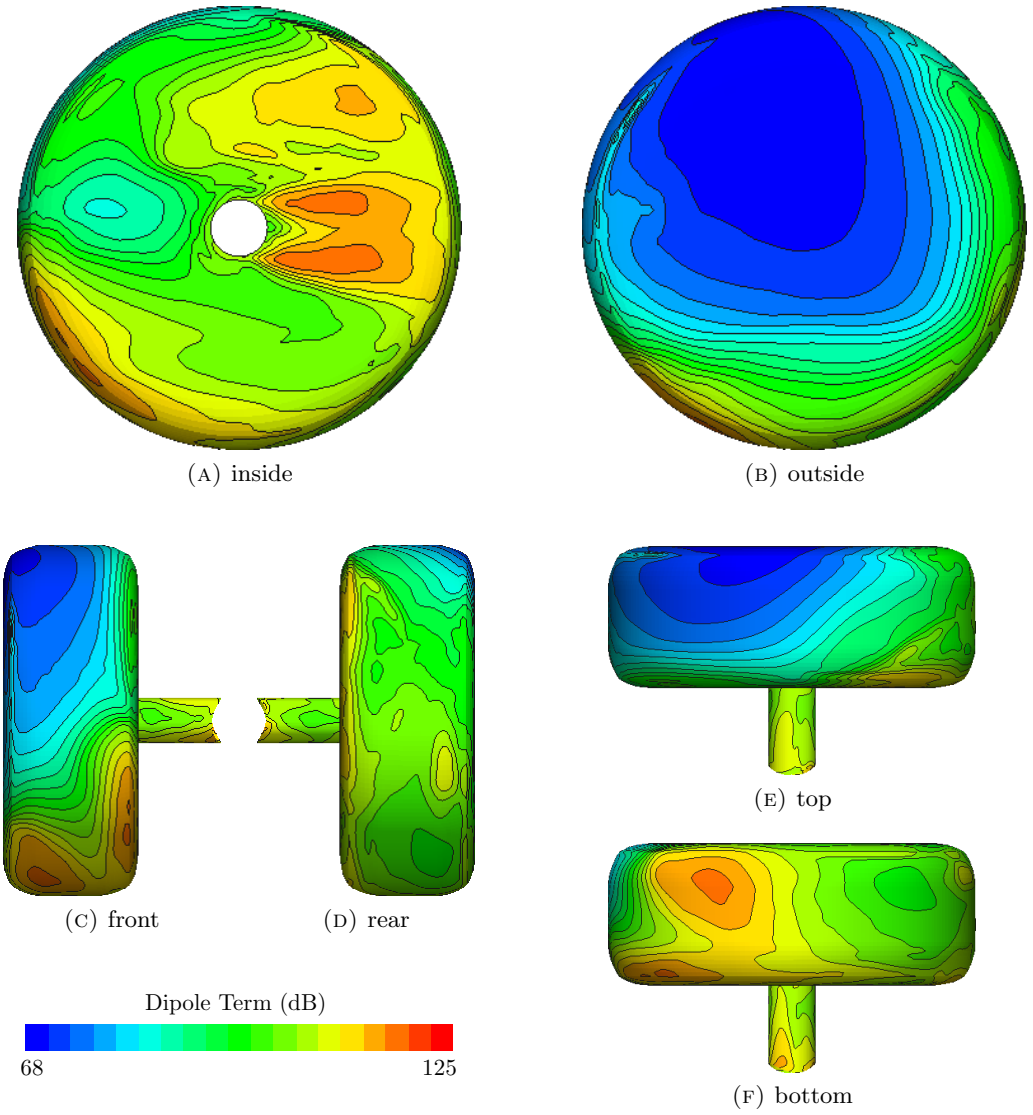

FIGURE B.6: Magnitude of the dipole source term on the rear wheel and axle of the simplified toe down configuration.

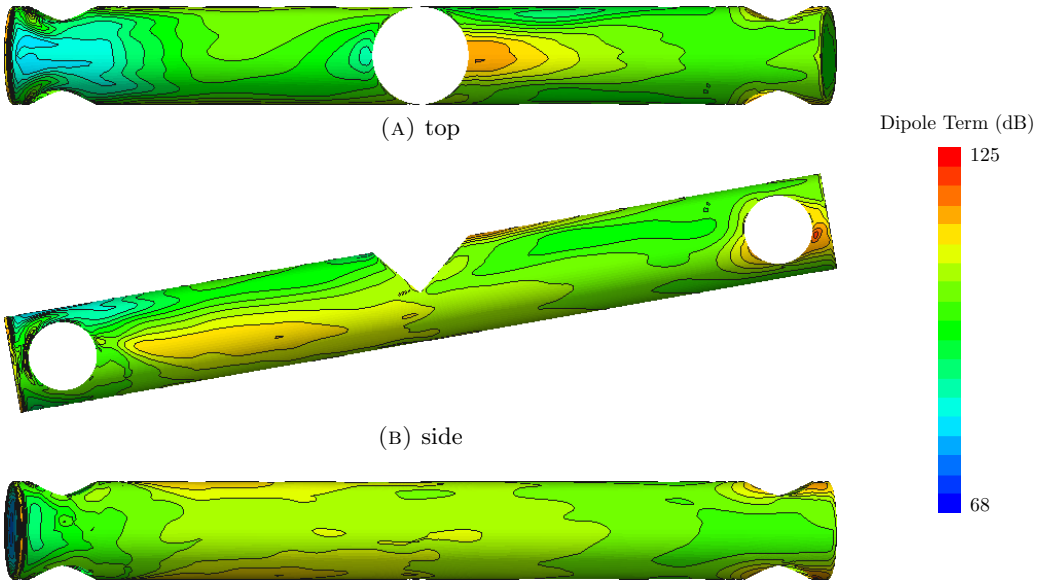

(A) top

(B) side

(C) bottom

FIGURE B.7: Magnitude of the dipole source term on the bogie of the simplified toe down configuration.

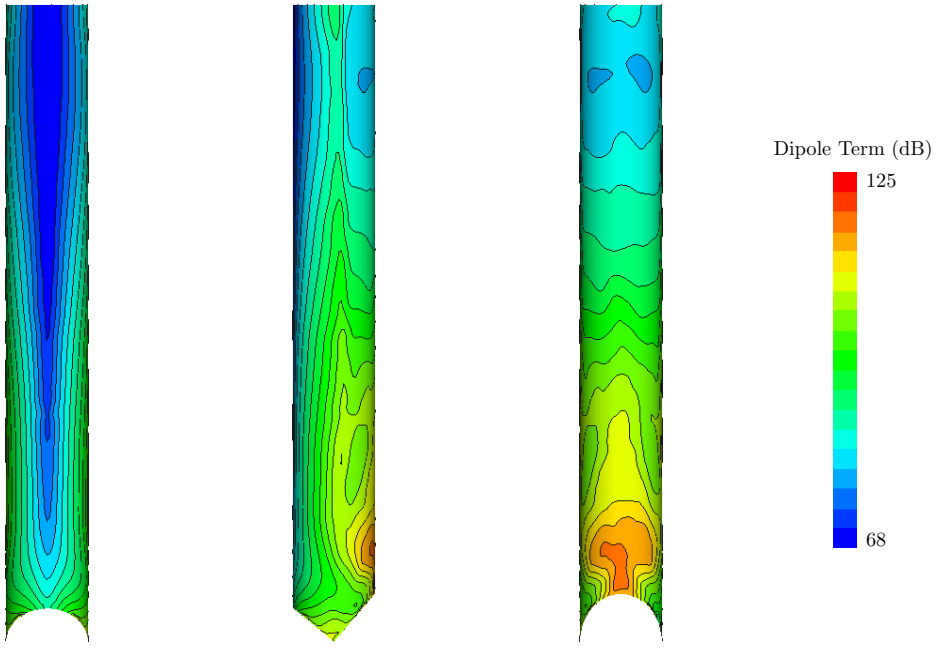

(A) front (B) side (C) rear

FIGURE B.8: Magnitude of the dipole source term on the lower half of the strut of the simplified toe down configuration.

B.3 Toe up configuration calculated from OpenFOAM results

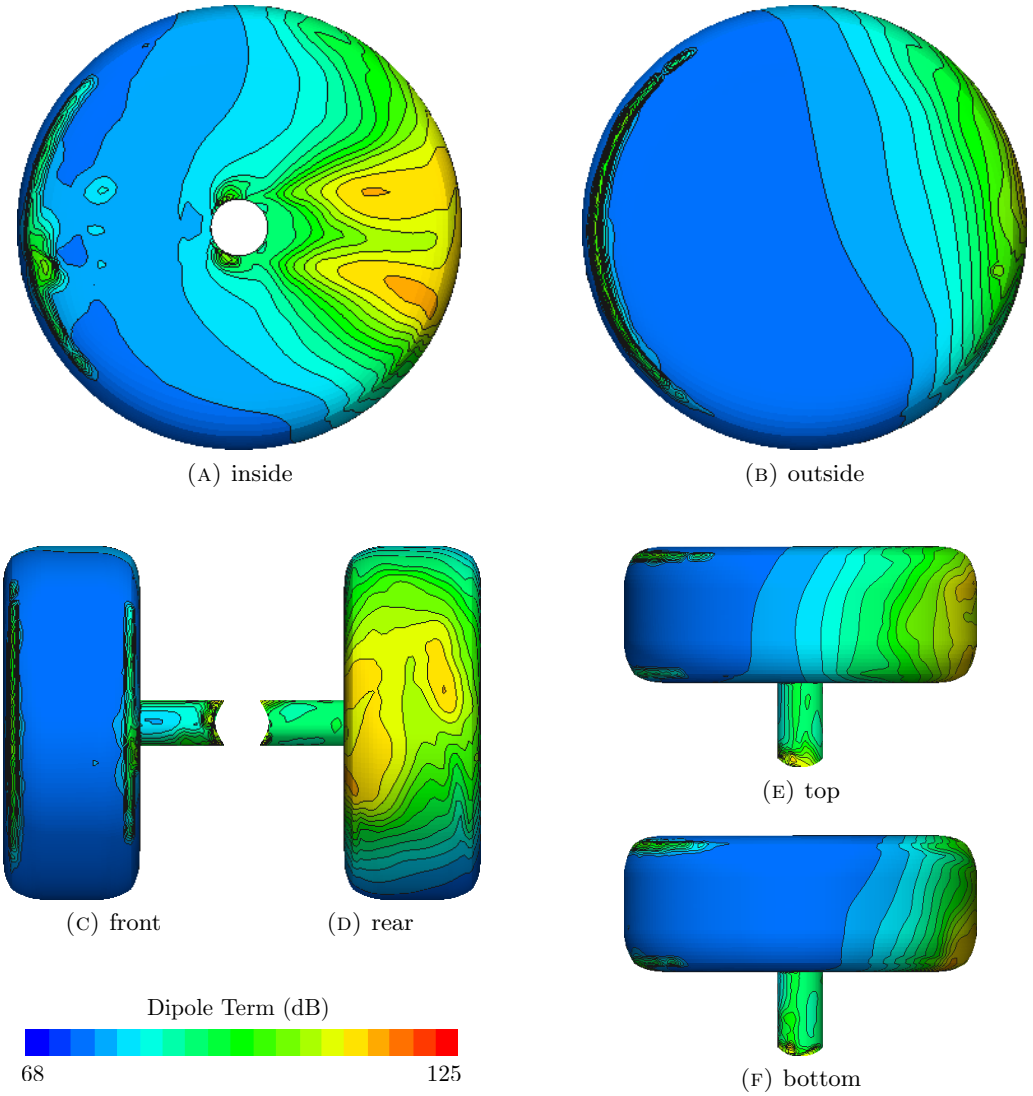

(A) inside (B) outside

(C) front (D) rear

(E) top

(F) bottom

FIGURE B.9: Magnitude of the dipole source term on the forward wheel and axle of the simplified toe up configuration.

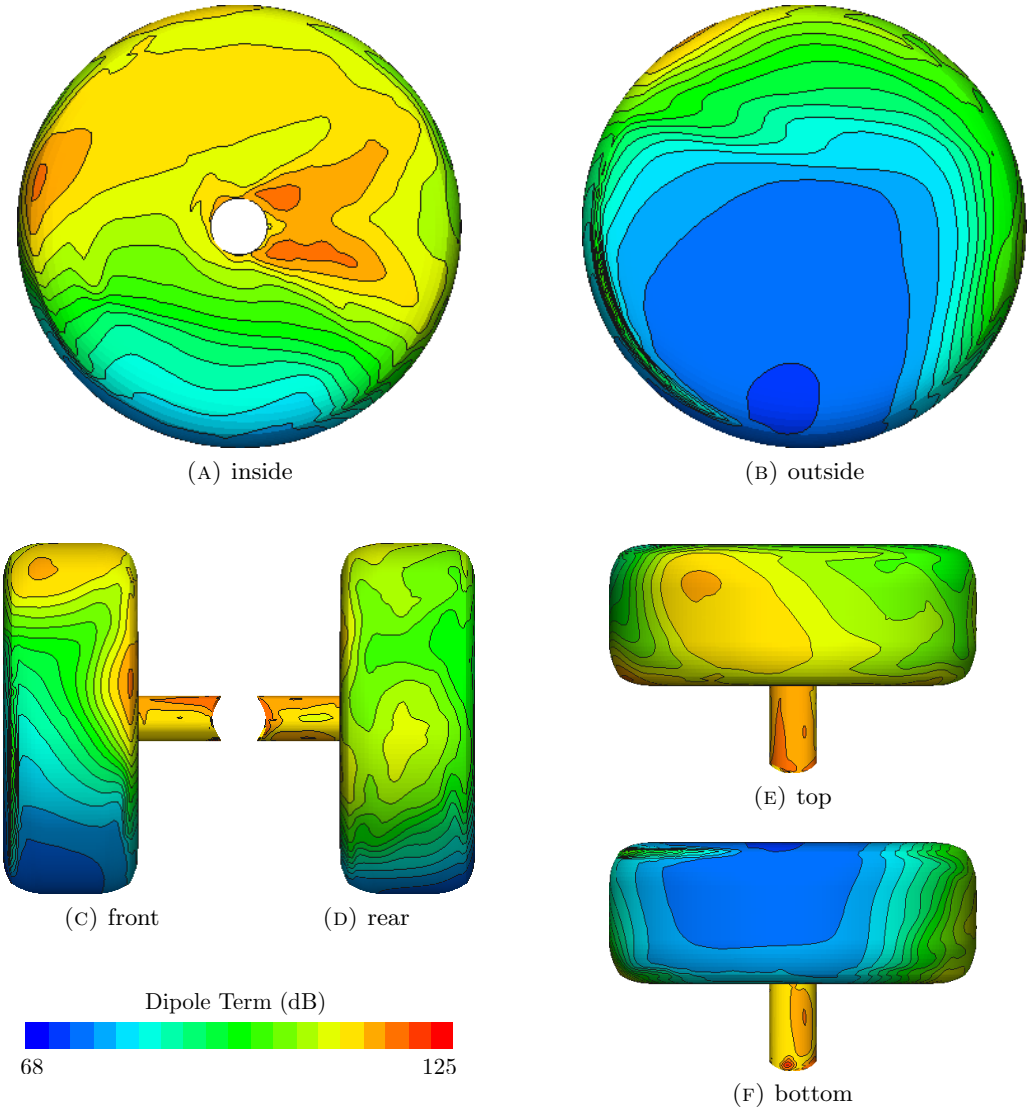

FIGURE B.10: Magnitude of the dipole source term on the rear wheel and axle of the simplified toe up configuration.

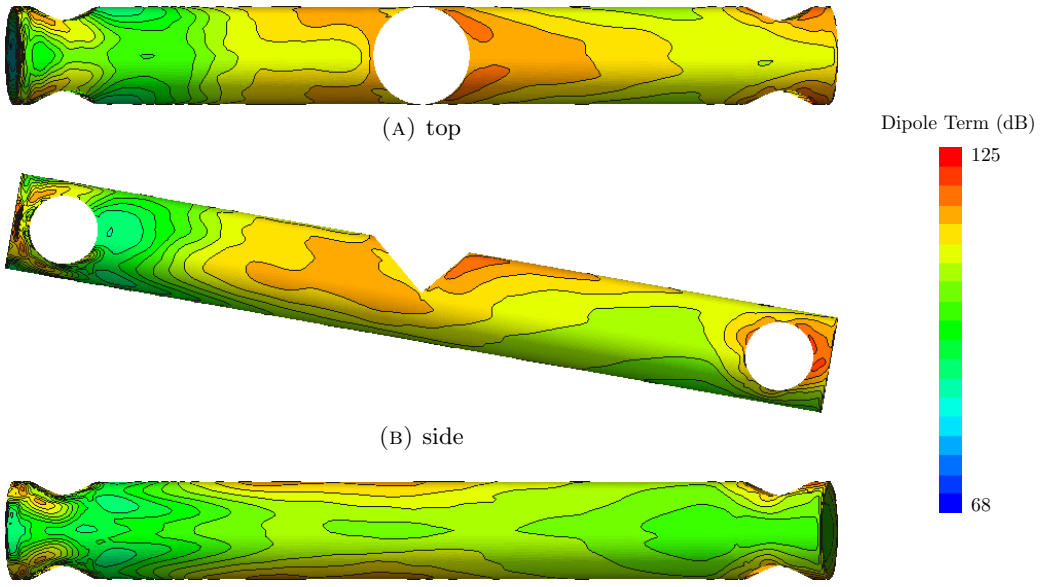

(A) top

(B) side

(C) bottom

FIGURE B.11: Magnitude of the dipole source term on the bogie of the simplified toe up configuration.

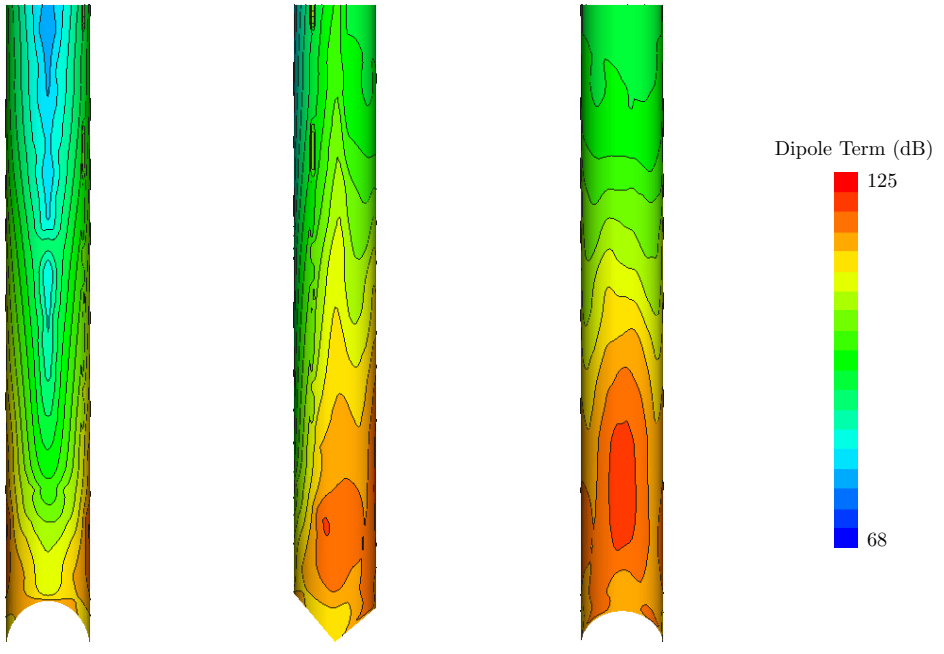

(A) front (B) side (C) rear

FIGURE B.12: Magnitude of the dipole source term on the lower half of the strut of the simplified toe up configuration.

Appendix C

Magnitude of the dipole source term of the complex main landing gear

The following figures show the magnitude of the dipole source term (equation 5.1) on the surface of the complex landing gear configurations. The magnitude of the dipole source term has been made non dimensional by multiplying it with the time step Δt of the CFD simulation ($1.0 \cdot 10^{-5}$ s) and then converted to dB using the reference pressure $2.0 \cdot 10^{-5}$ Pa. The figures are similar to the unsteady surface pressure distribution figures in chapter 8 as explained in section 5.1. The dipole source strength levels of the complex landing gear configurations are lower than those of the simple landing gear. This can be explained by the last term in equation 5.8 which is the product of the pressure at two consecutive time steps. The time step of the CFD simulations of the complex landing gear is smaller than that of the simple landing gear but the average grid spacing close to the landing gear geometry is similar. This means that the flow structures which can be resolved by the grid are of a similar size for both simulations. The smaller time step combined with similar sized flow structures increases the occurrence of consecutive pressure signals with the same sign which leads to a reduction of the dipole source strength level compared to the unsteady pressure level according to equation 5.8.

C.1 Horizontal configuration

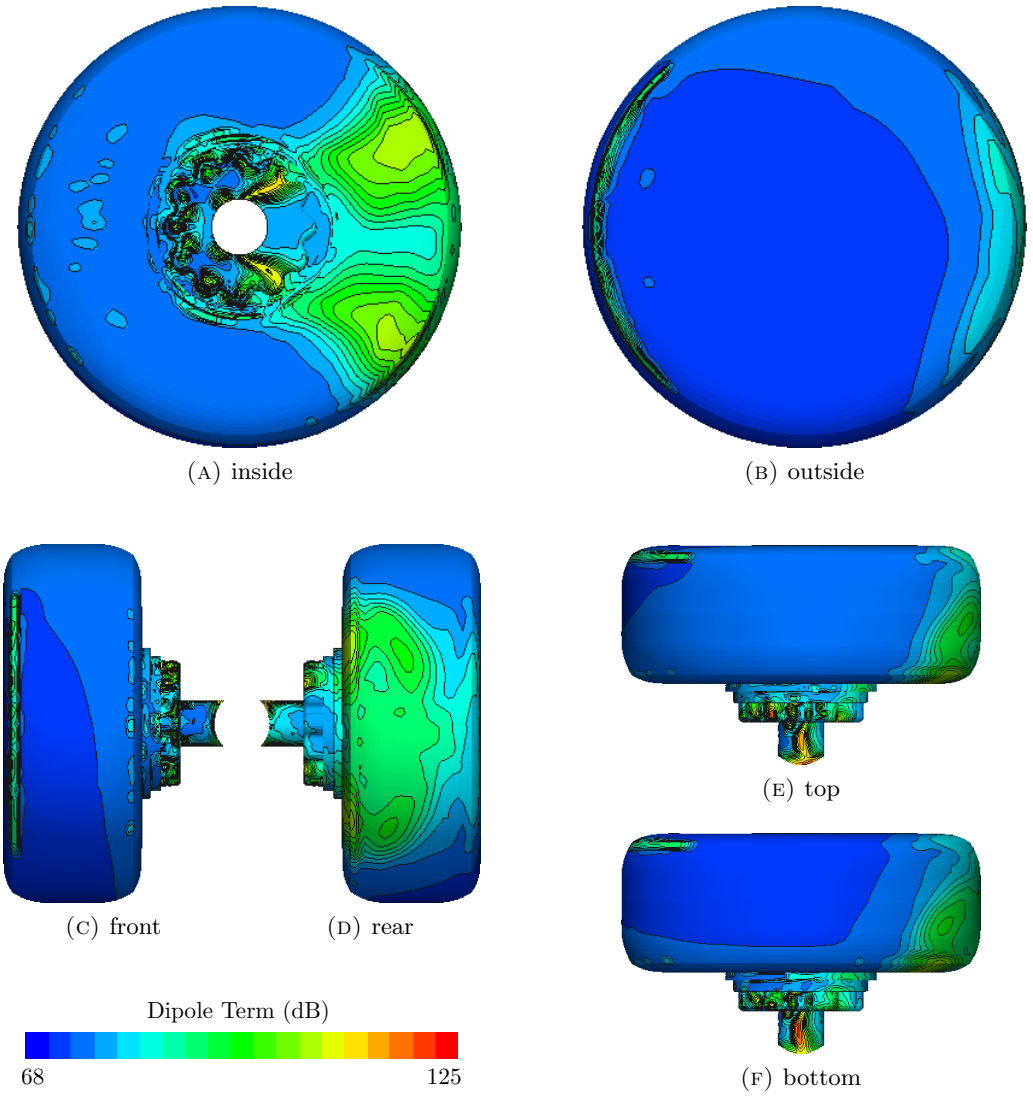

FIGURE C.1: Magnitude of the dipole source term on the forward wheel, brake and axle of the complex horizontal configuration.

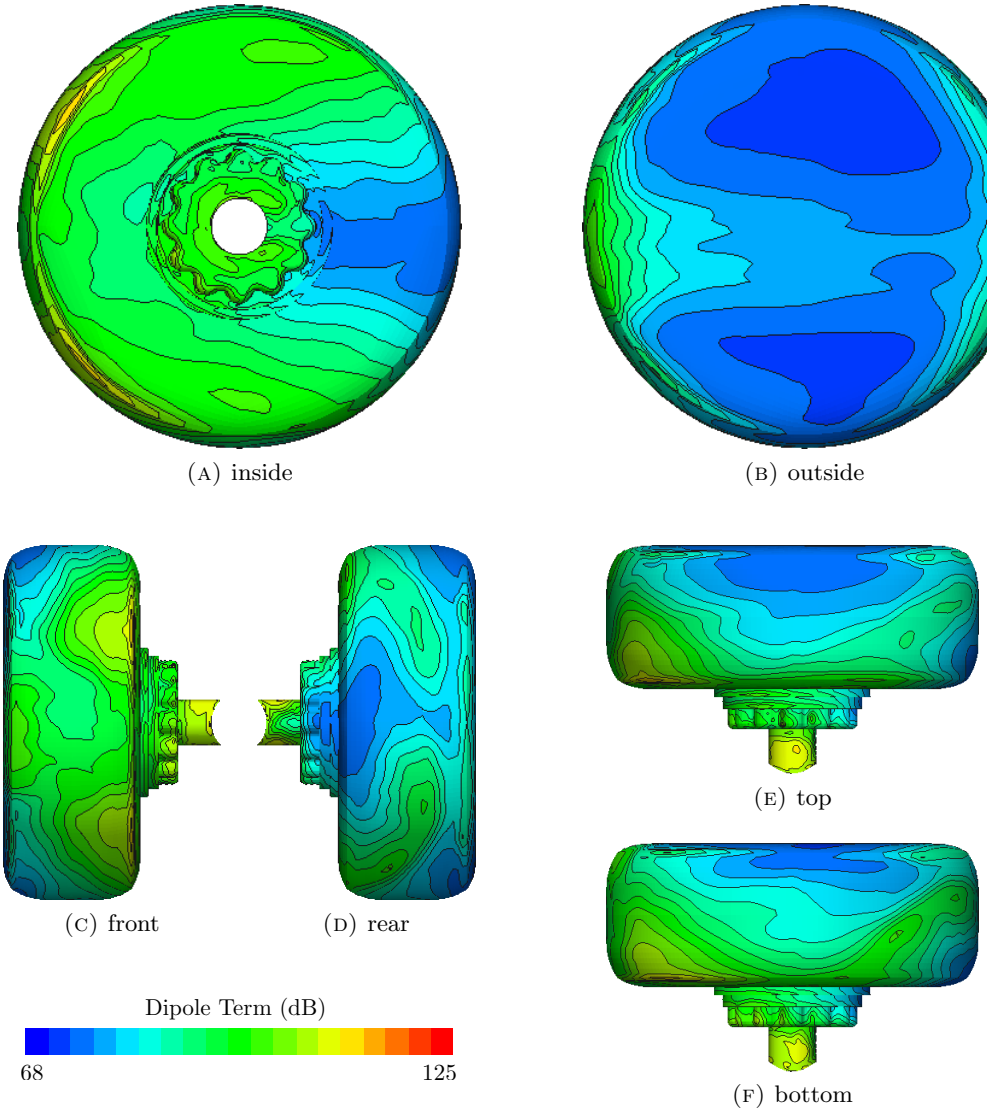

FIGURE C.2: Magnitude of the dipole source term on the rear wheel, brake and axle of the complex horizontal configuration.

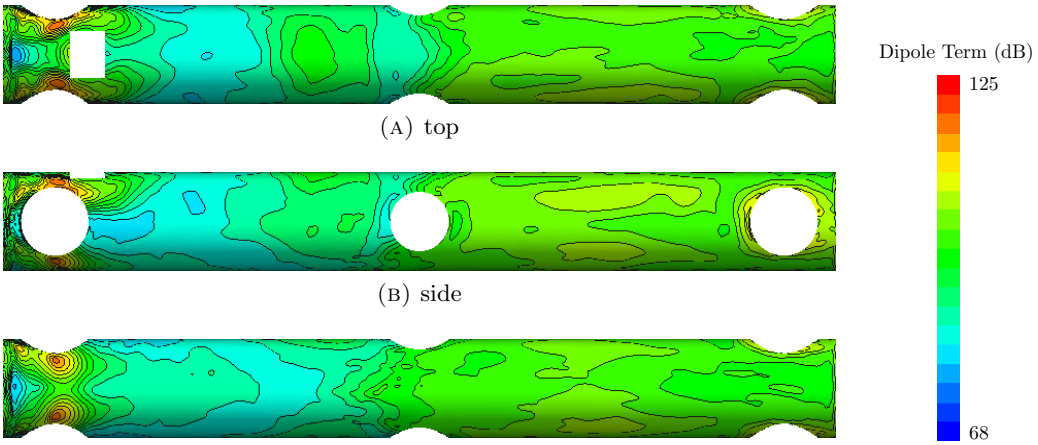

(A) top

(B) side

(C) bottom

FIGURE C.3: Magnitude of the dipole source term on the bogie of the complex horizontal configuration.

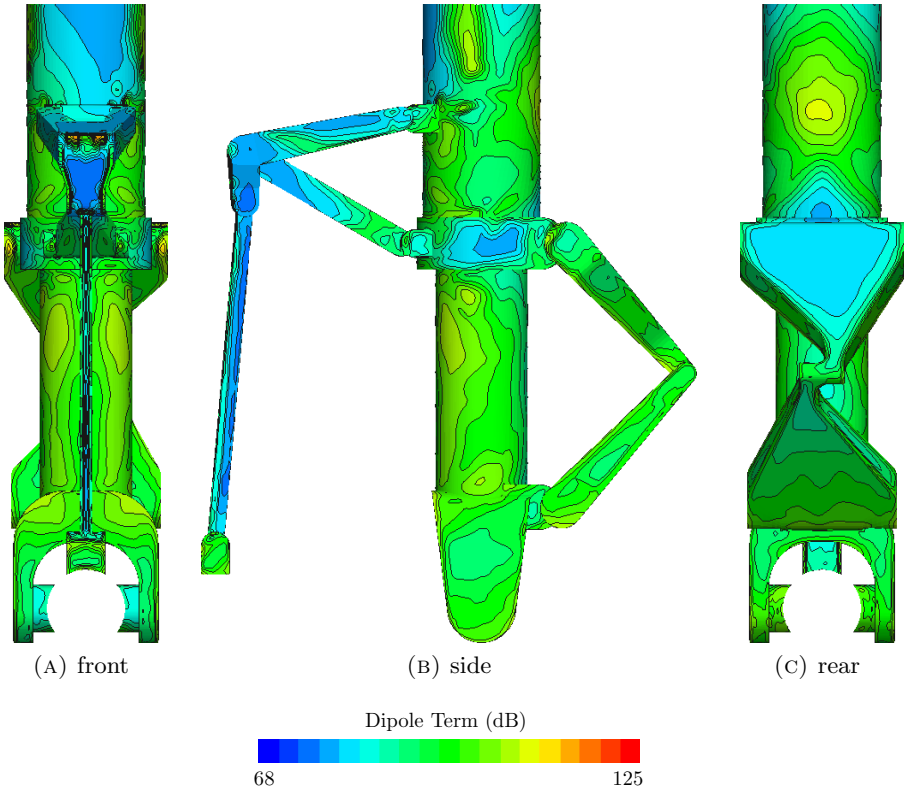

(A) front (B) side (C) rear

FIGURE C.4: Magnitude of the dipole source term on the lower half of the strut, articulation link and torque link of the complex horizontal configuration.

C.2 Toe up configuration

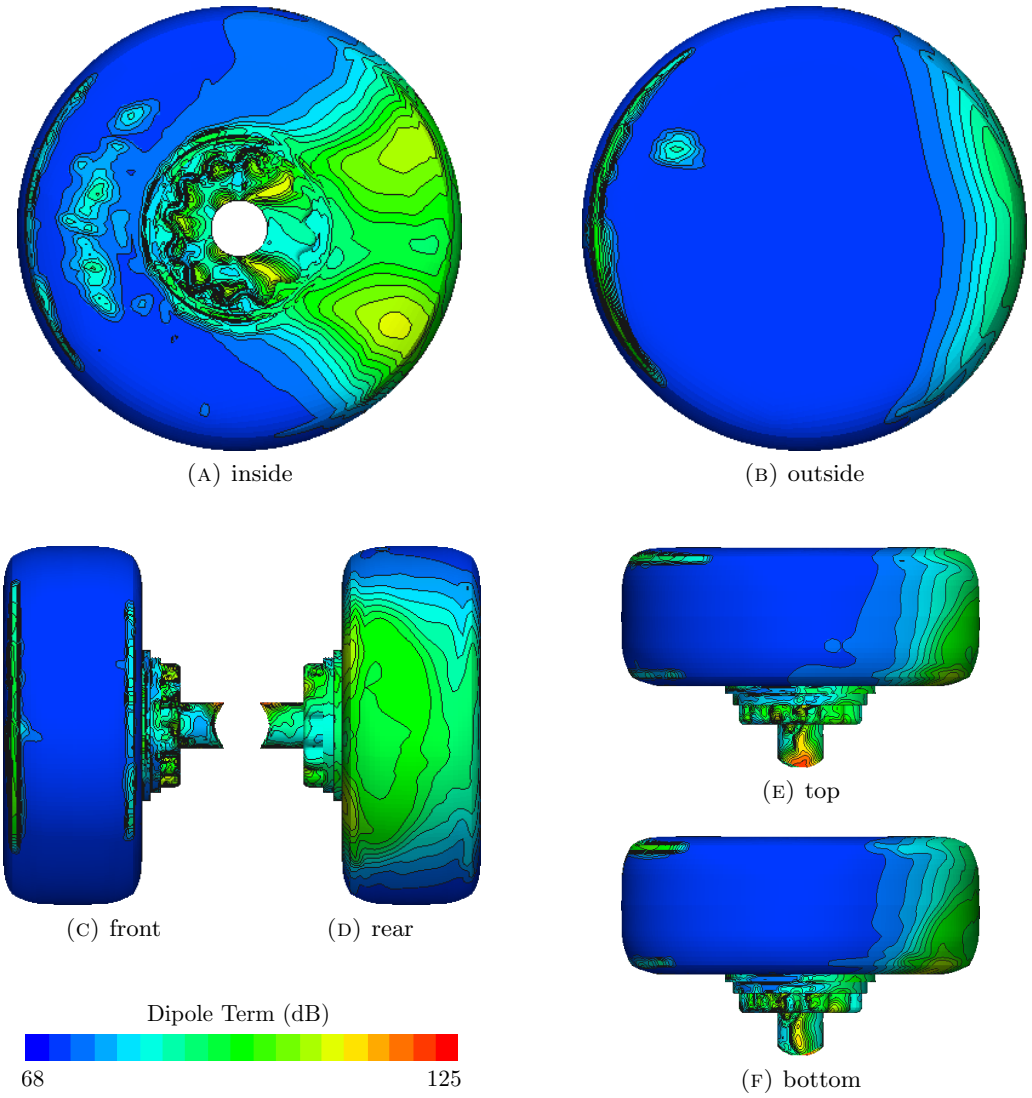

(A) inside (B) outside

(C) front (D) rear

(E) top

(F) bottom

FIGURE C.5: Magnitude of the dipole source term on the forward wheel, brake and axle of the complex toe up configuration.

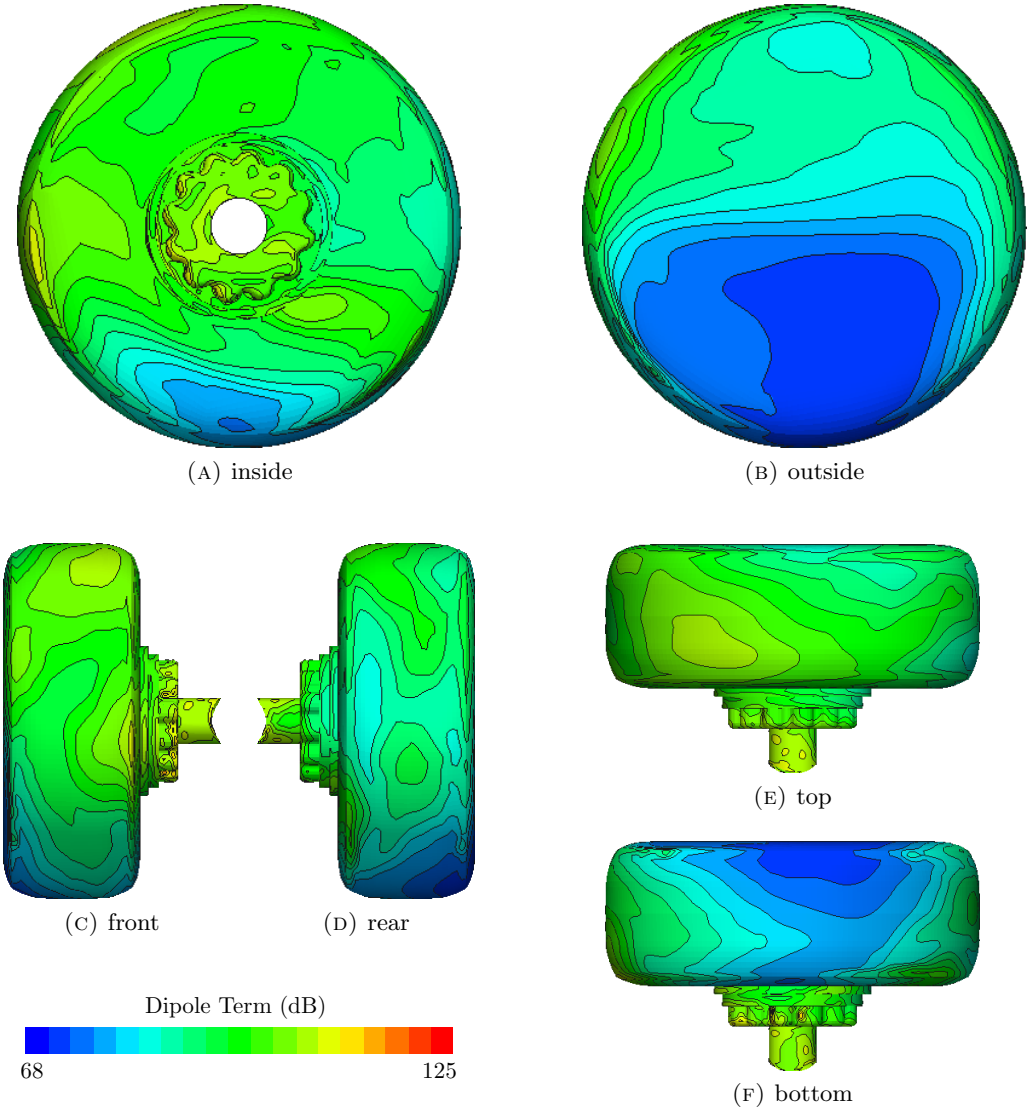

FIGURE C.6: Magnitude of the dipole source term on the rear wheel, brake and axle of the complex toe up configuration.

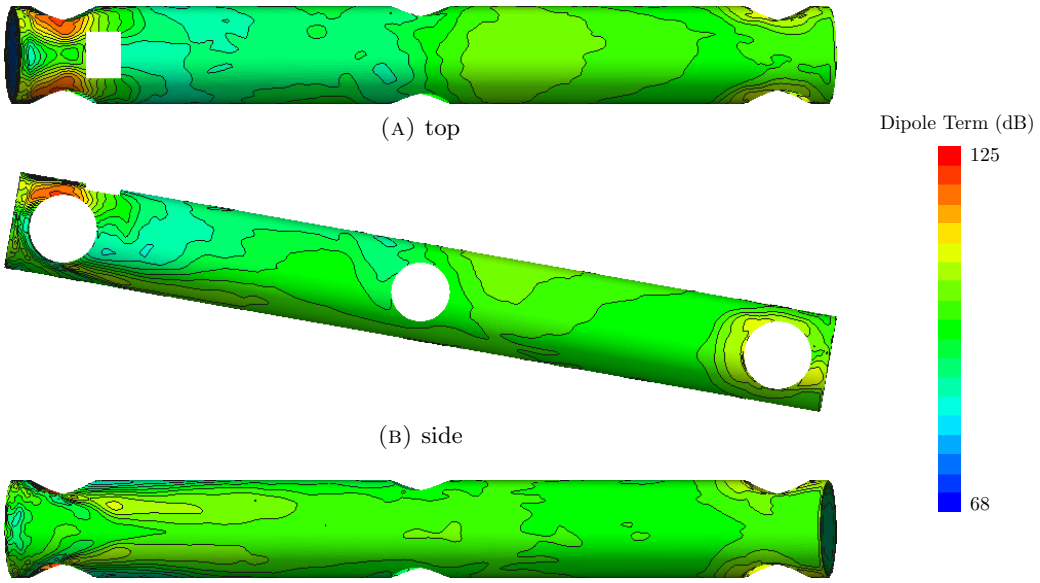

(A) top

(B) side

(C) bottom

FIGURE C.7: Magnitude of the dipole source term on the bogie of the complex toe up configuration.

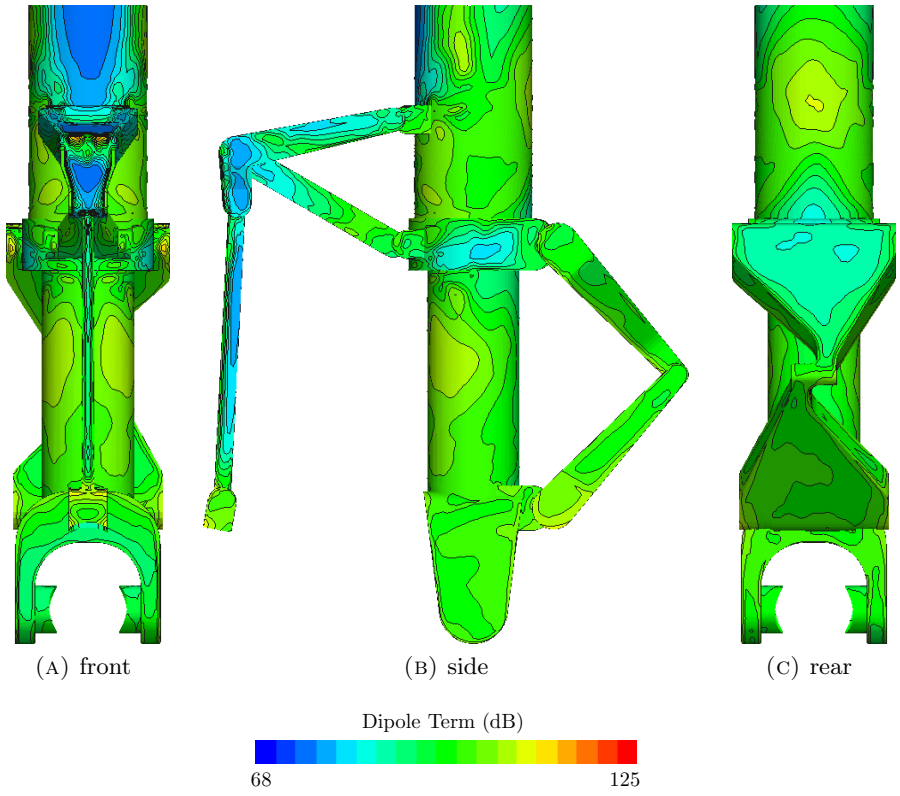

(A) front (B) side (C) rear

FIGURE C.8: Magnitude of the dipole source term on the lower half of the strut, articulation link and torque link of the complex toe up configuration.

C.3 Toe down configuration

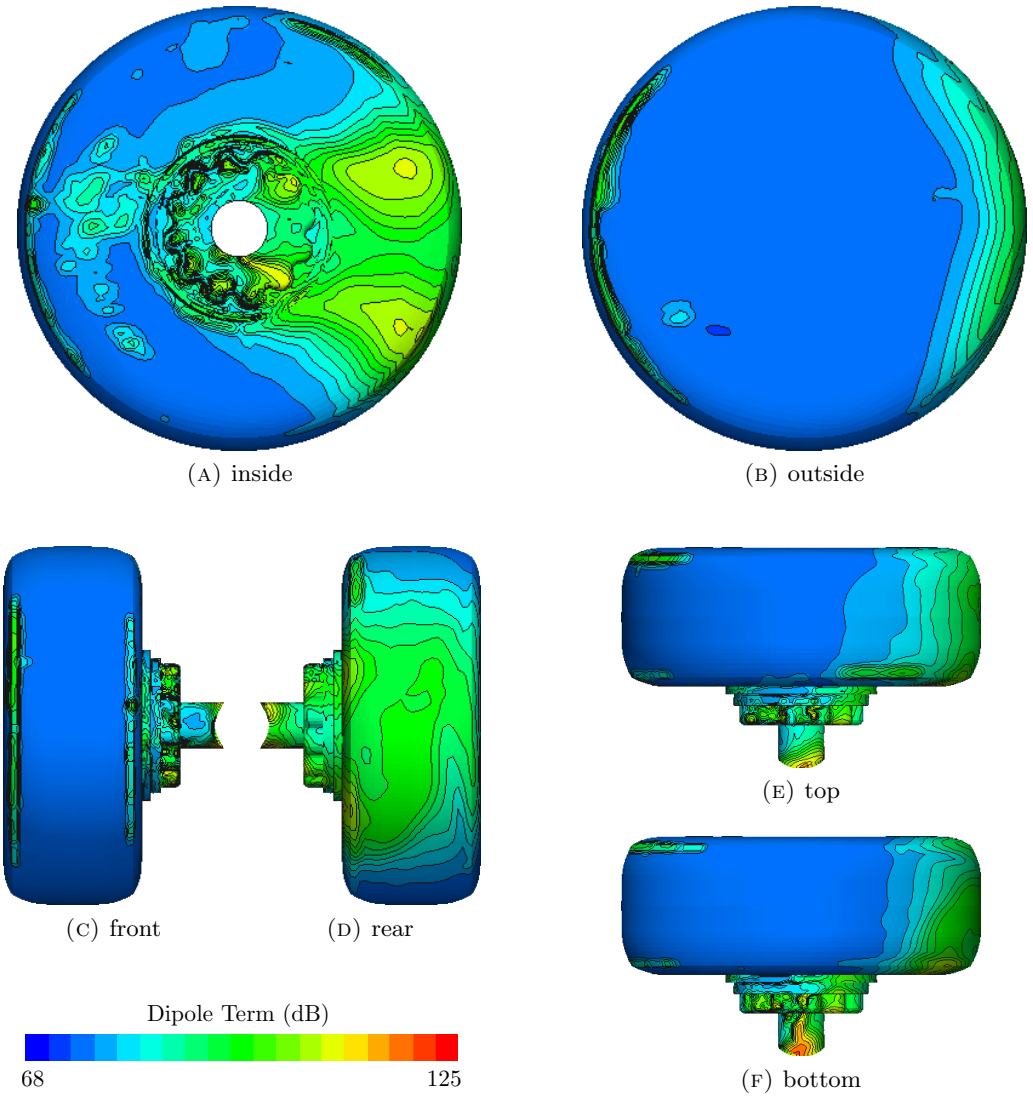

FIGURE C.9: Magnitude of the dipole source term on the forward wheel, brake and axle of the complex toe down configuration.

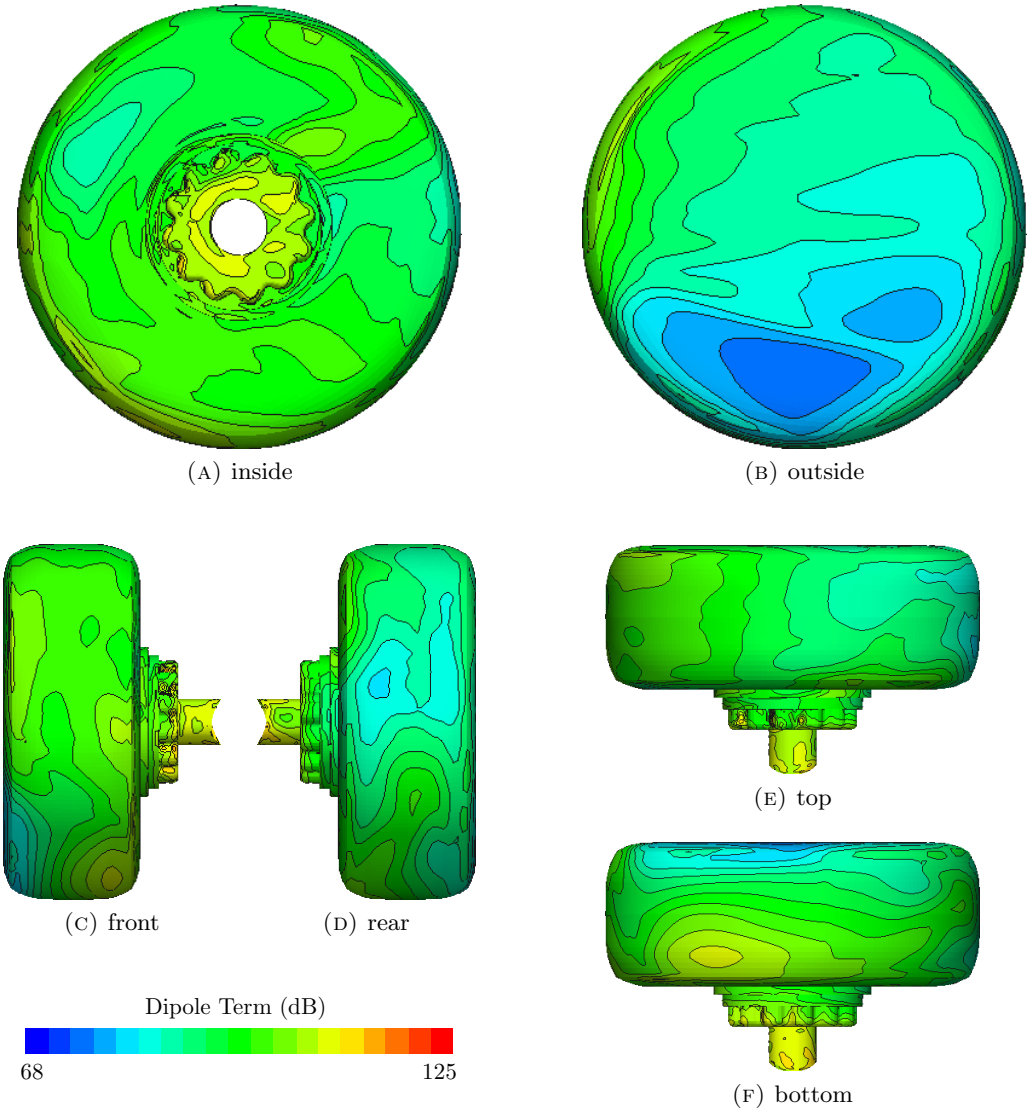

FIGURE C.10: Magnitude of the dipole source term on the rear wheel, brake and axle of the complex toe down configuration.

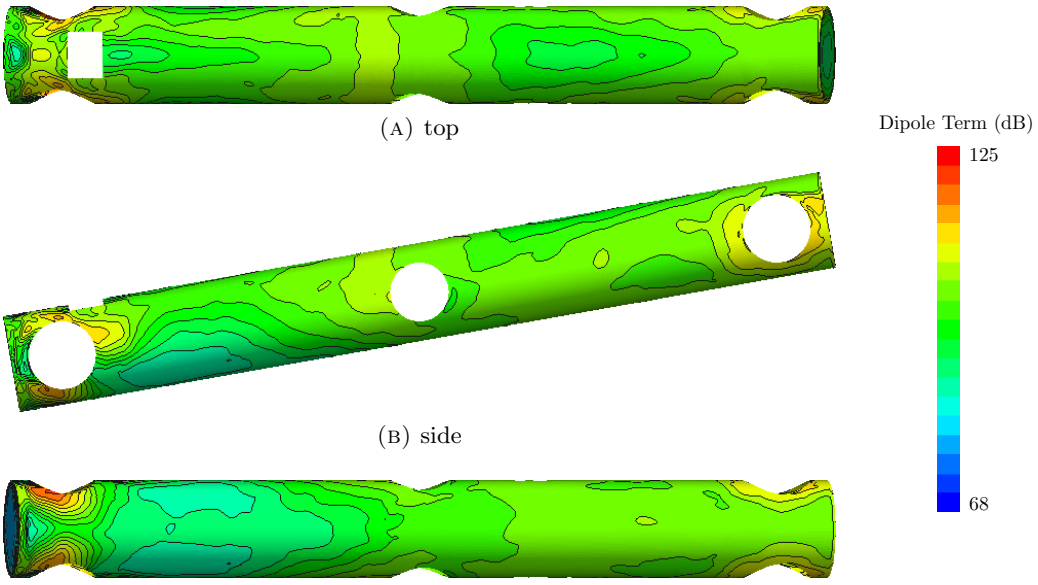

(A) top

(B) side

(C) bottom

FIGURE C.11: Magnitude of the dipole source term on the bogie of the complex toe down configuration.

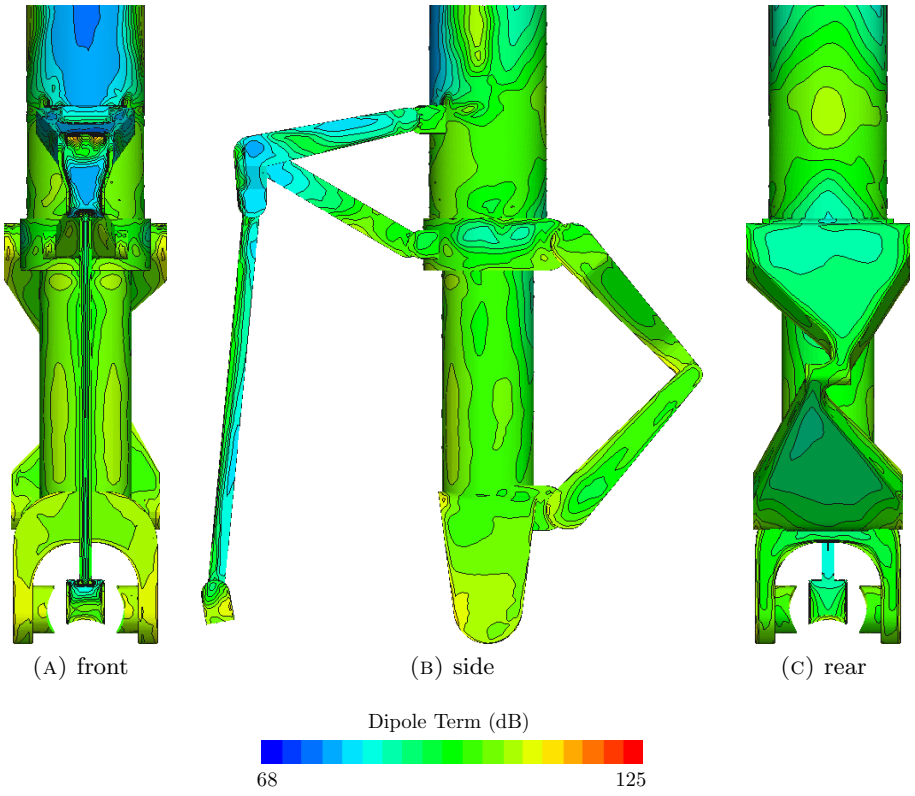

(A) front (B) side (C) rear

FIGURE C.12: Magnitude of the dipole source term on the lower half of the strut, articulation link and torque link of the complex toe down configuration.

Bibliography

[1] K.J. van Mierlo, K. Takeda, and E. Peers. Computational analysis of the effect of bogie inclination angle on landing gear noise. In *16th AIAA/CEAS Aeroacoustics Conference*. American Institute of Aeronautics and Astronautics, June 2010.

[2] K.J. van Mierlo and X. Zhang. Analysis of the aerodynamics and noise radiation of a complex main landing gear. In *submitted to the AIAA/CEAS Aeroacoustics Conference*, 2014.

[3] L.C. Chow, K. Mau, and H. Remy. Landing gears and high lift devices airframe noise research. *8 th AIAA/CEAS Aeroacoustics Conference and Exhibit, Breckenridge, CO*, 2002.

[4] W.M. Dobrzynski, B. Schöning, L.C. Chow, C. Wood, M. Smith, and C. Seror. Design and testing of low noise landing gears. *International Journal of Aeroacoustics*, 5(3):233–262, 2006.

[5] Y. Li, M.G. Smith, X. Zhang, and N. Molin. Noise sources control of an aircraft landing gear. *13th AIAA/CEAS Aeroacoustics Conference (28th AIAA Aeroacoustics Conference)*, 2007.

[6] L.S. Hedges, A.K. Travin, and P.R. Spalart. Detached-Eddy Simulations Over a Simplified Landing Gear. *Journal of Fluids Engineering*, 124:413, 2002.

[7] P.R. Spalart, S. Deck, M.L. Shur, K.D. Squires, M.K. Strelets, and A. Travin. A New Version of Detached-eddy Simulation, Resistant to Ambiguous Grid Densities. *Theoretical and Computational Fluid Dynamics*, 20(3):181–195, 2006.

[8] M.J. Lighthill. On Sound Generated Aerodynamically. I. General Theory. *Proceedings of the Royal Society of London. Series A, Mathematical and Physical Sciences*, 211(1107):564–587, 1952.

[9] N. Curle. The Influence of Solid Boundaries upon Aerodynamic Sound. *Proceedings of the Royal Society of London. Series A, Mathematical and Physical Sciences*, 231 (1187):505–514, 1955.

[10] J.E. Ffowcs Williams and D.L. Hawkings. Sound Generation by Turbulence and Surfaces in Arbitrary Motion. *Philosophical Transactions of the Royal Society of London. Series A, Mathematical and Physical Sciences*, 264(1151):321–342, 1969.

[11] P.A.M. Dirac. *The Principles of Quantum Mechanics. 3d ed.* Oxford, at the Clarendon Press, 1947.

[12] V.S. Vladimirov. *Generalized functions in mathematical physics. Translated from the second Russian edition by G. Yankovskii.* Mir, Moscow, 1979.

[13] J. Piet, U. Michel, and P. Boehning. Localization of the acoustic sources of the A340 with a large phased microphone array during flight tests. *8 th AIAA/CEAS Aeroacoustics Conference and Exhibit, Breckenridge, CO*, 2002.

[14] P. Sijtsma and R.W. Stoker. Determination of absolute contributions of aircraft noise components using fly-over array measurements. *Collection of Technical Papers - 10th AIAA/CEAS Aeroacoustics Conference*, 2:1780 – 1793, 2004. Fly-over array measurements;Frequency index;Microphone indices;Source power integration;.

[15] W.H. Herkes, R.F. Olsen, and S. Uellenberg. The quiet technology demonstrator program: Flight validation of airplane noise-reduction concepts. *12th AIAA/CEAS Aeroacoustics Conference*, 2006.

[16] H. Siller, U. Michel, C. Zwiener, and G. Saueressig. Reduction of approach noise of the md-11. *12th AIAA/CEAS Aeroacoustics Conference*, 2006.

[17] J.F. Piet, L.C. Chow, F. Laporte, and H. Remy. Flight test investigation of high-lift devices and landing gear modifications to achieve airframe noise reduction. *eccomas*, 2004.

[18] H.H. Heller and W.M. Dobrzynski. Sound Radiation from Aircraft Wheel-Well/Landing Gear Configurations. *Journal of Aircraft*, 14(8):768–774, 1977.

[19] F.R. Grosche, G. Schneider, and H. Stiewitt. Wind tunnel experiments on airframe noise sources of transport aircraft. *AIAA*, 1997.

[20] J.C. Hardin. Toward a comprehensive analysis of landing approach noise sources. *AIAA/CEAS Aeroacoustics Conference, 3 rd, Atlanta, GA, Proceedings*, pages 67–76, 1997.

[21] J.A. Hayes, W.C. Horne, P.T. Soderman, and P.H. Bent. Airframe Noise Characteristics of a 4.7% Scale DC-10 Model. *AIAA Paper*, 1594(3), 1997.

[22] P. Soderman, F. Kafyeke, N. Burnside, R. Chandrasekharan, S. Jaeger, and J. Boudreau. Airframe noise study of a CRJ-700 aircraft model in the NASA Ames 7- by 10-Foot Wind Tunnnel No. 1. *8 th AIAA/CEAS Aeroacoustics Conference and Exhibit, Breckenridge, CO*, 2002.

[23] R.W. Stoker, J.R. Underbrink, and G.R. Neubert. Investigations of airframe noise in pressurized wind tunnels. *AIAA*, 2001.

[24] B.S. Lazos. Mean flow features around the inline wheels of four-wheel landing gear. *AIAA Journal*, 40(2):193–198, 2002.

[25] B.S. Lazos. Surface topology on the wheels of a generic four-wheel landing gear. *AIAA Journal*, 40:2402– 2411, 2002.

[26] W. Dobrzynski and H. Buchholz. Full-scale noise testing on Airbus landing gears in the German Dutch Wind tunnel. *AIAA/CEAS Aeroacoustics Conference, 3 rd, Atlanta, GA, Proceedings*, pages 98–111, 1997.

[27] G.J.J. Ruijgrok. *Elements of Aviation Acoustics*. Delft University Press, 1993.

[28] W. Dobrzynski, L.C. Chow, P. Guion, and D. Shiells. A European study on landing gear airframe noise sources. *AIAA/CEAS, Aeroacoustics Conference and Exhibit, 6 th(21 st AIAA Aeroacoustics Conference), Lahaina, HI*, 2000.

[29] W. Dobrzynski, L.C. Chow, P. Guion, and D. Shiells. Research into Landing Gear Airframe Noise Reduction. *AIAA/CEAS Meeting Paper*, 2409, 2002.

[30] S.M. Jaeger, N.J. Burnside, P.T. Soderman, W.C. Horne, and K.D. James. Microphone Array Assessment of an Isolated 26%-Scale, High-Fidelity Landing Gear. *AIAA Paper*, 2410:2002, 2002.

[31] P.A. Ravetta, R.A. Burdisso, and W.F. Ng. Wind Tunnel Aeroacoustic Measurements of a 26%-scale 777 Main Landing Gear Model. *10th AIAA/CEAS Aeroacoustics Conference, AIAA Paper*, 2885, 2004.

[32] P.A. Ravetta, R.A. Burdisso, and W.F. Ng. Noise control of landing gears using elastic membrane-based fairings. *13th AIAA/CEAS Aeroacoustics Conference (28th AIAA Aeroacoustics Conference)*, 2007.

[33] P.A. Ravetta. *LORE Approach for Phased Array Measurements and Noise Control of Landing Gears*. PhD thesis, Virginia Polytechnic Institute and State University, 2005.

[34] M.C. Remillieux, H.E. Camargo, P.A. Ravetta, R.A. Burdisso, and W.F. Ng. Novel kevlar-walled wind tunnel for aeroacoustic testing of a landing gear. *AIAA Journal*, Vol. 46, No. 7, 2008.

[35] M.C. Remillieux, H.E. Camargo, R.A. Burdisso, and W.F. Ng. Aeroacoustic study of a 26landing gear in a semi-anechoic-wind-tunnel test section. *13th AIAA/CEAS Aeroacoustics Conference (28th AIAA Aeroacoustics Conference)*, 2007.

[36] W.M. Humphreys and T.F. Brooks. Noise spectra and directivity for a scale-model landing gear. *13th AIAA/CEAS Aeroacoustics Conference (28th AIAA Aeroacoustics Conference)*, 2007.

[37] C.L. Burley, T.F. Brooks, W.M. Humphreys, and J.W. Rawls. Anopp landing gear noise prediction comparisons to model-scale data. *13th AIAA/CEAS Aeroacoustics Conference (28th AIAA Aeroacoustics Conference)*, 2007.

[38] M.G. Smith, B. Fenech, L.C. Chow, W. Dobrzynski, and C. Seror. Control of Noise Sources on Aircraft Landing Gear Bogies. *12 th AIAA/CEAS Aeroacoustics Conference(27 th AIAA Aeroacoustics Conference)*, 2006.

[39] A.R. Quayle, A.P. Dowling, H. Babinsky, W.R. Graham, and Y Liu. Phased array measurements from landing gear models. *13th AIAA/CEAS Aeroacoustics Conference (28th AIAA Aeroacoustics Conference)*, 2007.

[40] M.C. Remillieux, H.E. Camargo, P.A. Ravetta, R.A. Burdisso, and W.F. Ng. Noise reduction of a model-scale landing gear measured in the virginia tech aeroacoustic wind tunnel. *14th AIAA/CEAS Aeroacoustics Conference (29th AIAA Aeroacoustics Conference)*, 2008.

[41] K. Boorsma, X. Zhang, and Molin N. Perforated fairings for landing gear noise control. *14th AIAA/CEAS Aeroacoustics Conference (29th AIAA Aeroacoustics Conference)*, 2008.

[42] M.G. Smith and L.C. Chow. Prediction method for aerodynamic noise from aircraft landing gear. *AIAA/CEAS Aeroacoustics Conference, 4 th(19 th AIAA Aeroacoustics Conference), Toulouse, France, Collection of Technical Papers. Pt. 1*, pages 153–161, 1998.

[43] M.G. Smith and L.C. Chow. Validation of a Prediction model for Aerodynamic Noise from Aircraft Landing Gear. *AIAA*, 2002.

[44] N. Molin, J.F. Piet, L.C. Chow, M. Smith, W.M. Dobrzynski, and C. Seror. Prediction of low noise aircraft landing gears and comparison with test results. *12 th AIAA/CEAS Aeroacoustics Conference(27 th AIAA Aeroacoustics Conference)*, 2006.

[45] Y.P. Guo, K.J. Yamamoto, and R.W. Stocker. An Empirical Model for Landing Gear Noise Prediction. *AIAA/CEAS Meeting Paper*, 2888, 2004.

[46] Y.P. Guo. Empirical prediction of aircraft landing gear noise. Technical report, NASA, 2005.

[47] Y.P. Guo. A Semi-Empirical Model for Aircraft Landing Gear Noise Prediction. *12 th AIAA/CEAS Aeroacoustics Conference(27 th AIAA Aeroacoustics Conference)*, 2006.

[48] Y.P. Guo, K.J. Yamamoto, and R.W. Stoker. Experimental study on aircraft landing gear noise. *Journal of Aircraft*, 43, 2006.

[49] Y.P. Guo. A component-based model for aircraft landing gear noise prediction. *Journal of Sound and Vibration*, 312:801–820, 2008.

[50] L.V. Lopes, K.S. Brentner, P.J. Morris, G.M. Lilley, and D.P. Lockard. Complex Landing Gear Noise Prediction Using a Simple Toolkit. *43 rd AIAA Aerospace Sciences Meeting and Exhibit*, 2005.

[51] M. Smith, J. Carrilho, N. Molin, J-F Piet, and L.C. Chow. Modelling landing gear noise with installation effects. *13th AIAA/CEAS Aeroacoustics Conference (28th AIAA Aeroacoustics Conference)*, 2007.

[52] Y. Guo. A study on local flow variations for landing gear noise research. *14th AIAA/CEAS Aeroacoustics Conference (29th AIAA Aeroacoustics Conference)*, 2008.

[53] F.J. Souliez, L.N. Long, P.J. Morris, and A. Sharma. Landing gear aerodynamic noise prediction using unstructured grids. *International Journal of Aeroacoustics*, 1(2):115–135, 2002.

[54] F. Li, M.R. Khorrami, and M.R. Malik. Unsteady Simulation of a Landing-Gear Flow Field. *Conference Paper, 8th AIAA/CEAS Aeroacoustics Conference*, 2002.

[55] D.P. Lockard, M.R. Khorrami, and F. Li. Aeroacoustic analysis of a simplified landing gear. *9 th AIAA/CEAS Aeroacoustics Conference and Exhibit*, 2003.

[56] D.P. Lockard, M.R. Khorrami, and F. Li. High Resolution Calculation of a Simplified Landing Gear. *10 th AIAA/CEAS Aeroacoustics Conference*, 2004.

[57] M.R. Khorrami and D.P. Lockard. A landing gear noise reduction study based on computational simulations. In *Inter-Noise 2006*, 2006.

[58] C. Seror, P. Sagaut, and A. Belanger. A Numerical Aeroacoustic Analysis of a Detailed Landing Gear. *10th AIAA/CEAS Aeroacoustics Conference*, 2004.

[59] Y. Li, R. Sattiy, P. Lewz, R. Shock, and S. Noelting. Computational aeroacoustic analysis of flow around a complex nose landing gear configuration. *14th AIAA/CEAS Aeroacoustics Conference (29th AIAA Aeroacoustics Conference)*, 2008.

[60] Philippe R. Spalart. Rudimentary landing gear - 4 wheel. online, June 2010. URL `https://info.aiaa.org/tac/ASG/FDTC/DG/BECAN_files_/Workshop_June_2010_Final_problem_Statements/Problem%203%20--%20Rudimentary%20Landing%20Gear/Problem_Statement_Rudimentary%20LG-4Wheel_v1.0.pdf`.

[61] L. Venkatakrishnan, N. Karthikeyan, and K. Mejia. Experimental studies on a rudimentary four-wheel landing gear. *AIAA journal*, 50(11):2435–2447, 2012. ISSN 0001-1452.

[62] P.R. Spalart, M.L. Shur, M.K. Strelets, and A.K. Travin. Initial noise predictions for rudimentary landing gear. *Journal of Sound and Vibration*, 2011.

[63] P. Spalart and K. Mejia. Analysis of experimental and numerical studies of the rudimentary landing gear. In *Aerospace Sciences Meetings*. American Institute of Aeronautics and Astronautics, 2011.

[64] P.R. Spalart. *Young-person's Guide to Detached-eddy Simulation Grids*. National Aeronautics and Space Administration, Langley Research Center; Available from NASA Center for Aerospace Information, 2001.

[65] H.G. Weller, G. Tabor, H. Jasak, and C. Fureby. A tensorial approach to computational continuum mechanics using object-oriented techniques. *Computers in physics*, 1998.

[66] H. Jasak. *Error analysis and estimation for the finite volume method with applications to fluid flows*. PhD thesis, 1996.

[67] G. Karypis and V. Kumar. A fast and highly quality multilevel scheme for partitioning irregular graphs. *SIAM Journal on Scientific Computing*, 1999.

[68] M. Shur, P.R. Spalart, M. Strelets, and A. Travin. Detached-eddy simulation of an airfoil at high angle of attack. *4th Int. Symposium on Eng. Turb. Modeling and Experiments*, 1999.

[69] R.S. Laramee, B. Jobard, and H. Hauser. Image space based visualization of unsteady flow on surfaces. In *Proceedings of the 14th IEEE Visualization 2003 (VIS'03)*, VIS '03, pages 18–, Washington, DC, USA, 2003. IEEE Computer Society. ISBN 0-7695-2030-8. doi: 10.1109/VISUAL.2003.1250364. URL `http://dx.doi.org/10.1109/VISUAL.2003.1250364`.

[70] *Fluent user manual*. URL `http://www.fluentusers.com`.

[71] J. McManus and X. Zhang. A computational study of the flow around an isolated wheel in contact with the ground. *Journal of fluids engineering*, 128:520–530, 2006.

[72] M. Minguez, R. Pasquetti, and E. Serre. High-order large-eddy simulation of flow over the ahmed body car model. *Physics of Fluids*, 20, 2008.

[73] D. Angland. *Aerodynamics and Aeroacoustics of Flap Side-Edges*. PhD thesis, University of Southampton, 2008.

[74] P.J. Roache. Quantification of uncertainty in computational fluid dynamics. *Annual Review of Fluid Mechanics*, 29:123–160, 1997.

[75] P.R. Spalart. Detached-eddy simulation. *Annual Review of Fluid Mechanics*, 41: 181–202, 2009.

[76] I. Celik, M. Klein, M. Freitag, and J. Janicka. Assessment measures for uran-s/des/les: an overview with applications. *Journal of Turbulence*, (7), 2006.